

---

**Kohärenz auf reaktiven Potentialflächen:  
Beobachtung und Analyse molekularer Dynamik**

Christian Schriever

---



Dissertation

München 2008



---

**Kohärenz auf reaktiven Potentialflächen:  
Beobachtung und Analyse molekularer Dynamik**

Christian Schriever

---

Dissertation  
an der Fakultät für Physik  
der Ludwig-Maximilians-Universität  
München

vorgelegt von  
Christian Schriever  
aus Zwiesel

München, im April 2008

1. Gutachter: Prof. Dr. E. Riedle

2. Gutachter: Prof. Dr. J. Rädler

Tag der mündlichen Prüfung: 9. Juli 2008

## Kurzfassung

Schwingungswellenpakete sind kohärente Überlagerungen von Eigenzuständen einer elektronischen Potentialfläche und liefern in gebundenen Potentialen den Nachweis atomarer Bewegungen in Molekülen. Während die klassische, chemische Reaktionskinetik Übergänge zwischen Konformationen durch Ratenprozesse beschreibt, wird in der vorliegenden Arbeit gezeigt, dass die korrekte Modellierung ultraschneller Prozesse als Wellenpaketbewegung erfolgen muss. Die reaktive Wellenpaketdynamik und interne Konversion in mittelgroßen Molekülen wird erstmals in Gasphase und in Lösung unter Verwendung desselben Abfrageprozesses in Echtzeit beobachtet und miteinander verglichen. Quantenchemische Rechnungen ermöglichen die Analyse der Wellenpaketbewegung und den Rückschluss auf den Reaktionspfad.

Durch technologische Weiterentwicklungen der Anrege-Abtast-Spektroskopie mit 20 fs Zeitauflösung wird eine Sensitivität von  $1,1 \times 10^{-6}$  OD erreicht. Eine langbrennweitige Fokussierung erlaubt große Strahltaillen und Probendicken von bis zu 50 mm. Ohne Veränderungen am Spektrometer können erstmalig gasförmige Proben von Molekülen mit niedrigem Dampfdruck und gelöste Proben im direkten Vergleich untersucht werden.

Die Formung sichtbarer Impulse in Phase und Amplitude und nachfolgende gestreckte Summenfrequenzmischung ermöglicht erstmals die Erzeugung strukturierter UV-Impulse mit sub-20 fs Strukturen. Diese UV-Impulse erlauben nicht nur die Beobachtung der Wellenpaketbewegung sondern auch deren selektive Anregung und Manipulation. Für die Erzeugung kurzer, abstimbarer Impulse bei Repetitionsraten von bis zu 2 MHz wird das Konzept des nichtkollinearen optisch parametrischen Verstärkers (NOPA) den Anforderungen neuer, hochrepetierender Faserlasersysteme angepasst. Durch Abstimmung des NOPAs und einfache Frequenzverdopplung werden sub-30 fs Impulse zwischen 250 und 990 nm mit einer Dauer bis hinab zu 13,4 fs und einer Energie von bis zu 860 nJ erzeugt.

Ultraschneller intramolekularer Protontransfer im elektronisch angeregten Zustand (ESIPT) und die nachfolgende interne Konversion werden als prototypische, ultraschnelle, reaktive Prozesse untersucht und detaillierte Bilder der Reaktionsmechanismen entwickelt. Durch Deuterierung wird gezeigt, dass die Masse des Protons keinen Einfluss auf die Geschwindigkeit des ESIPT sowie die reaktive Wellenpaketdynamik hat und der ESIPT damit als ballistische Wellenpaketbewegung und nicht als Tunnelprozess abläuft. Anhand eines Moleküls mit mehreren parallelen Reaktionskanälen wird gezeigt, dass jedem Reaktionspfad eine eigene Wellenpaketdynamik zugeordnet werden kann und die Wellenpaketdynamik eindeutig durch den reaktiven Prozess und nicht durch die optische Anregung ausgelöst wird. Der Vergleich zwischen einem Molekül mit flexiblem Gerüst und einem mit steifem Gerüst klärt den Einfluss interner Freiheitsgrade auf den reaktiven Prozess. Ein steiferes Molekülskelett führt durch höherfrequente Normalmoden zu einer Beschleunigung des Protontransferprozesses.

Vergleichende Messungen in mehreren Lösungsmitteln und in der Gasphase erlauben den Einfluss der Reaktionsumgebung, speziell der sterischen Freiheitsgrade und der Energiedissipation zur Umgebung, auf die Wellenpaketdynamik und die nachfolgende interne Konversion zu untersuchen. Die Protontransferzeit von weniger als 50 fs und die ESIPT induzierte Wellenpaketdynamik hängen nicht von der Reaktionsumgebung ab. Speziell läuft die Dephasierung der vibratorischen Wellenpakete in den hier untersuchten mittelgroßen, reaktiven Molekülen in Gasphase und in Lösung mit einer Zeitkonstante von etwa 1 ps gleich schnell ab, ist also durch intramolekulare Prozesse dominiert. Die Dephasierungszeit gibt das Zeitfenster für Kontrollexperimente vor, die vibratorische Kohärenzen ausnutzen. Die interne Konversion durch eine konische Durchschneidung läuft in der Gasphase mit einer Rate von  $(2,6 \text{ ps})^{-1}$  mehr als 40-mal schneller ab als in Lösung, da ohne die sterischen Hinderungen angrenzender Lösungsmittelmoleküle die Geometrie des konischen Schnitts schneller eingenommen werden kann.



# Veröffentlichungen

Die vorliegende Arbeit beruht auf folgenden eigenen Veröffentlichungen und Manuskripten, die im Anhang abgedruckt sind.

- 01     **"Tunable pulses from below 300 to 970 nm with durations down to 14 fs based on a 2 MHz ytterbium-doped fiber system"**  
C. Schriever, S. Lochbrunner, P. Krok, and E. Riedle  
Opt. Lett. 33, 192 – 194 (2008).
- 02     **"Octave wide tunable UV-pumped NOPA: pulses down to 20 fs at 0.5 MHz repetition rate"**  
C. Homann, C. Schriever, P. Baum, and E. Riedle  
Opt. Express 16, 5746 – 5756 (2008).
- 03     **"19 femtosecond shaped ultraviolet pulses"**  
C. Schriever, S. Lochbrunner, M. Optiz, and E. Riedle  
Opt. Lett. 31, 543 – 545 (2006).
- 04     **"Ultrasensitive ultraviolet-visible 20 fs absorption spectroscopy of low vapor pressure molecules in the gas phase"**  
C. Schriever, S. Lochbrunner, E. Riedle, and D. J. Nesbitt  
Rev. Sci. Instrum. 79, 013107 (2008).
- 05     **"Direct Observation of the Nuclear Motion during Ultrafast Intramolecular Proton Transfer"**  
S. Lochbrunner, C. Schriever, and E. Riedle  
in *Hydrogen-Transfer Reactions*, J. T. Hynes, J. P. Klinman, H.-H. Limbach, and R. L. Schowen, (Eds.), Wiley-VCH, Weinheim, pp. 349 – 375 (2006).
- 06     **"Can multidimensional wave packet dynamics be distinguished from tunneling?"**  
C. Schriever, S. Lochbrunner, A. Ofial, and E. Riedle  
Manuskript vorbereitet zur Einreichung an Phys. Rev. Lett. (2008).
- 07     **"Reaction path dependent coherent wavepacket dynamics in excited state intramolecular double proton transfer"**  
K. Stock, C. Schriever, S. Lochbrunner, and E. Riedle  
Chem. Phys. 349, 197 – 203 (2008).

08 **"The interplay of skeletal deformations and ultrafast excited-state intramolecular proton transfer: Experimental and theoretical investigation of 10-hydroxybenzo[h]quinoline"**

C. Schriefer, M. Barbatti, K. Stock, A. J. A. Aquino, D. Tunega, S. Lochbrunner, E. Riedle, R. de Vivie-Riedle, and H. Lischka  
Chem. Phys. 347, 446 – 461 (2008).

09 **"Comparison of the intramolecular proton transfer cycle in the gas phase and in solution"**

C. Schriefer, S. Lochbrunner, D. J. Nesbitt, and E. Riedle  
Manuskript vorbereitet zur Einreichung an J. Chem. Phys. (2008).

10 **"The ultrafast internal conversion of 2-(2'-hydroxyphenyl)benzothiazole in the gas phase"**

M. Barbatti, A. J. A. Aquino, H. Lischka, C. Schriefer, S. Lochbrunner, and E. Riedle  
Manuskript eingereicht an J. Am. Chem. Soc. (2008).

Im Rahmen meiner Doktorarbeit sind folgende weitere Veröffentlichungen entstanden, die allerdings nicht Grundlage dieser Arbeit sind.

11 **"Symmetry Breaking Wavepacket Motion and Absence of Deuterium Isotope Effect in Ultrafast Excited State Proton Transfer"**

S. Lochbrunner, K. Stock, C. Schriefer, and E. Riedle  
in *Femtochemistry and Femtobiology: Ultrafast Events in Molecular Science*, M. M. Martin and J. T. Hynes, (Eds.), Elsevier, Amsterdam, pp. 193 – 196 (2004).

12 **"Ultrafast double proton transfer: symmetry breaking wavepacket motion and absence of deuterium isotope effect"**

S. Lochbrunner, K. Stock, C. Schriefer, and E. Riedle  
in *Ultrafast Phenomena XIV*, T. Kobayashi, T. Okada, T. Kobayashi, K. Nelson, S. De Silvestri, (Eds.), Springer-Verlag, Berlin, pp. 491 – 495 (2005).

13 **"Shaped UV Pulses with 20 fs Substructures"**

C. Schriefer, S. Lochbrunner, and E. Riedle  
in *Ultrafast Phenomena XV*, Springer Series in Chemical Physics 88, P. Corkum, D. Jonas, R. J. D. Miller, and A. M. Weiner, (Eds.), Springer-Verlag, Berlin Heidelberg, pp. 145 – 147 (2007).



- 14     **"Wavepacket motion of ultrafast proton transfer in the gas phase"**  
S. Lochbrunner, C. Schrieffer, and E. Riedle  
in *Proceedings of the Thirteenth International Conference on Time-Resolved  
Vibrational Spectroscopy*, A. Laubereau, K.-H. Mantel, and W. Zinth, (Eds.), open  
access publication, <http://epub.ub.uni-muenchen.de/1193/>, pp. 7 – 9 (2007).



# Inhalt

<b>1</b>	<b>Einleitung.....</b>	<b>1</b>
<b>2</b>	<b>Erzeugung, Manipulation und Detektion ultrakurzer Lichtimpulse.....</b>	<b>5</b>
2.1	Abstimmbare sub-20 fs Impulse aus hochrepetierenden Ytterbium-basierten Lasersystemen .....	5
2.2	Erzeugung modulierter ultravioletter Impulse mit 20 fs Substrukturen.....	11
2.3	Anrege-Abtast-Spektroskopie mit 20 fs Zeitauflösung in Gasphase und in Lösung.....	14
<b>3</b>	<b>Kohärenz durch reaktive molekulare Prozesse.....</b>	<b>19</b>
3.1	Ultraschneller Protontransfer im elektronisch angeregten Zustand .....	20
3.2	Quantenchemische Methoden zur Aufklärung des ESIPT Mechanismus.....	23
3.3	Kinetik des Protontransfers durch Gerüstmoden bestimmt.....	25
3.4	Wellenpaketdynamik des ESIPT koppelt an den Reaktionspfad.....	27
3.5	ESIPT Reaktionspfad im Falle eines steifen Molekülskeletts.....	29
3.6	Einfluss der Reaktionsumgebung auf die ESIPT Dynamik .....	31
<b>4</b>	<b>Zusammenfassung und Ausblick .....</b>	<b>39</b>
	<b>Literaturverzeichnis .....</b>	<b>43</b>
	<b>Anhang A: ESIPT in protischen und polaren Lösungsmitteln.....</b>	<b>51</b>
	<b>Anhänge 1 – 10: Abdrucke der eigenen Veröffentlichungen.....</b>	<b>55</b>
	<b>Danksagung</b>	
	<b>Lebenslauf</b>	



# 1 Einleitung

Moleküle sind die Grundbausteine des Lebens und der Materie. Dabei bestimmen die mikroskopischen Eigenschaften der Moleküle und die Wechselwirkungen zwischen den Molekülen die makroskopischen Parameter der Stoffe, die sie aufbauen. Die Entwicklung neuer Nanomaterialien, Werkstoffe oder Medikamente erfordert ein fundiertes Verständnis von zugrunde liegenden Molekülstrukturen, Molekülwechselwirkungen und von chemischen und physikalischen Reaktionen, die auf molekularer Ebene ablaufen. Auch wenn sich viele biologisch oder chemisch relevante Prozesse in komplexen Makromolekülen auf relativ langsamen Zeitskalen von Millisekunden bis hin zu Sekunden abspielen, sind sie doch die Abfolge oder Kombination von vielen elementaren Schritten. Diese Einzelschritte, wie beispielsweise die Translation oder Rotation von Moleküluntereinheiten, der Energie- oder Ladungstransport, das Ausbilden oder Brechen von chemischen Bindungen finden typischerweise innerhalb von nur wenigen zehn bis einigen hundert Femtosekunden statt [1].

Moleküle sind quantenmechanisch komplexe Objekte, die sich immer noch einer vollständigen rechnerischen Behandlung verschließen. Um Prozesse zu verstehen, die auf molekularer Ebene ablaufen, ist es notwendig, vereinfachte Modelle zu entwerfen, die dennoch allen relevanten Aspekten Rechnung tragen [2]. Die Aufstellung derartiger Modelle erfordert den konzertierten Einsatz theoretischer Modellierungen und experimenteller Untersuchungen. Für das tiefer gehende Verständnis eines komplexen Gesamtprozesses ist es dabei oft hilfreich, die Einzelschritte näher zu untersuchen und zu verstehen. Experimentellen Zugang zur Zeitskala der schnellsten intramolekularen Prozesse bieten ultrakurze, spektral abstimmbare Lichtimpulse mit einer Dauer von wenigen Femtosekunden. Sie können ultraschnelle Photoreaktionen zu einem definierten Zeitpunkt starten und ihren Verlauf in „Echtzeit“ aufzeichnen [3-6]. Es ist essenziell, dass die experimentelle Zeitauflösung erlaubt, auch die schnellsten in die Reaktion involvierten Schritte aufzulösen, damit aus der Messung auf die reaktionsrelevanten Kernbewegungen rückgeschlossen werden kann.

Intramolekulare Kernbewegungen lassen sich als Superposition von Rotationen, Translationen oder Schwingungsmoden des betreffenden Moleküls verstehen. Durch kohärente Überlagerung mehrerer Schwingungszustände einer elektronischen Potentialfläche entstehen vibratorische Wellenpakete, die einer starken Lokalisation der Aufenthaltswahrscheinlichkeit des Systems in einer gewissen geometrischen Konfiguration entsprechen. Während die klassische, chemische Reaktionskinetik Übergänge zwischen Konformationen durch Ratenprozesse beschreibt [7], wird in der vorliegenden Arbeit gezeigt, dass die korrekte Modellierung ultraschneller Prozesse als Wellenpaketbewegung erfolgen muss.

Quantenchemische Rechnungen ermöglichen die Analyse der Wellenpaketbewegung und können Aufschluss über die strukturellen Verformungen des Systems während der Reaktion geben. Außerdem kann gezieltes Hinzufügen oder Entfernen von sterischen Freiheitsgraden oder die Wahl einer Reaktionsumgebung mit speziellen chemischen oder

physikalischen Eigenschaften helfen, die reaktionsrelevanten Koordinaten zu identifizieren. Die Dephasierung des Wellenpakets kann als lokale Probe der Potentialfläche im Bereich des Reaktionsprodukts dienen. Zu Beginn dieser Arbeit war allerdings über die Kopplung der Wellenpaketbewegung an den Reaktionspfad und den Ursprung und die Zeitskala der vibratorischen Dephasierung in mittelgroßen und großen reaktiven Moleküle nur wenig bekannt.

Vergleichende Messungen in unterschiedlichen Lösungsmitteln und in der Gasphase erlauben es, den Einfluss der Reaktionsumgebung, speziell der sterischen Freiheitsgrade und der Energiedissipation zur Umgebung, auf die Wellenpaketdynamik und die nachfolgende interne Konversion zu untersuchen. Ziel dieser Arbeit ist es, Methoden zu entwickeln, die es ermöglichen, ultraschnelle Konfigurationswechsel in verschiedenen Reaktionsumgebungen zu beobachten und ein detailliertes mikroskopisches Bild des Reaktionsmechanismus auf molekularer Ebene aufzustellen. Von speziellem Interesse ist, in welchen Fällen die Reaktionskinetik als barrierefreie Wellenpaketpropagation beschrieben werden kann, welchen Einfluss die Reaktionsumgebung oder die Molekülstruktur auf die Wellenpaketdynamik und Dephasierung hat und wann Tunnelprozesse berücksichtigt werden müssen. Durch Untersuchung prototypischer Systeme, die ultraschnellen Protontransfer im elektronisch angeregten Zustand zeigen [4,8,9], wird ein mikroskopisches Bild des elektronischen Konfigurationswechsels und der damit verbundenen Änderungen der Molekülstruktur erstellt. Die Modellbildung stützt sich auf die experimentelle Beobachtung und Analyse der durch die ultraschnelle Reaktion initiierten Wellenpaketbewegung und deren Dephasierung.

Um den Einfluss der Reaktionsumgebung zu untersuchen, ist es besonders hilfreich den Prozess nicht nur in unterschiedlichen Lösungsmittelumgebungen zu untersuchen, sondern auch das isolierte Molekül in der Gasphase. Für einen direkten Vergleich der Dynamik und Kinetik in Gasphase und in Lösung ist es essenziell, denselben experimentellen Abfrageprozess zu verwenden. Dabei erfordert speziell der niedrige Dampfdruck mittelgroßer und großer organischer Moleküle empfindliche Messverfahren, um auch noch kleine Signale nachweisen zu können. Durch wesentliche technologische Verbesserungen der Sensitivität der Anrege-Abtast-Spektroskopie mit 20 fs Zeitauflösung ist es in dieser Arbeit erstmals möglich, transiente Absorption an Systemen in Lösung und in der Gasphase direkt miteinander zu vergleichen.

Die Kontrolle ultraschneller Reaktionen durch geeignete Reaktionsumgebungen oder Anregungsbedingungen kann nicht nur für die produktive Chemie eingesetzt werden, sondern auch neue Erkenntnisse über Bereiche der Potentialfläche liefern, die mit normalen spektroskopischen Methoden nicht beobachtet werden können [10,11]. Viele Konzepte zur Kontrolle molekularer Prozesse beruhen auf Kohärenzen, die über die gesamte Dauer des Kontrollexperiments anhalten [12,13]. Da die elektronische Kohärenz in kondensierter Phase innerhalb einiger zehn Femtosekunden zerfällt, kann sie nur bedingt zur Kontrolle komplexer Systeme eingesetzt werden. Die länger anhaltende vibratorische Kohärenz kann in Form von Wellenpaketen mit einem kontrollierten Anfangsimpuls oder durch Interferenz zwischen Wellenpaketen ausgenutzt werden, um die Dynamik in einem

Molekül zu steuern. Dies setzt jedoch voraus, dass die Wellenpaketbewegung an den Reaktionspfad koppelt und die Dephasierungsprozesse langsamer sind als der Kontrollprozess. Für die Präparation spezifischer Wellenpakete in mittelgroßen organischen Molekülen sind abstimmbare und strukturierte Anregungsimpulse im ultravioletten Spektralbereich nötig, die Substrukturen mit weniger als 20 fs aufweisen sollten. Die Erzeugung derartiger Impulse öffnet für zukünftige Kontrollexperimente faszinierende Möglichkeiten und wird im Rahmen dieser Arbeit erstmals demonstriert.

In Kapitel 2 werden eigene technologische Entwicklungen zur Erzeugung, Manipulation und Detektion von ultrakurzen Lichtimpulsen dargestellt, die in Kapitel 3 eingesetzt werden, ein detailliertes mikroskopisches Bild des intramolekularen Protontransfers im elektronisch angeregten Zustand aufzustellen. In Kapitel 4 werden die Ergebnisse zusammengefasst und verallgemeinerte Schlussfolgerungen daraus gezogen. Es wird diskutiert, in welchem Umfang sich die neu gewonnenen Erkenntnisse und die vorgestellten Analyseverfahren auf andere ultraschnelle Prozesse übertragen lassen.





## 2 Erzeugung, Manipulation und Detektion ultrakurzer Lichtimpulse

Ultrakurze Lichtimpulse sind das optimale Werkzeug zur Beobachtung und Manipulation von Primärprozessen auf molekularer Ebene [3-5,14-41]. Amplituden-, Phasen- und Polarisationsmodulation im Frequenzraum ermöglichen die volle Kontrolle über das elektrische Feld der Lichtimpulse und die Formung beliebiger Impulsstrukturen im Zeitraum [36-44]. Für die Untersuchung ultraschneller Reaktionen werden ultrakurze Lichtimpulse benötigt, damit auch die schnellsten reaktionsrelevanten Schritte zeitlich noch aufgelöst werden können. Die Zeitskala intramolekularer Wellenpaketdynamik ist durch die Zeitskala der Gerüstschwingungen des Molekülskeletts gegeben. Relevante Gerüstschwingungen liegen typischerweise im Bereich einiger Hundert Wellenzahlen und erfordern eine Zeitauflösung von 20 – 30 fs zur Darstellung. Da viele interessante, prototypische Moleküle Absorptionsspektren im ultravioletten Spektralbereich (UV) besitzen, werden nicht nur kurze, abstimmbare und formbare Lichtimpulse im sichtbaren Spektralbereich sondern auch im UV benötigt. Die kommerzielle Verfügbarkeit neuer hochrepetierender Ytterbium basierter Faserlasersysteme für die hochsensitive Spektroskopie macht die Anpassung vorhandener Techniken zur Impulserzeugung an diese neuen Lichtquellen erstrebenswert.

Im Rahmen der vorliegenden Arbeit wurden auf den Gebieten der Erzeugung, Manipulation und Detektion ultrakurzer Impulse wesentliche technologische Entwicklungen erarbeitet. In den nachfolgenden Abschnitten werden Konzepte und Ergebnisse (i) zur Erzeugung von ultrakurzen, oktavbreit abstimmbaren Impulsen aus Ytterbium basierten Lasersystemen, (ii) zur Erzeugung ultrakurzer, in Amplitude und Phase geformter UV-Impulse, und (iii) zur ultrasensitiven Anrege-Abtast-Spektroskopie in Gasphase und in Lösung präsentiert. Von diesen Neuentwicklungen wird speziell die Anrege-Abtast-Spektroskopie für die in Kapitel 3 dargestellten vergleichenden Untersuchungen von reaktiven Prozessen in der Gasphase und in Lösung eingesetzt. Die Ergebnisse dieser Arbeiten sind in den in den Anhängen 1-4 abgedruckten Publikationen veröffentlicht. Die wesentlichen Aspekte der Untersuchungen sind im Folgenden zusammenfassend dargestellt und in den Rahmen dieser Arbeit eingeordnet.

### 2.1 Abstimmbare sub-20 fs Impulse aus hochrepetierenden Ytterbium basierten Lasersystemen

Spektral weit abstimmbare Impulse großer optischer Bandbreite können durch nicht-kollinear phasenangepasste optisch-parametrische Verstärkung eines kohärenten Saat-Impulses erzeugt werden (NOPA, noncollinear optical parametric amplifier) [45-48]. Dafür eignen sich Weißlichtkontinua aus Kristallen wie Saphir [45] oder Kalziumfluorid [49]

sowie möglicherweise verbreiterte Spektren aus mikrostrukturierten Glasfasern [50]. Die nichtkollineare Geometrie erlaubt nicht nur die Phasengeschwindigkeiten der wechselwirkenden Wellen, sondern auch die Gruppengeschwindigkeiten von Signal- und Idler-Impuls effektiv aneinander anzupassen und so extrem breitbandige Verstärkung zu erreichen [45-47,51]. Dies erlaubt es Ausgangsimpulse zu erzeugen, die um ein Vielfaches kürzer sind, als die dafür verwendeten Eingangsimpulse des Lasersystems.

Hochrepetierende Lasersysteme versprechen eine Verkürzung der Messdauer und ein besseres Signal-zu-Rausch-Verhältnis für Experimente, die nur kleine Signale oder Signaländerungen erlauben [52-58]. Erst neu entwickelte, hochrepetierende Ytterbium-basierte Faserlasersysteme, die Impulsenergien im Bereich von 10 Mikrojoule bei Impulslängen von unter 250 fs liefern, ermöglichen den einfachen, parallelen Betrieb zweier unabhängig voneinander einstellbarer NOPAs und somit spektroskopische Experimente bei Megahertz Repetitionsraten mit ultrakurzen Impulsen bei zwei unabhängig wählbaren Wellenlängen. Für die hier vorgestellten eigenen Experimente stand das erste Exemplar eines kommerziellen Ytterbium-basierten Faseroszillator / Faserverstärker Systems mit  $< 230$  fs Impulsdauer und  $> 10 \mu\text{J}$  Impulsenergie bei einer Zentralwellenlänge von 1035 nm (Frequenz  $\omega_0$ ) und einer Repetitionsrate von bis zu 2 MHz (IMPULSE; Clark-MXR) zur Verfügung.

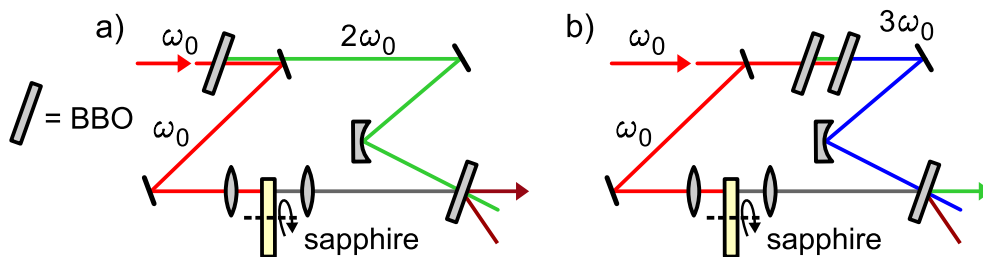


Abb. 2.1: Nichtkollineare optisch-parametrische Verstärkung. a) Frequenzverdopplung des gesamten fundamentalen Impulses (Frequenz  $\omega_0$ ) und Weißlichterzeugung mit dem unverdoppelten Restlicht. Rotieren des Saphir-Kristalls vermeidet schnelle Degeneration bei hohen Repetitionsraten. b) Erzeugung von UV-Pump-Impulsen durch kollineare Frequenzverdopplung und Summenfrequenzmischung.

Im Vergleich zu einem typischen Kilohertz Titan-Saphir-Verstärker (1 kHz, 1 mJ, 150 fs, 775 nm; CPA 2001; Clark-MXR) liefert das Faserlasersystem längere Impulse bei niedrigerer Energie. Dies stellt speziell Anforderungen an die Erzeugung eines stabilen Saatkontinuums für die parametrische Verstärkung. Die veränderte Zentralwellenlänge des Lasersystems beeinflusst den Abstimmbereich des NOPAs und die Möglichkeiten, kurze UV-Impulse zu erzeugen. Zur Adaption des NOPA Konzepts an die Parameter des Faserlasersystems werden zwei Konzepte getestet, die im Folgenden eingehender beschrieben sind. (i) In einem ersten Aufbau werden durch Frequenzverdopplung des gesamten Laserimpulses intensive Pump-Impulse (517 nm,  $2\omega_0$ ) für die parametrische Verstärkung erzeugt. Ein Weißlichtkontinuum in Saphir wird aus dem restlichen

fundamentalen Impuls erzeugt (s. Abb. 2.1 a und Anhang 1). (ii) In einem zweiten Aufbau wird ein Anteil des Laserimpulses für die Weißlichterzeugung abgespalten und der Rest frequenzverdreifacht (s. Abb. 2.1 b und Anhang 2). Durch Pumpen des NOPAs mit der Frequenzverdreifachten ( $345\text{ nm}$ ,  $3\omega_0$ ) kann der Abstimmbereich auf über eine optische Oktave ausgedehnt werden.

## **Weißlichterzeugung bei langen Impulsdauern und niedrigen Impulsenergien**

In Saphir erzeugte Saug-Impulse besitzen eine hohe Kohärenz zwischen den einzelnen Spektralkomponenten und lassen sich daher bis nahe an das Bandbreiten-begrenzte Limit zu zeitlich kurzen Impulsen komprimieren. Aus diesem Grund sind sie gegenüber Kontinua aus mikrostrukturierten Fasern zu bevorzugen, die nur eine geringe Kohärenz aufweisen [59]. Die Weißlichterzeugung in Festkörpern ist allerdings ein Mehrphotonenprozess mit hoher Intensitätsschwelle [60-62]. Die Impulsdauer des verwendeten Lasersystems von etwa  $230\text{ fs}$  erlaubt eine direkte Weißlichterzeugung in Saphir. Durch Fokussierung mit einer Brennweite von  $75\text{ mm}$ , die für den fundamentalen Strahl einer numerischen Apertur von  $0,035$  entspricht, wird ein stabiler Betrieb des Weißlichtkontinuums [60] mit  $2,5\text{ }\mu\text{J}$  erreicht, was  $25\%$  der Energie des Laserimpulses sind. Werden erst durch Frequenzverdopplung des gesamten Laserimpulses mit  $30\%$  Energieeffizienz die Pump-Impulse für die parametrische Verstärkung erzeugt, so ist es dann immer noch möglich aus dem unverdoppelten Restlicht ein stabiles Weißlichtkontinuum zu erzeugen. Mit  $2\omega_0$  Pump-Impulsen mit  $3\text{ }\mu\text{J}$  wurden  $860\text{ nJ}$  NOPA Impulse bei  $685\text{ nm}$  erzielt (s. Anhang 1). Die Effizienzen der nichtlinearen Prozesse und die Impulsenergien sind nahezu unabhängig von der Repetitionsrate des Lasersystems. Bei  $2\text{ MHz}$  wurde eine Ausgangsleistung von  $1,65\text{ W}$  gemessen.

## **Effiziente Erzeugung von UV-Pumpimpulsen für die parametrische Verstärkung**

Geringe Änderungen der Impulsdauer haben großen Einfluss auf die Weißlichtschwelle. Weiterentwicklungen am Lasersystem, speziell an der Impulskompression, haben die Schwelle für eine stabile Weißlichterzeugung auf  $1,5\text{ }\mu\text{J}$  pro Impuls erniedrigt. Dadurch ist es möglich, einen Teil des Laserimpulses für die Weißlichterzeugung abzuspalten und aus dem Rest die dritte Harmonische zum Pumpen der parametrischen Verstärkung zu erzeugen. Durch kollineare Typ-I Frequenzverdopplung mit nachgeschalteter Typ-II Summenfrequenzmischung der Verdoppelten mit dem Rest der Fundamentalen können intensive UV-Impulse bei  $345\text{ nm}$  erzeugt werden. Die Kombination des Typ-I und Typ-II Mischprozesses ermöglicht bei Wahl geeigneter Kristalldicken einen optimalen zeitlichen Überlapp der beteiligten Impulse in beiden Mischkristallen ohne dass zusätzliche Verzögerungsplatten oder optische Wegstrecken eingeführt werden müssen (s. Anhang 2). Die im Typ-I Prozess ( $o+o \rightarrow e$ ) erzeugten  $2\omega_0$  Impulse verlassen den  $0,8\text{ mm}$  dicken  $\beta$ -

Bariumborat (BBO) Verdopplungskristall 50 fs nach den  $\omega_0$  Impulsen, propagieren allerdings schneller durch den 1,5 mm dicken Typ-II (o+e  $\rightarrow$  e) BBO-Summenfrequenzkristall und überstreichen dabei die  $\omega_0$  Impulse. Eine langbrennweitige Fokussierung mit  $f = 500$  mm erlaubt es, den Verdopplungskristall vor dem Fokus und den Summenfrequenzkristall nach dem Fokus zu platzieren. Die Kristalle können unabhängig voneinander relativ zum Fokus positioniert werden und die Intensitäten in den Kristallen getrennt eingestellt werden. Der Aufbau kann auf Verdopplung oder Verdreifachung optimiert werden. Für Kristallpositionen 70 mm vor und 50 mm nach dem Fokus liegen Intensitäten von  $\sim 25$  GW/cm<sup>2</sup> vor, und die dritte Harmonische wird mit 15 % Energieeffizienz erzeugt. Dieses hier vorgestellte Verdreifachungsschema hat sich seither auch schon für die Impulserzeugung in der ultraschnellen Elektronenmikroskopie bewährt [63].

### **Abstimmbereich der parametrischen Verstärkung**

Das mit der fundamentalen Wellenlänge des Ytterbium Lasersystems (1035 nm) erzeugte Kontinuum in Saphir erstreckt sich typischerweise von 440 nm bis zur Fundamentalen (s. Abb. 2.2 a). Der Bereich aufwärts von  $\sim 1000$  nm und die Fundamentale werden durch einen Kurzpassfilter geblockt. Wird die Frequenzverdoppelte als Pumplicht verwendet, so erstreckt sich der Abstimmbereich der NOPA Stufe von 620 bis 970 nm.

Bei kurzen Signalwellenlängen führt die zunehmende Idler-Absorption im BBO-Verstärkungskristall ab  $3,1 \mu\text{m}$  [64] zum Zusammenbrechen der Verstärkung (s. Abb. 2.2 c). Der Abstimmbereich der  $3\omega_0$  gepumpten Verstärkerstufe umfasst den gesamten Spektralbereich des Saat-Kontinuums und ist bei kurzen Wellenlängen im Augenblick nur durch das Spektrum des Saphir-Weißlichts limitiert (s. Abb. 2.2 b). Ein Kontinuum, das sich zu noch kürzeren Wellenlängen erstreckt (z. B. aus Kalziumfluorid) sollte es ermöglichen Impulse bis hinab zu 385 nm zu verstärken, bis wiederum die Idler-Absorption in BBO zum Zusammenbrechen der Verstärkung führt. Die oktavbreite Abstimmbarkeit der  $3\omega_0$  gepumpten Verstärkerstufe zusammen mit einfacher Frequenzverdopplung erlaubt es, kurze Impulse im gesamten Spektralbereich von unter 250 nm bis fast  $1 \mu\text{m}$  zu erzeugen (s. Anhang 2). Die Erzeugung von UV-Impulsen aus der  $2\omega_0$  gepumpten Verstärkerstufe ist ungleich schwerer. Durch (i) Frequenzverdreifachung oder (ii) Verdopplung mit nachfolgender Summenfrequenzmischung des frequenzverdoppelten Impulses mit der Fundamentalen des Lasersystems können UV-Impulse im Spektralbereich von 206 bis 330 nm erzeugt werden (s. Anhang 1). UV-Impulse mit bis zu 2,5 nJ Energie und einer spektralen Breite, die 28 fs entspricht, wurden so bei 304 bzw. 288 nm explizit demonstriert. Für die effiziente Frequenzkonversion wird die spektrale Breite der NOPA Impulse so eingestellt, dass sie einer Fourier-limitierten Impulslänge von etwa 30 fs entspricht. Dies stellt einen Kompromiss zwischen äußerst kurzen und intensiven UV-Impulsen dar. Die spektral eingeschränkten Impulse erlauben statt der Verwendung von typischerweise  $100 \mu\text{m}$  dicken Mischkristallen den Einsatz von  $200 \mu\text{m}$  Kristallen, ohne dass wegen fehlender Akzeptanzbandbreite der Kristalle spektrale Teile des Eingangsimpulses nicht konvertiert werden können. Dadurch wird eine etwa zehnfach höhere Quanteneffizienz bei der UV-Erzeugung erreicht als mit  $100 \mu\text{m}$  Kristallen (s. Anhang 1).

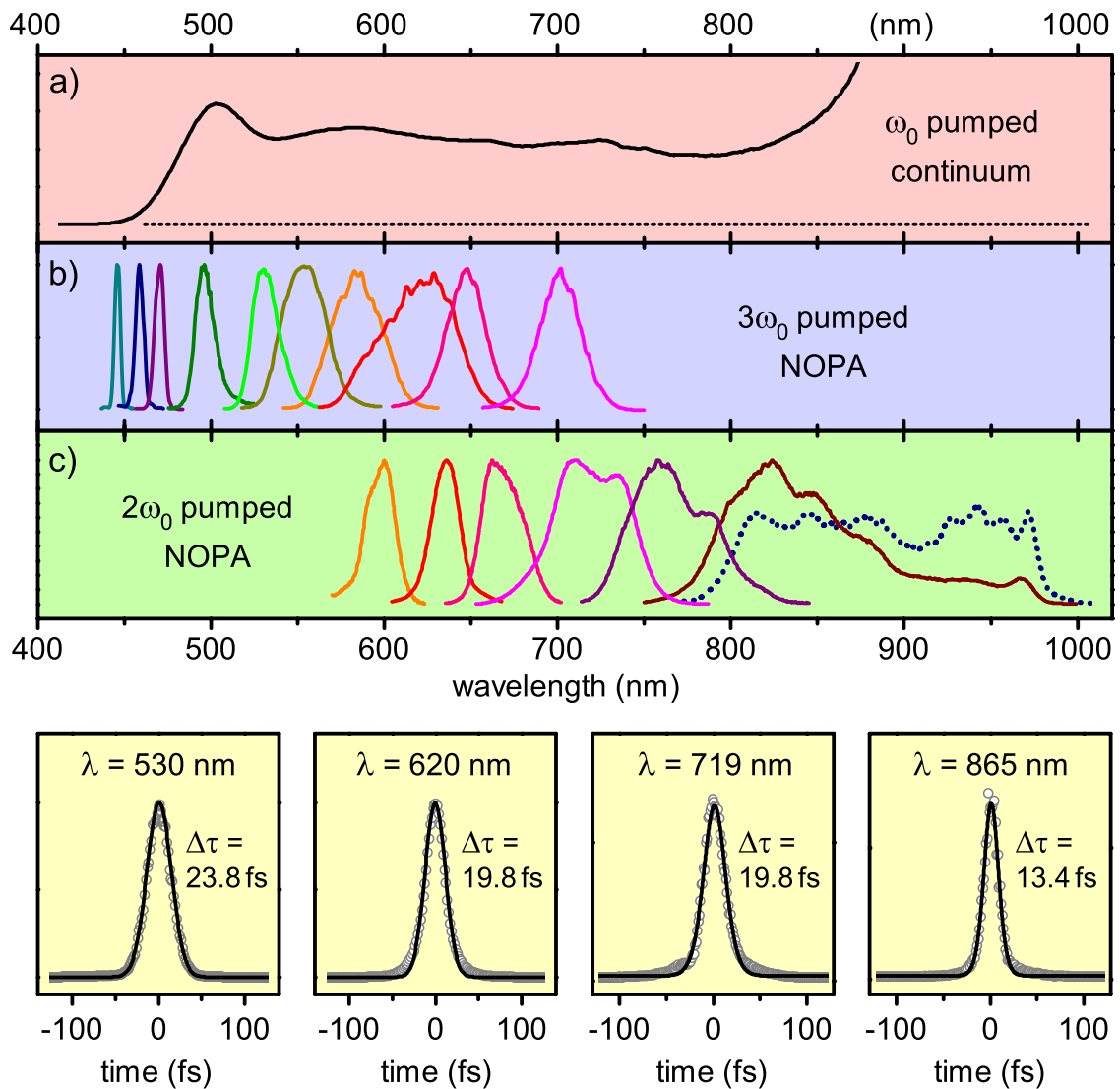


Abb. 2.2: Spektren und Autokorrelationen des 1035 nm gepumpten NOPAs. a) Mit 1035 nm erzeugtes Kontinuum in Saphir. Durch parametrische Verstärkung erzeugte Spektren bei  $3\omega_0$  (b) und  $2\omega_0$  (c) Pumpwellenlänge. Untere Zeile: Autokorrelationen (offene Kreise), Gauß-Anpassung (durchgezogene Linie) und entfaltete Impulslänge bei ausgewählten Zentralwellenlängen. Die vertikale Skala aller Graphen ist linear.

### Energiestabilität der NOPA Impulse

Bei der Weißlichterzeugung entstehen langlebige Defektzustände und Farbzentren in Saphir (s. Abb. 2.3), die speziell bei Repetitionsraten über 500 kHz zu einer allmählichen Zerstörung des Saphir-Kristalls führen. Die Verwendung einer rotierenden Saphirscheibe ermöglicht einen langzeitstabilen Betrieb. Selbst für die verwendete hochpräzise Saphirscheibe mit einem Keilwinkel  $< 2$  Bogensekunden und einer Zentrität von 0,02 mm führt die Rotation zu leichten Vibrationen der Halterung und zu Richtungsinstabilitäten im Weißlicht, die sich in Fluktuationen der NOPA Ausgangsenergie übersetzen. Durch die Rotation des Kristalls erhöhen sich die NOPA Schwankungen aber nur von 1,2 % auf 1,3 % (rms)

und sind immer noch vom technischen Rauschen des Lasersystems dominiert. Die Energiefluktuationen der NOPA Impulse ergeben sich sowohl aus den Fluktuationen des Saat-Impulses wie auch des Pump-Impulses. Im Kleinsignalbereich sollte der durch Frequenzverdopplung erzeugte  $2\omega_0$  Pump-Impuls doppelt so große und der  $3\omega_0$  Pump-Impuls dreimal so große Schwankungen zeigen wie der fundamentale Laserimpuls [65,66]. Unter den vorliegenden experimentellen Bedingungen sind die Schwankungen der verdoppelten Laserimpulse mit 0,68 % (rms) jedoch geringer als die der fundamentalen mit 0,81 % (rms). Für hohe Intensitäten im Verdopplungskristall ( $> 20 \text{ GW/cm}^2$ ) und hohe Verdopplungseffizienzen ( $> 30 \%$ ) führen sowohl Verarmung des fundamentalen wie auch Rückkonversion des verdoppelten Impulses zu einer passiven Energiestabilisierung [65]. Für die frequenzverdreifachten Impulse wird ein ähnlicher, aber nicht so starker Stabilisierungseffekt beobachtet. Statt dem dreimal höheren Rauschen, dass man im Kleinsignal erwarteten würde, weisen die erzeugten  $3\omega_0$  Impulse nur 1,75-fach größere Fluktuationen auf als die Fundamentale. Die Fluktuationen der NOPA Ausgangsenergie sind im Wesentlichen durch die an sich exponentielle parametrische Verstärkung gegeben. Mit einem Fokusbereich im Verstärkungskristall von  $100 \mu\text{m}$  für den  $3\omega_0$  Ast bzw.  $220 \mu\text{m}$  für den  $2\omega_0$  Ast lässt sich auch bei den niedrigen Pump-Energien (typisch  $3\omega_0$ :  $1,1 \mu\text{J}$ ;  $2\omega_0$ :  $1,7 \mu\text{J}$ ) eine Pump-Intensität von etwa  $170 \text{ GW/cm}^2$  erreichen, die notwendig ist, um die Verstärkung fast in Sättigung zu treiben [47,67]. Erst nahe der Sättigung ist der stabile NOPA Betrieb mit nur 1,3 % Fluktuationen der Ausgangsenergie möglich [46,47] (s. Anhang 2).



Abb. 2.3: Die Weißlichterzeugung in Saphir führt zu langlebigen Defektzuständen. Diese sind als blau leuchtender Ring zu erkennen

## Anwendbarkeit in der Ultrakurzzeitspektroskopie

Die meisten spektroskopischen Untersuchungen profitieren ungemein von der Verfügbarkeit zweier spektral unabhängig voneinander abstimmbarer Impulsquellen, die den Absorptions- oder Emissionsbanden der untersuchten Proben in Wellenlänge und spektraler Breite optimal angepasst werden können. Die niedrige Impulsenergie hochrepetierender Systeme spricht gegen zwei vollkommen voneinander getrennte NOPA Aufbauten. Da bei der hier vorgeschlagenen Frequenzverdreifachung gleichzeitig auch frequenzverdoppelte Impulse entstehen, ist der parallele Betrieb der  $2\omega_0$  und der  $3\omega_0$  gepumpten NOPA Stufen einfach möglich. Das Weißlicht kann entweder gleichwertig auf die Verstärkerstufen aufgeteilt werden oder es kann ein Strahlteiler eingesetzt werden, der es den Abstimmbereichen entsprechend verzweigt.

Mit der  $3\omega_0$  gepumpten Verstärkerstufe kann zwar der gesamte Spektralbereich des Weißlichts verstärkt werden, allerdings ist jenseits des Entartungspunktes (Signalwellen-

länge = Idlerwellenlänge = 690 nm) keine breitbandige Phasen Anpassung, somit keine Verstärkung breiter Spektren und Erzeugung kurzer Impulse möglich [66]. Aufwärts von 660 nm ermöglicht jedoch die  $2\omega_0$  gepumpte Verstärkerstufe Impulsdauern von unter 20 fs (s. Anhänge 1, 2). Die  $2\omega_0$  und die  $3\omega_0$  gepumpte Verstärkerstufe ergänzen sich in dieser Hinsicht und erlauben in Kombination die Erzeugung von sub-30 fs Impulsen im Spektralbereich von 500 – 990 nm (s. Abb. 2.2, Anhang 2). Speziell können gleichzeitig und sehr einfach ein ultravioletter Anregungsimpuls durch Frequenzverdopplung des Ausgangs der  $3\omega_0$  gepumpten Verstärkerstufe und ein sichtbarer/nahinfraroter Abfrageimpuls direkt aus der  $2\omega_0$  gepumpten Verstärkerstufe erzeugt werden. In dieser Konfiguration befindet sich das hier beschriebene System an der Arbeitsgruppe Widdra (Martin-Luther-Universität Halle-Wittenberg) seit mehreren Monaten im stabilen Dauerbetrieb. Es werden durch Frequenzverdopplung 34 nJ UV-Impulse bei 290 nm erzeugt und zusammen mit nahinfraroten Impulsen bei  $\sim 900$  nm für die Zwei-Photonen-Spektroskopie an Oberflächen eingesetzt [68,69].

Die Phasen Anpassung begrenzt die Verstärkungsbandbreite der  $3\omega_0$  gepumpten Verstärkerstufe auf etwa 13 fs und der  $2\omega_0$  gepumpten Verstärkerstufe auf etwa 8 fs. Bei geeignetem Dispersionsmanagement sollten entsprechend kurze Impulse realisierbar sein (s. Anhang 2). Da die Impulse aus der  $2\omega_0$  und  $3\omega_0$  gepumpten NOPA Stufe zueinander phasenstabil sind, ist es möglich, das Kontinuum in mehreren parallelen NOPA Stufen zu verstärken, die in unterschiedlichen Spektralbereichen breitbandige Phasen Anpassung erreichen. Die verstärkten Impulse können individuell komprimiert werden, bevor sie wieder rekombiniert werden. Die Erzeugung von Single-Cycle-Impulsen im Sichtbaren ist dadurch prinzipiell möglich.

Durch die hier vorgestellten Entwicklungen sind hochrepetierende Ytterbium Faserlasersysteme trotz der niedrigeren Impulsenergie und längerwelligen Zentralwellenlänge in vielen Aspekten der Impulserzeugung gleichwertig zu Titan-Saphir-Verstärkern geworden. Gleichzeitig bieten sie den Vorteil von Repetitionsraten im Megahertz-Bereich.

## 2.2 Erzeugung modulierter ultravioletter Impulse mit 20 fs Substrukturen

Lichtimpulse mit genau kontrollierten spektralen und temporalen Eigenschaften können komplexe quantenmechanische Systeme, wie zum Beispiel Moleküle, selektiv anregen und deren zeitliche Entwicklung beeinflussen [30-41,70]. Die Kontrolle molekularer Dynamik erfordert Impulse, die Sub-Strukturen auf der Zeitskala molekularer Schwingungsperioden haben. Um mittelgroße organische Moleküle anzuregen, werden UV Impulse benötigt. Optische Flüssigkristall-Impulsmodulatoren werden erfolgreich für die Formung von sichtbaren und nahinfraroten Impulsen eingesetzt [39,44]. Aufgrund des begrenzten Spektralbereichs, in dem diese Modulatoren transparent sind, ist es jedoch nicht möglich, mit ihnen UV-Impulse zu modulieren. Impulsmodulatoren, die direkt im UV arbeiten (breitbandige akustooptische Modulatoren aus Quarzglas [71] und KDP [72] oder

Mirkospiegel-Matrizen [73]) waren zu Beginn dieser Arbeit noch nicht kommerziell erhältlich. Aber auch aktuelle akustooptische Modulatoren [74,75] bieten immer noch nicht die Möglichkeit ähnlich breite Spektren zu modulieren wie der im Folgenden beschriebene Ansatz.

In eigenen Arbeiten (s. Anhang 3) wird gezeigt, dass die Summenfrequenzmischung eines geformten sichtbaren Impulses mit einem zweiten quasi monochromatischen Impuls die Amplituden- und Phaseigenschaften des geformten Eingangsimpulses auf den Ausgangsimpuls transferiert. Dieses Mischschema ermöglicht die direkte Übertragung von beliebigen Amplituden- und Phasenfunktionen eines ultrakurzen, geformten, sichtbaren Impulses auf einen UV-Impuls und somit die Erzeugung beliebig geformter UV-Impulse. Wird der nahinfrarote, fundamentale Impuls des spektral schmalbandigen Titan-Saphir-Lasersystems zeitlich stark gestreckt, so stellt dieser für die zeitlich kurzen Strukturen des geformten Eingangsimpulses einen quasi monochromatischen Mischimpuls dar.

Die Details der theoretischen Herleitung sind in Anhang 3 wiedergegeben. Die Grundidee besteht darin, dass im Kleinsignalbereich und im Falle von Summenfrequenzmischung mit breitbandiger Phasen Anpassung das komplexe elektrische Feld des Ausgangsimpulses ( $E_{UV}(t)$ ) als das Produkt der elektrischen Felder der beiden Eingangsimpulse geschrieben werden kann.

$$E_{UV}(t) \propto A_{VIS}(t) A_{NIR}(t) \cdot \exp[-i(\phi_{VIS}(t) + \phi_{NIR}(t))] \cdot \exp[-i(\omega_{VIS} + \omega_{NIR})t]$$

Dabei bezeichnen  $A$  die zeitliche Einhüllende,  $\phi$  die Phase und  $\omega$  die Zentralfrequenz der entsprechenden Impulse (VIS = geformter Impuls, NIR = gestreckter Impuls). Für den zeitlich langen, nahinfraroten Impuls ist die Einhüllende  $A_{NIR}$  auf der Dauer des geformten sichtbaren Impulses ( $A_{VIS}$ ) quasi konstant. Die spektrale Phase des stark gestreckten nahinfraroten Impulses ist vom quadratischen Term dominiert, der dem linearen Chirp entspricht:  $\phi_{NIR}(t) = -it^2 / (2D_{2,NIR})$ . Für große Werte des Chirp-Parameters  $D_{2,NIR}$ , d. h. für einen stark gestreckten Impuls, nimmt die nahinfrarote Phase während der Dauer des modulierten Mischimpulses einen nahezu konstanten Wert an. Amplitude und Phase des UV-Impulses sind also durch Amplitude und Phase des modulierten, sichtbaren Eingangsimpulses gegeben.

In der experimentellen Realisierung (s. Anhang 3) wird ein spektral breiter und zeitlich komprimierter NOPA Impuls durch einen Flüssigkristall-Impulsmodulator mit 128 Pixeln in der Fourierebene eines 4-f-Aufbaus in Amplitude und Phase moduliert. Der fundamentale Impuls des Lasersystems wird durch einen Glasblock auf  $\sim 1,2$  ps gestreckt ( $D_{2,NIR} = 4,4 \times 10^4 \text{ fs}^2$ ) und seine Intensität wird mit  $\sim 100 \mu\text{J}$  so gewählt, dass sie etwa der der geformten Eingangsimpulse entspricht. Die daraus resultierende Phasenverschiebung für einen Eingangsimpuls mit einer Dauer von  $\Delta t_{FWHM,VIS} = 20$  fs beläuft sich auf  $\Delta \phi_{UV} \approx (2\Delta t_{FWHM,VIS})^2 (2D_{2,NIR})^{-1} = 18$  mrad. Typische UV-Impulsenergien liegen bei  $\sim 300$  nJ und entsprechen einer Quanteneffizienz für den geformten Impuls von  $\sim 8$  %.

Durch Abstimmung des NOPAs können UV-Impulse mit einer frei wählbaren Zentralwellenlänge im Bereich von 295 bis 370 nm erzeugt werden. Mit diesem Mischansatz ist,



im Gegensatz zu ähnlichen früheren Ansätzen [76,77], erstmalig die Erzeugung von Doppel- und Dreifach-Impulsen mit Einzelimpulsdauern von nur 20 fs möglich (s. Abb. 2.4). Damit ist nun der Weg offen zur Formung komplexerer ultrakurzer Impulsstrukturen im UV und ihrer Anwendung für die Kontrolle ultraschneller Photoreaktionen [78,79]. Aktuelle theoretische Arbeiten schlagen geformte UV-Impulse unter anderem für die selektive Präparation von Enantiomeren [80,81] oder selektive Bindungsbrüche [82,83] vor. Für die experimentelle Realisierung dieser Impulsformen und Kontrollziele unter Laborbedingungen bieten sich geschlossene Lernschleifen an [40,84]. Das vorgestellte Mischschema erlaubt es Impulse in einem multidimensionalen Parameterraum zu erzeugen und lässt sich in zukünftige Experimente mit Lernschleife einfach integrieren.

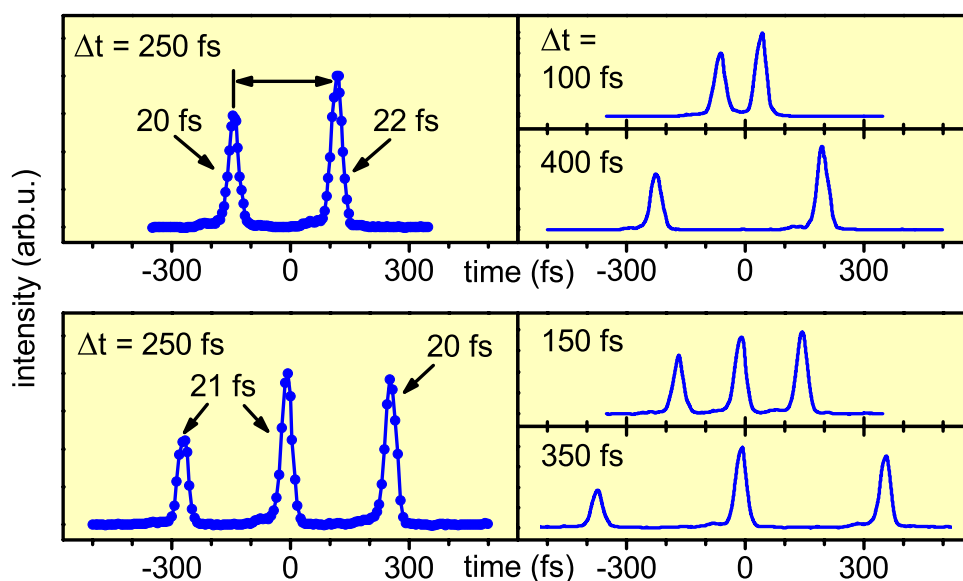


Abb. 2.4: Kreuzkorrelationsmessungen von UV Doppel- (oben) und Dreifach-Impulsen (unten) bei einer Zentralwellenlänge von 344 nm für jeweils mehrere Impulsabstände.

Strukturierte UV-Impulse ermöglichen den experimentellen Zugang zur Klasse der mittelgroßen organischen Moleküle mit Absorptionsspektren im nahen UV. Diese Modellsysteme sind einerseits komplex genug, um neue, interessante, dynamische Phänomene im Wechselspiel der verschiedenen internen Freiheitsgrade zu zeigen, können aber zugleich mit theoretischen Methoden noch gut behandelt werden. Die in Kapitel 3 untersuchten Protontransfersysteme zeigen nach Anregung mit einem ultrakurzen UV-Impuls eine lang anhaltende kohärente Schwingungsdynamik. Dies prädestiniert sie zur Analyse und Kontrolle von Wellenpaketbewegungen. Mit den nun möglichen 20 fs UV-Impulsen besteht die Hoffnung, dass sich durch selektive Mehrfachanregung mehrere Wellenpakete präparieren lassen und durch Interferenz der Wellenpakete die Moleküle in bestimmte Reaktionskanäle gesteuert werden können [33-36,85-88].

## 2.3 Anrege-Abtast-Spektroskopie mit 20 fs Zeitauflösung in Gasphase und in Lösung

Die Anrege-Abtast-Spektroskopie ermöglicht die Untersuchung von Photoreaktionen mit einer Zeitauflösung von wenigen Femtosekunden und erlaubt es auch noch die schnellsten intramolekularen Atombewegungen (z. B. C-H Streckschwingungen) darzustellen [5,89]. Die experimentelle Zeitauflösung ist durch die Dauer des Anrege- und Abtast-Impulses gegeben. Dabei löst der Anregungsimpuls einen photoinduzierten Prozess aus; die nachfolgende Entwicklung des Systems wird von einem zweiten, verzögerten Abtast-Impuls aufgezeichnet [6,90]. Da die Probe nach jeder optischen Anregung dieselbe Reaktion durchläuft, kann durch kontinuierliche Veränderung der Zeitverzögerung zwischen Anrege- und Abtastimpuls sukzessive die zeitaufgelöste Transmissionsänderung der Probe aufgenommen werden. Ein schematischer Versuchsaufbau ist in Abbildung 2.5 dargestellt.

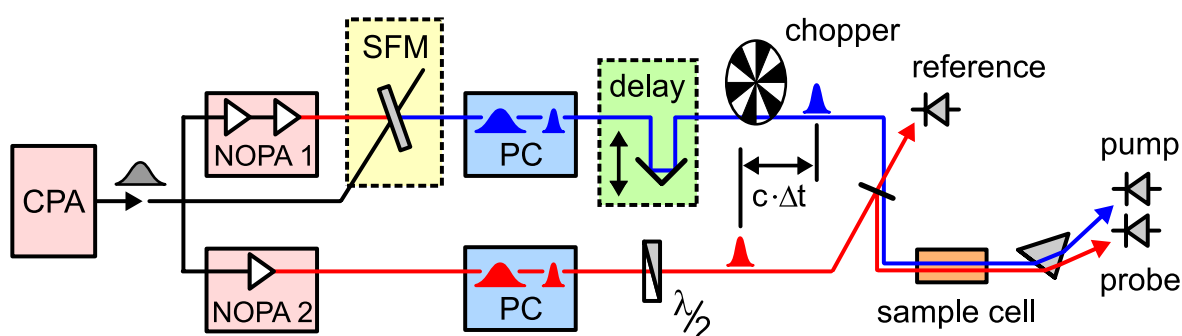


Abb. 2.5: Schematischer Aufbau eines Anrege-Abtast-Experiments.

Die Größe der Signaländerung bei Anrege-Abtast-Messungen  $\Delta OD$  lässt sich näherungsweise durch den molaren Extinktionskoeffizienten der angeregten Moleküle  $\varepsilon^*$ , die optische Dichte der Probe bei der Anregungswellenlänge  $OD_0(\lambda_{pump})$  und den Fluss der Anregungsphotonen  $\Phi_{pump}$  ausdrücken als

$$\Delta OD(\lambda, \tau) \propto \varepsilon^*(\lambda, \tau) OD_0(\lambda_{pump}) \Phi_{pump}.$$

$\varepsilon^*$  beschreibt dabei effektiv die elektronische Relaxation der Probe, chemische Prozesse, vibronische und vibratorische Wellenpaketbewegung und Solvation. Nimmt man in erster Näherung an, dass die Größenordnung von  $\varepsilon^*$  von der Probenumgebung unabhängig ist, so ist es notwendig  $OD_0$  und  $\Phi_{pump}$  beim Übergang von Lösungsmittel- zu Gasphasenmessungen konstant zu halten, um in der Gasphase ähnlich große Signaländerungen zu erhalten wie in Lösung.

Durch Verwendung je eines NOPAs für die Erzeugung von Anrege- und Abtastimpuls sind Zeitaufösungen von 20 fs bei gleichzeitiger Abstimmbarkeit von Anregung und Abfrage problemlos möglich [19,22,91]. Wie in eigenen Arbeiten ausführlich untersucht (s. Anhang 4), ist zur Messung sehr kleiner Transmissionsänderungen die Kombination zweier

Messverfahren vorteilhaft. (i) Die durch die Probe transmittierte Energie ( $sig$ ) wird auf die im Abfrageimpuls vorhandene Energie ( $ref$ ) normiert. (ii) Zu jeweils alternierenden Abfrageimpulsen wird die Transmission durch die Probe mit ( $sig^*/ref^*$ ) und ohne ( $sig^0/ref^0$ ) vorherige Anregung gemessen. Die Signale mit Anregung werden auf die ohne Anregung normiert, um relative Transmissionsänderungen zu erfassen. Gleichzeitig erlaubt dieses Messschema die effektive Unterdrückung von niederfrequenten Schwankungen der Laserausgangsenergie. Die relative Transmissionsänderung ( $\Delta T/T_0$ ) der Probe ergibt sich daraus wie folgt:

$$1 + \frac{\Delta T}{T_0} = \left\langle \frac{sig_{2i}^*}{ref_{2i}^*} \right\rangle_N \left\langle \frac{sig_{2i+1}^0}{ref_{2i+1}^0} \right\rangle_N^{-1}.$$

Dabei deutet  $\langle \cdot \rangle_N$  den Mittelwert über  $N$  Lichtimpulse an.

Bisher wurden Anrege-Abtast-Messungen mit Femtosekunden Zeitauflösung hauptsächlich an Systemen in Lösung, an Oberflächen oder dünnen Filmen durchgeführt. Die Anwendung auf Proben mit geringer optischer Dichte wie beispielsweise Moleküle mit niedrigem Dampfdruck in der Gasphase stellt die zusätzliche Herausforderung, die aus den geringen optischen Dichten resultierenden kleinen Signaländerungen noch zu detektieren. Im Rahmen dieser Arbeit wurde Anrege-Abtast-Spektroskopie mit 20 fs Zeitauflösung zum ersten Mal auf Moleküle mit geringem Dampfdruck in der Gasphase angewandt (s. Anhänge 4, 9).

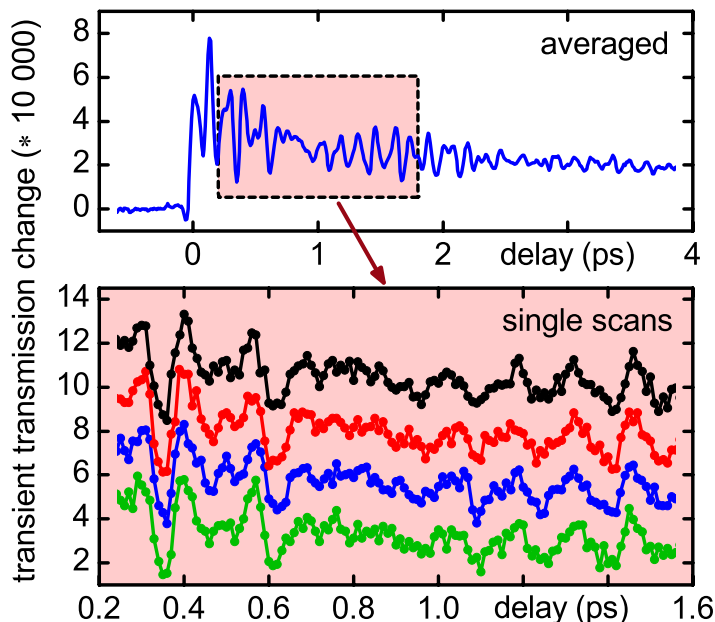


Abb. 2.6: Transiente Transmission von 10-hydroxybenzo[h]quinoline in der Gasphase (Anregung: 350 nm, Abfrage: 625 nm; vgl. Kap. 3.6). Oberer Graph: Mittelung über 4 Einzelmessungen und Glättung über 4 benachbarte Zeitpunkte. Unterer Graph: Einzelmessungen mit Zeitschritt  $\Delta t = 10$  fs und Mittelung über  $N = 421$  Paare von Lichtimpulsen pro Zeitpunkt. Die Einzelmessungen zeigen, dass auch Transmissionsänderungen von weniger als  $10^{-4}$  reproduziert werden.

Verbesserungen im Messschema, speziell in der Datenerfassung und Detektion der Lichtimpulse erlauben es nun Absorptionsänderungen von bis zu  $1.1 \times 10^{-6}$  OD aufzulösen. Eigenentwickelte Photodiodenmodule, die Impulse mit 2 nJ ohne vorherige optische Abschwächung detektieren können, erlauben die initiale Erzeugung vieler Photoelektronen

und erfordern nur eine geringe elektronische Nachverstärkung von  $5 \times 10^4$  V/A. Ein 2 nJ Impuls bei 500 nm entspricht einer Photonenzahl von  $\sim 5 \times 10^9$  und einem Schrotrauschen von  $1,7 \times 10^{-5}$ . Die Photodiodenmodule geben  $\sim 50$   $\mu$ s lange, elektrische Impulse aus, die von 20  $\mu$ s vor bis 80  $\mu$ s nach dem Laserimpuls mit 10 MHz abgetastet werden. Subtraktion der Basislinie und Integration des Signals liefern mit effektiven 14 Bit Genauigkeit einen Zahlenwert, der zur Impulsenergie proportional ist. Die 14 Bit entsprechen dabei einer Auflösung von  $6,1 \times 10^{-5}$ , die vergleichbar ist mit dem Schrotrauschen der Impulse. Der Messaufbau wurde wie folgt modifiziert, um auch bei Proben mit niedrigem Dampfdruck eine ausreichende optische Dichte und damit gut messbare Signaländerungen (Anhang 4) zu erzielen. (i) Eine kollineare Strahlführung mit einer langbrennweitigen Fokussierung führt zu einer langen Rayleighlänge, einem langen, nutzbaren, räumlichen Überlapp von Anrege- und Abtaststrahl und erlaubt es Probendicken von bis zu 50 mm zu verwenden. (ii) Eine heizbare Gaszelle ermöglicht es auch bei Substanzen, die bei Raumtemperatur kristallin sind und einen niedrigen Dampfdruck haben, auf einer Probendicke von 50 mm optische Dichten  $> 0,1$  OD zu erreichen, die vergleichbar mit denen von gelösten Proben sind. Durch differenzielles Pumpen der Zelle wird die Kondensation von Probenmolekülen an die Fenster der Zelle vermieden.

Für die im Rahmen dieser Arbeit untersuchten Moleküle mit einem Grundzustands-extinktionskoeffizienten von  $\epsilon \approx 10\,000$   $\text{M}^{-1} \text{cm}^{-1}$  ergibt sich bei einem Anregungsfokus von 250  $\mu$ m und einer Anregungsenergie von 500 nJ einen Anteil angeregter Moleküle ( $\epsilon \Phi_{\text{pump}}$ ) von  $\sim 2,5$  %. Unter diesen Bedingungen werden Mehrfachanregungen effektiv vermieden, bei gleichzeitiger Maximierung der Signalthöhe.

Das hier vorgestellte Anrege-Abtast-Spektrometer erlaubt es erstmalig transiente Transmission mit 20 fs Zeitauflösung an Proben in Gasphase und in Lösung reproduzierbar zu messen (s. Abb. 2.6). Ohne Veränderungen am Spektrometer können direkt nacheinander, unter denselben experimentellen Bedingungen, Messungen an gasförmigen, gelösten oder kondensierten Proben durchgeführt werden, indem einfach die Probenzellen getauscht werden. So ist es auf einfache Art möglich, aussagekräftige Vergleiche zwischen der Dynamik des isolierten und gelösten Systems anzustellen und den Einfluss der Reaktionsumgebung auf die ultraschnelle Dynamik zu identifizieren. In Kapitel 3 wird der Aufbau für die Detektion der Wellenpaketdynamik in Protontransfersystemen in der Gasphase und in Lösung eingesetzt. Die hohe Sensitivität und Zeitauflösung erlauben es allerdings eine Vielzahl weiterer, ultraschneller, prototypischer Reaktionen in der Gasphase zu untersuchen. In Kombination mit geformten UV-Anregungsimpulsen (s. Kap. 2.2) ermöglicht dieser Messaufbau vergleichende Kontrollexperimente in Gasphase und in Lösung.

Eine weitere Verbesserung der Detektionsempfindlichkeit könnte durch eine alternative Datenerfassungsstrategie möglich werden. Aktuell wird, wie oben beschrieben, die relative Transmissionsänderung zu einer gewissen Anrege-Abtast-Verzögerung aus  $N$  aufeinanderfolgenden Lichtimpulsen bestimmt; die Zeitverzögerung wird zur Aufnahme einer Transmissionskurve einmal langsam durchgeföhren ("slow scan"). Eine typische Messung dauert  $\sim 10$  Minuten. Langsame Laserfluktuationen föhren zu einer hohen Korrelation aufeinander-

derfolgender Laserimpulse und dazu, dass die Mittelwertbildung das Rauschen nicht um  $\sqrt{N}$  unterdrückt, wie es von  $N$  statistisch unabhängigen Messwerten zu erwarten wäre (s. Anhang 4, [53,92-94]). Werden allerdings  $N$  Lichtimpulse pro Anrege-Abtast-Verzögerung derart aufgenommen, dass die Zeitverzögerung schnell und häufig nacheinander durchgeföhren wird (“fast scan”), so sind die einzelnen Messwerte zu einer bestimmten Zeitverzögerung fast vollkommen unkorreliert, da sie im Abstand einiger Sekunden aufgenommen werden, und föhren bei derselben Gesamtmessdauer zu einer besseren Statistik [53,95,96]. Eine derartige Erweiterung des Spektrometers ist gerade im Gange.

In Hinblick auf neue, hochrepetierende Laserquellen (s. Kap. 2.1) ergeben sich für die ultrasensitive Detektion entscheidende Änderungen. Anstatt einer Einzelimpulsdetektion bietet es sich an, durch entsprechend langsame Detektoren zeitlich gemittelte Strahlenergien zu erfassen. Eine doppelte Lock-in Detektion mit Modulation von Anregungs- und Abfrageimpuls [97,98] kann daraus die transiente Transmissionsänderung als untergrundfreies Signal extrahieren. Ein Vergleich zu ähnlichen Detektionsschemata, die schon in Kombination mit Oszillatoren oder CPM-Farbstofflasern zum Einsatz kamen, lässt die Detektion von Signaländerungen von  $10^{-8}$  möglich erscheinen [54-58].



### 3 Kohärenz durch reaktive molekulare Prozesse

Die Anregung mit einem ultrakurzen Lichtimpuls kann in einem Molekül sowohl elektronische wie vibratorische Kohärenzen erzeugen. Die kohärente Superposition der elektronischen Wellenfunktionen des Grund- und angeregten Zustands (elektronische Kohärenz) dephasiert in Lösungsumgebung innerhalb weniger zehn Femtosekunden [99,100]. Ein Großteil der Dephasierung findet schon innerhalb der Zeitauflösung der hier vorgestellten Experimente statt und hat keinen Einfluss auf die in diesem Kapitel präsentierten Ergebnisse.

Durch einen senkrechten optischen Übergang wird der höher gelegene elektronische Zustand in der Molekülgeometrie des Ausgangszustands präpariert. Besitzt der angeregte Zustand eine von dieser Ausgangsgeometrie abweichende Gleichgewichtsgeometrie, so entwickelt sich die Kernwellenfunktion entlang des stärksten Gradienten auf der multidimensionalen elektronischen Potentialfläche des elektronisch angeregten Zustands. Erfolgt die Entwicklung entlang eines barrierefreien Reaktionspfades, so bleibt die nach der optischen Anregung stark lokalisierte Aufenthaltswahrscheinlichkeit des Systems während der Entwicklung weitgehend erhalten und man spricht von einer ballistischen Wellenpaketbewegung. Endet diese initiale, reaktive Wellenpaketbewegung in einem gebundenen Zustand, so können sich dort periodische Bewegungsformen ausbilden, die sich in Form von Schwingungsmoden des gebundenen Zustands beschreiben lassen. Der Impuls des Wellenpakets führt dabei dazu, dass hauptsächlich die Moden partizipieren, die eine große Projektion auf den Reaktionspfad besitzen [15,19,101,102].

Ist der optische Anregungsimpuls deutlich kürzer als die Periode der Schwingungsmoden im Produktzustand, so werden diese kohärent angeregt [103], und können im transienten Transmissionssignal als Oszillationen beobachtet werden. Durch Formung des Anregungsimpulses kann dem Wellenpaket ein definierter Startimpuls gegeben werden und so die photochemische Reaktion früh in eine bestimmte Richtung gesteuert werden [70]. Die Dämpfungszeit der Oszillationen kann Auskunft über die Topographie der Potentialfläche in dem Bereich, in dem sich das Wellenpaket bewegt, geben, sowie über die Dephasierung durch Schwingungsumverteilung.

Die Analyse reaktiver Schwingungswellenpaketdynamik hat großes Potential für die Aufklärung der zugrunde liegenden Reaktionsmechanismen und wurde bisher schon sehr erfolgreich auf kleine und mittelgroße Systeme angewandt [25-30,104,105]. Die reaktiv angeregten Schwingungsmoden können in Kombination mit quantenchemischen Berechnungen Aufschluss über die strukturellen Umformungen des Systems entlang des Reaktionspfades geben und damit über den Reaktionspfad selbst. Die niederfrequenten Gerüstmoden mit wenigen Hundert Wellenzahlen, die maßgeblich zur reaktiven Wellenpaketdynamik beitragen, weisen in mittelgroßen Molekülen in kondensierter Phase typischerweise Dephasierungszeiten von 0,5 bis 2 ps auf [89,106-110]. Die Dephasierung gibt das Zeitfenster für Kontrollexperimente vor, die vibratorische Kohärenzen ausnutzen. Über den

Ursprung und die Zeitskala der vibratorischen Dephasierung in mittelgroßen, reaktiven Molekülen war zu Beginn der Arbeit nur wenig bekannt.

Die Analyse der reaktiven Wellenpaketdynamik und der nachfolgenden Dephasierung wird im Rahmen dieser Arbeit beispielhaft an Molekülen durchgeführt, die ultraschnellen Protontransfer im elektronisch angeregten Zustand zeigen. Die angewandten Methoden und Konzepte sind allerdings allgemein und sollten sich auch einfach auf andere reaktive Systeme übertragen lassen. Speziell wird im Folgenden durch Beobachtung des Reaktionsverlaufs in Echtzeit geklärt, ob

- (i) sich die Reaktionskinetik als barrierefreie Wellenpaketpropagation beschreiben lässt, oder ob Tunnelprozesse berücksichtigt werden müssen.
- (ii) die Wellenpaketdynamik an den Reaktionspfad koppelt oder durch die optische Anregung initiiert ist.
- (iii) die Reaktionsumgebung oder die Molekülstruktur die Wellenpaketdynamik und Dephasierung maßgeblich beeinflussen.

Die eigenen Untersuchungen zu diesen Fragestellungen sind in Publikationen oder Manuskripten, die sich in den Anhängen 5-10 finden, dargestellt. Ihre wesentlichen Aspekte sind in den folgenden Kapiteln übergreifend und zusammenfassend dargestellt und in den Rahmen dieser Arbeit eingeordnet.

### 3.1 Ultraschneller Protontransfer im elektronisch angeregten Zustand

Protontransfer ist ein fundamentaler Teilschritt vieler biologischer Reaktionen wie der molekularen Erkennung [111-113] oder des Ionentransports durch Membranen und ist die Basis grundlegender Phänomene in Physik und Chemie [114-117]. Selbst dieser einfache Prozess involviert typischerweise mehr als nur die Kernbewegung des Protons. Die zugrunde liegende Dynamik und Kinetik kann in den wenigsten Fällen klassisch beschrieben werden [3,4,116-118].

Moleküle, die intramolekularen Protontransfer im elektronisch angeregten Zustand (ESIPT) [4,8,25,117-122] zeigen, sind als Modellsysteme für zeitaufgelöste Untersuchungen besonders interessant. Durch den intramolekularen Charakter besitzen sie eine wohl definierte Ausgangsgeometrie, der ESIPT lässt sich durch Anregung mit einem ultrakurzen Lichtimpuls auslösen und die Reaktionsdynamik kann mit einer Zeitauflösung von wenigen Femtosekunden verfolgt werden. Nachfolgend wird der ESIPT mittels zeitaufgelöster Anrege-Abtast-Spektroskopie mit 20 fs Zeitauflösung an drei ausgewählten Molekülen untersucht: 2-(2'-hydroxyphenyl)-benzothiazole (HBT), 10-hydroxybenzo[h]-quinoline (10-HBQ), (2,2'-bipyridyl)-3,3'-diol [BP(OH)<sub>2</sub>] (s. Abb. 3.1).

Den hier untersuchten Molekülen ist der H-Chelatring ( $\text{N}=\text{C}-\text{C}=\text{C}-\text{O}-\text{H}$ ; Abb. 3.1) als Reaktionszentrum gemein. Die grundzustandsstabile enol Konformation geht nach Anregung in den ersten elektronisch angeregten Zustand ( $S_1$ ) in die keto\* Konformation über



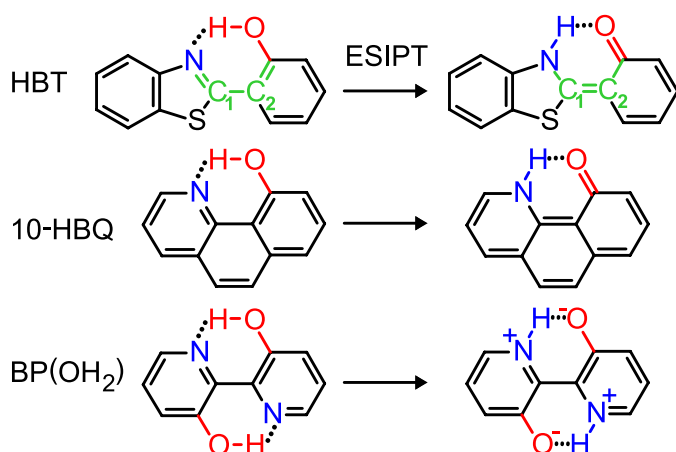


Abb. 3.1: Strukturformeln der untersuchten ESIPT Moleküle. Der in HBT farblich eingezeichnete H-Chelatingring ( $N=C_1-C_2=C-O-H$ ) stellt das reaktive Zentrum der Moleküle dar. Im Grundzustand ist die enol Konformation ( $O-H$ ) stabil, während im ersten elektronisch angeregten Zustand ( $S_1$ ) die keto Konformation ( $C=O$ ) die stabile elektronische Konfiguration darstellt. Wasserstoffbrücken sind als  $\cdots$  angedeutet.

(\* deutet  $S_1$  Konformere an). Der ESIPT führt zu einer um  $7000 - 10\,000\text{ cm}^{-1}$  Stokes-verschobenen keto\* Fluoreszenz. Diese Verschiebung ergibt sich in etwa zu gleichen Teilen aus der Absenkung der Potentialfläche des angeregten Zustands und aus dem Anstieg der Grundzustandspotentialfläche (s. Abb. 3.2 und Anhänge 5, 8). Nach dem ESIPT geht die keto\* Konformation durch interne Konversion (internal conversion, IC) in den keto Grundzustand über, der ultraschnellen Protontransfer zurück zur enol Konformation macht (s. Abb. 3.2). In HBT kann durch die IC auch der transketo Grundzustand gebildet werden, der keinen ultraschnellen Protonrücktransfer zeigt. Der Protontransferzyklus und die interne Konversion von HBT sind im Detail in Kap 3.6 beschrieben. In protischen Lösungsmitteln wie Ethanol kommt es in einem gewissen Anteil der ESIPT Moleküle zum Aufbrechen des H-Chelatingrings [123,124]. Die intramolekulare Wasserstoffbrücke wird durch mehrere intermolekulare Wasserstoffbrücken zum Lösungsmittel ersetzt. In diesen Molekülen ist nach optischer Anregung kein Protontransfer möglich und sie fluoreszieren aus dem enol\* Zustand (s. Abb. 3.2 und Anhang A). Die spektral getrennte keto\* Fluoreszenz erlaubt die zweifelsfreie Zuordnung der in diesem Spektralbereich beobachteten Dynamik zum ESIPT Reaktionsprodukt.

In zeitaufgelösten Transmissionsmessungen (s. Abb. 3.3) stellt sich der Protontransfer für Abfragewellenlängen im Bereich der statischen keto Fluoreszenz als stufenförmiger Anstieg des Transmissionsignals dar. Die instantan mit der Anregung einsetzende Absorption in höhere Zustände führt zu einer anfänglichen Transmissionsabnahme, das verzögerte Auftreten des Emissionsbeitrags deutet an, dass die Bildung der keto\* Form eine gewisse Zeit erfordert. Die Verzögerung zwischen Zeitnullpunkt und Anstieg der Emission kann als Maß für die Protontransferzeit verwendet werden (s. Anhang 8). Der Protontransfer findet innerhalb von 25 fs (10-HBQ, s. Kap. 3.5), 33 fs (HBT, s. Kap 3.6), bzw. 50 fs ( $BP(OH)_2$ , s. Kap. 3.4) nach der optischen Anregung statt. Diese Protontransferzeiten sind deutlich länger als man von einem einfachen elektronischen Konfigurationswechsel oder von einer direkten Protonbewegung erwarten würde [3].

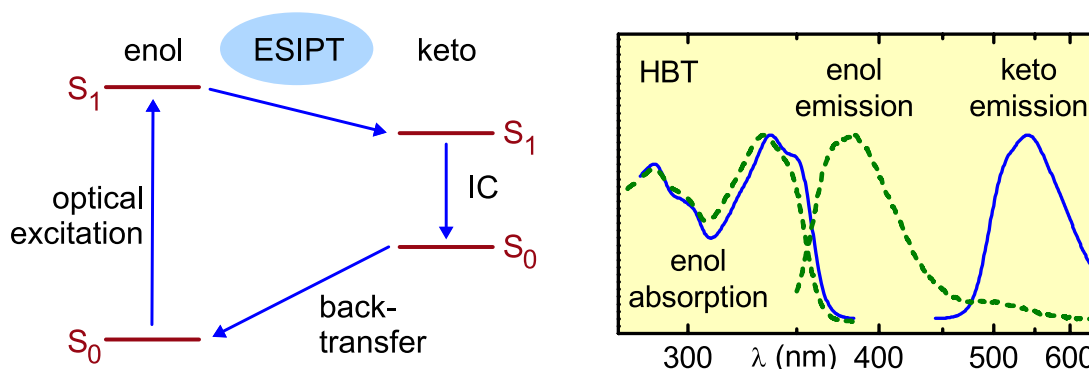


Abb. 3.2: ES IPT Schema und statische Absorption und Fluoreszenz von HBT. HBT in Cyclohexan zeigt stark Stokes-verschobene Emission aus der keto Form (blau) während in Ethanol hauptsächlich nicht verschobene enol Emission auftritt (grün).

Die nachfolgenden Signaländerungen zeigen ausgeprägte Oszillationen, die mit einer Zeitkonstante von  $\sim 1$  ps abklingen (s. Abb. 3.3) und die charakteristischen Signaturen einer vibratorischen Wellenpaketbewegung sind. Der Vergleich der experimentell beobachteten Oszillationsfrequenzen mit quantenchemischen Rechnungen (vgl. Kap 3.2) belegt, dass die nach dem ES IPT kohärent angeregten Normalmoden planare Verformungen des Molekülskeletts sind, die zur Verkürzung der Proton Donor-Akzeptor Distanz beitragen.

Frühere Untersuchungen an HBT und anderen ES IPT Systemen, die teilweise nicht im Rahmen dieser Arbeit entstanden sind, haben zu einem vorläufigen Model des ES IPT geführt, das im Übersichtsartikel in Anhang 5 ausführlich dargestellt ist. Es lässt sich wie folgt zusammenfassen: Durch die optische Anregung des enol Konformers tritt eine Änderung der elektronischen Bindungen bzw. der Bindungsstärken ein. Die enol\* Form stellt keine Gleichgewichtskonfiguration mehr dar, und das Molekül bewegt sich auf der Potentialfläche näherungsweise entlang des stärksten Gradienten zum keto\* Minimum. Dabei ermöglicht erst eine initiale Verkürzung der Proton Donor-Akzeptor Distanz ( $O \leftrightarrow N$ ) einen barrierefreien Reaktionspfad von der enol\* zur keto\* Konformation. Ist die Distanz zwischen Proton-Donor und Akzeptor hinreichend verkürzt, so erfolgt die elektronische Umkonfiguration, bei der sich die Elektronen im Chelatring perizyklisch verschieben [125]. Der  $S_1$  Zustand ist eine Mischung der elektronischen enol\*- und keto\*-Konfiguration, wobei das Mischungsverhältnis von den Kernkoordinaten abhängt. Der Konfigurationswechsel stellt sich als eine Besetzungszahl-Umverteilung in den Molekülorbitalen dar und führt zum Bruch der O-H Bindung und zum Aufbau der N-H Bindung. Auf der Zeitskala der Kernbewegungen reagiert die Elektronendichte instantan auf die Geometrieänderungen. Die Protontransferzeit ergibt sich aus der Trägheit des Systems für die initiale Kontraktion des Chelatrings (für Details s. Anhänge 5, 8). Eine auf diesem Model basierende Anpassung (für Details s. Anhänge 5, 9) beschreibt die Messdaten sehr gut (s. Abb. 3.3 b).

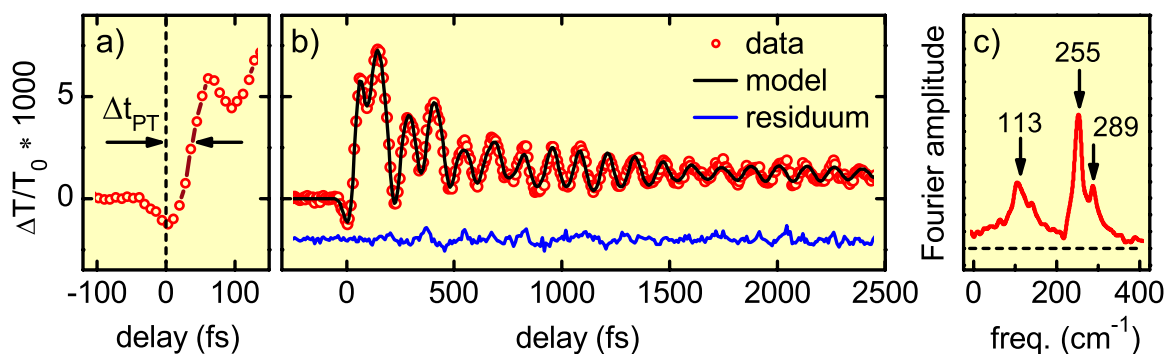


Abb. 3.3: Transmissionsänderung von HBT bei Anregung mit 347 nm und Abfrage mit 505 nm. a) Der verzögerte Anstieg der Emission entspricht der Protontransferzeit ( $\Delta t_{PT}$ ). b) Ausgeprägte Wellenpaketdynamik mit  $\sim 1$  ps Dephasierungszeit. Die Daten werden durch die Modellfunktion sehr gut beschrieben. c) Die Fouriertransformation der oszillatorischen Anteile besitzt drei Frequenzkomponenten mit 113, 255 und 289  $\text{cm}^{-1}$ .

Die diesem Modell zugrunde liegenden Experimente konnten nicht eindeutig klären, ob (i) die Wellenpaketdynamik tatsächlich durch den reaktiven Prozess und nicht durch die optische Anregung erzeugt wird, ob (ii) der Reaktionspfad barrierefrei ist und kein Tunneln des Protons für die Dynamik betrachtet werden muss und ob (iii) die Reaktionsumgebung oder die Molekülstruktur die Wellenpaketdynamik und Dephasierung maßgeblich beeinflussen. Diese ausstehenden Beweise für das ESIPT Modell werden in den Kapiteln 3.3 bis 3.6 erbracht.

## 3.2 Quantenchemische Methoden zur Aufklärung des ESIPT Mechanismus

Die Berechnung von Molekülstrukturen mit quantenchemischen Rechenprogrammen ist Routine in der modernen theoretischen Chemie [126-128]. Die verführerische Stärke dieser Rechenverfahren liegt darin, nicht nur Energieminima auf der Potentialhyperfläche zu ermitteln, die mit experimentellen Werten verglichen und zunehmend als deren Ersatz benutzt werden. Sie werden immer mehr eingesetzt, auch experimentell nur indirekt zugängliche Information zu liefern, wie zum Beispiel den Verlauf des Pfades geringster potentieller Energie (minimum energy path, MEP) von einem Bereich der Potentialfläche zu einem anderen. Die Analyse der experimentell beobachteten Wellenpaketdynamik ist auf quantenchemische Rechnungen angewiesen, die den beobachteten Oszillationen Bewegungsformen zuordnen, aufgrund derer auf den Reaktionspfad geschlossen werden kann. Verschieden aufwendige quantenchemische Rechenverfahren können Ergebnisse liefern, die mit der experimentell bestimmten Wellenpaketdynamik verglichen werden können. Entweder in eignen Rechnungen oder in Form von Kooperationen mit den Theoriegruppen von Professor Regina de Vivie-Riedle (LMU München) und Professor

Hans Lischka (Universität Wien) wurden im Rahmen dieser Arbeit folgende Methoden eingesetzt und Informationen extrahiert:

(i) Durch Geometrieoptimierung des Produktzustandes können die Normalmoden im Produktminimum berechnet werden. Die Identifikation der experimentell beobachteten Oszillationen mit diesen Normalmoden ermöglicht dann Rückschluss auf den Reaktionspfad, wenn sich während des reaktiven Prozesses die Normalmoden in ihrer Bewegungsform und Frequenz nur wenig verändern. Letztere Anforderung erlaubt es, oft auch die Rechnungen im Eduktzustand durchzuführen (s. Anhänge 5, 7, 9).

(ii) Eine Normalmodenanalyse bezüglich der Produktgeometrie entlang des MEP liefert die Auslenkung der einzelnen Normalmoden während des reaktiven Prozesses. Das Molekül im Produktminimum schwingt in diesen Moden weiter und sie sollten den experimentell bestimmten Oszillationen entsprechen. Die Normalmodenanalyse erfordert die Kenntnis der elektronischen Potentialfläche in den reaktionsrelevanten Koordinaten und ist auf wenige Freiheitsgrade beschränkt (s. Anhang 8).

(iii) Wellenpaketpropagationen auf der reaktiven Potentialfläche können im Gegensatz zur Normalmodenanalyse entlang des MEP die Reaktionsdynamik, d. h. den Impuls des Wellenpakets abbilden. Die Eigenmoden, die signifikant zur Gesamtwellenfunktion im Produkt beitragen, sollten den experimentell bestimmten Oszillationen entsprechen (s. Anhang 8).

(iv) Klassische Trajektorienrechnungen können im Gegensatz zu Rechnungen, die eine vorausberechnete Potentialfläche erfordern, alle Freiheitsgrade des Systems berücksichtigen [127-129]. Aus Gründen der Rechenzeit können dabei allerdings nicht so aufwendige und präzise Verfahren verwendet werden wie für statische Rechnungen. Die Trajektorien bilden die gesamte Dynamik des Moleküls in der Born-Oppenheimer Näherung ab und können bezüglich der angeregten Normalmoden analysiert werden (s. Anhänge 8, 10).

Sieht man die Protontransferzeit als die Zeit, die das Wellenpaket nach der optischen Anregung benötigt, um den keto Bereich der Potentialfläche zu erreichen, so bietet sich an als experimentelles Maß der Protontransferzeit die Zeitverzögerung von der Anregung bis zum Anstieg der keto\* Emission bei einer Wellenlänge in der blauen Flanke des Emissionsspektrums an. Für die Wellenpaketpropagation eignet sich die Zeitdauer, bis der Schwerpunkt des Wellenpakets zum ersten Mal die keto\* Region der Potentialfläche erreicht. In den Trajektorienrechnungen ist ein gleich großer OH und ON Abstand ein gutes Maß dafür, dass der ESIPT stattfindet. Trotz dieser unterschiedlichen Kriterien liefern die drei Methoden ein sehr konsistentes Bild der Protontransferzeit, wie in Anhang 8 für HBT und 10-HBQ gezeigt ist. Dies spricht dafür, dass es im Falle eines Prozesses, der als Wellenpaketpropagation abläuft, sinnvoll ist, von einer Zeitdauer des Prozesses zu reden und dass diese Dauer experimentell bestimmt werden kann.

Berechnungen im elektronisch angeregten Zustand erfordern komplexe Rechenmethoden und oft auch Näherungen, wie beispielsweise die Einführung von Zwangsbedingungen. Dabei hängt das Ergebnis der Rechnung teilweise stark von der verwendeten Rechenmethode und den Näherungen ab, für die von Fall zu Fall geprüft werden muss, ob

sie für das untersuchte System zulässig sind. Der Vergleich zu experimentellen Ergebnissen ist für die Verfeinerung und Rechtfertigung der Rechenverfahren absolut notwendig. In Abbildung 3.4 sind die für den enol Zustand berechneten Normalmoden dargestellt, die den in HBT experimentell beobachteten Oszillationen entsprechen (vgl. Abb. 3.3). Den Normalmoden ist gemein, dass sie planare Verformungen des Molekülskeletts sind, die die Proton Donor-Akzeptor Distanz stark verkürzen.

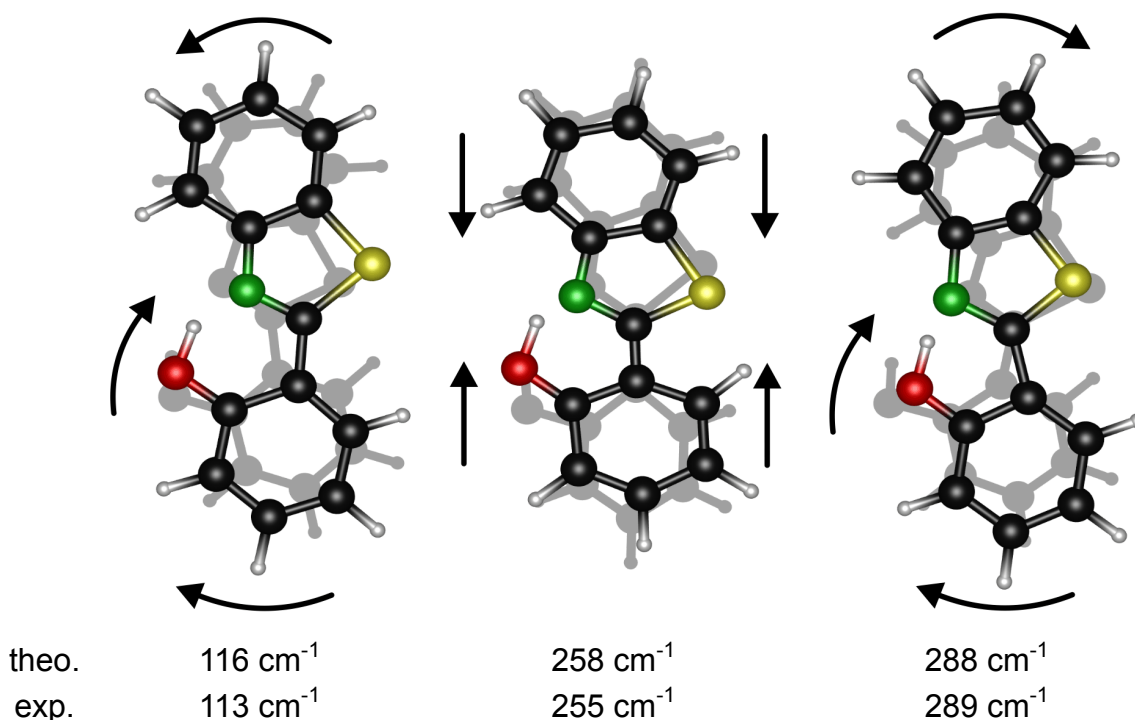


Abb. 3.4: Berechnete Eigenfrequenzen und Normalmoden für HBT. Die relaxierte Geometrie ist grau dargestellt, die farbigen Moleküle zeigen die Geometrie bei Auslenkung der Normalmoden. Die Frequenzen der berechneten Normalmoden entsprechen sehr gut den experimentell beobachteten Oszillationen aus Abb. 3.3.

### 3.3 Kinetik des Protontransfers durch Gerüstmoden bestimmt

Die beobachtete Protontransferzeit von 35 fs in HBT ist deutlich länger als man von einer direkten Bewegung des Protons vom Donor zum Akzeptor und dem damit einhergehenden elektronischen Konfigurationswechsel erwarten würde [3]. Bisherige Untersuchungen deuten darauf hin, dass transiente Verformungen des gesamten Molekülskeletts das Proton adiabatisch von Donor zum Akzeptor transferieren [25]. Die Zeitskala des Protontransfers ist in diesem Fall durch die Zeitskala dieser unterstützenden Gerüstschwingungen gegeben. Alternativ könnte es sein, dass sich das Molekülskelett nicht aus der Gleichgewichtsgeometrie heraus verformt. In diesem Fall muss das Tunneln des reaktiven Protons durch eine Potentialbarriere entlang des Reaktionspfades für die Protontransferzeit verantwortlich sein (s. Abb. 3.5). Im Falle eines Tunnelmechanismus sollte sich für Deuterium eine deutlich

langsamere „Protontransferrate“ ergeben. Im Falle eines ESIPT Mechanismus, der auf Gerüstschwingungen beruht, sollte sich keine Änderung der Protontransferzeit ergeben. Um experimentell zu klären, ob Tunneln des reaktiven Protons bei der Beschreibung der ESIPT Dynamik berücksichtigt werden muss, wird das reaktive Proton in HBT durch Deuterium ersetzt und die transienten Transmissionsänderungen in beiden Systeme mit 20 fs Zeitauflösung verglichen (s. Anhang 6).

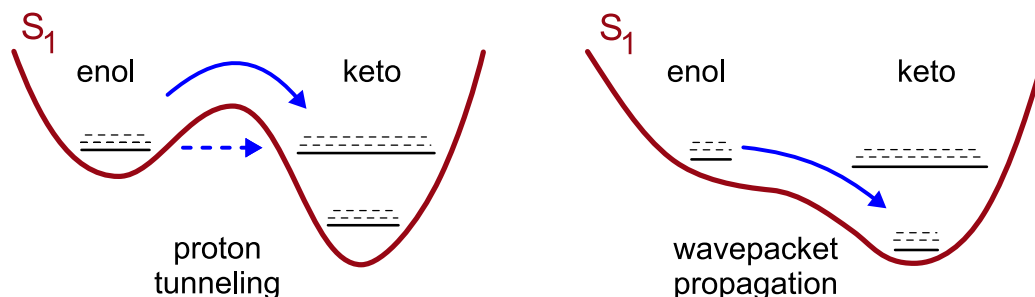


Abb. 3.5: Zwei Modelle für die Potentialfläche im elektronisch angeregten Zustand. Links: Das angeregte System muss durch eine Potentialbarriere tunneln, um in die keto Konformation zu gelangen. Rechts: Es kann sich auf einer barrierefreien Potentialfläche direkt in die keto Konformation entwickeln.

In einem eindimensionalen Modell ergibt sich die semi-empirische Tunnelrate  $k$  aus der klassischen „Anklopfrequenz“  $\nu$  des Teilchens an die Barriere und der Tunnelwahrscheinlichkeit  $p$  durch die Barriere zu:  $k = p \cdot \nu$ . Dabei gilt

$$p = \exp\left(-\frac{2}{\hbar}\sqrt{2m} \int dr \sqrt{V(r) - E}\right),$$

wobei  $m$  die Masse des tunnelnden Teilchens,  $E$  seine Energie und  $V$  die zu durch-tunnelnde Barriere darstellt. Damit erniedrigt sich bei Deuterierung die Protontransferrate aufgrund von drei Faktoren: (i) Die Frequenz  $\nu$  der lokalen OH Streckschwingung reduziert sich um den Faktor  $\sqrt{2}$ , (ii) die Masse des tunnelnden Teilchens verdoppelt sich, und (iii) die Nullpunktsenergie des Teilchens reduziert sich um den Faktor  $\sqrt{2}$  was zu einer effektiv höheren und breiteren Barriere führt. Ohne weitere Annahmen über die Barriere zu machen, ergibt sich unter Berücksichtigung der ersten beiden Effekte eine Erhöhung der Tunnelrate von  $k_H = (50 \text{ fs})^{-1}$  für Wasserstoff auf  $k_D = (131 \text{ fs})^{-1}$  für Deuterium, was einem 2,6-fach verlangsamten Anstieg des transienten keto\* Emissionsbeitrags entspricht. Ein zweidimensionales Tunnelmodell, das Modulationen der Proton Donor-Akzeptor Distanz durch Gerüstschwingungen berücksichtigt, führt zu einem mehrstufigen Anstieg des keto\* Emissionsbeitrags mit der Periodizität der Gerüstschwingung. Deuterierung führt in diesem Fall dazu, dass sich der Populationstransfer pro Oszillation verringert und der Anstieg mehr und kleinere Stufen aufweist (für Details s. Anhang 6). In beiden Fällen würde das transiente Transmissionsignal also eindeutig detektierbare Signaturen des Tunnelprozesses aufweisen.

Die zeitaufgelösten Messungen an deuteriertem und undeuteriertem HBT wurden unter denselben experimentellen Bedingungen direkt nacheinander ausgeführt. Der Deuterierungsgrad der Probe wurde mittels NMR sowohl vor wie auch nach den zeitaufgelösten Messungen bestimmt und lag während den Messungen bei 80 %. Die Präzision der zeitaufgelösten Messungen erlaubt es, eine Verlängerung der Protontransferzeit um 10 fs zweifelsfrei nachzuweisen. Im Rahmen dieser Messgenauigkeit konnte allerdings keine Veränderung der Protontransferzeit unter Deuterierung beobachtet werden (s. Anhang 6).

Die hier vorgestellten Messungen zeigen durch Echtzeitbeobachtung des ESIPT zum ersten Mal zweifelsfrei, dass der Protontransfer in HBT als ballistische Wellenpaketpropagation ohne signifikante Beteiligung von Tunnelprozessen abläuft. Dieses Ergebnis ist nicht spezifisch für HBT und experimentelle und theoretische Untersuchungen zur ESIPT Dynamik in 10-HBQ (s. Kap. 3.5) unterstützen das Wellenpaketmodell. Die Protontransferzeit in 10-HBQ ist etwa 30 % kürzer als in HBT, was sehr gut den höheren Frequenzen der Gerüstmoden von 10-HBQ entspricht, die zur Verkürzung des H-Chelatrings beitragen und im Wellenpaketmodell die Protontransferzeit bestimmen.

### 3.4 Wellenpaketdynamik des ESIPT koppelt an den Reaktionspfad

Doppelprotontransfersysteme sind interessante Prototypen für DNA-Basenpaare, die ebenfalls über zwei Wasserstoffbrücken miteinander verknüpft sind. In inter- wie intramolekularen Mehrfachprotontransfersystemen ist vor allem die Frage von besonderem Interesse, ob die einzelnen Protontransferreaktionen sequenziell ablaufen, oder ob es auch Reaktionskanäle gibt, die konzertierten Protontransfer zeigen [114,130-135]. Intramolekulare Modellsysteme wie BP(OH)<sub>2</sub> bieten im Gegensatz zu intermolekularen Systemen den Vorteil einer wohldefinierten Ausgangsgeometrie und können helfen, Mechanismen und Signaturen des sequenziellen und konzertierten Reaktionskanals zu identifizieren, die auch auf intermolekulare Systeme übertragbar sind.

Die Analyse der Wellenpaketdynamik aus transienten Transmissionsmessungen macht den Rückschluss von den kohärent angeregten Normalmoden, die im zeitaufgelösten Signal beobachtet werden, auf den Reaktionspfad möglich. Dies setzt voraus, dass die Oszillationen nicht durch den optischen Pump-Impuls kohärent angeregt werden, sondern an den Reaktionspfad koppeln und tatsächlich das Nachschwingen des Moleküls in den Verformungen darstellen, die für die ESIPT Reaktion notwendig sind. Der Nachweis unterschiedlicher Wellenpaketdynamik für unterschiedliche Reaktionskanäle würde beweisen, dass die Dynamik durch den reaktiven Prozess und nicht durch die optische Anregung ausgelöst wird.

Das Doppelprotontransfersystem BP(OH)<sub>2</sub> zeigt in aprotischen Lösungsmitteln nach optischer Anregung sowohl ultraschnellen intramolekularen Einfach- wie auch Doppelprotontransfer [136-139], der zum monoketo\* respektive diketo\* Produkt führt (s. Abb. 3.6). Das Verhältnis der Verzweigung in die beiden Reaktionskanäle kann durch die Anregungsüberschussenergie kontrolliert werden. Bei 310 nm findet in 40 % der angeregten

Moleküle instantaner Einfachprotontransfer statt, bei 350 nm in 30 % und bei 380 nm in 12 % [138,139]. Falls die Anregungsüberschussenergie einen systematischen Einfluss auf die Amplituden der angeregten Normalmoden hat, belegt dies, dass einzelne Normalmoden an einen speziellen Reaktionskanal gekoppelt sind.

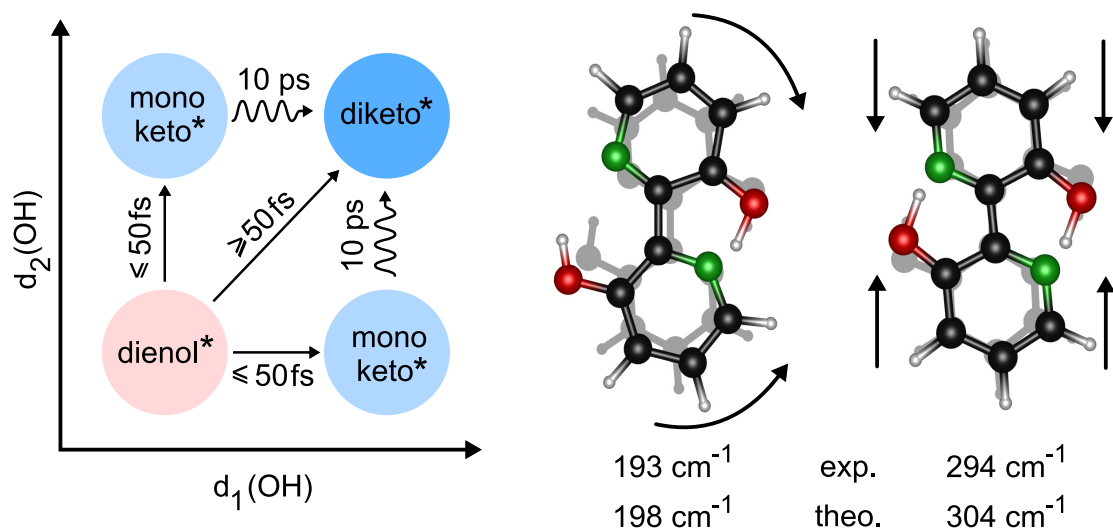


Abb. 3.6: Links: Schematische Darstellung der Potentialfläche von  $\text{BP(OH)}_2$  im  $S_1$  Zustand. Die Abstände  $d_{1,2}(\text{OH})$  beziehen sich auf den Proton-Donor Abstand in den beiden H-Chelatrings. Die Potentialfläche weist für die multidimensionalen Reaktionspfade von der dienol\* Konformation in die monoketo\* und diketo\* Produktzustände keine effektiven Barrieren auf. Rechts: Durch Geometrieoptimierung der enol Konformation berechnete Normalmoden. Die  $193\text{ cm}^{-1}$  Mode entspricht einer planaren Biegeschwingung und führt zu einer initialen Verkürzung des Donor-Akzeptor Abstands in nur einem H-Chelatring. Die  $294\text{ cm}^{-1}$  Mode entspricht einer planaren Streckschwingung und führt zu einer initialen Verkürzung des Donor-Akzeptor Abstands in beiden H-Chelatrings.

Eigene zeitaufgelöste Transmissionsmessungen bei Anregung mit 350 und 380 nm (s. Anhang 7) finden jeweils drei kohärent angeregte Moden mit 193, 294 und  $331\text{ cm}^{-1}$ . Die Amplitude der  $193\text{ cm}^{-1}$  Mode nimmt mit zunehmender Anregungsüberschussenergie zu, wohingegen die Amplituden der Moden mit 294 und  $331\text{ cm}^{-1}$  bei zunehmender Anregungsüberschussenergie relativ zur  $193\text{ cm}^{-1}$  Mode abnehmen. Quantenchemische Rechnungen zeigen, dass die  $193\text{ cm}^{-1}$  Mode einer planaren Biegeschwingung entspricht, wohingegen die Moden mit 294 und  $331\text{ cm}^{-1}$  planare Streckschwingungen sind (vgl. Abb. 3.6).

Die Anregung der  $193\text{ cm}^{-1}$  Biegeschwingung korreliert mit der Bildung des monoketo\* Konformers und kann deshalb mit dem monoketo Reaktionspfad assoziiert werden. In einem intuitiven Bild entspricht die Biegeschwingung einer initialen einseitigen Verkürzung der Proton Donor-Akzeptor Distanz und unterstützt diese Zuordnung. Die Streckschwingungen mit 294 und  $331\text{ cm}^{-1}$  korrelieren mit der diketo\* Bildung und entsprechen einer Verkürzung des Proton Donor-Akzeptor Abstands in beiden H-Chelatrings. Der



multidimensionale barrierefreie Reaktionspfad koppelt die Protonkoordinate an den Donor-Akzeptor Abstand (s. Kap. 3.1 und 3.5). Der Protontransfer findet folglich in beiden H-Chelatringen nahe dem inneren Umkehrpunkt der Kontraktionsbewegung statt. Die Periode der beiden relevanten Streckschwingungen von  $\sim 100$  fs bestimmt die Gleichzeitigkeit des ESIPT in den beiden H-Chelatringen auf etwa 10 fs genau. Ob auf einer noch kürzeren Zeitskala gesehen der elektronische Konfigurationswechsel in beiden H-Chelatringen konzertiert oder sequenziell abläuft, werden erst detaillierte theoretische Modellierungen endgültig beantworten können.

Das Doppelprotontransfer Molekül  $\text{BP(OH)}_2$  hat im Grundzustand und damit auch noch direkt nach der optischen Anregung  $C_{2h}$  Symmetrie [140]. Die  $193\text{ cm}^{-1}$  Mode führt zu einer einseitigen Kontraktion des Moleküls und zum Einfachprotontransfer und bricht somit die Symmetrie des Moleküls. Aufgrund der Auswahlregeln für elektronische Übergänge [141] kann diese Mode nicht optisch angeregt werden. Da die  $193\text{ cm}^{-1}$  Mode im Grundzustand bereits thermisch besetzt ist, projiziert der ultrakurze optische Anregungsimpuls Moleküle auch in einer Geometrie leicht außerhalb des symmetrischen Franck-Condon Punkts auf die  $S_1$  Potentialfläche. Von dort aus kann sich das Wellenpaket dann leicht entlang eines symmetriebrechenden Reaktionspfades entwickeln. Die durch den Einfachprotontransfer in  $\text{BP(OH)}_2$  angeregte Biegeschwingung belegt eindeutig, dass die im transienten Signal beobachtete Wellenpaketdynamik durch den Protontransfer angeregt wird und an den Reaktionspfad gekoppelt ist. Auch in den anderen, im Rahmen dieser Arbeit untersuchten, Protontransfersystemen führen die kohärent angeregten Normalmoden zu einer starken Verkürzung des Proton Donor-Akzeptor Abstands und haben damit eine große Projektion auf den Reaktionspfad. Es ist somit auch in diesen Fällen sehr sicher, dass die Wellenpaketbewegung durch den ESIPT ausgelöst wird.

Die Analyse der reaktiven vibronischen Schwingungswellenpaketbewegung kann auch in intermolekularen Mehrfachprotontransfersystemen bei der Klärung helfen, ob die einzelnen Protontransferschritte konzertiert oder sequenziell ablaufen. Theoretische Modellierungen und zeitaufgelöste Infrarotspektroskopie von 7-Azaindol Dimeren haben beispielsweise bereits gezeigt, dass die symmetrische Dimer-Streckschwingung an die lokale NH-Protontransfermode koppelt [142,143]. Entsprechende Experimente mit UV Anregung könnten basierend auf der angeregten Dimer-Schwingung klären, ob der intramolekulare Protontransfer in 7-azaindole Dimeren konzertiert oder sequenziell abläuft.

### 3.5 ESIPT Reaktionspfad im Falle eines steifen Molekülskeletts

Die vorangehend präsentierten Untersuchungen haben klar gezeigt, dass der Mechanismus des ultraschnellen ESIPT darauf beruht, dass sich das Molekülskelett soweit verformt, dass sich ein barrierefreier Reaktionspfad für die Wellenpaketbewegung von der enol\* zur keto\* Konformation ergibt. 10-HBQ hat eine stark Stokes-verschobene statische Fluoreszenz [124,144] und die zeitaufgelösten Transmissionskurven weisen die Charakteristika des ultraschnellen ESIPT auf [19]. Aufgrund seines verbrückten Molekülskeletts sollte

10-HBQ allerdings nicht in der Lage sein, die Proton Donor-Akzeptor Distanz soweit zu verkürzen, wie dies in HBT oder BP(OH)<sub>2</sub> passiert (vgl. Abb. 3.1). Aufgrund dieser Besonderheiten wird der ESIPT Mechanismus von 10-HBQ nachfolgend detailliert untersucht.

Eigene Untersuchungen der Reaktionsdynamik von 10-HBQ in Echtzeit (s. Anhang 8) finden eine Protontransferzeit von 25 fs, die im Vergleich zu HBT (33 fs) etwa 30 % schneller ist. Die reaktiv angeregten Normalmoden sind hochfrequenter als bei HBT, was auf das steifere Molekülskelett zurückzuführen ist. Im Bild des ESIPT Mechanismus korrespondiert die schnellere Protontransferzeit zu den höherfrequenten Normalmoden, da eine schnellere Kontraktion des H-Chelatrings zu einem früheren Protontransfer führt.

Quantenchemische Berechnungen der Potentialfläche und Wellenpaketpropagationen auf dieser Potentialfläche zeigen, dass sich das Wellenpaket barrierefrei vom enol\* zum keto\* Bereich der Potentialfläche entwickelt. Klassische Trajektorienrechnungen belegen, dass der Reaktionspfad tatsächlich viel stärker einer alleinigen Verschiebung des Protons und weniger der Verkürzung des Chelatrings entspricht wie in HBT. Das steife Molekülskelett verhindert, dass sich der Chelatingring soweit kontrahieren kann wie in HBT (s. Abb. 3.7; Anhang 8). Im Bild vom „aktiven“ und „passiven“ Proton dominiert im Fall von 10-HBQ die Proton-Koordinate den Reaktionspfad.

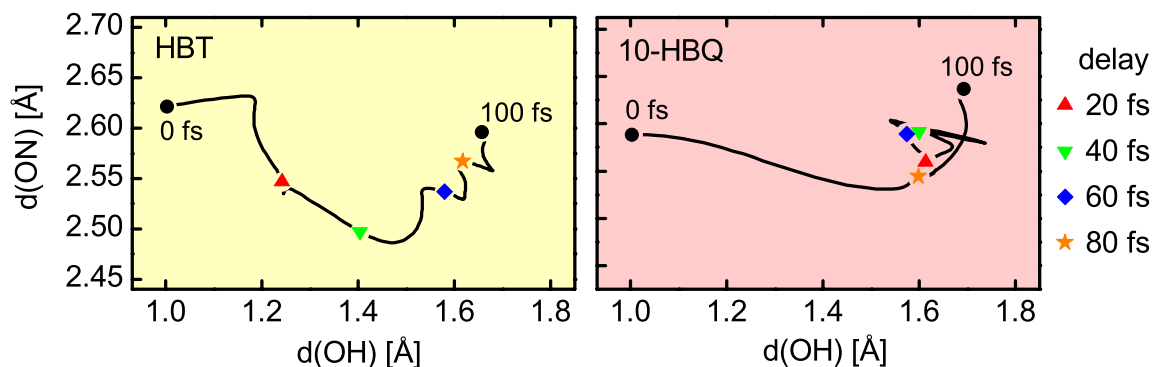


Abb. 3.7: Visualisierung der Trajektorien Rechnungen für den ESIPT in HBT und 10-HBQ. Der barrierefreie Reaktionspfad erfordert eine viel größere Verkürzung des ON-Abstandes in HBT als in 10-HBQ.

Geometrieoptimierungen mit der B3LYP/6-311+G(d,p) Methode zeigen, dass die Wasserstoffbrückenbindung in 10-HBQ 2,0 kcal/mol stärker ist als in HBT. Vergleichende NMR Messungen an 10-HBQ und 2-(2'-pyridyl)phenol finden einen deutlich größeren Proton-Peak-Shift in 10-HBQ ( $\delta = 14,9$  ppm) als in 2-(2'-pyridyl)phenol ( $\delta = 12,0$  ppm) [145] und unterstützen die Ergebnisse der Rechnungen. Die stärkere Wasserstoffbrücke in 10-HBQ führt dazu, dass selbst in protischen Lösungsmitteln der H-Chelatingring nur in sehr wenigen Molekülen aufbricht und der intramolekulare Protontransfer nicht unterbunden wird [124,144,146]. In 10-HBQ bindet die Wasserstoffbrücke das reaktive Proton schon im Grundzustand sehr stark an den Akzeptor und ermöglicht den schnellen und barrierefreien

Protontransfer nach Anregung in den  $S_1$ . Die starke Wasserstoffbrücke könnte intuitiv erklären, warum keine großen Verformungen des Molekülskeletts notwendig sind, um einen barrierefreien Reaktionspfad für das Proton zu ermöglichen.

Quantenchemische Untersuchungen der Topographie der  $S_1$  Potentialfläche zeigen eindeutig, dass die – wenn auch kleine – initiale Verformung des Molekülskeletts für einen barrierefreien Reaktionspfad unbedingt notwendig ist (s. Abb. 3.7). Für die direkte Verschiebung des Protons vom Donor zum Akzeptor liefern die Rechnungen eine Barriere von  $\sim 0,1$  eV; erst die Kontraktion des Chelatrings ermöglicht, dass der ESIPT in 10-HBQ, wie in HBT, als ballistische Wellenpaketbewegung und nicht als Tunnelprozess verläuft. Durch die Verformung des gesamten Molekülskeletts entlang des Reaktionspfades wird auch in 10-HBQ ein Wellenpaket präpariert, das im keto\* Minimum der Potentialfläche in den für die Chelatringskontraktion notwendigen Moden oszilliert.

### 3.6 Einfluss der Reaktionsumgebung auf die ESIPT Dynamik

Wie in den vorangehenden Kapiteln gezeigt wurde, sind für den ultraschnellen intramolekularen Protontransfer Verformungen des gesamten Molekülskeletts notwendig, um die Proton Donor-Akzeptor Distanz zu verkürzen, bevor der elektronische Konfigurationswechsel von der enol\* zur keto\* Konfiguration stattfindet. Es ist allerdings nur wenig über den Einfluss der Reaktionsumgebung auf die Wellenpaketbewegung bekannt und wie Änderungen der Umgebung die Wellenpaketbewegung und damit den Ausgang der Reaktion beeinflussen. Transiente Transmissionsmessungen am isolierten Molekül in der Gasphase ermöglichen es, die intramolekulare Dynamik ohne den Einfluss der Umgebung zu untersuchen. Im Vergleich zu Experimenten in Lösung ergeben sich dabei folgende Veränderungen:

(i) Ohne statistische Stöße zu umgebenden Molekülen ist die Entwicklung des Systems alleine durch die Startbedingungen und die inneren Eigenschaften gegeben. Die Dephasierung der elektronischen Wellenfunktion und der Zerfall vibratorischer Kohärenzen ist durch die intrinsischen Eigenschaften des Systems gegeben und sollte langsamer ablaufen als unter Wechselwirkung mit der Umgebung.

(ii) Viskose Umgebungen können zu effektiven Barrieren führen. Das isolierte System kann sich auch entlang flacher Gradienten der elektronischen Potentialfläche ungehindert entwickeln, es hat mehr sterische Freiheitsgrade, Translationen und Rotationen von Moleküluntereinheiten werden nicht gebremst und es kann zu keinem schnellen Transfer der Anregungsüberschussenergie an das Lösungsmittel kommen.

(iii) Experimente am isolierten Molekül sind am besten mit theoretischen Modellierungen zu vergleichen. Die in Kapitel 3.2 besprochenen, quantenchemischen Rechenmethoden betrachten alle das isolierte Molekül; ohne Wechselwirkungen mit der Umgebung ist das zu behandelnde Gesamtsystem kleiner, es ist weniger Rechenzeit erforderlich und es können präzisere Rechenverfahren eingesetzt werden.

Für einen aussagekräftigen Vergleich der Experimente in Gasphase und in Lösung ist es notwendig in beiden Umgebungen denselben Abfrageprozess zu verwenden, damit die Wellenfunktion auf dieselben Endzustände projiziert wird; ansonsten kann dieselbe Dynamik zu unterschiedlichen Signaturen führen. Transiente Transmissionsmessungen besitzen die nötige Zeitauflösung und durch das im Rahmen dieser Arbeit weiterentwickelte Anrege-Abtast-Spektrometer (s. Kap. 2.3) zum ersten Mal auch die nötige Sensitivität, zur Echtzeitbeobachtung des Protontransfers in Gasphase und Lösung. Der direkte Vergleich der ESIPT Dynamik und der nachfolgenden IC Kinetik in Gasphase und in Lösung ist in Anhang 9 detailliert beschrieben. Nachfolgend werden die zentralen Ergebnisse der Untersuchungen zusammenfassend dargestellt.

Die Ultrakurzzeitmessungen an HBT in der Gasphase liefern im Rahmen der Messgenauigkeit dieselbe Protontransferzeit wie in Lösung. Die ESIPT induzierte Wellenpaketdynamik ist von einer Oszillation mit  $250\text{ cm}^{-1}$  dominiert, die in beiden Umgebungen dieselbe Frequenz und Phase aufweist. In der Gasphase tritt zusätzlich ein langsamer Oszillationsbeitrag mit  $41\text{ cm}^{-1}$  auf, der in Lösung nicht beobachtet wird. Die zeitaufgelösten Messungen von 10-HBQ liefern in Gasphase und Lösung ebenfalls eine identische Protontransferzeit. Die Wellenpaketsignatur während der ersten 500 fs stimmt bezüglich der dominanten Oszillationen und deren Phasen überein. Aber auch in 10-HBQ treten in der Gasphase zusätzliche Moden auf, wie aus den Fouriertransformationen der Zeitkurven ersichtlich ist (s. Abb. 3.8).

Das Übereinstimmen der Protontransferzeit und der Wellenpaketdynamik bei kurzen Verzögerungszeiten erlaubt die Schlussfolgerung, dass der ESIPT Mechanismus in der Gasphase und in Lösung der gleiche ist, und die Umgebung praktisch keinen Einfluss auf diesen ultraschnellen intramolekularen Prozess hat. Der Gradient der reaktiven Potentialfläche führt einerseits zu einer treibenden Kraft, die deutlich stärker ist als die Hinderungen der Umgebung, andererseits stellen die für den ESIPT notwendigen Geometrieänderungen relativ kleine Verformungen dar, die sich innerhalb der Lösungsmittelschale abspielen. Die Dephasierungszeiten der schnellen Oszillationen sind in der Gasphase nur wenig länger als in der Lösung und liegen bei 1 – 2 ps. Dies zeigt eindeutig, dass die Dephasierung der Oszillationen in diesem reaktiven System nur in geringem Maße durch die Umgebung bedingt und hauptsächlich dem Molekül intrinsisch ist. Dieses Ergebnis ist sehr überraschend und steht in starkem Kontrast zum Dephasierungsverhalten nicht-reaktiver mittelgroßer Moleküle in der Gasphase [147-149]. So besitzen beispielsweise Perylene oder Benzol vibratorische Dephasierungszeiten im  $S_1$  Zustand von 100 ps [110] bzw. 1  $\mu\text{s}$  [150].

Durch die Anregung und den ESIPT werden hohe Schwingungszustände besetzt, die in einem anharmonischen Potential zu einer effizienten Verbreiterung von Wellenpaketen führen können [151]. Innerhalb der Zeit bis zu einer möglichen Rephasierung [16,70] ist die Schwingungsenergie durch intramolekulare Schwingungsumverteilung an andere Moden abgegeben [152], bzw. im Fall von HBT die interne Konversion in den Grundzustand erfolgt (s. unten). Es ist auch möglich, dass unterschiedliche initiale Besetzungszustände von nicht kohärent angeregten Schwingungsmoden im Ensemble durch an-

harmonische Kopplungen [18] zu einer leicht unterschiedlichen Entwicklung der einzelnen Moleküle und so zur Dephasierung führen.

Ein Vergleich der Protontransferzeit und der ESIPT induzierten Wellenpaketdynamik in verschiedenen Lösungsmitteln findet sich in Anhang A und bestätigt den geringen Einfluss der Reaktionsumgebung auf den ESIPT und die Wellenpaketdynamik. Die Protontransferzeit ist im Rahmen der Messgenauigkeit von  $\sim 5$  fs in allen untersuchten Lösungsmitteln, in denen ESIPT stattfindet, gleich; die Wellenpaketdynamik weist bezüglich Phase, Frequenz und Dephasierung nur minimale Unterschiede auf.

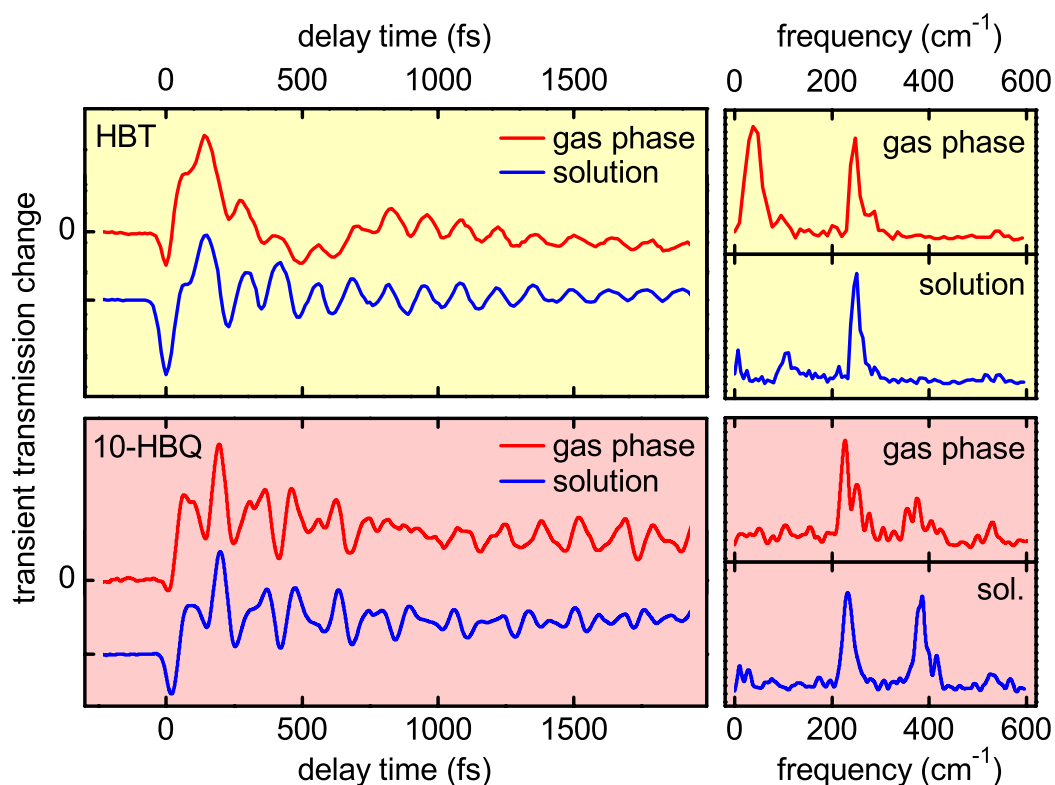


Abb. 3.8: Linke Spalte: Vergleich der Kurzzeitdynamik von HBT (Anregung/Abfrage: 350/510 nm) und 10-HBQ (350/625 nm) in Cyclohexan Lösung und in Gasphase. Rechte Spalte: Fouriertransformationen der oszillierenden Signalanteile.

Die transienten Transmissionsmessungen in der Gasphase zeigen die Anregung zusätzlicher Schwingungsbewegungen, die darauf hindeuten, dass neben oder nach dem ESIPT zusätzliche kohärente Prozesse ablaufen, die eine nähere Betrachtung verdienen. Die Entvölkerung des angeregten  $S_1$  Zustands von HBT vollzieht sich in Lösung mit etwa 100 ps, wie der Zerfall der keto\* Emission belegt, und entspricht der internen Konversion zurück in den elektronischen Grundzustand. Das isolierte Molekül zeigt überraschenderweise eine stark beschleunigte interne Konversion mit einer Zeitkonstante von 2,6 ps bei Anregung mit 325 nm und 4,2 ps bei Anregung mit 350 nm. Dies ist etwa 40-mal schneller als in

Lösung. Der  $S_1$  Zustand von 10-HBQ hat in Cyclohexan eine Lebensdauer von 300 ps, die sich in der Gasphase auf 34 ps verkürzt (s. Abb. 3.9).

Im Fall von HBT zeigen sowohl quantenchemische Berechnungen der  $S_1$  Potentialfläche wie auch klassische Trajektorienrechnungen (s. Anhang 10), dass die, durch den ultraschnellen ESIPT gebildete, planare keto\* Konformation bezüglich einer Torsionsbewegung bei der sich der Benzothiazol-Teil des Moleküls um die  $C_1 - C_2$  Bindung gegen den Phenol-Ring verdreht (s. Abb. 3.1 und 3.10) ein Energie-maximum darstellt. Die Potentialfläche entlang der Torsionskoordinate führt barrierefrei zu einer konischen Durchschneidung mit dem  $S_0$  Grundzustand bei einem Torsionswinkel von  $\phi = 90^\circ$ . Durch den Protontransfer wird der  $\pi$ -Bindungscharakter der  $C_1 - C_2$  Distanz verringert. Dies erlaubt eine einfache Torsion um die  $C_1 - C_2$  Bindung, wie sie auch in Ethen oder Stilben auftritt [153]. Die p-Orbitale der  $\pi$ -Bindung stehen bei  $\phi = 90^\circ$  senkrecht aufeinander, bilden ein Biradikal und sind energetisch entartet, was zur Energieabsenkung gegenüber der planaren Konformation führt [7,141]. Durch die konische Durchschneidung ist eine schnelle interne Konversion in den  $S_0$  Grundzustand möglich, bei der das keto Konformer ( $\phi = 0^\circ$ ) oder das transketo Konformer ( $\phi = 180^\circ$ ) gebildet werden kann (s. Anhänge 9, 10).

Die in der Gasphase beobachtete Schwingungsbewegung mit  $41 \text{ cm}^{-1}$  deutet auf eine Wellenpaketbewegung entlang der Torsionskoordinate hin, da die Torsion den Proton Donor-Akzeptor Abstand nicht verkürzt, folglich nicht zum ESIPT Reaktionspfad beiträgt, und so auch nicht durch den ESIPT kohärent angeregt werden kann. Klassische Trajektorienrechnungen (s. Anhang 10) zeigen explizit, dass sich die durch den ESIPT gebildete planare keto\* Konfiguration entlang des Gradienten der Torsionskoordinate entwickelt. Mit zunehmendem Torsionswinkel kommt es zusätzlich zu einer Pyramidalisierung am  $C_1$ -Kohlenstoffatom, d. h. die  $C_1 - C_2$  Bindung klappt aus der Ebene des Thiazolrings heraus. Dies bewirkt eine leichte Reduktion der Länge der OH-Wasserstoffbrücke und eine weitere Energieabsenkung der Konformation [154].

Die experimentell beobachtete  $41 \text{ cm}^{-1}$  Oszillation deutet im Widerspruch zu den quantenchemischen Rechnungen auf einen gebundenen Zustand und somit auf eine – zumindest kleine – Barriere entlang der Torsionskoordinate hin. Die Hypothese der Barriere wird durch die Anregungsüberschussenergieabhängigkeit der Rate der internen Konversion

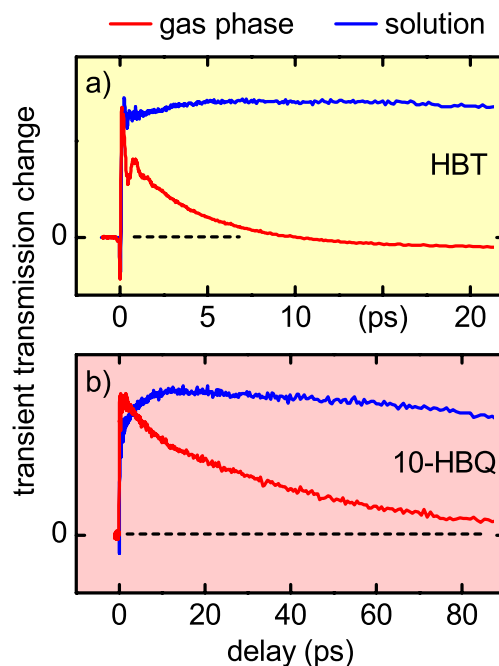


Abb. 3.9: Vergleich der internen Konversion von HBT (Anregung/Abfrage: 350/560 nm) und 10-HBQ (350/660 nm) in Gasphase und Lösung.

substanziert. Die Lage der Barriere entlang der Torsionskoordinate ist allerdings noch nicht vollständig geklärt, und damit auch nicht die Bewegungsform der  $41\text{ cm}^{-1}$  Oszillation. Findet die Torsion um  $\phi = 0^\circ$  herum statt, so durchläuft das Wellenpaket zweimal pro Oszillation das experimentelle Beobachtungsfenster bei  $\phi = 0^\circ$  und die tatsächliche Frequenz der Bewegung ist nur  $20,5\text{ cm}^{-1}$ . Findet die Oszillation in einen Winkelbereich  $0^\circ < \phi < 90^\circ$  statt, so erreicht das Wellenpaket nur einmal pro Umlauf das Beobachtungsfenster, die tatsächliche Oszillationsfrequenz ist  $41\text{ cm}^{-1}$  und die Potentialfläche weist im Bereich der Wellenpaketbewegung eine effektiv doppelt so starke Krümmung auf wie im ersten Fall.

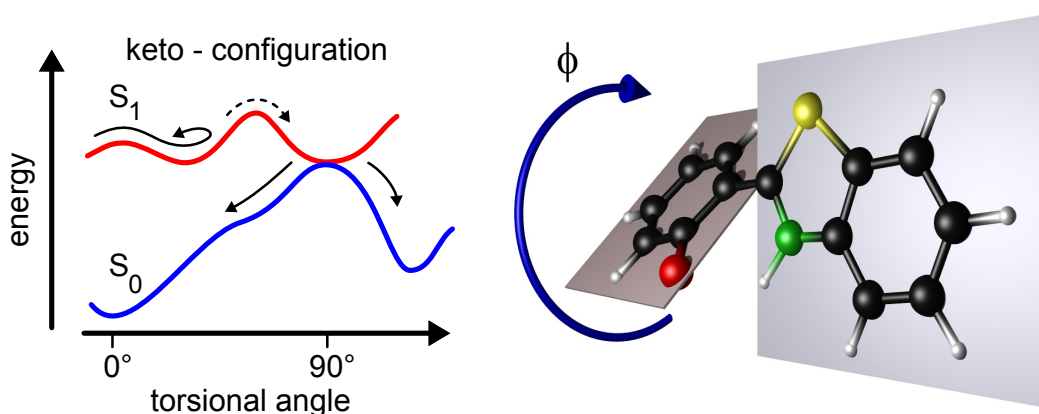


Abb. 3.10: Modellpotential für die interne Konversion von HBT in der Gasphase. Eine Torsion entlang der Benzol-Thiazol-Bindung führt bei einem Winkel von  $\phi = 90^\circ$  zu einer konischen Durchschneidung mit dem Grundzustand. Eine Potentialbarriere entlang der Reaktionskoordinate erlaubt periodische Bewegungsformen.

Anrege-Abtast-Spektroskopie mit sichtbaren Abtastimpulsen kann keine direkten Aussagen über die Molekülgeometrie treffen und die Frage, in welchem Bereich der Torsionskoordinate die beobachtete Wellenpaketbewegung in der Gasphase stattfindet, nicht beantworten. Transiente Infrarotspektroskopie könnte es allerdings erlauben, aus der Rotverschiebung der C=O Streckschwingung, die den Produktzustand des ESIPT darstellt, direkt auf die Stärke und damit die Länge der Wasserstoffbrücke zur NH-Gruppe zu schließen [18]. Über die Wasserstoffbrücke koppelt die Torsion an die lokale C=O Streckschwingung und die Frequenzverschiebung der C=O Bande sollte mit der Frequenz der Torsion moduliert sein [18,21,155]. Aus der absoluten Verschiebung der Bande sollte sich die Länge der Wasserstoffbrücke und damit der Winkelbereich, in dem die Torsion stattfindet, bestimmen lassen.

In Lösung wird die Torsionsbewegung durch Wechselwirkung mit angrenzenden Lösungsmittelmolekülen überdämpft. Im Gegensatz zu den höherfrequenten Moden, die sich in der Lösungsmittelschale abspielen, erfordert die Torsion eine Verschiebung angrenzender Moleküle. Die Wellenpaketbewegung in der Gasphase entlang der Torsionskoordinate wird in Lösung zu einem statistischen Prozess, der zu einer signifikant lang-

sameren internen Konversion führt. Für 2,2'-bipyridyl-3-ol und 2-(2'-pyridyl)phenol zwei Einfachprotontransfersysteme sehr ähnlich zu BP(OH)<sub>2</sub>, wird eine energetisch tiefer liegende konische Durchschneidung mit dem Grundzustand für einen Torsionswinkel von 90° um die zentrale Kohlenstoff-Kohlenstoff-Bindung vorhergesagt [156]. Dies unterstützt das für HBT vorgeschlagene Modell und substantiiert, dass die zugrunde liegende Torsion ein weitverbreiteter Mechanismus sein könnte. Das Chromophor des grün fluoreszierenden Proteins (GFP), beispielsweise, weist innerhalb des Proteins eine Fluoreszenzquantenausbeute von  $\Phi_F = 0.8$  auf, die außerhalb der Proteinumgebung auf  $\Phi_F \sim 10^{-3}$  abfällt [18,157]. Quantenchemische Berechnungen führen zu der Schlussfolgerung, dass die beiden Hälften des freien GFP Chromophors im S<sub>0</sub> Grundzustand planar sind, wohingegen sie im S<sub>1</sub> aufeinander senkrecht stehen. Dieser IC Mechanismus ähnelt sehr stark dem hier für HBT vorgestellten. Die hohe Fluoreszenzquantenausbeute des GFP Chromophors im Protein ergibt sich wahrscheinlich dadurch, dass diese Konformationsänderung blockiert wird. Allgemeiner könnte die Kontrolle chemischer Konformationen durch Einbettung in eine starre Matrix oder Proteinumgebung ein wichtiger Mechanismus sein, wie die Natur die Effizienz von photochemischen Ereignissen steuert.

Ähnlich wie in HBT ist die interne Konversion von 10-HBQ in der Gasphase ebenfalls beschleunigt gegenüber der Lösungsumgebung (s. Abb. 3.9) und die Gasphasenmessungen zeigen die zusätzliche kohärente Anregung weiterer Schwingungsbewegungen. Die in Lösungsumgebung kohärent angeregten Oszillationen entsprechen planaren Verformungen des Molekülskeletts, die den Proton Donor-Akzeptor Abstand verkürzen (vgl. Kap. 3.5 und Anhang 8). Eine Zuordnung der in der Gasphase zusätzlich beobachteten Oszillationsfrequenzen zu berechneten Normalmoden zeigt klar auf, dass diese nichtplanaren Gerüstschwingungen entsprechen. In Analogie zum Mechanismus der internen Konversion von HBT könnte es auch bei 10-HBQ eine außerplanare konische Durchschneidung geben, durch die eine schnelle Relaxation in den Grundzustand möglich ist. In Lösung werden die nichtplanaren Moden durch angrenzende Lösungsmittelmoleküle wiederum überdämpft und treten nicht als kohärente Oszillationen in den zeitaufgelösten Messungen auf. Im Fall von 10-HBQ ist der Unterschied der internen Konversionsgeschwindigkeit zwischen Gasphase und Lösung deutlich geringer als bei HBT. Dies ist leicht verständlich, da sich 10-HBQ aufgrund des steifen Molekülskeletts nicht so weit verformen kann wie HBT, und folglich eine Behinderung durch die Lösungsmittelschale keinen so starken Einfluss auf die Dynamik der internen Konversion hat. Zur endgültigen Klärung des Mechanismus der internen Konversion von 10-HBQ in der Gasphase, sind allerdings noch weitere Modellierungen der Potentialfläche nötig, die die Lage der konischen Durchschneidung und den dorthin führenden Reaktionspfad aufzeigen.

Der Vergleich zwischen Gasphase und Lösung zeigt, dass der ultraschnelle ESIPT nicht durch die Reaktionsumgebung beeinflusst wird. Der Gradient der Potentialfläche entlang des ESIPT Reaktionspfades ist sehr steil: der keto\* Zustand ist in den hier untersuchten Molekülen mehr als 3000 cm<sup>-1</sup> gegenüber dem enol\* Zustand angesenkt. Der ESIPT und ähnliche ultraschnelle reaktive Prozesse verlaufen nicht über thermisch relaxierte Zustände und sind deshalb wenig anfällig auf den Einfluss von Lösungsmitteln und anderen Um-



gebungsvariablen. Speziell für die ESIPT Reaktion tragen die kleinen Konformationsänderungen entlang des Reaktionspfads dazu bei, dass der Prozess innerhalb der Lösungsmittelschale abläuft und sterische Hinderungen durch angrenzende Lösungsmittelmoleküle keinen Einfluss auf den Reaktionspfad und Mechanismus haben.

Ganz anders verhält es sich mit der nachfolgenden internen Konversion. Die dafür notwendigen Verformungen des Molekülskeletts sind wesentlich größer, als die entsprechenden entlang des ESIPT Pfades. Hinzu kommt, dass die Torsion die Energie nur um  $960\text{ cm}^{-1}$  absenkt (MRCI+Q, s. Anhang 10), der Gradient der Potentialfläche in dieser Koordinate also deutlich flacher ist. Insgesamt wird die Geschwindigkeit der Torsion und damit der Kanal der internen Konversion durch die konische Durchschneidung stark durch die effektive Barriere der Lösungsmittelviskosität beeinflusst. Existiert entlang der Torsionskoordinate eine Potentialbarriere, so kann auch diese durch verschiedene Umgebungsvariablen effektiv verändert werden. Die in Anhang A präsentierten Messungen in unterschiedlichen Lösungsmitteln zeigen, dass die IC Rate zunimmt, wenn die Viskosität des Lösungsmittels abnimmt, und unterstützen das hier vorgeschlagene Modell. Die konische Durchschneidung kann auch in Lösung immer noch zur internen Konversion beitragen, allerdings ist durch die Dämpfung des Lösungsmittels keine Wellenpaketbewegung in dieser Koordinate mehr zu beobachten.



## 4 Zusammenfassung und Ausblick

In den bisherigen Kapiteln und in den angehängten eigenen Veröffentlichungen sind Neuentwicklungen zur Erzeugung, Manipulation und Detektion von Femtosekunden-Lichtimpulsen beschrieben. Diese technologischen Neuentwicklungen haben es erstmals ermöglicht, mittels ultrasensitiver Anrege-Abtast-Spektroskopie Photoreaktionen in Gasphase und in Lösung mit demselben Abfrageprozess und derselben Zeitauflösung direkt miteinander zu vergleichen. Durch Kombination von Anrege-Abtast-Spektroskopie und quantenchemischen Berechnungen ist es am Beispiel des ultraschnellen Protontransfers im elektronisch angeregten Zustand gelungen, ein detailliertes Modell eines reaktiven molekularen Prozesses auf quantenmechanischer Ebene aufzustellen.

Nachfolgend sind die Erkenntnisse zur Impulserzeugung und Messtechnik sowie zur Analyse der Wellenpaketdynamik in Bezug auf Reaktionsmechanismen und Reaktionskontrolle zusammengefasst. Mögliche Weiterentwicklungen und Perspektiven diesbezüglich werden aufgezeigt und neue, verallgemeinerte Erkenntnisse dargelegt.

### **Messtechnik und Impulserzeugung – Perspektiven und Anwendbarkeit**

Im Rahmen dieser Arbeit wurde das Konzept des nichtkollinear gepumpten optisch parametrischen Verstärkers (NOPA) an die Parameter neuartiger Ytterbium basierter Faserlasersysteme angepasst, und abstimmbare Impulse von 250 bis 990 nm bei Impulsdauern bis hinab zu 13,4 fs und Megahertz Repetitionsraten wurden erzeugt.

Für viele Kontrollexperimente dringend benötigte, modulierte und strukturierte UV-Impulse mit Substrukturen von nur 20 fs wurden durch Amplituden- und Phasenmodulation sichtbarer Impulse im Frequenzraum und nachfolgende gestreckte Summenfrequenzmischung erzeugt.

Verbesserungen der Detektion und Datenerfassung erlauben ultrasensitive Anrege-Abtast-Spektroskopie mit einer Sensitivität von  $1,1 \times 10^{-6}$  OD in der Gasphase und in Lösung, und damit den direkten Vergleich ultraschneller Prozesse in beiden Reaktionsumgebungen in Echtzeit.

Weitere Verbesserungen im Dynamikbereich und Signal-zu-Rausch-Verhältnis von Anrege-Abtast-Messungen könnten sich durch aktive und passive Stabilisierung der Lichtquellen oder durch den Einsatz neuer, rauschärmerer Lasersysteme wie folgt ergeben.

(i) Das Rauschen der Anrege-Abtast-Messungen ist trotz der Verwendung eines Referenzkanals und der alternierenden Anregung der Probe von den technischen Fluktuationen der Anregungs- und Abtastimpulse dominiert. Stabilere Lichtquellen sollten sich daher direkt auf das Rauschen im Transmissionssignal auswirken. Aktive Stabilisierung [158] des Lasersystems verspricht Ausgangsfluktuationen von nur 0,1 % rms, was einer zehnfachen Verringerung gegenüber dem in dieser Arbeit verwendeten Titan-Saphir Ver-

stärker entspricht. Noch größeres Potential hat eine aktive Stabilisierung, die direkt auf NOPA Impulse angewandt werden kann [159].

(ii) Durch Frequenzverdopplung mit hoher Quanteneffizienz können Pump-Impulse für die parametrische Verstärkung erzeugt werden, die geringere Fluktuationen aufweisen als die fundamentalen Impulse des Lasersystems (s. Kap. 2.1). Wenn sich die parametrische Verstärkung in einem ähnlichen Regime betreiben lässt, in dem Sättigung und Rückkonversion entscheidend sind, könnten NOPA Impulse erzeugt werden, die geringere Fluktuationen aufweisen als das Lasersystem. Möglicherweise lassen sich auch ähnlich zur Erzeugung sehr stabiler, mittelinfraroter Impulse [160] durch Differenzfrequenzmischung von Signal- und Idler-Impulsen einer UV gepumpten NOPA Stufe sehr stabile sichtbare Impulse erzeugen.

(iii) Für Messungen, die nur kleine Signale erlauben, wie beispielsweise Photoelektronenspektroskopie oder transiente Absorption optisch dünner Proben, verspricht der Einsatz hochrepetierende Laser wesentliche Verbesserungen im Signal-zu-Rausch-Verhältnis und in der Messdauer. Da die spektrale Rauschdichte hochrepetierender Systeme deutlich geringer ist als die von Kilohertz-Verstärkern, könnten sich durch ihren Einsatz in der Anrege-Abtast-Spektroskopie gleichartige Verbesserungen ergeben. Bei Experimenten mit Megahertz Repetitionsraten ist jedoch zu beachten, dass die Probe wieder hinreichend schnell vollständig relaxiert, da ein Probenaustausch zwischen den Laserimpulsen praktisch nicht möglich ist.

Wartungsarme und justagefreie („turn-key“) Pikosekunden-Lasersysteme werden schon seit Längerem für die Materialbearbeitung in der Industrie angeboten. Neue computergesteuerte, Ytterbium-basierte Faserlasersysteme versprechen jetzt auch Langzeitstabilität und Benutzerkomfort bei Impulsdauern von nur wenigen Hundert Femtosekunden. Zusammen mit einfach zu bedienenden Frequenzkonvertern, wie die im Rahmen dieser Arbeit entwickelten NOPAs, bilden sie die Voraussetzung, dass die experimentelle Datengewinnung stark vereinfacht wird. Dadurch können die inhaltlichen Aspekte chemischer und biologischer Fragestellungen in entsprechenden Kooperationen zielstrebig angegangen werden.

## **Wellenpaketdynamik zur Aufklärung ultraschneller multidimensionaler Reaktionsmechanismen**

Der intramolekulare Protontransfer in elektronisch angeregten Zustand (ESIPT) ist der Prototyp eines ultraschnellen reaktiven Prozesses, der Wellenpaketdynamik induziert. Es wurde gezeigt, dass der ESIPT als ballistische Wellenpaketbewegung entlang eines effektiv barrierefreien Reaktionspfades verläuft und in Gasphase wie in Lösung dieselbe Kinetik und Dynamik zeigt. Die angeregten Normalmoden entsprechen einer planaren Verformung des Molekülskeletts, die innerhalb der Lösungsmittelschale stattfindet, sodass Reibung und sterische Hinderung durch angrenzende Moleküle darauf keinen Einfluss haben.

Für den ESIPT konnte eindeutig gezeigt werden, dass die Masse des Wasserstoffkerns keinen Einfluss auf die Reaktionskinetik hat und dass bei der Beschreibung des ESIPT kein Tunneln des Protons berücksichtigt werden muss. Die Wellenpaketdynamik von parallelen Reaktionskanälen kann voneinander unterschieden werden.

Die interne Konversion in ESIPT Molekülen ist ein Beispiel für eine sehr effiziente Relaxation in den elektronischen Grundzustand. Die IC Rate hängt sehr stark von der Molekülstruktur, der Anregungsenergie und der Reaktionsumgebung ab. Der erste Schritt der internen Konversion verläuft in der Gasphase als ballistische Wellenpaketbewegung, in Lösung als ratenartigen Prozess.

Aus der Kombination dieser Resultate lassen sich allgemeinere Erkenntnisse zur reaktiven Dynamik ableiten, die universellen Charakter für reaktive Prozesse haben. Diese generalisierten Schlussfolgerungen sind nachfolgend zusammengefasst.

(i) Die Analyse reaktiver Wellenpaketdynamik hat sich als mächtiger Ansatz herausgestellt, um Reaktionsmechanismen aufzuklären. Prozesse im elektronisch angeregten Zustand lassen sich durch einen ultrakurzen Anregungsimpuls zu einem wohldefinierten Zeitpunkt starten und erlauben so ein Wellenpaket zu präparieren. Die meisten chemisch relevanten Reaktionen finden jedoch im elektronischen Grundzustand statt. Es bleibt eine große Herausforderung für die Zukunft, die kohärente Entwicklung einer Reaktion auch im Grundzustand zu beobachten. In diesen Fällen kann jedoch der Durchbruch im Verständnis des Mechanismus erreicht werden, wenn stattdessen ein ähnlicher Prozess im elektronisch angeregten Zustand untersucht wird, wie es in dieser Arbeit für den Protontransfer geschehen ist.

(ii) An allen hier untersuchten ultraschnellen Prozessen sind mehrere Kernkoordinaten signifikant beteiligt. Eine eindimensionale Projektion auf eine verallgemeinerte Reaktionskoordinate kann nicht allen Charakteristika von ultraschnellen Prozessen Rechnung tragen. Für eine adäquate Beschreibung ist ein multidimensionales Bild notwendig, das die Funktionen der unterschiedlichen Kernkoordinaten wiedergibt, der Impulserhaltung der Wellenpaketpropagation Rechnung trägt und die Irreversibilität auf ultraschnellen Zeitskalen erklärt [25]. Von einem ultraschnellen eindimensionalen Prozess würde man stets erwarten, dass die Vor- und Rückreaktion gleichermaßen ablaufen können – ein multidimensionaler Prozess muss jedoch erst wieder in allen Koordinaten zurückkehren, was ein viel längeres Zeitfenster für die Energiedissipation öffnet und somit auch in der Gasphase die Rückreaktion effektiv ausschließt.

(iii) Die in dieser Arbeit gewonnen Erkenntnisse unterstützen das Modell, dass eine effiziente interne Konversion mit großen Konformationsänderungen verknüpft ist [161]. Die quantenchemischen Modellierungen zeigen die hohe Relevanz von konischen Durchschneidungen für die ultraschnelle interne Konversion. Hieraus ergeben sich wichtige Folgerungen für viele chemische Reaktionen, da diese per Definition Konformations- und Strukturänderungen zur Folge haben. Es eröffnen sich neue Möglichkeiten und Wege für das Design von effizienten photochromen Schaltern, die es erlauben, einen Kompromiss zwischen ultraschnellem IC und schneller Konversion zum Photoprodukt zu finden.

## Ausblick

Die untersuchten Protontransfersysteme haben gezeigt, dass die vibratorische Dephasierung mittelgroßer reaktiver Systeme in der Gasphase nicht langsamer ablaufen muss als in Lösung. Durch speziell geformte Anregungsimpulse wurde für Halogene in Edelgasmatrizen gezeigt, dass die vibratorische Dephasierung teilweise reversibel ist und durch entsprechende Anregung ein Wellenpaket zu einem späteren Zeitpunkt fokussiert werden kann [16,70]. Sollte sich diese Methode von der eindimensionalen Wellenpaketbewegung in biatomaren Molekülen auf die hier vorgestellten multidimensionalen Systeme übertragen lassen, könnten es äußerst aufschlussreiche Einblicke in den Mechanismus des multidimensionalen Dephasierungsprozesses ermöglichen.

Die elektronische Dephasierungszeit von komplexen reaktiven Systemen in der Gasphase ist noch weitgehend ungeklärt. Genauso wie die vibratorische Dephasierung könnte sie großteils durch intramolekulare Prozesse bestimmt sein und viel schneller ablaufen, als man von nichtreaktiven Systemen wie Benzol [150] erwarten würde [162]. Experimente mit zueinander phasenstabilen Impulsen an Protontransfersystemen in der Gasphase könnten zur Beantwortung dieser Frage beitragen. Im Rahmen dieser Arbeit wurden die technischen Grundlagen für derartige, zukünftige Untersuchungen gelegt.

Die Kontrolle chemischer Reaktionen unter Ausnutzung vibratorischer Kohärenzen wurde bereits erfolgreich eingesetzt, beispielsweise selektiv Bindungen in kleinen Molekülen oder Clustern zu brechen [79,163-166]. Die hier vorgestellten Erkenntnisse zur Wellenpaketdynamik in mittelgroßen aromatischen Molekülen könnten es in Zukunft erlauben, in diesen Systemen Wellenpakete in lokalen Moden anzuregen und selektiv Bindungen zu brechen. Geformte UV-Impulse ermöglichen dabei Experimente, die die Evolution auf mehreren elektronischen Potentialflächen ausnutzen. Auch die Kombination von geformten UV und nahinfraroten Impulsen ist denkbar und durch die hier vorgestellten Entwicklungen in der Impulserzeugung scheint sie auch realisierbar.

Vibratorische Wellenpakete mit einem kontrollierbaren Anfangsimpuls [167,168] oder die Interferenz zwischen Wellenpaketen [16,28,169-171] kann ausgenutzt werden, um die Dynamik in einem Molekül mit parallelen Reaktionspfaden zu steuern. Dies ist insbesondere dann vorstellbar, wenn sich die Reaktionspfade in ihrer Wellenpaketdynamik deutlich unterscheiden, wie es im Doppelprotontransfersystem  $\text{BP}(\text{OH})_2$  der Fall ist. Zur Kontrolle der Wellenpaketbewegung im elektronisch angeregten Zustand sollten sich die hier entwickelten, geformten UV-Impulse hervorragend einsetzen lassen.

Quantenchemische Modellierungen helfen bei der Interpretation experimenteller Ergebnisse und der kritische Vergleich experimenteller und theoretischer Daten ermöglicht die ständige Weiterentwicklung der Rechenverfahren. Es ist bereits in greifbare Nähe gerückt, durch Molekulardynamikrechnungen funktionale Moleküle gemäß spezieller Anforderungen zu entwickeln [172-174]. In Zukunft ist es damit durchaus im Bereich des Möglichen neue Medikamente zu entwickeln, die beispielsweise durch wenige Wasserstoffbrückenbindungen an die gesunde Form des Prion-Proteins binden und es so stabilisieren.

## Literaturverzeichnis

- [1] A. H. Zewail, *Science* **242**, 1645 (1988).
- [2] M. Klessinger, and J. Michl, *Excited States and Photochemistry of Organic Molecules*, VCH, Weinheim (1995).
- [3] J. L. Herek, S. Pedersen, L. Bañares, and A. H. Zewail, *J. Chem. Phys.* **97**, 9046 (1992).
- [4] A. Douhal, F. Lahmani, and A. Zewail, *Chem. Phys.* **207**, 477 (1996).
- [5] D. Polli, L. Lüer, and G. Cerullo, *Rev. Sci. Instrum.* **78**, 103108 (2007).
- [6] W. Demtröder, *Laserspektroskopie*, Springer, Berlin (2007).
- [7] A. Nitzan, *Chemical Dynamics in Condensed Phases*, Oxford University Press, New York (2006).
- [8] M. D. Cohen, and S. Flavian, *J. Chem. Soc. B* **317** (1967).
- [9] A. Mordzinski, A. Grabowska, W. Kühnle, and A. Krówczyński, *Chem. Phys. Lett.* **101**, 291 (1983).
- [10] P. Hamm, J. Helbing, and J. Bredenbeck, *Chem. Phys.* **323**, 54 (2006).
- [11] J. Hauer, T. Buckup, and M. Motzkus, *J. Phys. Chem. A* **111**, 10517 (2007).
- [12] M. Petković, and O. Kühn, *Chem. Phys.* **304**, 91 (2004).
- [13] M. Shapiro, Z. Chen, and P. Brumer, *Chem. Phys.* **217**, 325 (1997).
- [14] T. Arthen-Engeland, T. Bultmann, N. P. Ernsting, M. A. Rodriguez, and W. Thiel, *Chem. Phys.* **163**, 43 (1992).
- [15] U. Banin, A. Waldman, and S. Ruhman, *J. Chem. Phys.* **96**, 2416 (1992).
- [16] M. Gühr, M. Bargheer, M. Fushitani, T. Kiljunen, and N. Schwentner, *Phys. Chem. Chem. Phys.* **9**, 779 (2007).
- [17] M. J. Rosker, T. S. Rose, and A. H. Zewail, *Chem. Phys. Lett.* **146**, 175 (1988).
- [18] M. Rini, A. Kummrow, J. Dreyer, E. T. J. Nibbering, and T. Elsaesser, *Faraday Discuss.* **122**, 27 (2002).
- [19] S. Takeuchi and T. Tahara, *J. Phys. Chem. A* **109**, 10199 (2005).
- [20] C. J. Bardeen, Q. Wang, and C. V. Shank, *Phys. Rev. Lett.* **75**, 3410 (1995).
- [21] J. Stenger, D. Madsen, J. Dreyer, E. T. J. Nibbering, P. Hamm, and T. Elsaesser, *J. Phys. Chem. A* **105**, 2929 (2001).
- [22] S. Lochbrunner, A. J. Wurzer, and E. Riedle, *J. Chem. Phys.* **112**, 10699 (2000).
- [23] R. de Vivie-Riedle, and U. Troppmann, *Chem. Rev.* **107**, 5082 (2007).
- [24] V. Blanchet, C. Nicole, M. A. Bouchene, and B. Girard, *Phys. Rev. Lett.* **78**, 2716 (1997).
- [25] S. Lochbrunner, A. J. Wurzer, and E. Riedle, *J. Phys. Chem. A* **107**, 10580 (2003).
- [26] R. M. Bowman, M. Dantus, and A. H. Zewail, *Chem. Phys. Lett.* **156**, 131 (1989).
- [27] N. P. Ernsting, S. A. Kovalenko, T. Senyushkina, J. Saam, and V. Farztdinov, *J. Phys. Chem. A* **105**, 3443 (2001).
- [28] N. F. Scherer, R. J. Carlson, A. Matro, M. Du, A. J. Ruggiero, V. Romero-Rochin, J. A. Cina, G. R. Fleming, and S. A. Rice, *J. Chem. Phys.* **95**, 1487 (1991).
- [29] A. J. Wurzer, S. Lochbrunner, and E. Riedle, *Appl. Phys. B* **71**, 405 (2000).

- [30] S. Lochbrunner, K. Stock, and E. Riedle, *J. Mol. Struct.* **700**, 13 (2004).
- [31] W. S. Warren, H. Rabitz, and M. Dahleh, *Science* **259**, 1581 (1993)
- [32] H. Rabitz, R. de Vivie-Riedle, M. Motzkus, and K. Kompa, *Science* **288**, 824 (2000).
- [33] D. Geppert, L. Seyfarth, and R. de Vivie-Riedle, *Appl. Phys. B* **79**, 987 (2004).
- [34] D. Geißler, B. J. Pearson, and T. Weinacht, *J. Chem. Phys.* **127**, 204305 (2007).
- [35] T. Baumert, M. Grosser, R. Thalweiser, and G. Gerber, *Phys. Rev. Lett.* **67**, 3753 (1991).
- [36] J. L. Herek, W. Wohlleben, R. J. Cogdell, D. Zeidler and M. Motzkus, *Nature* **417**, 533 (2002).
- [37] J. Hauer, T. Buckup, and M. Motzkus, *J. Chem. Phys.* **125**, 061101 (2006).
- [38] T. Brixner, N. H. Damrauer, P. Niklaus, and G. Gerber, *Nature* **414**, 57 (2001).
- [39] T. Baumert, T. Brixner, V. Seyfried, M. Strehle, and G. Gerber, *Appl. Phys. B* **65**, 779 (1997).
- [40] T. Brixner, and G. Gerber, *Chem. Phys. Chem.* **4**, 418 (2003).
- [41] J. Hauer, H. Skenderovic, K. L. Kompa, and M. Motzkus, *Chem. Phys. Lett.* **421**, 523 (2006).
- [42] F. Verluise, V. Laude, Z. Cheng, Ch. Spielmann, and P. Tournois, *Opt. Lett.* **25**, 575 (2000).
- [43] M. Ninck, A. Galler, T. Feurer, and T. Brixner, *Opt. Lett.* **32**, 3379 (2007).
- [44] A. M. Weiner, *Rev. Sci. Instrum.* **71**, 1929 (2000).
- [45] T. Wilhelm, J. Piel, and E. Riedle, *Opt. Lett.* **22**, 1494 (1997).
- [46] E. Riedle, M. Beutter, S. Lochbrunner, J. Piel, S. Schenkl, S. Spörlein, and W. Zinth, *Appl. Phys. B* **71**, 457 (2000).
- [47] G. Cerullo, and S. De Silvestri, *Rev. Sci. Instrum.* **74**, 1 (2003).
- [48] A. Baltuska, T. Fuji, and T. Kobayashi, *Opt. Lett.* **27**, 306 (2002).
- [49] R. Huber, H. Satzger, W. Zinth, and J. Wachtveitl, *Opt. Commun.* **194**, 443 (2001).
- [50] T. V. Andersen, J. Thøgersen, S. R. Keiding, and J. J. Larsen, *Appl. Phys. B* **76**, 639 (2003).
- [51] G. M. Gale, M. Cavallari, T. J. Driscoll, and F. Hache, *Opt. Lett.* **20**, 1562 (1995).
- [52] M. Punke, F. Hoos, C. Karnutsch, U. Lemmer, N. Linder and K. Streubel, *Opt. Lett.* **31**, 1157 (2006).
- [53] J. A. Moon, *Rev. Sci. Instrum.* **64**, 1775 (1993).
- [54] P. Bado, S. B. Wilson, and K. R. Wilson, *Rev. Sci. Instrum* **53**, 706 (1982).
- [55] L. Andor, A. Lörincz, J. Siemion, D. D. Smith, and S. A. Rice, *Rev. Sci. Instrum.* **55**, 64 (1984).
- [56] M. van Exter and A. Lagendijk, *Rev. Sci. Instrum.* **57**, 390 (1986).
- [57] J. M. Chwalek and D. Dykaar, *Rev. Sci. Instrum.* **61**, 1273 (1990).
- [58] G. C. Cho, W. Kütt, and H. Kurz, *Phys. Rev. Lett.* **65**, 764 (1990).
- [59] T. V. Andersen, O. Schimd, C. Bruchmann, J. Limpert, C. Aguergaray, E. Cormier, and A. Tünnermann, *Opt. Express* **14**, 4765 (2006).
- [60] J. B. Ashcom, R. R. Gattass, C. B. Schaffer, and E. Mazur *J. Opt. Soc. Am. B* **23**, 2317 (2006).



- [61] A. Brodeur, and S. L. Chin, Phys. Rev. Lett. **80**, 4406 (1998).
- [62] A. Brodeur, and S. L. Chin, J. Opt. Soc. Am. B **16**, 637 (1999).
- [63] H. S. Park, J. S. Baskin, O.-H. Kwon, and A. H. Zewail, Nano Lett. **7**, 2545 (2007).
- [64] G. C. Bhar, U. Chatterjee, and S. Das, Appl. Phys. Lett. **58**, 231 (1991).
- [65] D. Kühlke, and U. Herpers, Opt. Comm. **69**, 75 (1988).
- [66] J. C. Diels, and W. Rudolph, *Ultrashort laser pulse phenomena*, Academic Press (2006).
- [67] J. Piel, E. Riedle, L. Gundlach, R. Ernstorfer, and R. Eichberger, Opt. Lett. **31**, 1289 (2006).
- [68] K. Duncker and W. Widdra, Institut für Physik, Martin-Luther-Universität Halle-Wittenberg, Hoher Weg 8, 06120 Halle, Germany, persönliche Mitteilung (2008).
- [69] K. Duncker, M. Kiel, and W. Widdra, XVI International Conference on Ultrafast Phenomena 2008, Conference Program Information (European Physical Society, Mulhouse, France), THUIIIId.24.
- [70] M. Gühr, H. Ibrahim, and N. Schwentner, Phys. Chem. Chem. Phys. **6**, 5353 (2004).
- [71] M. Roth, M. Mehendale, A. Bartelt, and H. Rabitz, Appl. Phys. B **80**, 441 (2005).
- [72] S. Coudreau, D. Kaplan, and P. Tournois, Opt. Lett. **31**, 1899 (2006).
- [73] M. Hacker, G. Stobrawa, R. Sauerbrey, T. Buckup, M. Motzkus, M. Wildenhain, and A. Gehner, Appl. Phys. B **76**, 711 (2003).
- [74] B. J. Pearson, and T. C. Weinacht, Opt. Express **15**, 4385 (2007).
- [75] Fastlite, DAZZLER T-UV-250-400 Specifications (22<sup>th</sup> Nov. 2007).
- [76] M. Hacker, T. Feurer, R. Sauerbrey, T. Lucza, and G. Szabo, J. Opt. Soc. Am. B **18**, 866 (2001).
- [77] H. Wang and A. M. Weiner, IEEE J. Quantum Electron. **40**, 937 (2004).
- [78] P. Nuernberger, G. Vogt, R. Selle, S. Fechner, T. Brixner and G. Gerber, Appl. Phys. B **88**, 519 (2007).
- [79] D. Geppert, and R. de Vivie-Riedle, J. Photochem. Photobiol. A **180**, 282 (2006).
- [80] L. González, J. Manz, B. Schmidt, and M. F. Shibl, Phys. Chem. Chem. Phys. **7**, 4096 (2005).
- [81] S. S. Bychkov, B. A. Grishanin, V. N. Zadkov, and H. Takahashi, J. Raman Spectrosc. **33**, 962 (2002).
- [82] K. Hoki, Y. Ohtsuki, H. Kono, and Y. Fujimura, J. Phys. Chem. A **103**, 6301 (1999).
- [83] K. B. Møller, H. C. Westtoft, and N. E. Henriksen, Chem. Phys. Lett. **419**, 65 (2006).
- [84] P. Nuernberger, G. Vogt, T. Brixner, and G. Gerber, Phys. Chem. Chem. Phys. **9**, 2470 (2007).
- [85] R. de Vivie-Riedle, L. Kurtz, A. Hofmann, and K. Sundermann, J. Inf. Recording **25**, 175 (2000).
- [86] R. de Vivie-Riedle, L. Kurtz, and A. Hofmann, Pure Appl. Chem. **73**, 525 (2001).
- [87] D. Geppert, and R. de Vivie-Riedle, Chem. Phys. Lett. **404**, 289 (2005).
- [88] N. F. Scherer, A. J. Ruggiero, M. Du, and G. R. Fleming, J. Phys. Chem. **93**, 856 (1990).

- [89] M. Ikuta, Y. Yuasa, T. Kimura, H. Matsuda, and T. Kobayashi, *Phys. Rev. B* **70**, 214301 (2004).
- [90] R. Menzel, *Photonics – Linear and Nonlinear Interactions of Laser Light and Matter*, Springer, Berlin (2001).
- [91] C. Manzoni, D. Polli, and G. Cerullo, *Rev. Sci. Instrum.* **77**, 023103 (2006).
- [92] R. Paschotta, *Appl. Phys. B* **79**, 153 (2004).
- [93] D. von der Linde, *Appl. Phys. B* **39**, 201 (1986).
- [94] N. R. Draper, and H. Smith, *Applied Regression Analysis*, 3<sup>rd</sup> Ed., John Wiley and Sons, New York (1998).
- [95] D. C. Edelstein, R. B. Romney, and M. Scheuermann, *Rev. Sci. Instrum.* **62**, 579 (1991).
- [96] M. J. Rosker, F. W. Wise, and C. L. Tang, *Phys. Rev. Lett.* **57**, 321 (1986).
- [97] J. Goree, *Rev. Sci. Instrum.* **56**, 1662 (1985).
- [98] S. V. Frolov, and Z. V. Vardeny, *Rev. Sci. Instrum.* **69**, 1257 (1998).
- [99] P. C. Becker, H. L. Fragnito, J. Y. Bigot, C. H. Brito Cruz, R. L. Fork, and C. V. Shank, *Phys. Rev. Lett.* **63**, 505 (1998).
- [100] L. D. Book, and N. F. Scherer, *J. Chem. Phys.* **111**, 792 (1999).
- [101] Q. Wang, R. W. Schoenlein, L. A. Peteanu, R. A. Mathies and C. V. Shank, *Science* **266**, 422 (1994).
- [102] T. Tahara, S. Takeuchi, and K. Ishii, *J. Chin. Chem. Soc.* **53**, 181 (2006).
- [103] L. Dhar, J. A. Rogers, and K. A. Nelson, *Chem. Rev.* **94**, 157 (1994).
- [104] T. S. Rose, M. J. Rosker, and A. H. Zewail, *J. Chem. Phys.* **91**, 7415 (1989).
- [105] J. A. Yeazell, and T. Uzer, *The Physics and Chemistry of Wave Packets*, John Wiley and Sons, New York (2000).
- [106] K. S. Schweizer, and D. Chandler, *J. Chem. Phys.* **76**, 2296 (1982).
- [107] W. G. Rothschild, *J. Chem. Phys.* **65**, 455 (1976).
- [108] A. L. Dobryakov, S. A. Kovalenko, and N. P. Ernsting, *J. Chem. Phys.* **123**, 044502 (2005).
- [109] T. Joo, and A. C. Albrecht, *Chem. Phys.* **173**, 17 (1993).
- [110] A. Pigliucci, G. Duvanel, L. M. Lawson Daku, and E. Vauthey, *J. Phys. Chem. A* **111**, 6135 (2007).
- [111] S.-G. Kim, K.-H. Kim, Y. K. Kim, S. K. Shin, and K. H. Ahn, *J. Am. Chem. Soc.* **125**, 13819 (2003).
- [112] E. Fan, S. A. Van Arman, S. Kincaid, and A. D. Hamilton, *J. Am. Chem. Soc.* **115**, 369 (1993).
- [113] S. Hanessian, M. Simard, and S. Roelens, *J. Am. Chem. Soc.* **117**, 7630 (1995).
- [114] K.-D. Kreuzer in *Hydrogen-Transfer Reactions*, J. T. Hynes, J. P. Klinman, H.-H. Limbach, and R. L. Schowen, (Eds.), Wiley-VCH, Weinheim, 709 (2006).
- [115] E. T. J. Nibbering, and T. Elsaesser, *Chem. Rev.* **104**, 1887 (2004).
- [116] M. V. Basilevsky, and M. V. Vener, *Russ. Chem. Rev.* **72**, 1 (2003).
- [117] J. T. Hynes, J. P. Klinman, H.-H. Limbach, and R. L. Schowen (Eds.), *Hydrogen-Transfer Reactions*, Wiley-VCH, Weinheim (2006), and references therein.

- [118] T. Elsaesser, and H. J. Bakker (Eds.), *Ultrafast Hydrogen Bonding Dynamics and Proton Transfer Processes in the Condensed Phase*, Kluwer, Academic Publishers, Dordrecht (2002).
- [119] A. Weller, *Z. Elektrochem.* **60**, 1144 (1956).
- [120] T. P. Smith, K. A. Zaklika, K. Thakur, G. C. Walker, K. Tominaga, and P. F. Barbara, *J. Phys. Chem.* **95**, 10465 (1991).
- [121] D. Le Gourri rec, S. M. Ormson, and R. G. Brown, *Prog. React. Kinet.* **19**, 211 (1994).
- [122] S. M. Ormson, and R. G. Brown, *Prog. React. Kinet.* **19**, 45 (1994).
- [123] K. Das, N. Sarkar, A. K. Ghosh, D. Majumdar, D. N. Nath, and K. Bhattacharyya, *J. Phys. Chem.* **98**, 9126 (1994).
- [124] P.-T. Chou, Y.-C. Chen, W.-S. Yu, Y.-H. Chou, C.-Y. Wei, and Y.-M. Cheng, *J. Phys. Chem. A* **105**, 1731 (2001).
- [125] W. Fu , S. Lochbrunner, A. M. M ller, T. Schikarski, W. E. Schmid, and S. A. Trushin, *Chem. Phys.* **232**, 161 (1998).
- [126] B. M. Rode, T. Hofer, and M. Kugler, *The Basics of Theoretical and Computational Chemistry*, Wiley-VCH, Weinheim (2007).
- [127] P. W. Atkins, and R. S. Friedman, *Molecular Quantum Mechanics*, Oxford University Press, New York (2004).
- [128] A. R. Leach, *Molecular Modelling: Principles and Applications*, Prentice Hall, Harlow (2001).
- [129] L. Sun and W. L. Hase, *Rev. Comp. Chem.* **19**, 79 (2003).
- [130] O.-H. Kwon, and A. H. Zewail, *Proc. Natl. Acad. Sci.* **104** (2007) 8703.
- [131] S. Takeuchi, and T. Tahara, *Proc. Natl. Acad. Sci.* **104** (2007) 5285.
- [132] C. Burisch, P. R. L. Markwick, N. L. Doltsinis, and J. Schlitter, *J. Chem. Theory Comput.* **4**, 164 (2008).
- [133] B. Herrera, and A. Toro-Labb , *Phys. Chem. A* **111**, 5921 (2007).
- [134] J. Waluk, *Acc. Chem. Res.* **39**, 945 (2006).
- [135] G. Wiosna-Sa yga, J. Dobkowski, M. S. Mudadu, I. Sazanovich, R. P. Thummel, and J. Waluk, *Chem. Phys. Lett.* **423**, 288 (2006).
- [136] H. Bulska, *Chem. Phys. Lett.* **98**, 398 (1983).
- [137] A. L. Sobolewski, and L. Adamowicz, *Chem. Phys. Lett.* **252**, **33** (1996).
- [138] H. Zhang, P. van der Meulen, and M. Glasbeek, *Chem. Phys. Lett.* **253**, 97 (1996).
- [139] D. Marks, P. Proposito, H. Zhang, and M. Glasbeek, *Chem. Phys. Lett.* **289**, 535 (1998).
- [140] R. Wortmann, K. Elich, S. Lebus, W. Liptay, P. Borowicz, and A. Grabowska, *J. Phys. Chem.* **96**, 9724 (1992).
- [141] P. W. Atkins, and J. de Paula, *Physikalische Chemie*, (4<sup>th</sup> Ed.), Wiley-VCH, Weinheim (2006).
- [142] J. R. Dwyer, J. Dreyer, E. T. J. Nibbering, and T. Elsaesser, *Chem. Phys. Lett.* **432**, 146 (2006).
- [143] T. Elsaesser, N. Huse, J. Dreyer, J. R. Dwyer, K. Heyne, and E. T. J. Nibbering, *Chem. Phys.* **341**, 175 (2007).

- [144] J. C. del Valle, and J. Catalán, *Chem. Phys.* **270**, 1 (2001).
- [145] M. L. Martinez, W. C. Cooper and P.-T. Chou, *Chem. Phys. Lett.* **193**, 151 (1992).
- [146] A. Sytnik, and J. C. Del Valle, *J. Phys. Chem.* **99**, 13028 (1995).
- [147] D. J. Nesbitt, and R. W. Field, *J. Phys. Chem.* **100**, 12735 (1996).
- [148] H. S. Yoo, M. J. DeWitt, and B. H. Pate, *J. Phys. Chem. A* **108**, 1348 (2004).
- [149] B. Fourmann, C. Jouvet, A. Tramer, J. M. Le Bars, and P. Millie, *Chem. Phys.* **92**, 25 (1985).
- [150] E. Riedle, persönliche Mitteilung (2008).
- [151] P. Vöhringer, R. A. Westervelt, T.-S. Yang, D. C. Arnett, M. J. Feldstein, and N. F. Scherer, *J. Raman Spectrosc.* **26**, 535 (1995).
- [152] J. Jortner, *Faraday Discuss.* **108**, 1 (1997).
- [153] (a) Barbatti, M.; Paier, J.; Lischka, H. *J. Chem. Phys.* **121**, 11614 (2004).  
(b) Quenneville, J.; Martinez, T. J. *J. Phys. Chem. A* **107**, 829 (2003).
- [154] (a) R. Vianello, H. Maskill, and Z. B. Maksic, *Eur. J. Org. Chem.* 2581 (2006).  
(b) L. Esposito, L. Vitagliano, A. Zagari, and L. Mazzarella, *Protein Sci.* **9**, 2038 (2000).
- [155] D. Madsen, J. Stenger, J. Dreyer, E. T. J. Nibbering, P. Hamm and T. Elsaesser, *Chem. Phys. Lett.* **341**, 56 (2001).
- [156] D. LeGourriérec, V. Kharlanov, R. G. Brown, and W. Rettig, *J. Photochem. Photobiol. A* **117**, 209 (1998).
- [157] A. Toniolo, S. Olsen, L. Manohara and T. J. Martínez, *Faraday Discuss.* **127**, 149 (2004).
- [158] T. Oksenhendler, F. Legrand, M. Perdrix, O. Gobert, and D. Kaplan, *Appl. Phys. B* **79**, 933 (2004).
- [159] D. I. Kim, H.-G. Rhee, J.-B. Song, and Y.-W. Lee, *Rev. Sci. Instrum.* **78**, 103110 (2007).
- [160] P. Hamm, R. A. Kaindl, and J. Stenger, *Opt. Lett.* **25**, 1798 (2000).
- [161] H. Fidder, M. Rini, and E. T. J. Nibbering, *J. Am. Chem. Soc.* **126**, 3789 (2004).
- [162] H. Hwang, and P. J. Rossky, *J. Phys. Chem. B* **108**, 6723 (2004).
- [163] C. Daniel, E. Kolba, L. Lehr, J. Manz, and T. Schröder, *J. Phys. Chem.* **98**, 9823 (1994).
- [164] J. L. Herek, A. Materny, and A. H. Zewail, *Chem. Phys. Lett.* **228**, 15 (1994).
- [165] A. Sanov, S. Nandi, and W. C. Lineberger, *J. Chem. Phys.* **108**, 5155 (1998).
- [166] A. Shnitman, I. Sofer, I. Golub, A. Yogev, and M. Shapiro, *Phys. Rev. Lett.* **76**, 2886 (1996).
- [167] J. Cao, and K. R. Wilson, *J. Chem. Phys.* **107**, 1441 (1997).
- [168] S. Zou, A. Kondorskiy, G. Mil'nikov, and H. Nakamura, *J. Chem. Phys.* **122**, 084112 (2005).
- [169] H. Katsuki, K. Hosaka, H. Chiba, and K. Ohmori, *Phys. Rev. A* **76**, 013403 (2007).
- [170] D. Tannor, and S. A. Rice, *J. Chem. Phys.* **83**, 5013 (1985).
- [171] D. Tannor, R. Kosloff, and S. A. Rice, *J. Chem. Phys.* **85**, 5805 (1986).
- [172] I. Paci, J. C. Johnson, X. Chen, G. Rana, D. Popovic, D. E. David, A. J. Nozik, M. A. Ratner, and J. Michl, *J. Am. Chem. Soc.* **128**, 16546 (2006).

- [173] M. Gerhards, Seminarvortrag, LMU München, Institut für Biomolekulare Optik, (2004).
- [174] L. Baltzer in *Hydrogen-Transfer Reactions*, J. T. Hynes, J. P. Klinman, H.-H. Limbach, and R. L. Schowen, (Eds.), Wiley-VCH, Weinheim, 1079 (2006).
- [175] S. R. Vázquez, M. C. R. Rodríguez, M. Mosquera, and F. Rodríguez-Prieto, *J. Phys. Chem. A* **111**, 1814 (2007).
- [176] O. K. Abou-Zied, *Chem. Phys.* **337**, 1 (2007).
- [177] M. Mosquera, J. Carlos Penedo, M. C. R. Rodriguez, and F. Rodriguez-Prieto, *J. Phys. Chem.* **100**, 5398 (1996).
- [178] C. A. S. Potter, R. G. Brown, F. Vollmer, and W. Rettig, *J. Chem. Soc. Faraday Trans.* **90**, 59 (1994).
- [179] Y. Fu, R. Liu, L. Liu and Q.-X. Guo, *J. Phys. Org. Chem.* **17**, 282 (2004).
- [180] T. Elsaesser, and B. Schmetzer, *Chem. Phys. Lett.* **140**, 293 (1987).
- [181] R. S. Becker, C. Lenoble, and A. Zein, *J. Phys. Chem.* **91**, 3509 (1987).



## Anhang A:

### ESIPT in protischen und polaren Lösungsmitteln

Der Vergleich des Protontransfers von HBT in Cyclohexan und in der Gasphase hat gezeigt, dass die Cyclohexan Lösungsumgebung keinen Einfluss auf den ultraschnellen ESIPT hat (s. Kap. 3.6). Dasselbe ist von anderen aprotischen, unpolaren Lösungsmitteln zu erwarten [18]. Wird HBT hingegen in polaren Lösungsmitteln wie Dimethylsulfoxid (DMSO), Acetonitril, Alkoholen oder Wasser gelöst, so konkurriert die Bildung der intramolekularen Wasserstoffbrücke (H-Brücke) mit intermolekularen H-Brücken zu Lösungsmittelmolekülen (Abb. A.1). Abhängig von der H-Brücken Konfiguration ergibt sich eine unterschiedliche Dynamik.

Ist die intramolekulare H-Brücke aufgebrochen, so erlaubt dies eine Rotation der OH-Gruppe um die C-O Bindung und eine Torsion des Moleküls um die zentrale Phenol-Benzothiazol-Bindung (s. Abb. A.1) [175-177]. In Ethanol bricht die intramolekulare H-Brücke in ~30 % der Moleküle auf [175,178], in Dimethylsulfoxid (DMSO) höchstwahrscheinlich in über 90 %; möglicherweise kommt es sogar zur Deprotonierung von HBT und zur Bildung des HBT Anions (s. Abb. A.1 a) [179-181].

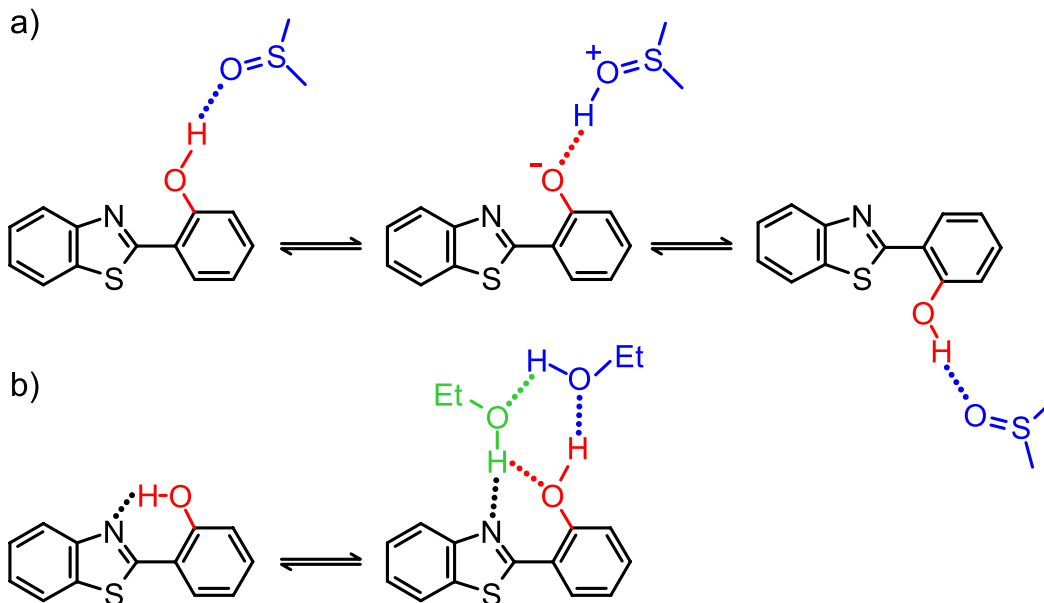


Abb. A.1: Einige der möglichen HBT  $S_0$  Konformere in a) Dimethylsulfoxid und b) Ethanol [176]. Ist die intramolekulare H-Brücke aufgebrochen, so sind Rotationen und Torsionen des Moleküls möglich und die  $S_0$  enol Geometrie ist nicht mehr wohldefiniert. Wasserstoffbrückenbindungen sind als  $\cdots$  dargestellt.

Nach optischer Anregung zeigen nur die HBT Moleküle, die eine intramolekulare H-Brücke besitzen, ultraschnellen ESIPT. Die Protontransferzeit von HBT in Chloroform, Ethanol, Methanol und Acetonitril ist identisch zu der in Cyclohexan (Abb. A.2). Trotz der unterschiedlichen Viskosität und Polarität sind die ESIPT induzierte Wellenpaketdynamik und vibratorische Dephasierung in diesen Lösungsmitteln nahezu identisch. Die korrespondierenden transienten Spektren (Abb. A.3) zeigen ebenfalls dieselben spektralen Banden, die auch in Cyclohexan beobachtet werden und ausführlich in Anhang 9 beschrieben sind. Das Fehlen einer klaren spektralen Signatur eines stabilisierten enol\* Tautomers bei langen Verzögerungszeiten in Ethanol, Methanol und Acetonitril (vgl. Abb. A.1) deutet darauf hin, dass (i) entweder die interne Konversion der enol\* Form auf derselben oder einer schnelleren Zeitskala abläuft wie die der keto\* Form, oder dass (ii) es in den HBT Molekülen mit intermolekularer H-Brücke nach Anregung durch mehrstufigen, intermolekularen Protontransfer schließlich doch noch zur Bildung des keto\* Tautomers kommt.

Die Depopulation des keto\* Zustands durch interne Konversion verläuft in den unterschiedlichen Reaktionsumgebungen mit deutlich anderen Zeitkonstanten. Die IC Rate hängt von der Viskosität und der Polarität des Lösungsmittels ab. Dabei führt ein niedrig viskoses, stark polares Lösungsmittel zu einer schnelleren internen Konversion (Abb. A.2). Dies unterstützt einen IC Mechanismus wie er in Kap. 3.6 vorgeschlagen wird, der große Verformungen der Molekülgeometrie erfordert und biradikale oder polare Konformationen involviert.

In DMSO zeigt HBT eine Kurzzeitdynamik und spektrale Signaturen, die sich deutlich von denen in anderen Lösungsmitteln unterscheiden. Die Zeitkurve weist nur einen sehr geringen Emissionsbeitrag und Oszillationen mit sehr kleiner Amplitude auf. Den transienten Spektren fehlt der keto\* typische Emissionsbeitrag bei ~550 nm. Dies unterstützt die obige Annahme, dass in fast allen HBT Molekülen die intramolekulare H-Brücke aufgebrochen und die Bildung der keto\* Form durch ESIPT unterbunden ist. Da DMSO nur H-Brücken Akzeptor und nicht auch Donor ist, kann es zu keinem indirekten Protontransfer durch das Lösungsmittel auf einer langsameren Zeitskala kommen, wie dies vielleicht in Alkoholen der Fall ist. Die genaue Photophysik von HBT in DMSO erfordert allerdings noch weitergehende Untersuchungen und ist noch nicht endgültig aufgeklärt.



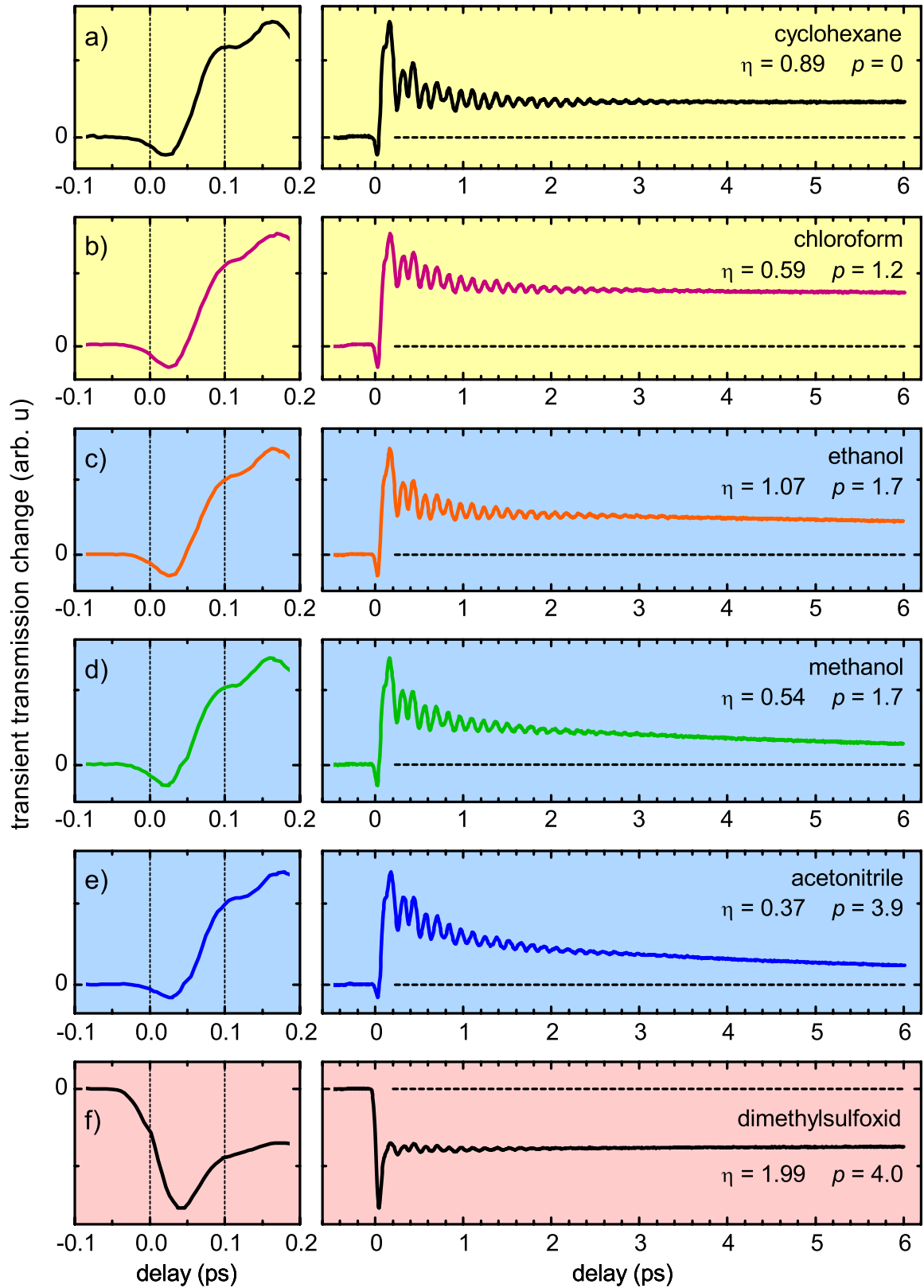


Abb. A.2: Transiente Transmission von HBT in Cyclohexan, Chloroform, Ethanol, Methanol, Acetonitril und Dimethylsulfoxid bei 325 nm Anregung und 510 nm Abfrage. Die Viskosität  $\eta$  [mPa·s] und das Dipolmoment  $p$  [D] der Lösungsmittel sind in den entsprechenden Graphen angegeben.

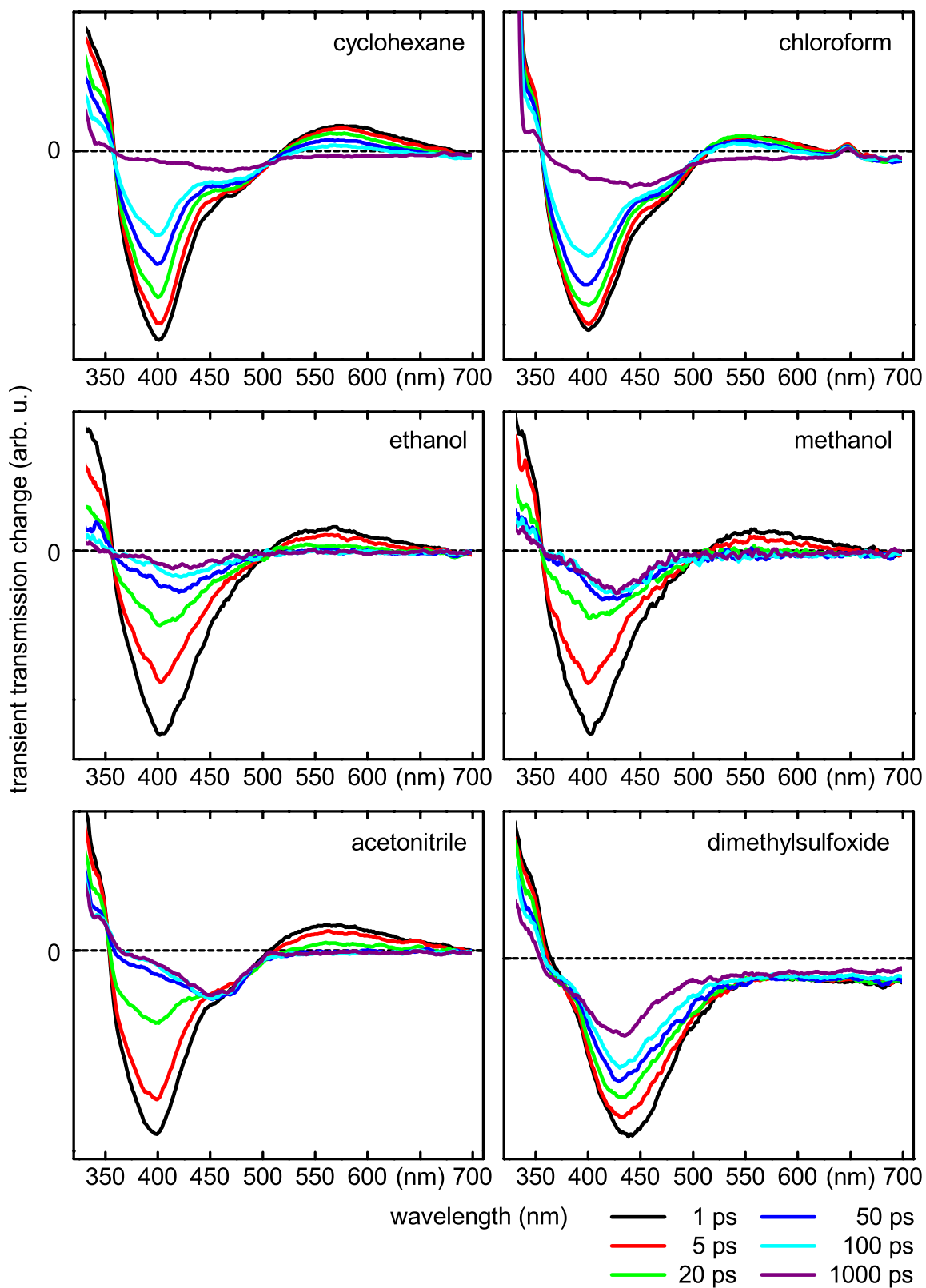


Abb. A.3: Transiente Spektren von HBT in Cyclohexan, Chloroform, Ethanol, Methanol, Acetonitril und Dimethylsulfoxid bei 325 nm Anregung.

# Anhang 1

**"Tunable pulses from below 300 to 970 nm with durations down to 14 fs  
based on a 2 MHz ytterbium-doped fiber system"**

C. Schriever, S. Lochbrunner, P. Krok, and E. Riedle

Opt. Lett. 33, 192 – 194 (2008)



# Tunable pulses from below 300 to 970 nm with durations down to 14 fs based on a 2 MHz ytterbium-doped fiber system

Christian Schriever,<sup>1</sup> Stefan Lochbrunner,<sup>1,3</sup> Patrizia Krok,<sup>1</sup> and Eberhard Riedle<sup>1,2</sup>

<sup>1</sup>Lehrstuhl für BioMolekulare Optik, Department für Physik, Ludwig-Maximilians-Universität, Oettingenstrasse 67, 80538 München, Germany

<sup>2</sup>Corresponding author: eberhard.riedle@physik.uni-muenchen.de

<sup>3</sup>Present address: Institut für Physik, Universität Rostock, Universitätsplatz 3, 18055 Rostock

Received October 16, 2007; revised November 28, 2007; accepted November 28, 2007; posted November 30, 2007 (Doc. ID 88686); published January 14, 2008

A noncollinearly phase-matched optical parametric amplifier pumped by a commercial 2 MHz fiber laser is presented and discussed. The pump system allows the direct generation of a seed continuum from a sapphire plate. Clean pulses with up to 860 nJ energy and down to 14 fs pulse length can be obtained over a fundamental tuning range from 620 to 970 nm. Conversion by second- and third-harmonic generation as well as sum frequency mixing results in an extended tuning range down to well below 300 nm. © 2008 Optical Society of America

OCIS codes: 060.2320, 190.4970, 320.7080.

For laser imaging and machining, ultrashort pulses can render the necessary high intensities and fields. The investigation of ultrafast molecular dynamics requires tunable pulses in the sub-20 fs regime. To avoid sample damage in spectroscopy, for good signal-to-noise ratios, and for efficient machining, high repetition rates are needed. Megahertz, fiber-based femtosecond laser systems with pulse energies in the multimicrojoule regime promise a breakthrough for these applications. Recently, a fiber-laser-pumped parametric amplifier was reported that was seeded by a photonic crystal fiber and delivered tunable 250 fs pulses [1]. Noncollinear optical parametric amplifiers (NOPAs) pumped by Ti:sapphire amplifiers efficiently generate tunable visible sub-20 fs pulses at kHz repetition rates and pump energies above 100  $\mu$ J [2,3]. They were also demonstrated at 100 kHz and pump energies below 10  $\mu$ J [4], and lately even for a cavity-dumped Yb:KYW oscillator at 1 MHz [5]. In this Letter we present a novel NOPA design for a 2 MHz fiber laser system, with a white-light seed generated in a bulk medium. Our new NOPA provides the desired tunability in the visible and near-infrared (NIR) and accesses the 10 fs regime. In addition, we transfer these pulses into the blue and ultraviolet (UV) spectral region, which is essential for spectroscopic applications.

Figure 1(a) shows the NOPA, which is pumped by a commercial Yb-doped fiber-oscillator/amplifier system (IMPULSE; Clark-MXR, Inc.) delivering 10  $\mu$ J pulses at 1035 nm (frequency  $\omega$ ) with sub-250 fs length. To efficiently generate green pump light for the parametric process, the entire 1035 nm light is focused into a 800  $\mu$ m thick type I BBO crystal. Doubling efficiencies up to 30% are achieved, while the remaining NIR pulse is still suitable for continuum generation. A dichroic mirror transmits the NIR part used for white-light generation in a 4 mm thick sapphire crystal with highly parallel faces. Out of several focal lengths tested, we find for the pump beam

diameter of  $\sim$ 5 mm a length of 75 mm optimal for low threshold and stability, corresponding to a numerical aperture of 0.035. Due to the comparatively long pump, pulse energies of at least 2.5  $\mu$ J have to be used. In a static setup this energy in combination with the high repetition rate damages the sapphire crystal. By rotating the crystal [6] stable operation is achieved. A short-pass filter (Model 102927, LAYERTEC GmbH; 6.35 mm fused silica) blocks the fundamental and transmits the continuum part from 480 to 1000 nm [see Fig. 2(a)]. A 30 mm fused silica lens recollimates and focuses the continuum into a 5 mm type I BBO crystal cut at 26.5° for the para-

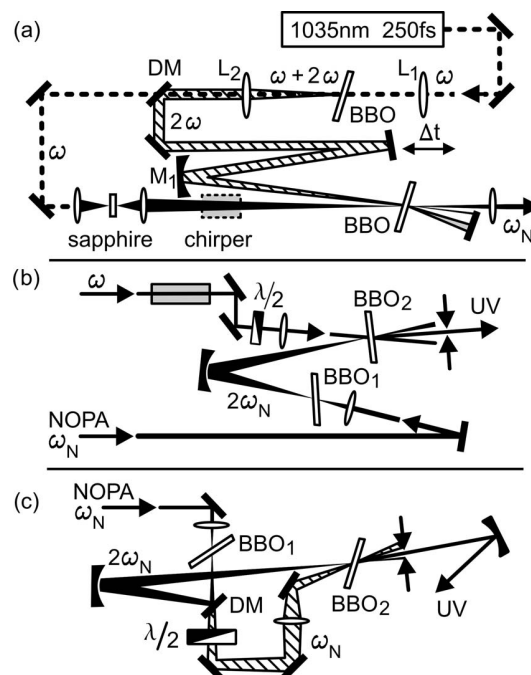


Fig. 1. (a) 2 MHz NOPA. (b) SFM of the doubled NOPA output with the fundamental of the pump. (c) THG of the NOPA. DM, dichroic mirror; L, lens; M, mirror.

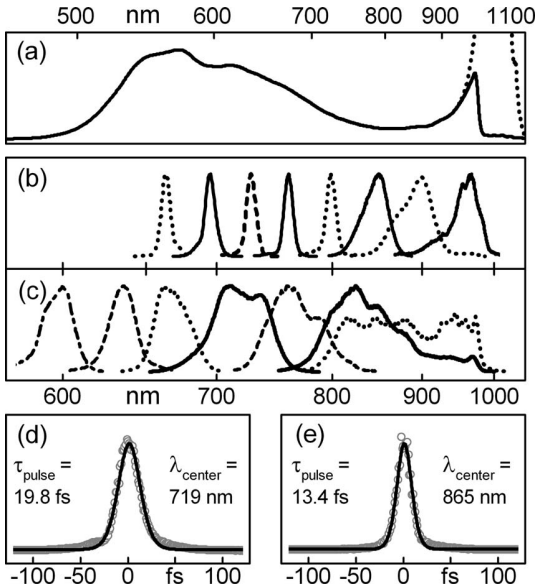


Fig. 2. (a) Spectrum of the seed continuum. (b) NOPA spectra with bandwidth reduced by 10 mm SF57 chirper. (c) NOPA spectra with full bandwidth [spectra of (d) and (e): solid curves]. (d), (e) Autocorrelation (with Gauss fit) at 719 and 865 nm, respectively. The vertical scale is linear in all panels.

metric amplification. The resulting chirp on the continuum corresponds to a group delay between the 650 and 900 nm spectral components of  $\sim 0.66$  ps. The pulses are characterized with a fiber-coupled spectrometer (not intensity calibrated) and a dispersion-free autocorrelator [7].

The distance between the lenses  $L_1$  and  $L_2$  (both  $f = 250$  mm) is adjusted such that the green beam has a diameter of  $\sim 2$  mm on the focusing mirror  $M_1$  ( $f = 300$  mm). A focal diameter of  $125 \mu\text{m}$  and a Rayleigh range of 25 mm are achieved allowing us to place the amplifier crystal within the Rayleigh range [4] and match the spot sizes of pump and seed. For broadband amplification a noncollinear geometry with an external angle of  $\sim 3.7^\circ$  between the pump and the seed beam is employed [1,2]. The precise value is adjusted together with the phase-matching angle for the desired output wavelength. Due to the chirp of the seed only part of its spectrum overlaps temporally with the pump pulse in the crystal and is amplified. To tune the NOPA, the arrival time of the pump pulse is changed by translating a plane mirror. The NOPA output is collimated with an antireflection-coated lens ( $f = 500$  mm), and the chirp of the pulses is corrected with a prism sequence. To reduce the bandwidth of the NOPA output the chirp of the white light can be increased by inserting LF7 or SF57 glass (chirper) into the white light (10 mm of SF57 increase the 650/900 nm group delay to  $\sim 2.6$  ps). Most of the measurements were performed at 500 kHz; experiments at 2 MHz proved that the pulse bandwidth, duration, and spatial shape remain the same at higher repetition rates and the output energies are nearly equal for equal pump energies.

The smooth spectrum of the seed [see Fig. 2(a)] and the compressibility of the NOPA pulses are a direct

consequence of the seed generation in bulk sapphire. The latter is only possible for the sub-250 fs pump duration, for longer pulses a photonic crystal fiber has to be used [1], resulting in a low degree of coherence. Figure 2(c) shows typical spectra of NOPA pulses at different center wavelengths. The tuning range extends from below 620 nm to beyond 970 nm. It is limited on the blue side by the absorption of the idler beam in the BBO crystal starting at about  $2.7 \mu\text{m}$  and on the red side by the short-pass filter in the seed light.

Spectral widths of over 44 THz can easily be amplified, providing sufficient bandwidth for pulses with a transform limit around 10 fs [Figs. 2(c) and 3]. Pulse durations (assuming Gaussian pulse shape) of 13.4 fs at 865 nm and 19.8 fs at 719 nm are demonstrated with compression in fused silica prisms [Figs. 2(d) and 2(e)]. They correspond to time-bandwidth products of 0.51 and 0.57, close to the theoretical limit of 0.441. Due to the smooth spectra and the high coherence of the seed, the pulses show nearly no wings. If the seed is chirped with LF7 or SF57 glass, the spectral width is reduced by a factor of about 1.5 or 2.5 [Fig. 2(b) and Fig. 3]. Figure 3 gives an overview of output energies and Fourier limited pulse lengths for the various configurations. The possible durations decrease toward longer wavelengths due to the decreasing seed chirp and due to the increasing group velocity mismatch between the seed and the green pump in the 5 mm BBO crystal that allows the pump to sweep over the seed [group delay 650(o)/517(e) nm,  $\sim 0$  ps; 900(o)/517(e) nm,  $\sim 0.35$  ps]. Throughout the fundamental tuning range, energies well above 400 nJ are obtained, with a maximum of 860 nJ at 685 nm. At 2 MHz an average output power of 1.65 W has been observed.

Three schemes were applied to convert the NOPA output (frequency  $\omega_N$ ) to the blue and near-UV spectral region: second-harmonic generation (SHG,  $2\omega_N$ ), sum frequency mixing (SFM,  $2\omega_N + \omega$ ) and third-harmonic generation (THG,  $3\omega_N$ ). For SHG, the NOPA output is focused ( $f = 75$  mm) into a  $200 \mu\text{m}$  type I BBO crystal [BBO<sub>1</sub>, cut at  $27.5^\circ$ ; see Fig. 1(b)] placed slightly behind the focus. For SFM [see Fig.

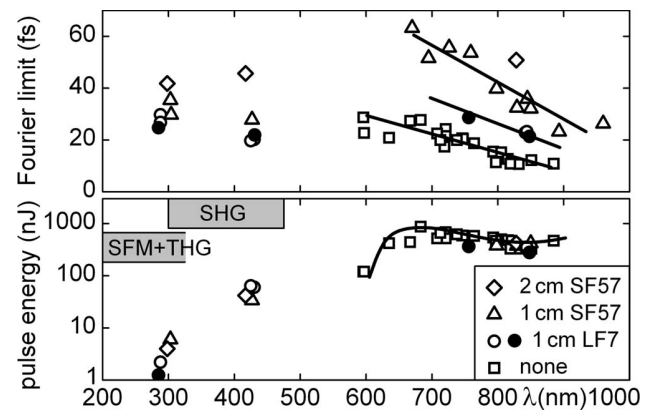


Fig. 3. Fourier limits and energies of the NOPA, SHG, SFM, and THG pulses with and without additional chirpers in the seed at 500 kHz ( $\circ$ ) and 2 MHz ( $\bullet$ ). Solid lines are guides to the eye.

1(b)] 400 nJ of the 1035 nm pump pulse are stretched by passing through 210 mm of SF57 glass [8]. The polarization is rotated and the beam is focused ( $f=150$  mm) into a 200  $\mu\text{m}$  type-I BBO crystal (BBO<sub>2</sub>, cut at 36°). The second harmonic (SH) of the NOPA is refocused by an aluminum mirror ( $f=150$  mm) and overlapped with the NIR pulse under a small angle to spatially separate the SFM pulse. For THG [see Fig. 1(c)] the SH part is reflected off a dichroic mirror and the polarization of the transmitted fundamental is rotated with an achromatic half-wave plate. The SH pulses are refocused by an aluminum mirror ( $f=150$  mm) and overlapped slightly noncollinearly with the focused ( $f=100$  mm) fundamental in a 200  $\mu\text{m}$  type I BBO crystal (BBO<sub>2</sub>, cut at 36°). For all conversion processes the seed was chirped with 10 mm LF7 to reduce the NOPA bandwidth and match the acceptance bandwidths of the crystals. Without sacrificing efficiency, 20% of the NOPA pulses can be split off prior to SHG to allow two-color experiments.

Tuning of the NOPA allows SHG from 310 to 485 nm, SFM from 238 to 330 nm, and THG from 206 to 323 nm. The conversion schemes were tested for selected wavelengths (see Figs. 3 and 4). A SHG conversion efficiency up to 21% is observed. For SFM an energy efficiency of 18% (SH to SFM) is achieved, i.e., a pulse energy of 6 nJ at 304 nm. The spectral bandwidth supports pulse lengths of less than 40 fs. Reducing the crystal length to 100  $\mu\text{m}$  does not change the bandwidth but decreases the energy by a factor of  $\sim 10$ , because the NIR mixing pulse is too short to convert the whole SH pulse. Compression of the SH pulse should overcome this problem, but the compressor length has to be readjusted with the NOPA wavelength. For THG, an efficiency (SHG to THG) of 5% is achieved, i.e., energies up to 2.5 nJ. The spectral width of 12 THz at 288 nm supports a pulse duration of 36 fs. The bandwidth was slightly increased by using a 100  $\mu\text{m}$  crystal, leading to a spectral width of 15.7 THz, but again at nearly tenfold lower energy.

The newly developed NOPA is to our knowledge the first parametric amplifier that can efficiently generate tunable sub-20 fs pulses from a purely fiber-based pump system. The minimum pulse length of 13.4 fs represents a  $\sim 20$ -fold shortening of the pump duration. The primary tuning range covering the red and

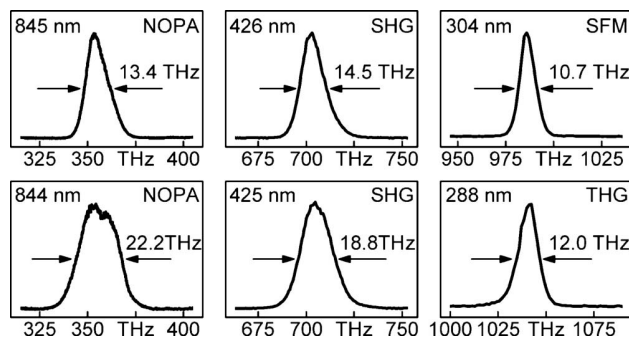


Fig. 4. Spectra of the NOPA (first column), SHG (second column), SFM (top right graph), and THG (bottom right graph) pulses.

NIR should be ideal for nonlinear imaging techniques. Compared with a MHz oscillator pump system [5], the setup is simplified, the output energy is increased by more than an order of magnitude, and the tuning is largely improved. The obtained pulse duration is similar to recent optical parametric chirped pulse amplifiers (OPCPA) in the TW regime [9,10] relying on the same amplifier concept. However, continuum seeding allows extended tunability compared with seeding with a large-bandwidth Ti:sapphire oscillator. The presented nonlinear conversion experiments demonstrate that the whole range down to below 300 nm is accessible and the system should therefore become a most valuable alternative for spectroscopic applications in femto-science. We expect to further increase the bandwidth of the pulses by reducing the chirp in the seed light (e.g., by chirped mirrors) and thus shorten their temporal width. By pumping with the tripled fiber-laser output, the full spectral range of the seed continuum will become available for amplification. In this way the primary NOPA tuning range would be widened to well below 500 nm, and UV pulses could then be generated directly by simple frequency doubling.

*Note added in proof:* Very recently a NOPA pumped by a 2 MHz Yb-doped fiber amplifier was reported. It delivers sub-20 fs pulses at a fixed wavelength of 800 nm [11].

We thank Clark-MXR, Inc., for the generous loan of the IMPULSE system and Johannes Piel and Peter Baum for valuable discussions. The work was supported by the DFG-Cluster of Excellence: Munich-Centre for Advanced Photonics and by the Austrian Science Fund within the Special Research Program F16 (Advanced Light Sources).

## References

1. T. V. Andersen, O. Schimid, C. Bruchmann, J. Limpert, C. Aguerararay, E. Cormier, and A. Tünnermann, *Opt. Express* **14**, 4765 (2006).
2. E. Riedle, M. Beutter, S. Lochbrunner, J. Piel, S. Schenkl, S. Spörlein, and W. Zinth, *Appl. Phys. B* **71**, 457 (2000).
3. G. Cerullo and S. De Silvestri, *Rev. Sci. Instrum.* **74**, 1 (2003).
4. J. Piel, E. Riedle, L. Gundlach, R. Ernstorfer, and R. Eichberger, *Opt. Lett.* **31**, 1289 (2006).
5. A. Killi, A. Steinmann, G. Palmer, U. Morgner, H. Bartelt, and J. Kobelke, *Opt. Lett.* **31**, 125 (2006).
6. P. Tzankov, I. Buchvarov, and T. Fiebig, *Opt. Commun.* **203**, 107 (2002).
7. I. Z. Kozma, P. Baum, U. Schmidhammer, S. Lochbrunner, and E. Riedle, *Rev. Sci. Instrum.* **75**, 2323 (2004).
8. I. Z. Kozma, P. Baum, S. Lochbrunner, and E. Riedle, *Opt. Express* **11**, 3110 (2003).
9. N. Ishii, L. Turi, V. S. Yakovlev, T. Fuji, F. Krausz, A. Baltuška, R. Butkus, G. Veitas, V. Smilgevičius, R. Danielius, and A. Piskarskas, *Opt. Lett.* **30**, 567 (2005).
10. S. Witte, R. Th. Zinkstok, A. L. Wolf, W. Hogervorst, W. Ubachs, and K. S. E. Eikema, *Opt. Express* **14**, 8168 (2006).
11. J. Rothhardt, S. Hädruch, D. N. Schimpf, J. Limpert, and A. Tünnermann, *Opt. Express* **15**, 16729 (2007).





## Anhang 2

**"Octave wide tunable UV-pumped NOPA: pulses down to 20 fs  
at 0.5 MHz repetition rate"**

C. Homann, C. Schriever, P. Baum, and E. Riedle

Opt. Express 16, 5746 – 5756 (2008)



# Octave wide tunable UV-pumped NOPA: pulses down to 20 fs at 0.5 MHz repetition rate

C. Homann\*, C. Schriever, P. Baum, and E. Riedle

*Lehrstuhl für BioMolekulare Optik, Fakultät für Physik, Ludwig-Maximilians-Universität München, Oettingenstrasse 67, 80538 München, Germany*

\*Corresponding author: [christian.homann@physik.uni-muenchen.de](mailto:christian.homann@physik.uni-muenchen.de)

**Abstract:** Femtosecond laser pulses, which are tunable from 440 to 990 nm, are generated at MHz repetition rates by noncollinear parametric amplification (NOPA). The pulses have durations of 20 to 30 fs over the major part of the tuning range and a high energy stability of 1.3% (rms). The NOPA is pumped with ultraviolet pulses from the third harmonic of an ytterbium doped fiber laser system and seeded by a smooth continuum generated in bulk sapphire. The residual second harmonic is used to pump an additional NOPA, which is independently tunable from 620 to 990 nm. Interference experiments show that the two NOPA systems have a precisely locked relative phase, despite of being pumped by different harmonics with a random phase jitter. This demonstrates that the phase of pulses generated by optical parametric amplification does not depend on the pump phase.

©2008 Optical Society of America

**OCIS codes:** (060.2320) Fiber optics amplifiers and oscillators; (190.2620) Harmonic generation and mixing; (190.4410) Nonlinear optics, parametric processes; (320.7080) Ultrafast devices; (320.7110) Ultrafast nonlinear optics;

---

## References and links

1. C. Schriever, S. Lochbrunner, P. Krok, and E. Riedle, "Tunable pulses from below 300 to 970 nm with durations down to 14 fs based on a 2 MHz ytterbium-doped fiber system," *Opt. Lett.* **33**, 192-194 (2008).
2. M. Marangoni, R. Osellame, R. Ramponi, G. Cerullo, A. Steinmann, and U. Morgner, "Near-infrared optical parametric amplifier at 1 MHz directly pumped by a femtosecond oscillator," *Opt. Lett.* **32**, 1489-1491 (2007).
3. J. Rothhardt, S. Hädrich, D. N. Schimpf, J. Limpert, and A. Tünnermann, "High repetition rate fiber amplifier pumped sub-20 fs optical parametric amplifier," *Opt. Express* **15**, 16729-16736 (2007).
4. J. M. Dudley, G. Genty, and S. Coen, "Supercontinuum generation in photonic crystal fiber," *Rev. Mod. Phys.* **78**, 1135-1184 (2006).
5. M. Ghotbi, Z. Sun, A. Majchrowski, E. Michalski, I. V. Kityk, and M. Ebrahim-Zadeh, "Efficient third harmonic generation of microjoule picosecond pulses at 355 nm in BiB<sub>3</sub>O<sub>6</sub>," *Appl. Phys. Lett.* **89**, 173124 1-3 (2006).
6. A. Dubietis, G. Tamošauskas, and A. Varanavičius, "Femtosecond third-harmonic pulse generation by mixing of pulses with different duration," *Opt. Commun.* **186**, 211-217 (2000).
7. SNLO nonlinear optics code available from A. V. Smith, Sandia National Laboratories, Albuquerque, NM 87185-1423.
8. H. S. Park, J. S. Baskin, O.-H. Kwon, and A. H. Zewail, "Atomic-Scale Imaging in Real and Energy Space Developed in Ultrafast Electron Microscopy," *Nano Lett.* **7**, 2545-2551 (2007).
9. G. M. Gale, M. Cavallari, T. J. Driscoll, and F. Hache, "Sub-20-fs tunable pulses in the visible from an 82-MHz optical parametric oscillator," *Opt. Lett.* **20**, 1562-1564 (1995).
10. T. Wilhelm, J. Piel, and E. Riedle, "Sub-20-fs pulses tunable across the visible from a blue-pumped single-pass noncollinear parametric converter," *Opt. Lett.* **22**, 1494-1496 (1997).
11. G. Cerullo and S. De Silvestri, "Ultrafast optical parametric amplifiers," *Rev. Sci. Instrum.* **74**, 1-18 (2003).
12. R. Butkus, R. Danielius, A. Dubietis, A. Piskarskas, and A. Stabinis, "Progress in chirped pulse optical parametric amplifiers," *Appl. Phys. B* **79**, 693-700 (2004).
13. F. Tavella, A. Marcinkevičius, and F. Krausz, "90 mJ parametric chirped pulse amplification of 10 fs pulses," *Opt. Express* **14**, 12822-12827 (2006).
14. S. Witte, R. Th. Zinkstok, A. L. Wolf, W. Hogervorst, W. Ubachs, and K. S. E. Eikema, "A source of 2 terawatt, 2.7 cycle laser pulses based on noncollinear optical parametric chirped pulse amplification," *Opt. Express* **14**, 8168-8177 (2006).

15. I. Z. Kozma, P. Baum, U. Schmidhammer, S. Lochbrunner, and E. Riedle, "Compact autocorrelator for the online measurement of tunable 10 femtosecond pulses," *Rev. Sci. Instrum.* **75**, 2323-2327 (2004).
16. K. Duncker and W. Widdra, Institut für Physik, Martin-Luther-Universität Halle-Wittenberg, Hoher Weg 8, 06120 Halle, Germany (personal communication, 2008).
17. P. Baum, S. Lochbrunner, J. Piel, and E. Riedle, "Phase-coherent generation of tunable visible femtosecond pulses," *Opt. Lett.* **28**, 185-187 (2003).
18. P. Baum, E. Riedle, M. Greve, and H. R. Telle, "Phase-locked ultrashort pulse trains at separate and independently tunable wavelengths," *Opt. Lett.* **30**, 2028-2030 (2005).
19. P. Tzankov, T. Fiebig, and I. Buchvarov, "Tunable femtosecond pulses in the near-ultraviolet from ultrabroadband parametric amplification," *Appl. Phys. Lett.* **82**, 517-519 (2003).
20. A. Killi, A. Steinmann, G. Palmer, U. Morgner, H. Bartelt, and J. Kobelke, "Megahertz optical parametric amplifier pumped by a femtosecond oscillator," *Opt. Lett.* **31**, 125-127 (2006).
21. A. Steinmann, A. Killi, G. Palmer, T. Binhammer, and U. Morgner, "Generation of few-cycle pulses directly from a MHz-NOPA," *Opt. Express* **14**, 10627-10630 (2006).
22. H. Merdji, T. Auguste, W. Boutu, J.-P. Caumes, B. Carré, T. Pfeifer, A. Jullien, D. M. Neumark, and S. R. Leone, "Isolated attosecond pulses using a detuned second-harmonic field," *Opt. Lett.* **32**, 3134-3136 (2007).

## 1. Introduction and overview

For the generation of intense femtosecond pulses, laser amplifiers based on fiber technology promise high peak power at high repetition rates, excellent beam quality and good stability. Such characteristics are essential in machining, nonlinear imaging, microscopy, and ultrafast spectroscopy. The combination of high peak intensities with high repetition rates allows for studying or making use of the entire range of nonlinear effects with a high processing or data acquisition rate. To apply fiber lasers in ultrafast spectroscopy, the relevant absorption and emission spectra of the investigated systems must be matched and pulse durations of ~20 fs are required. Typically, molecules and condensed matter absorb in the UV, visible, and near infrared spectral region. A frequency converter for fiber lasers, typically operating around 1035 nm for ytterbium doping, into an as wide as possible tuning range is therefore essential to take advantage of the high repetition rate and stability of fiber lasers in spectroscopy.

Noncollinear optical parametric amplifiers (NOPAs) pumped by Ti:sapphire lasers are well proven devices for the generation of few-cycle tunable pulses. They allow accessing the temporal signatures of ultrafast wavepacket dynamics and structural oscillations in molecules and condensed matter. Now we investigate the use of an ytterbium-doped fiber laser operating at 1035 nm as pump source for NOPAs that allow the full coverage of the near UV, visible and NIR spectral range. In contrast to earlier work performed in our laboratory [1], we focus on a NOPA pumped by the third harmonic of the 1035 nm fiber laser pulses. This should allow extending the tuning range significantly to shorter wavelengths and accessing the UV with simple frequency doubling. To retain the demonstrated NIR coverage, we combine the 345 nm pumped NOPA with a NOPA pumped by the residual frequency doubled pump light.

The manuscript is outlined as follows. In Section 2, we present the experimental arrangement. In Section 3 and 4, we explain the considerations and technical details for seed and pump light generation. Section 5 addresses the NOPA processes and relevant phase matching concepts. The measured spectra, Fourier limits, pulse durations and pulse energies are presented and discussed. The results of a noise analysis and phase investigations are shown and reviewed in Section 6 and 7. We conclude with final remarks in Section 8.

## 2. Experimental arrangement

The two NOPAs (sketched in Fig. 1) are pumped by an Yb-doped fiber-oscillator/amplifier system (IMPULSE; Clark-MXR, Inc.), which delivers 10 to 12  $\mu\text{J}$  pulses at 1035 nm (frequency  $\omega_0$ , red in Fig. 1) with a pulse length of 230 fs at a selectable repetition rate between 200 kHz and 2 MHz. A half-wave plate for 1035 nm in combination with a thin film polarizing beam splitter is used to split off 1.5  $\mu\text{J}$  pulses for continuum generation (Fig. 1, grey; explained in more detail in Section 3). This scheme is chosen to be able to maintain a constant energy for continuum generation, independent of slight variations of the output energy of the fiber laser. The remaining 8.5 to 10.5  $\mu\text{J}$  pulses are focused with the lens  $L_1$  towards two BBO crystals for frequency doubling and subsequent tripling. The details of the mixing concept are

discussed in section 4. The resulting light (Fig. 1, blue) is separated by a dichroic mirror (DM), which is highly reflective at 345 nm and highly transmissive at 517 and 1035 nm. After recollimation by the lens  $L_2$ , a spherical mirror focuses the 345 nm pulses into a 2 mm thick type-I BBO crystal, cut at  $37^\circ$ , where they act as pump pulses for the NOPA process. A second dichroic mirror (highly reflective for 517 nm and highly transmissive at 1035 nm) extracts the remaining  $2\omega_0$  light (Fig. 1, green), which is likewise recollimated by a lens ( $L_3$ ) and focused by a spherical mirror into a 5 mm thick type-I BBO crystal, cut at  $26.5^\circ$ . As will be shown later in detail, the  $3\omega_0$  pumped NOPA works best in the visible part of the spectrum up to 700 nm. In contrast, the  $2\omega_0$  pumped NOPA is advantageous in the 700 to 990 nm regime. Therefore a spectral splitting of the seed continuum at approximately 700 nm, for example with a dichroic mirror, is appropriate to obtain the highest seed energy in both NOPAs. If the full tuning range from 440 to 990 nm of the  $3\omega_0$  pumped NOPA shall be exploited, a broadband 50% beam splitter can be used instead.

Wavelength tuning is achieved for large parts of the spectral range in both branches by only varying the time delay between the chirped continuum seed and the respective pump pulses. Only towards the short and long wavelength ends of the tuning ranges small changes of the phase matching angles of the BBO crystals and/or the noncollinearity angles are necessary.

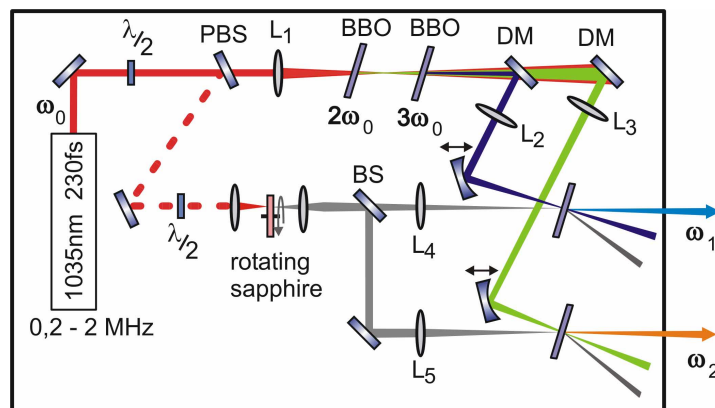


Fig. 1. Experimental arrangement.  $\lambda/2$ , half-wave plate; PBS, polarization beam splitter;  $L_1$ - $L_5$ , lenses; DM, dichroic mirror; BS, beam splitter (50%, broadband coating or dichroic mirror)

Most of the experiments described below were performed at 200 kHz repetition rate. Since then the system has been operated continuously at 500 kHz without any noticeable deterioration of performance and with unchanged output pulse energies. Scaling to the full repetition rate of the fiber laser system (2 MHz) should be straightforward and as before we do not expect any significant changes in the NOPA pulse parameters [1]. The whole setup is placed in a box with dimensions of approximately  $80 \times 80 \times 20 \text{ cm}^3$ , is therefore easily portable, compact and protected from the environment.

### 3. Seed generation

Different approaches for seed light generation with high repetition rate pump systems were reported, such as optical parametric generation in periodically poled lithium niobate [2] or soliton generation in a highly nonlinear photonic crystal fiber [3]. Optical parametric generation often shows high energy fluctuations, and nonlinear fibers typically result in highly structured spectra with phase modulations [4].

Here we use a continuum generated by filamentation in a 4 mm thick sapphire crystal. With a lens of 75 mm focal length we focus pulses at 1035 nm into the sapphire. Collimation of the continuum is achieved by a 30 mm achromatic lens. It smoothly covers a spectral region from 430 to 1000 nm, whereof the region from 500 to 850 nm forms a nearly flat plateau ( $\pm 30\%$  spectral energy density). In contrast to earlier approaches [1], where a minimum energy of  $2.5 \mu\text{J}$  per pulse was needed for stable continuum generation, we now find a minimum

gy of 2.5  $\mu\text{J}$  per pulse was needed for stable continuum generation, we now find a minimum threshold energy of only 1.5  $\mu\text{J}$  per pulse. This is due to an improved beam profile of the pump light, since we now directly use the output of the fiber laser and avoid prior frequency doubling. In addition, even small improvements in pulse duration seem to have significant effects on the continuum threshold. To avoid damage accumulation due to the high average power, the sapphire disc is rotated at approximately 60 Hz. Instabilities and degradation of the filament are sometimes assumed as drawbacks of continua generated in bulk materials [3]. This was not observed; in contrary we measure energy fluctuations of the continuum as low as 1.1% rms (see Section 6).

#### 4. Ultraviolet pump pulses

In parametric processes, the wavelength of the pump pulses limits the shortest achievable amplification wavelength for a given nonlinear crystal. If the amplified spectrum approaches the pump wavelength, energy conservation results in idler pulses with long wavelengths in the infrared, which are eventually absorbed in the nonlinear crystal. For example, when using the second harmonic of the 1035 nm pulses, amplification of wavelengths below 620 nm ceases in BBO due to idler absorption above 3.1  $\mu\text{m}$  [1]. To be able to amplify a wide spectral range of the seed light on the short wavelength side, a sufficiently short pump wavelength is needed. Therefore we choose the third harmonic at 345 nm as pump pulses.

We apply frequency doubling and subsequent sum-frequency mixing with the remaining fundamental pulses for overall tripling. In the fs-regime, group-velocity mismatch (GVM) between the three pulses plays an important role, because the difference in transit time through the nonlinear crystals becomes comparable to the pulse lengths. Therefore the pulses lose temporal overlap during propagation inside the crystals, which leads to reduced efficiency. The fundamental and second harmonic pulses exit the doubling stage at different times and have to be suitably delayed to restore the temporal overlap in the mixing stage. Conventional schemes for tripling of ultrafast pulses therefore use dichroic beam separation, mechanical delay, and recombination between the doubling and mixing stages [5, 6].

In contrast to these approaches, we use a sequence of two specially selected BBO crystals, which allow for group velocity matching in a simple collinear geometry without the need of additional delay elements. The concept is based on the following considerations. In type-I second harmonic generation in BBO, the fundamental pulses (o-polarized) have a larger group

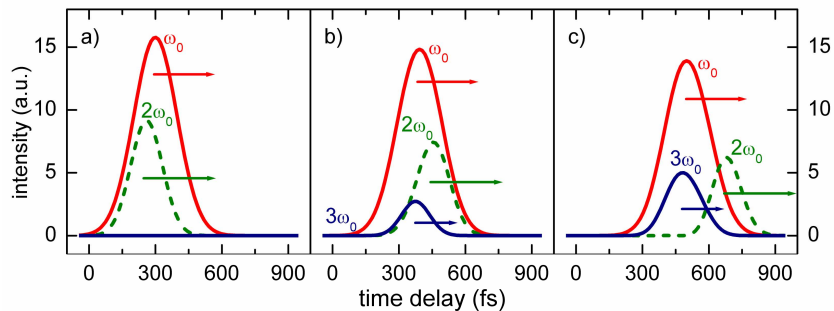


Fig. 2. Simulation of the  $3\omega_0$  generation using SNLO [7]. (a) When entering the type-II BBO mixing crystal, the  $\omega_0$  pulse leads the  $2\omega_0$  pulse by 50 fs due to GVM in the BBO crystal used for second harmonic generation. (b) After 0.5 mm in the mixing crystal, the  $2\omega_0$  pulse has overtaken the  $\omega_0$  pulse. (c) After 1.0 mm, the  $2\omega_0$  pulse starts to separate from the  $\omega_0$  pulse, which reduces the efficiency of  $3\omega_0$  generation.

velocity than the second harmonic pulses (e-polarized). In our setup, using fundamental pulses with a duration of 230 fs at 1035 nm and a 0.8 mm thick BBO doubling crystal, this group velocity mismatch leads to a separation of the  $\omega_0$  and  $2\omega_0$  pulses of approximately 50 fs after the doubling crystal (see Fig. 2(a)). For the following sum-frequency mixing process

$\omega_0 + 2\omega_0 \rightarrow 3\omega_0$ , there are three phase matching possibilities in BBO (see table 1). They result in different group delays that affect the temporal synchronization between the involved pulses.

A first important consideration is the group delay between the fundamental and the second harmonic pulses (table 1, middle column). In contrast to earlier approaches, which used sum-frequency mixing of type-I ( $o + o \rightarrow e$ ) or type-II ( $e + o \rightarrow e$ ) [5,6], the third possibility,  $o + e \rightarrow e$ , offers a negative group delay between the  $\omega_0$  and  $2\omega_0$  pulses. Because the  $\omega_0$

**Table 1: Group delay of pulses of the quoted frequencies after propagating through 1 mm of BBO for different phase matching configurations ( $\omega_0$  corresponding to a wavelength of 1035 nm).**

Group delay	$\omega_0$ vs. $2\omega_0$	$\omega_0$ vs. $3\omega_0$
Type-I $o + o \rightarrow e$	174 fs	369 fs
Type-II $e + o \rightarrow e$	346 fs	468 fs
Type-II $o + e \rightarrow e$	-190 fs	85 fs

pulses enter the tripling crystal 50 fs before the  $2\omega_0$  pulses, a subsequent negative group velocity mismatch in the tripling crystal, as given by the  $o + e \rightarrow e$  process, allows for the second harmonic pulses to overtake the fundamental pulses during the propagation. This restores a good temporal overlap within the crystal, in order to achieve high conversion efficiency without applying external delay elements (see Figs. 2(b) and 2(c)). The nonlinear conversion coefficient,  $d_{\text{eff}}$ , is about one fifth of the type-I scheme, but the damage threshold of BBO is high enough to compensate this by slightly reducing the beam sizes for increased intensity. A second advantage of the  $o + e \rightarrow e$  mixing scheme is the small group velocity mismatch between the original  $\omega_0$  and  $2\omega_0$  pulses with respect to the generated  $3\omega_0$  pulses (table 1, right column). Frequency tripled light that is generated in different parts of the crystal therefore adds up without temporal pulse lengthening.

In addition, with the  $o + e \rightarrow e$  scheme no rotation of the polarization between the two crystals is necessary and wave plates or geometrical polarization rotation is avoided. The generated  $3\omega_0$  pulses have the same polarization as the  $2\omega_0$  pulses and can directly be used for pumping the NOPAs.

Experimentally, an  $f = 500$  mm lens is used to focus the fundamental  $\omega_0$  pulses towards the two BBO crystals (type-I, 0.8 mm,  $23.5^\circ$  and type-II, 1.5 mm,  $62.8^\circ$ ). The type-I doubling crystal is placed about 70 mm before the focus and the type-II tripling crystal about 50 mm behind. This allows independent fine-tuning of the respective conversion efficiencies by moving the crystals in order to adjust the spot sizes. Total energy conversion efficiencies to the third harmonic of more than 15% are observed. In routine operation, we operated at approximately 11%, to maintain a good energy balance between the  $2\omega_0$  and the  $3\omega_0$  light, which are both used for NOPA pumping. We did not observe degradation or damage of the BBO crystals in long-term operation.

Our tripling scheme was already successfully used in ultrafast electron microscopy utilizing the same pump laser [8]. The presented concept of group-velocity management in frequency tripling is generally applicable, if conditions can be found where the group velocity difference of  $\omega_0$  and  $2\omega_0$  changes sign between frequency doubling and sum-frequency-mixing. For BBO, this is the case for type-I frequency doubling and type-II sum-frequency mixing for fundamental wavelengths above 905 nm up to about 1.5  $\mu\text{m}$ .

## 5. NOPA design and output characteristics

For simultaneous parametric amplification in the UV pumped and green pumped NOPA unit, the collimated seed continuum is split suitably as explained in Section 2. For the UV pumped NOPA, it is then focused with an  $f = 300$  mm fused silica lens towards the corresponding BBO crystal (type-I, 2.0 mm,  $37^\circ$ ), which is placed approximately 340 mm behind the lens, and overlapped spatially and temporally with the pump pulses.

To obtain the highest possible amplification bandwidth and thereby the shortest pulses, a noncollinear geometry is chosen. This concept has originally been demonstrated for 400 nm pumping [9-12] and is now widely used for 532 nm pumped optical parametric chirped pulse amplifiers (OPCPAs) [13,14]. The concept can be readily extended to 345 nm pumping. The external noncollinearity angle between the seed and the pump beam is set to  $\sim 5.5^\circ$  for broadband amplification around 590 nm. The crystal is oriented for tangential phase matching to obtain the highest efficiency and the cleaner output beam profile, as compared to the walk-off compensated orientation. The collimated UV pump beam is focused with a spherical mirror ( $f = 250$  mm), placed approximately 260 mm before the BBO crystal, resulting in a beam diameter of about  $100 \mu\text{m}$  in the crystal.

In the green pumped NOPA, we use an  $f = 350$  mm lens for focusing the seed continuum towards the BBO crystal (type-I, 5.0 mm,  $26.5^\circ$ ), which is placed about 450 mm behind the lens. The collimated green pump pulses are focused with a spherical mirror ( $f = 250$  mm), which is placed about 270 mm before the BBO crystal, resulting in a beam diameter of about  $220 \mu\text{m}$  on the crystal surface. The external noncollinearity angle is set to  $\sim 5^\circ$  for broadband amplification around 820 nm.

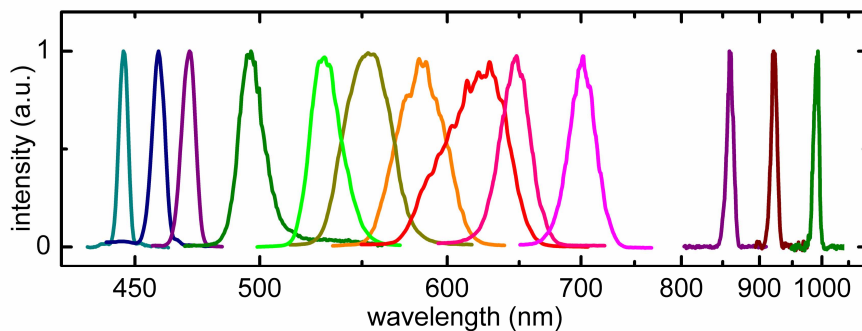


Fig. 3. Typical output spectra of the 345 nm pumped noncollinear optical parametric amplifier, showing the more than octave wide continuous tuning range.

Figure 3 shows typical output spectra from the UV pumped NOPA. Tuning is mainly achieved by delaying the UV pump pulses with respect to the longer (and chirped) continuum pulse (495 – 665 nm), and by slightly adjusting the phase matching angle and noncollinearity for parametric amplification. The resulting output pulses are continuously tunable over more than one optical octave from 440 to 990 nm (303 – 682 THz). Throughout all of the tuning range, the spectra are very smooth and have nearly Gaussian shape. The pulses were compressed using a sequence of fused silica prisms with an apex angle of  $68.7^\circ$ . Typical prism separations (edge to edge) are 500 to 1000 mm. For temporal pulse characterization, autocorrelation traces were obtained with a dispersion-free autocorrelator [15]. Figure 4 shows typical traces, from which the pulse durations are evaluated by assuming a Gaussian pulse shape. The

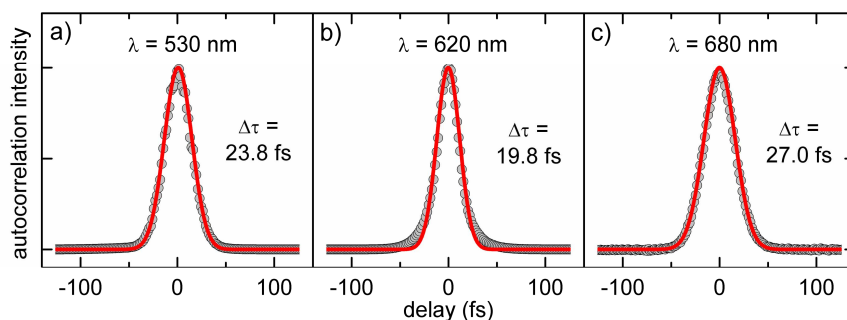


Fig. 4. Typical measured autocorrelation traces (dots) and Gaussian fits to the data (red line) at various wavelengths. The autocorrelation traces are very smooth and pedestal-free, indicating pulses without temporal satellites.



smooth Gaussian shaped spectra in combination with insignificant higher order chirp allow for almost Fourier-limited pulse shapes without temporal satellites, as evident from the pedestal-free autocorrelation traces.

Figure 5 summarizes the calculated Fourier-limits of measured spectra (blue squares) and the measured pulse durations (red diamonds). Between 520 and 680 nm pulse durations of sub-30 fs were measured. The observed increase of the Fourier limits towards shorter and longer wavelengths can be explained by considering phase matching and chirp effects. In the short wavelength region, estimates show that broadband noncollinear phase matching is well possible and that the residual wave vector mismatch between signal and idler allows for Fourier limits of 13 fs from 430 to 690 nm (see blue dashed line in Fig. 5). However, even with perfect phase matching, parametric amplification can only affect such spectral components of the seed light that overlap in time with the pump pulses. The seed continuum is chirped, mainly by dispersion in the achromatic lens used for collimating and the fused silica lens used for relay imaging. Because such material dispersion is particularly severe at short wavelengths, the continuum is chirped strongest in this spectral range and longer Fourier limits are observed. With a proper chirp management, e.g., by compressing the continuum and/or stretching the pump pulses, an amplification bandwidth sufficient for sub-20 fs pulses is expected all the way down to 440 nm.

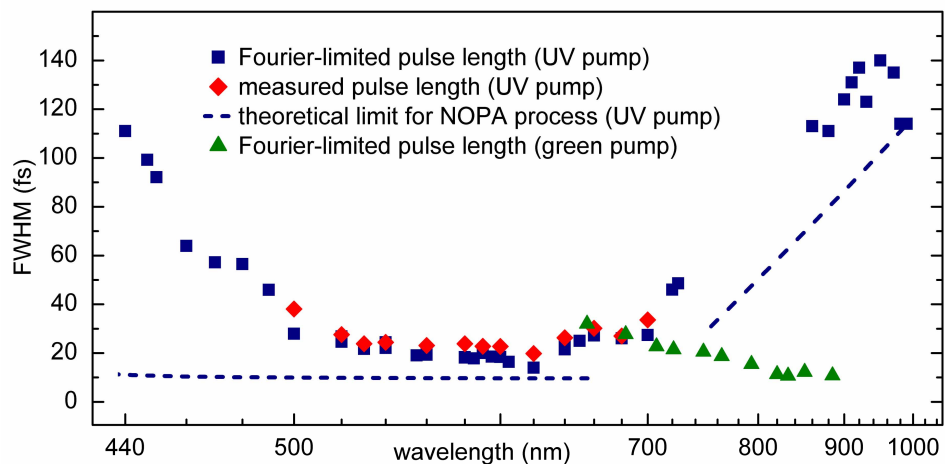


Fig. 5. Summary of calculated Fourier-limited pulse lengths from measured spectra (blue squares for UV pumping, green triangles for green pumping [1]) and calculated pulse lengths from measured autocorrelation traces (red diamonds). The dotted blue lines show theoretical limits for the minimum pulse length, assuming group-velocity matching in the spectral range below 660 nm and based on the group-velocity mismatch between signal and idler above 750 nm.

Above the degeneracy point of 690 nm effective group-velocity matching by a noncollinear geometry is not possible. Therefore a collinear arrangement is advantageous and the amplification bandwidth is mainly given by the first order wave vector mismatch between signal and idler. The dashed blue line shown in Fig. 5 above 750 nm depicts the resulting lower limit for the achievable pulse duration. The somewhat higher measured Fourier limits are explained by a small residual noncollinearity angle that was used in the experiments. The second NOPA, pumped by green pulses at  $2\omega_0 \hat{=} 517$  nm, therefore exhibits an ideal complement as it delivers sub-30 fs over its complete fundamental tuning range from 620 to 990 nm (see green triangles in Fig. 5). In combination, the two NOPAs provide Fourier-limited pulse lengths of sub-30 fs in a spectral range from 500 to 990 nm.

The output pulse energies are in the range of 140 nJ for the UV pumped NOPA, best at the center of its tuning range. Simultaneously, the second harmonic pumped NOPA delivers pulses with up to 250 nJ energy in a broad range around 800 nm. For both NOPAs the beam profile is visually round and homogeneous. The pulse energies are well sufficient for subsequent frequency conversion processes, for example to extend the tuning range into the ultra-

violet region. The generation of 34 nJ pulses at 290 nm has already been demonstrated [16]. The octave-wide tuning range together with simple frequency doubling leads to a continuous spectral coverage from below 250 nm to nearly 1  $\mu\text{m}$  without any gap.

## 6. Fluctuation analysis

To elucidate the usability of the MHz NOPA for low-noise spectroscopic applications, we performed a detailed analysis of the pulse-to-pulse intensity fluctuations. The energy in each single pulse was measured by a moderately fast photodiode module, of which the output voltage trace was recorded in time with a fast digital oscilloscope. Such oversampling significantly decreases digitizing effects on low-noise data. To reveal fluctuation correlations between different pulse trains, two identical photodiodes were employed simultaneously. The relative deviations of the individual pulse energies  $E_k$  from the average  $\bar{E}$  is referred to as laser noise. For the primary fiber laser system, we obtain a total noise of 0.8 % rms when recording 100,000 subsequent pulses at 208 kHz. The frequency-resolved noise density is shown in Fig. 6(a). The relative noise intensity, i.e. the spectral power density normalized to the average power, is below -85 dB/Hz throughout the frequency range of 1 – 100 kHz. We note that the noise spectrum of the fiber laser output is mostly composed of uniform white noise, with a resonance at about 44 kHz.

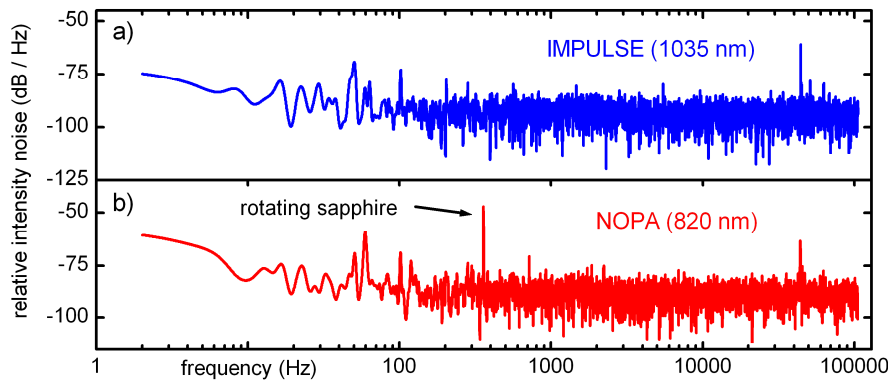


Fig. 6. Relative intensity noise of (a) the fiber laser system and (b) the NOPA.

For the output fluctuations of the green pumped NOPA unit, we obtain a total noise of 1.3 % rms. The spectrum of the NOPA fluctuations (Fig. 6(b)) shows an additional low frequency resonance at 355 Hz, which originates from the rotating sapphire disc and is attributed to slight changes in the overlap between the continuum and the pump pulses in the NOPA crystal, caused by not perfectly parallel surfaces of the disc. However, this rotation is found to contribute only insignificantly to the total noise of the NOPA (1.2 % rms, when excluding the 355 Hz resonance). From the noise spectrum of the NOPA we conclude that a modulation frequency in the range of 5 – 15 kHz is most suitable for low-noise lock-in detection. The fluctuations of the UV-pumped NOPA unit were not analyzed in detail. Since the output is in the visible, the visual impression of no significant instabilities can be taken as indication for comparable fluctuations as in the green pumped NOPA.

The total NOPA output noise is only 1.6 times larger than that of the primary fiber laser, although four nonlinear optical conversion processes are involved (frequency doubling, sum-frequency mixing, continuum generation, and parametric amplification). To investigate the origin of the NOPA noise, we measured energy correlations between the different beams involved within the NOPA. Such an analysis allows for measuring the order of nonlinearity of the involved frequency conversion processes and to investigate the effects of saturation.

Correlation plots of the measured pulse energies as two-dimensional histograms are expected to show tilted ellipsoids with the slope of the main axis given by the order  $m$  of the

nonlinearity. Deviations of the measured slope  $m^*$  from the expected value  $m$  indicate saturation in the conversion process.

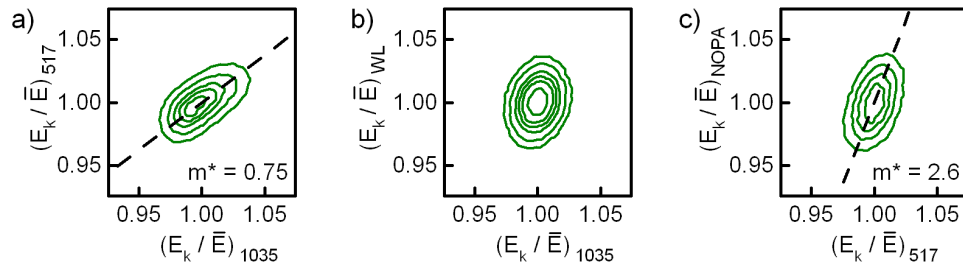


Fig. 7. Scatter density plots of output vs. input noise of various nonlinear processes involved in the generation of the NOPA pulses.

Figure 7(a) shows the noise correlation (binned into a  $75 \times 75$  histogram) between the fundamental fiber laser pulse energy and the energy of the green pump pulses. For frequency doubling  $m = 2$  is expected, but experimentally we observe  $m^* = 0.75$ . This means that the fluctuations in the green pulses are even smaller than those of the fundamental pulses. For high input intensities and doubling efficiencies of more than 30 % depletion of the input pulse becomes significant and the second harmonic pulses are partially back-converted. Exceptionally intense fundamental pulses therefore generate attenuated frequency doubled output pulses, which can result in self-stabilization when a proper intensity regime is chosen. We believe that such a mechanism is the reason for the low fluctuations of the second harmonic and consequently the remarkably high NOPA stability.

Figure 7(b) shows the noise correlation between the fundamental fiber laser pulses and the continuum pulses (800 to 840 nm band pass). For two distinct time scales of 0.5 s and 1 ms (data not shown), we find no correlation and no tilt of the ellipse is measurable. The energy of our continuum pulses has no significant dependence on the pump pulse intensity. This is the result of the threshold behavior of the self-focusing, channeling, and spectral broadening mechanisms involved in the continuum generation. Some noise of about 1.1 % rms is nevertheless observed and contributes to the overall NOPA noise.

The correlation between the output of the green pumped NOPA and the green pump pulses is reasonably high (see Fig. 7(c)). A further improvement of the pump laser stability would therefore lead to an even better NOPA stability. The observed slope of  $m^* = 2.6$  is below the expectation for an unsaturated parametric amplification. A similar observation was made for the UV pumped NOPA. This indicates that the two parametric amplification processes are both operated fairly close to saturation, even for the low pump pulse energies used in this setup. Stable NOPA operation is not limited to highly energetic pump pulses, when focus sizes, pulse durations, and beam diameters within the setup are properly designed.

## 7. Experimental investigation of phase dependencies in optical parametric amplification

The overlapping amplification regions of the two differently pumped NOPA units allow for an instructive interference experiment that renders information about the phase dependencies in the parametric amplification process. The two NOPA units, seeded by the same continuum, are tuned to the same center wavelength of 720 nm and brought to interference with a small angle on a distant screen (see schematic Fig. 8(a)). Such an interferogram yields information about the relative phase jitter between the two NOPAs. In earlier experiments it was demonstrated that stable interference is observed, when two NOPAs are pumped by replicas of the same blue pulse, i.e. pulses with equal phase fluctuations [17,18]. In contrast, the presented experiment involves pump pulses that are derived from different harmonics ( $2\omega_0$  and  $3\omega_0$ ) of the primary fiber laser, which is not phase stabilized. The second and third harmonic pulses therefore have carrier-envelope phases with twice or threefold the original phase fluctuations, which makes their relative phase jitter random. Hence, if the phase of the pump pulse has in-

fluence on the phase of the amplified pulse in optical parametric amplification, the phase of the interference pattern, i.e. the position of the minima and maxima, should change statistically from shot to shot.

To test this, we recorded the time dependence of the interference pattern with a linear detector array operated at 1 kHz. A typical measurement is depicted in Fig. 8(c). Over times of several seconds, the position of the interference pattern is extremely stable (see Fig. 8(b)). The associated relative phase between the two NOPAs, shown in Fig. 8(d) and 8(e), has fluctuations of less than 20 mrad rms in the measured frequency range of 0.1 to 1000 Hz. This means that the relative phase of the two parametrically amplified pulses is extremely stable and independent of the phase of the pump pulses.

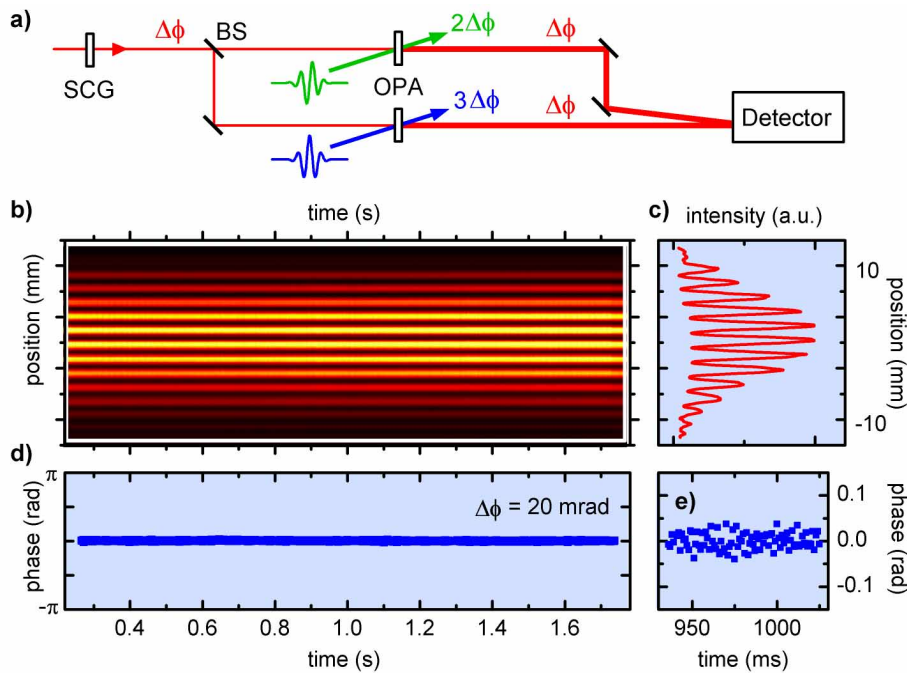


Fig. 8. Interference experiment to investigate phase dependencies in optical parametric amplification (OPA). (a) Experimental setup. SCG: supercontinuum generation, BS: beam splitter. (b) Wrong-color representation of the amplitude of successive interference patterns showing the high phase stability. (c) Single measured spatial interference pattern. (d) and (e) Phase of the interference pattern over time.

## 8. Concluding remarks

The presented results show that a NOPA based on a MHz fiber laser system is capable of generating sub-20 fs pulses with energies above 100 nJ and is tunable from 440 to 990 nm without a gap. This more than octave wide tuning range is made possible by pumping the parametric amplification with the frequency tripled pump pulses at 345 nm. With simple and straight forward frequency doubling the range from below 250 nm to nearly 1  $\mu\text{m}$  is accessible. Ti:sapphire based systems have so far not been shown to allow this complete spectral coverage. Attempts to pump a NOPA with the third harmonic of the Ti:sapphire system at 267 nm were hampered by the strong two photon absorption in the BBO crystal and the large group velocity mismatch between the three interacting waves [19]. Additionally, the Yb-doped fiber laser system allows at least a tenfold higher repetition rate than Ti:sapphire based amplifier systems. The present rate around 1 MHz is ideal for applications as it provides sufficiently intense pulses for nonlinear interactions, high averaging capability and still ample time for sample exchange or relaxation. The sub-250 fs pulse duration of the used pump system allows direct generation of a high quality continuum in bulk sapphire. This permits a much wider tun-

ing range and smoother spectra than obtained with precompression of longer pump pulses [20,21] or seeding by a spectrally broadened Ti:sapphire laser [3].

The presented NOPA is based on a single stage traveling wave amplifier. Since the parametric amplification depends on the pump intensity and higher pump energies can be accommodated by an increased pump diameter, nearly arbitrary power scaling of the device seems realistic. This opens up the route to UV-pumped OPCPAs at the millijoule or even joule level and OPCPAs with combined green and UV pumping for increased spectral width and pulse durations approaching 5 fs.

The demonstrated phase stability in the optical parametric amplification is an important requirement for many future experiments, such as light wave synthesis. The measured phase stability between the two NOPAs of 20 mrad corresponds to a temporal jitter of only 8 attoseconds. Since our measurement averaged over 200 pulses, we expect a true pulse-to-pulse jitter of not more than 110 attoseconds. The presented amplification concept with its tunability of more than an octave is most promising for generating single attosecond pulses in recently proposed schemes based on a strong pulse with frequency  $\omega$  and a phase-locked second pulse slightly off the second-harmonic, e.g.,  $2.2\omega$  [22].

The two NOPAs pumped by the second and the third harmonic have their best performance in different spectral regions and therefore provide powerful sources for two-color ultrafast pump-probe spectroscopy. The high repetition rate is expected to advance for example spectroscopy on surfaces, where extremely weak signals have to be detected and long averaging is needed. As a consequence of the phase stability, the full temporal resolution corresponding to the reported short pulse durations can be utilized even for long averaging times.

### **Acknowledgments**

We thank Clark-MXR, Inc. and HORIBA Jobin Yvon for the generous loan of the IMPULSE system. This work was supported by the Austrian Science Fund within the framework of the Special Research Program F16 (Advanced Light Sources) and by the DFG-Cluster of Excellence: Munich-Centre for Advanced Photonics. The International Max Planck Research School on Advanced Photon Science (C. H.) is gratefully acknowledged.



## Anhang 3

### **"19 femtosecond shaped ultraviolet pulses"**

C. Schriever, S. Lochbrunner, M. Optiz, and E. Riedle

Opt. Lett. 31, 543 – 545 (2006)





# 19 fs shaped ultraviolet pulses

C. Schriefer, S. Lochbrunner, M. Optiz, and E. Riedle

*Lehrstuhl für BioMolekulare Optik, Department für Physik, Ludwig-Maximilians-Universität, Oettingenstrasse 67, 80538 München, Germany*

Received July 12, 2005; revised September 30, 2005; accepted October 11, 2005; posted November 8, 2005 (Doc. ID 63408)

We report the generation of shaped tunable ultrashort ultraviolet pulses with full control over the spectral phase and amplitude. The output of a noncollinearly phase-matched optical parametric amplifier is shaped in phase and amplitude by a liquid-crystal spatial light modulator. The resulting structured visible pulses are transferred into the ultraviolet by sum-frequency mixing with strongly chirped 775 nm pulses. Single, double, and triple pulses at 344 nm with subpulses as short as 19 fs are explicitly demonstrated. The method can easily be adapted to arbitrarily shaped pulses throughout the 295–370 nm range. © 2006 Optical Society of America

OCIS codes: 320.5540, 320.7110, 260.7190.

Light pulses with precisely controlled spectral and temporal characteristics can selectively address and manipulate inherent resonances and dynamics of complex quantum mechanical systems.<sup>1</sup> To control molecular dynamics, shaped pulses with substructures on the time scale of vibrations are needed. To match the electronic absorption of organic molecules, they have to be in the ultraviolet (UV).

As liquid-crystal spatial light modulators (LC SLMs), frequently used for shaping visible and near infrared (NIR) pulses,<sup>2</sup> are not available with high transmission in the UV, alternative techniques have been developed: shaped Ti:sapphire pulses have been frequency doubled<sup>3</sup> or transferred into the UV by type I<sup>4</sup> and type II<sup>5</sup> sum-frequency mixing (SFM). A fused-silica acousto-optical modulator<sup>6</sup> and a micro-mirror array<sup>7</sup> have been used for direct shaping of 400 nm pulses. Yet none of these devices is commercially available, nor have any of these schemes proved to be able to generate ultrashort UV pulses.

We shape spectrally broad, tunable pulses in the visible with a LC SLM and transfer them into the UV by SFM. We extend the mixing scheme for the generation of shaped tunable ultrashort UV pulses by strongly chirping and thereby stretching the NIR pulse. SFM with intense chirped NIR pulses from a Ti:sapphire amplifier has already proved to provide a high efficiency and a tuning range of 295–370 nm (Ref. 8). It is here applied for the first time to our knowledge to shaped pulses. Contrary to other schemes,<sup>4</sup> a high spectral resolution is achieved without reducing the bandwidth and the energy of the NIR pulses. The phase and amplitude of the visible (VIS) pulse are directly transferred into the UV, as outlined in the following: for SFM with broadband phase matching, the generated electric field  $E_{UV}(t) \propto E_{VIS}(t)E_{NIR}(t)$ . Assuming a Gaussian NIR pulse, strongly chirped by propagation through dispersive material, the phase of the pulse is approximated by a purely linear chirp, and the electric field  $E_{NIR}$  can be written in the frequency domain as

$$E_{NIR}(\omega) \propto \exp\left[-\frac{(\omega - \omega_{NIR})^2}{2\sigma^2} + i\frac{D_2}{2}(\omega - \omega_{NIR})^2\right]. \quad (1)$$

Here  $\sigma$  denotes the spectral width,  $\omega_{NIR}$  the angular carrier frequency, and  $D_2$  the quadratic spectral phase coefficient corresponding to the linear chirp.<sup>9,10</sup> Assuming  $\sigma^2 D_2 \gg 1$ , the pulse in the time domain can be approximated by

$$E_{NIR}(t) \propto A_{NIR}(t) \exp\left(-i\frac{t^2}{2D_2}\right) \exp(-it\omega_{NIR}), \quad (2)$$

with the temporal amplitude  $A_{NIR}(t) = \exp[-t^2/(2\sigma^2 D_2^2)]$ . The UV pulse is given by

$$E_{UV}(t) \propto A_{VIS}(t)A_{NIR}(t) \exp\left[-i\phi_{VIS}(t) - i\frac{t^2}{2D_2}\right] \times \exp[-it(\omega_{VIS} + \omega_{NIR})], \quad (3)$$

where  $A_{VIS}$  is the arbitrary temporal amplitude,  $\phi_{VIS}$  the phase, and  $\omega_{VIS}$  the carrier frequency of the visible shaped pulse. The amplitude  $A_{UV} = A_{VIS}(t)A_{NIR}(t)$  of the generated UV pulse at  $\omega_{UV} = \omega_{VIS} + \omega_{NIR}$  has the same shape as the amplitude of the visible pulse, since the NIR amplitude is almost constant during the interaction. Besides, this regime guarantees the most efficient transfer of the shaped pulse. For large values of  $D_2$ , the temporal phase of the UV pulse  $\phi_{UV} = \phi_{VIS}(t) + t^2/(2D_2)$  approaches the phase of the visible pulse. Relation (3) gives a simple recipe for how to design and shape the visible pulse for a desired UV pulse.

In the setup (Fig. 1) a regenerative 1 kHz Ti:sapphire laser system (CPA 2001, Clark-MXR) pumps two noncollinear optical parametric amplifiers<sup>11</sup> (NOPAs) with 150 fs long pulses at 387 THz (775 nm) exhibiting a bandwidth of 3.5 THz. The dispersion of both NOPAs is compensated to first order by fused-silica prism compressors (PCs). The pulses for the

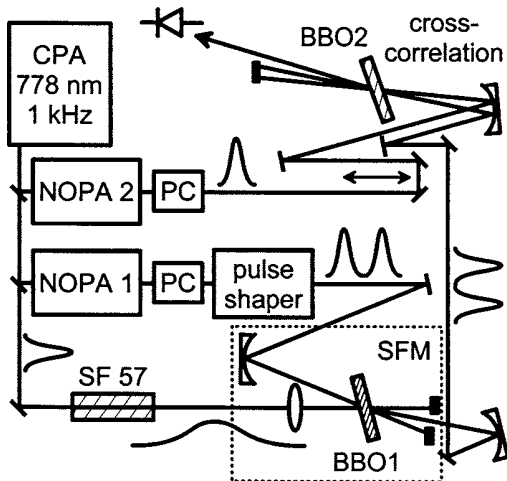


Fig. 1. Setup for the generation and characterization of shaped tunable UV pulses.

SFM process are generated by the two-stage NOPA 1 and shaped in spectral amplitude and phase by a 128 pixel, double-layered LC SLM (SLM 256, CRI Inc.), placed in the Fourier plane of a 4- $f$  zero-dispersion grating compressor<sup>2</sup> (pulse shaper) with a resolution of  $\Delta\nu=0.9$  THz/pixel at 500 THz. For part of the experiments the spectral width of NOPA 1 is increased from 35 to 160 nm by stretching the internal blue pump pulses with 170 mm of fused silica.<sup>10</sup> NOPA 2 (single stage) generates 20 fs long pulses at 700 nm and is used to characterize the temporal shape of the UV pulses by difference-frequency mixing (DFM) in a 50  $\mu\text{m}$  type I BBO crystal (BBO2). 100  $\mu\text{J}$  per pulse is split from the Ti:sapphire output and passes 185 mm of SF 57 glass, introducing a linear chirp of  $D_2=4.4 \times 10^4$  fs<sup>2</sup> and stretching the pulse to 1.2 ps. For SFM the VIS and NIR pulses are focused with a small angle between the beams onto a type I BBO crystal (BBO1).

Figure 2 demonstrates the transfer of spectral features to the UV. The spectra are recorded with a 0.5 m grating spectrometer. Spectral components beyond the region from 433 to 540 THz pass outside the structured area of the liquid-crystal modulator and cannot be modulated. Every tenth pixel of the mask is set to zero transmission [Fig. 2(a)]. The spectra of the UV pulses resulting from SFM in a 100 and a 25  $\mu\text{m}$  thick crystal are depicted in Figs. 2(b) and 2(c). The thinner crystal supports the transfer of the whole spectrum, which, allowing for an UV spectrum, extends from 804 THz (373 nm) to 926 THz (324 nm) with a Fourier limit of 7.2 fs. The smaller phase-matching bandwidth of the 100  $\mu\text{m}$  thick crystal results in a reduced UV bandwidth with a Fourier limit of 14 fs and in wings characteristic for the sinc<sup>2</sup> acceptance function of the crystal. The position of the dips in the UV spectra corresponds to the dips in the visible shifted by the addition of a 387 THz photon. The reproduced spacings on the frequency scale demonstrate that no distortion of the frequency axis occurs. The overshoots at the sides of the dips and the wiggles in the dips can be exactly reproduced by numerical simulations. They appear because spectrally

narrow features (the dips) result in temporally long structures, which pick up a slight phase distortion in the SEM process as given by Eq. (3). In summary, the spectrum of the temporally short, shaped pulses is transferred into the UV with negligible deformations if the crystal is sufficiently thin.

Figure 3(a) shows the autocorrelation and 3(b) the spectrum of a NOPA pulse, and Fig. 3(c) shows the cross correlation and 3(d) the spectrum of the UV pulse, generated by SFM in a 100  $\mu\text{m}$  thick BBO crystal. This thickness is a good compromise between UV energy and mixing bandwidth. In both cases the linear chirp and the quadratic chirp were minimized with the pulse shaper. The FWHM of the visible pulse is 10.3 fs and lies within 10% of the transform limit, demonstrating that the pulse shaper can correct the typical phase distortions. For SFM the visible pulses are precompressed with the shaper so

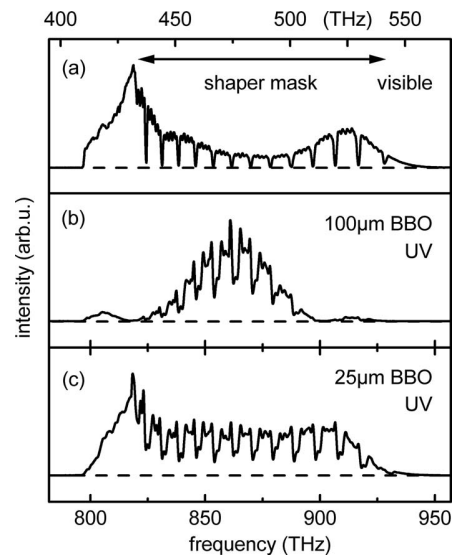


Fig. 2. (a) Spectrum of the visible pulse after the pulse shaper, with every tenth pixel set to zero transmission. UV spectra generated by SFM of this spectrum in (b) a 100  $\mu\text{m}$  thick and (c) a 25  $\mu\text{m}$  thick BBO crystal.

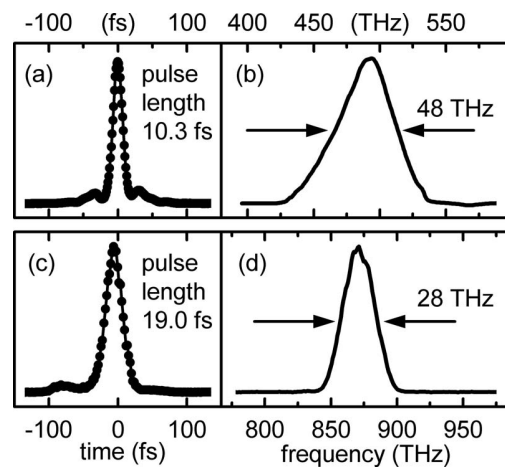


Fig. 3. (a) Autocorrelation and (b) spectrum of a NOPA pulse optimally compressed with the pulse shaper. (c) Cross correlation and (d) spectrum of a UV pulse with optimized precompression.

that no compressor in the UV is needed. The applied correction for the linear chirp is  $D'_2 = -190 \text{ fs}^2$  and for the quadratic chirp  $D'_3 = 1080 \text{ fs}^3$ . The calibration of the phase versus electrical input was performed according to the instructions of the SLM manufacturer.  $D'_2$  accounts for the group-delay dispersion accumulated up to the point of the cross-correlation measurements, while  $D'_3$  compensates for the quadratic chirp introduced by the prisms. Since the visible pulse has a significant amplitude only within  $\pm 2\Delta t_{\text{FWHM,VIS}}$ , the phase of the UV pulse deviates from the visible phase due to the NIR chirp by less than  $\Delta\Phi_{\text{UV}} \approx (2\Delta t_{\text{FWHM,VIS}})^2 (2D'_2)^{-1}$ . For our experimental conditions we obtain  $\Delta\Phi_{\text{UV}} = 18 \text{ mrad}$ . The duration of the UV pulses is determined by DFM with NOPA 2 and subsequent deconvolution to 19 fs and lies within 20% of the Fourier limit. The temporal shape is very clean and exhibits only a small prepulse. The energy of the shown UV pulse is 90 nJ. Optimizing the alignment for pulse energy leads to slightly longer UV pulses with 300 nJ and a quantum efficiency of 8%. Taking the different length and energy of the NIR pulses into account, this agrees well with the results of Ref. 8.

For multipulses evenly spaced in time we apply the filter function

$$H_n(\omega) = N \sum_{p=-(n-1)/2}^{(n-1)/2} \exp(-ip\Delta t\omega), \quad (4)$$

with  $n$  the number of subpulses,  $\Delta t$  their separation in time,  $\omega$  the angular frequency relative to the carrier frequency, and  $N$  a normalization factor. For double and triple pulses  $H_n(\omega)$  reads as  $H_2(\omega) = \cos(\Delta t\omega/2)$  and  $H_3(\omega) = \frac{2}{3} \cos(\Delta t\omega) + \frac{1}{3}$ . The spectral filtering performed by the shaper is  $T(\omega) = |H_n(\omega)|^2$ , and the phase shift including the chirp compensations given above<sup>2</sup> is  $\Delta\Phi(\omega) = \arg[H_n(\omega)] + (D'_2/2)\omega^2 + (D'_3/6)\omega^3$ .

The cross correlations of double and triple UV pulses generated at a center wavelength of 344 nm (872 THz) are depicted in Fig. 4. The subpulses have durations between 20 and 22 fs. To the best of our knowledge, these are the shortest substructures reported for shaped UV pulses. The temporal separation can be continuously tuned up to 500 fs for double pulses and up to 350 fs for triple pulses without distortions to the temporal shape. Cross-correlation measurements spanning several picoseconds show no satellite pulses outside the range displayed in Fig. 4. Although the spectral filtering attenuates the visible pulses, the structured UV pulses still have an energy of 100 nJ. The center frequencies of the subpulses are shifted with respect to one another by  $\Delta\nu = \Delta t / (2\pi D'_2)$  according to relation (3). This is less than 2 THz for  $\Delta t \leq 500 \text{ fs}$  and is negligible compared with the pulse width of 28 THz.

In summary, full control over the spectral phase and amplitude of tunable UV pulses is obtained by SFM of shaped visible pulses with strongly chirped

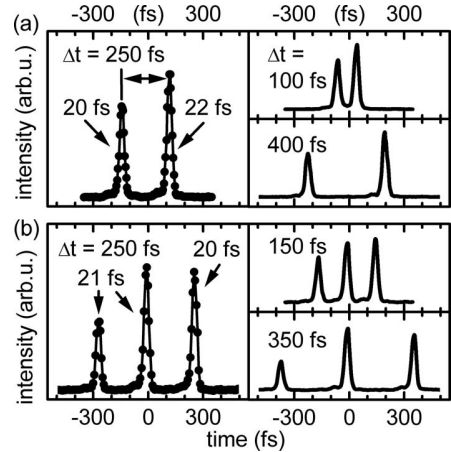


Fig. 4. Cross correlations of UV (a) double and (b) triple pulses at a center wavelength of 344 nm (872 THz) for various pulse separations  $\Delta t$ .

NIR pulses. Substructures with durations down to 20 fs are achieved, which, to our knowledge, are up to now the shortest features reported for shaped UV pulses. The demonstrated multipulses should be most suitable for driving coherent vibrations and wavepacket dynamics of molecules absorbing in the UV. For clarity we demonstrated regular structures, but complex arbitrary pulse shapes can be generated just as easily because of the direct transfer of phase and amplitude to the UV. By a simple realignment of the NOPA and the pulse shaper, the full spectral range from 295 to 370 nm is accessible.

We thank Kai Stock and Peter Baum for valuable contributions and the Deutsche Forschungsgemeinschaft and the Austrian Science Fund (grant F016 SFB Advanced Light Sources) for funding. S. Lochbrunner's e-mail address is stefan.lochbrunner@physik.uni-muenchen.de.

## References

1. H. Rabitz, R. de Vivie-Riedle, M. Motzkus, and K. Kompa, *Science* **288**, 824 (2000).
2. A. M. Weiner, *Rev. Sci. Instrum.* **71**, 1929 (2000).
3. M. Hacker, R. Netz, M. Roth, G. Stobrawa, T. Feurer, and R. Sauerbrey, *Appl. Phys. B* **73**, 273 (2001).
4. M. Hacker, T. Feurer, R. Sauerbrey, T. Lucza, and G. Szabo, *J. Opt. Soc. Am. B* **18**, 866 (2001).
5. H. Wang and A. M. Weiner, *IEEE J. Quantum Electron.* **40**, 937 (2004).
6. M. Roth, M. Mehendale, A. Bartelt, and H. Rabitz, *Appl. Phys. B* **80**, 441 (2005).
7. M. Hacker, G. Stobrawa, R. Sauerbrey, T. Backup, M. Motzkus, M. Wildenhain, and A. Gehner, *Appl. Phys. B* **76**, 711 (2003).
8. I. Z. Kozma, P. Baum, S. Lochbrunner, and E. Riedle, *Opt. Express* **11**, 3110 (2003).
9. I. Walmsley, L. Waxer, and C. Dorrer, *Rev. Sci. Instrum.* **72**, 1 (2001).
10. P. Baum, S. Lochbrunner, and E. Riedle, *Appl. Phys. B* **79**, 1027 (2004).
11. E. Riedle, M. Beutter, S. Lochbrunner, J. Piel, S. Schenkl, S. Spörlein, and W. Zinth, *Appl. Phys. B* **71**, 457 (2000).



## Anhang 4

**"Ultrasensitive ultraviolet-visible 20 fs absorption spectroscopy  
of low vapor pressure molecules in the gas phase"**

C. Schriefer, S. Lochbrunner, E. Riedle, and D. J. Nesbitt

Rev. Sci. Instrum. 79, 013107 (2008).



## Ultrasensitive ultraviolet-visible 20 fs absorption spectroscopy of low vapor pressure molecules in the gas phase

C. Schriever, S. Lochbrunner,<sup>a)</sup> and E. Riedle<sup>b)</sup>

*Lehrstuhl für BioMolekulare Optik, Fakultät für Physik, Ludwig-Maximilians-Universität (LMU), Oettingenstrasse 67, 80538 München, Germany*

D. J. Nesbitt

*Joint Institute for Laboratory Astrophysics, NIST, Department of Chemistry and Biochemistry, University of Colorado, Boulder, Colorado 80309-0040, USA*

(Received 30 October 2007; accepted 24 December 2007; published online 24 January 2008)

We describe an ultrasensitive pump-probe spectrometer for transient absorption measurements in the gas phase and in solution. The tunable UV pump and the visible (450–740 nm) probe pulses are generated by two independently tunable noncollinear optical parametric amplifiers, providing a temporal resolution of 20 fs. A homebuilt low gain photodetector is used to accommodate strong probe pulses with a shot noise significantly lower than the overall measurement noise. A matched digitizing scheme for single shot analysis of the light pulses at kilohertz repetition rates that minimizes the electronic noise contributions to the transient absorption signal is developed. The data processing scheme is optimized to yield best suppression of the laser excess noise and thereby transient absorbance changes down to  $1.1 \times 10^{-6}$  can be resolved. A collinear focusing geometry optimized for a 50 mm interaction length combined with a heatable gas cell allows us to perform measurements on substances with low vapor pressures, e.g., on medium sized molecules which are crystalline at room temperature. As an application example highlighting the capability of this instrument, we present the direct time-domain observation of the ultrafast excited state intramolecular proton transfer of 2-(2'-hydroxyphenyl)benzothiazole in the gas phase. We are able to compare the resulting dynamics in the gas phase and in solution with a temporal precision of better than 5 fs. © 2008 American Institute of Physics. [DOI: 10.1063/1.2834877]

### I. INTRODUCTION

Pump-probe spectroscopy with femtosecond time resolution is a powerful tool for investigating molecular dynamics and kinetics in systems that are of interest to chemistry and biology. In prominent cases it provided the crucial breakthrough in understanding the underlying mechanisms.<sup>1</sup> Molecular processes are usually governed by intramolecular properties as well as interaction with the surrounding medium; thus in most situations it is impossible to exclude *a priori* the relevance of the environment. High level *ab initio* quantum chemical descriptions usually consider the isolated molecule, i.e., the diluted gas phase situation. To understand the interplay between intra- and intermolecular dynamics, it is therefore most important to disentangle them. This can be done most simply by investigation of the isolated molecule in the gas phase and comparison to its behavior under condensed phase conditions. With the advent of quantum control and quantum computing, the role of coherence, vibrational as well as electronic, and the nature of dephasing processes become more and more important.<sup>2–4</sup> In this context, the comparison of gas phase and condensed phase re-

sults is particularly interesting if a time resolution is achieved which allows the observation of conformational changes and vibronic wavepacket dynamics.

In the gas phase, very sensitive detection techniques are necessary due to the low particle densities. In most cases, photoionization and mass selective detection have been utilized as probe processes since ions and electrons can be detected with almost single particle efficiency.<sup>5,6</sup> In the condensed phase, however, ionization techniques cannot be applied and one has to resort to optical signals. Transient absorption spectroscopy has proven to be a very suitable probing technique since it is sensitive, gives absolute numbers for molecular observables such as concentrations or transition strengths, and provides in practice a superior time resolution compared to most other techniques.<sup>7,8</sup> However, comparison of absorption experiments in the condensed phase with ionization experiments in the gas phase is not straightforward because both techniques probe different properties of the molecules and project the wave function of the system onto very different final state manifolds. Moreover, the photoionization process needs probe pulses far in the ultraviolet, which are difficult to generate with a suitably broad bandwidth and extreme time resolution.

To overcome this dilemma, we have developed a transient absorption spectrometer that extends this technique to low pressure gas phase samples. A low pressure situation is typical for samples of chemical interest, since the large mol-

<sup>a)</sup>Present address: Institut für Physik, Universität Rostock, Universitätsplatz 3, 18055 Rostock, Germany.

<sup>b)</sup>Author to whom correspondence should be addressed. Tel.: +49-89-2180-9210. FAX: +49-89-2180-9202. Electronic mail: riedle@physik.uni-muenchen.de.

ecules investigated possess a very low vapor pressure even at elevated temperature. Our instrument provides the required sensitivity and a time resolution suitable for observing coherent molecular wavepacket motions. The progress results from the combination of four strategies tackling different critical points of the experiment (see Sec. II). (i) A focusing geometry with a long Rayleigh range gives an optimized overlap of the pump and probe beams and a usable path length of 50 mm. (ii) An improved detection scheme and adapted amplification electronics allow us to observe changes in the absorbance down to  $1.1 \times 10^{-6}$ . (iii) A differentially pumped, heatable gas cell allows us to reach sufficiently high vapor pressures even for crystalline molecular substances. (iv) The high time resolution is achieved by using noncollinearly phase matched optical parametric amplifiers<sup>9-11</sup> (NOPAs) as sources of pump and probe pulses, which provide tunable sub-20-fs pulses over the full visible spectrum. Absorption bands of small and medium sized molecules, which are usually in the ultraviolet (UV) spectral region, can be addressed by sum frequency mixing or second harmonic generation without sacrificing time resolution.<sup>12</sup> As an example demonstrating the capabilities of this instrument, we present a comparison of the direct time-domain observation of the excited state intramolecular proton transfer (ESIPT) of 2-(2'-hydroxyphenyl)benzothiazole<sup>13</sup> (HBT) (i) in the gas phase and (ii) in cyclohexane solution (see Sec. III). The measurements in both phases have been performed immediately one after another by simply exchanging the sample cells. In both cases, the temporal overlap of the pump and probe (time zero) can be determined with a precision better than 5 fs. To the best of our knowledge these are the first transient absorption measurements in gas phase with a time resolution of 20 fs.

## II. DESIGN AND IMPLEMENTATION OF THE EXPERIMENTAL SETUP

### A. Required sample length

In this section we discuss the requirements for transient absorption measurements in the gas phase on medium sized molecules, such as organic molecules with three or four aromatic rings. We assume excitation densities well below saturation and the probe wavelength  $\lambda$  outside the absorption spectrum of the molecule. In the case of an optically thin sample with an optical density (OD) of  $OD_0(\lambda_{\text{pump}})$  at the pump wavelength  $\lambda_{\text{pump}}$ ,<sup>14</sup> the transient optical density change  $\Delta OD$  for the pump-probe signal can be approximated by

$$\Delta OD(\lambda, \tau) \propto \varepsilon^*(\lambda, \tau) OD_0(\lambda_{\text{pump}}) \Phi_{\text{pump}}, \quad (1)$$

where  $\varepsilon^*(\lambda, \tau)$  is the molar extinction coefficient of the molecules transferred by the pump pulse from the electronic ground state to some excited state and  $\Phi_{\text{pump}}$  is the fluence of pump photons per unit area.  $\varepsilon^*$  effectively describes electronic relaxation, chemical processes, vibronic wavepacket motion, and solvation. It typically depends on the probe

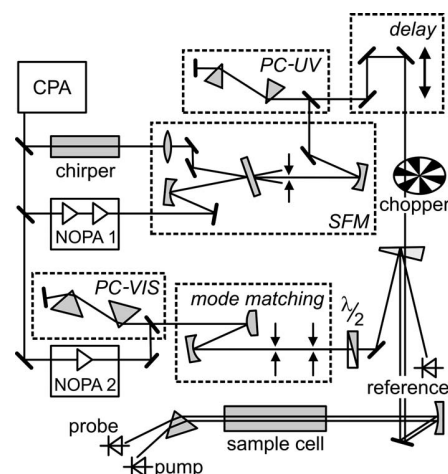


FIG. 1. Overview of the experimental setup.

wavelength  $\lambda$  and the pump-probe delay  $\tau$ . In the gas and solution phases, the effective  $\varepsilon^*$  is expected to be similar. For a molecule exhibiting an ultrafast reactive process, all lines will be homogeneously broadened and, in addition, the broad spectral width of the femtosecond pulse smoothens out any possible gas phase line structure. Therefore, to get the same pump-probe signal amplitude, the product of the sample optical density times the pump photon fluence has to be kept constant when going from the solution to the gas phase. For solution experiments,  $OD_0(\lambda_{\text{pump}})$  is typically 0.3 OD. The fraction of excited molecules  $\varepsilon \Phi_{\text{pump}}$  should be kept at or below the 5% level to avoid sequential multiphoton effects.  $\varepsilon$  is the molar extinction coefficient of the ground state molecules, which is typically comparable to  $\varepsilon^*$ . Taking the pump beam radius into account, this constraint eventually limits the pulse energy that can be used for the experiment. The maximum absorbance change that can be induced is thus typically 0.01 OD. Since a signal-to-noise ratio of 100:1 is desirable to characterize molecules exhibiting complex wavepacket dynamics,<sup>15</sup> a detection sensitivity of at least 100  $\mu OD$  is needed.

The substance HBT, which we use to demonstrate the performance of our setup, is crystalline at ambient temperature with vanishing vapor pressure. We performed a series of cw absorption measurements, showing that we need a sample length of 50 mm and a temperature of approximately 110 °C to get an optical density of 0.15. In secs. II C, II D, and II F, it is discussed in detail how these requirements can be fulfilled.

### B. Overview of the setup

A schematic of the experimental apparatus is shown in Fig. 1. The pump-probe spectrometer is based on two noncollinearly phase matched optical parametric amplifiers (NOPA 1 and NOPA 2) which generate tunable visible pulses with a bandwidth suitable for pulse durations down to 10 fs.<sup>9-11</sup> The laser source is a regenerative Ti:sapphire amplifier system (CPA 2001; Clark-MXR Inc.) delivering pulses at 1 kHz repetition rate with 775 nm center wavelength, 150 fs duration, and 950  $\mu J$  energy. A fraction of 220  $\mu J$  of the CPA pulses is used to pump each of the NOPAs. A vari-



able fraction of 60–100  $\mu\text{J}$  is split off for chirped sum frequency mixing (SFM) with the output of NOPA 1 to generate tunable UV pump pulses with energies up to 3  $\mu\text{J}$ .<sup>12</sup> The CPA pulses are stretched in a 70 mm long block of SF57 glass to a length of approximately 380 fs and focused by an  $f=200$  mm lens into a  $\beta$ -barium borate (BBO) crystal cut for type I phase matching. The NOPA 1 pulses are focused by an  $f=200$  mm spherical mirror into the SFM mixing crystal. For broadband UV spectra, a 60  $\mu\text{m}$  thick BBO crystal was used, whereas for high UV pulse energies, a 135  $\mu\text{m}$  BBO crystal was employed. In the latter case the bandwidth of NOPA 1 was limited to approximately one-half of the acceptance bandwidth of the crystal. Without sacrificing output power, the bandwidth of NOPA 1 can be easily decreased by chirping the continuum seed. To generate distinct NOPA spectra with a center wavelength between 700 and 740 nm and a bandwidth suitable for 30 fs, a glass block of 1 cm LF7 proved suitable. For the experiments presented below, pump center wavelengths of 325 and 350 nm are chosen according to the first absorption maximum of HBT and the half maximum in its red wing, respectively. However, it can be set anywhere in the spectral region between 285 and 375 nm,<sup>12</sup> which is particularly well suited to excite medium sized molecules. To compress the *s*-polarized UV pulses, they are sent through a sequence of two antireflection coated fused silica prisms with an apex angle of 45° (PC-UV). The transmission through the UV compressor is more than 90%.<sup>12</sup> A chopper is placed in the UV beam path to block every second pump pulse for a shot to shot referencing procedure. The arrival time of the pump pulse at the sample, and thereby the delay time between pump and probe pulse, is adjusted via a hollow retroreflector mounted on a motorized, computer controlled translation stage (delay) with a positioning accuracy and a reproducibility of 0.1  $\mu\text{m}$  (M-014.D01; Physik Instrumente GmbH) resulting in a 0.67 fs timing resolution. The maximum travel of the stage allows one to measure pump-probe delay times of up to 150 ps.

The pulses from NOPA 2 are used for transiently probing the molecular sample. A thin achromatic half-wave-plate for the visible (RAC 3.2.10L; B. Halle Nachf. GmbH) is used to rotate the polarization of the probe light and to measure the molecular dynamics under different polarizations. After transversing a standard double-pass prism compressor of fused silica Brewster prisms (PC-VIS), they are matched in diameter and convergence via a telescope and irises (mode matching) to the pump pulses to assure that the probe focus lies within the pumped volume of the sample (see Sec. II C). For a collinear propagation through the sample, the pump and probe beams are superimposed on a fused silica wedge which is transversed by the pump beam from the back. For the actual probing, only the front-side reflection of the visible NOPA beam is used. The back-side reflection is guided to a homebuilt photodiode module (see Sec. II D) to generate the reference signal. Pump and probe beam are focused into the sample cell by a spherical aluminum mirror with a focal length of 500 mm. A gas cell (see Sec. II F) and a flow cuvette can readily be exchanged and the dynamics in the gas phase and in solution can be measured in direct sequence without further changes to the setup. After the cell,

the beams are separated from each other by a fused silica Brewster prism. The transmitted energy of the probe beam is measured with a second photodiode module. This integral detection without wavelength dispersion results in an optimal time resolution and avoids signal contributions (coherent artifacts) during the temporal overlap of the pump and probe pulses that would mask the dynamics around time zero.<sup>16</sup> The pump energy, and thereby the synchronization signal for the shot to shot referencing procedure, is measured by a third photodetector. To determine the time zero of the pump and probe pulses, a difference frequency cross correlation is measured in a 10  $\mu\text{m}$  thick BBO crystal. A detailed description of the procedure is given in Sec. II G.

To record ultrafast wavepacket dynamics on a time scale up to 6 ps, the pump-probe delay is scanned with a constant step size of typically 3 or 5 fs. To measure short and long time scale dynamics within one scan, a linear-logarithmic time scale is applied. For pump-probe delays between  $-1$  and 1 ps, a constant step size is chosen, which is then exponentially increased such that the same number of data points is recorded between 0 and 1 ps as between 1 and 10 ps and so forth. The variation in the step size is smooth and continuous around 1 ps.

### C. Focusing geometry

For the following discussion we assume an ultraviolet pump and a visible probe beam.

To optimize the pump-probe signal, the waist of the probe beam in the sample should be definitely smaller than the waist of the excitation beam. In most femtosecond experiments in solution, the sample thickness is in the range of 50  $\mu\text{m}$  to 1 mm to avoid deterioration of the temporal resolution due to group velocity mismatch.<sup>17</sup> The pump radius at the focus is typically on the order of 50  $\mu\text{m}$  and the probe radius of 35  $\mu\text{m}$ . In this regime, the probe focus can be placed easily within the pumped volume; the whole sample lies within the Rayleigh range of the beams and the overlap is guaranteed over the total thickness [see Fig. 2(b)]. Due to much lower particle densities in the gas phase, the sample and the overlap region can be extended to several centimeters without loss of time resolution. Accordingly, the Rayleigh range has to be extended to the length of the sample [see Eq. (1)]. This results in larger focus diameters and a lower fluence of photons. To be able to optimize the setup for the pulse duration rather than for the pulse energy (see choice of SFM crystal discussed above), a minimal waist of the pump pulse has to be found, which results in a sufficiently long Rayleigh range and an adequate excitation density with moderate pulse energies [see Fig. 2(c)]. A suitable focusing geometry can be found with Fig. 2(a). The curves represent the combinations of Gaussian UV pump beam radii  $w_{\text{UV}}$  and probe radii  $w_{\text{vis}}$  at the focus for which the  $1/e^2$  border of the probe beam intersects the  $1/e^2$  border of the pump at the given distance  $z_X$  from the focus [see Fig. 2(b)]. The curves are labeled by the distance  $z_X$  in millimeters. Assuming Gaussian beams with  $M^2 > 1$  (Ref. 18) and  $w_{\text{vis}} < w_{\text{UV}}$ , the intersection distance  $z_X$  can be written as

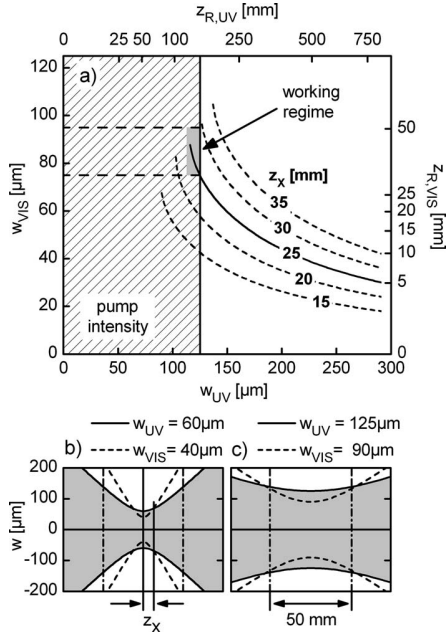


FIG. 2. (a) Focal radius  $w_{\text{vis}}$  of the visible probe beam and dependence on the focal radius  $w_{\text{UV}}$  of the UV pump beam according to Eq. (2) for  $\lambda_{\text{UV}} = 325$  nm,  $M_{\text{UV}}^2 = 1.7$  and  $\lambda_{\text{vis}} = 560$  nm,  $M_{\text{vis}}^2 = 1.4$ . The more tightly focused probe beam intersects the pump beam at a distance  $z_X$  that is given in millimeters as a label on the curves.  $z_{R,\text{vis}}$  and  $z_{R,\text{UV}}$  are the Rayleigh lengths of the pump and the probe beam. The region with a pump radius below  $125 \mu\text{m}$  is hatched and the parameter space used in the experiment is in gray. (b) Focusing geometry typically for solution experiments. (c) Focusing geometry used in the gas phase experiment.

$$z_X = \pi \sqrt{\frac{w_{\text{UV}}^2 w_{\text{vis}}^4 - w_{\text{UV}}^4 w_{\text{vis}}^2}{\lambda_{\text{UV}}^2 M_{\text{UV}}^4 w_{\text{vis}}^2 - \lambda_{\text{vis}}^2 M_{\text{vis}}^4 w_{\text{UV}}^2}}. \quad (2)$$

In Fig. 2 the pump wavelength  $\lambda_{\text{UV}}$  is set to 325 nm and the probe wavelength  $\lambda_{\text{vis}}$  to 560 nm. According to the experiment, the beam quality parameters  $M_{\text{UV}}^2$  and  $M_{\text{vis}}^2$  were set to 1.7 and 1.4, respectively. Within a region extending over  $2z_X$  around the focus, the probe beam is smaller than the pump. The Rayleigh lengths of the pump  $z_{R,\text{UV}}$  and probe  $z_{R,\text{vis}}$  beams which depend quadratically on the focal beam radius<sup>9</sup> can also be read from the diagram [Fig. 2(a)]. The hatched area in Fig. 2(a) indicates the region for which the focal pump radius is below  $125 \mu\text{m}$ . The gray area in the figure indicates the actual parameter region of the experiment. It shows that with a pump radius of  $125 \mu\text{m}$ , we can achieve intersection distances up to 30 mm, and thereby overlap regions up to 60 mm by choosing a focal probe radius of about  $95 \mu\text{m}$ . The quite large focal radii call for a weak focusing regime which was implemented with a focal length of 500 mm (see Sec. II B). The focusing geometry and beam quality parameters were verified with a beam camera. The  $M^2$  values are in good agreement with parameters found previously for NOPA beams.<sup>9</sup>

From Eq. (1) it follows that the pump energy  $E_{\text{pump}} \propto \Phi_{\text{pump}}(w_{\text{UV}})^2$  in the gas phase experiment should be chosen such that the fluence of pump photons is the same as for the solution phase focusing geometry. The increase of the focal diameter by a factor of 2.5 implies an increase of the pump

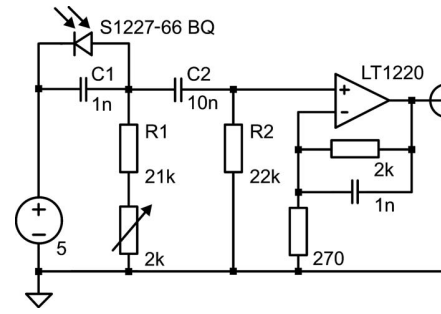


FIG. 3. Schematic circuit of the homebuilt photodetector.

energy by a factor of 6, yielding an absolute value of 450–500 nJ at the sample, which is readily achievable.

#### D. Photodetectors and data acquisition

For the highest possible detection sensitivity of the transmission changes, the pulse energies of the probe and the reference beam are measured with two matched homebuilt photodetectors. The probe and reference pulse energies are typically 5–10 nJ; thus the detectors are designed to allow the direct measurement of pulse energies up to 2 nJ. In the experiment, the pulses are only slightly attenuated by suitable optical filters. At 500 nm, the 2 nJ correspond to  $5 \times 10^9$  photons and a shot noise limit of  $1.7 \times 10^{-5}$  results (a typical photodiode quantum efficiency is  $\sim 70\%$ ). Assuming a Gaussian spatial profile, the  $1/e^2$  beam diameter of the pulses on the photodiode should be at least three times smaller than the dimension size of the active area to detect the pulse energy with an accuracy of more than  $10^{-5}$ . On the other hand, the input pulses should not be focused too tightly onto the detector to avoid local saturation.

A schematic of the amplifier circuit is shown in Fig. 3. It transforms the photogenerated charge into a voltage at the 1 V level and leads to a signal duration long enough for an accurate analog-to-digital conversion (ADC) without the need for a boxcar integrator or a sample and hold unit. A large area ( $5 \times 5 \text{ mm}^2$ ) photodiode (S1227-66BQ; Hamamatsu Photonics K.K.) is reversely biased with 5 V. Even for this large area photodiode, the dark current (25 pA) on the time scale of the output signal ( $50 \mu\text{s}$ ) is orders of magnitude below the shot noise limit of the probe pulses. The charge carriers generated instantaneously by the laser pulse in the photodiode are stored on the internal capacitance of the diode and on the capacitor  $C_1$  connected in parallel, resulting in a total capacitance of 2 nF. For a pulse energy of 1 nJ, the charge generated on the photodiode corresponds to 150 mV, which is well below the bias voltage and even the bandgap of silicon. The capacitance is discharged via  $R_1$  and  $R_2$  in parallel, giving a time constant of  $22 \mu\text{s}$ . A trim potentiometer connected in series to  $R_1$  allows to precisely match the time constants of two detectors. The ac coupling via  $C_2$  reduces the influence of background cw light. The voltage drop across  $R_2$  is amplified by a factor of 8.4 with an operational amplifier (LT1220; Linear Technology Corp.). Here any amplifier which has a low input offset voltage and a low input bias current can be chosen. The gain is rolled off at 50 kHz with an RC low pass circuit in the feedback loop.

The detector output signal is linear to the input pulse energy up to 1 V output. The two detectors for signal and reference pulses, terminated with 50  $\Omega$ , are sampled by a two channel, 14 bit, high speed digitizer (NI 5122; National Instruments) over a period from 20  $\mu\text{s}$  before to 80  $\mu\text{s}$  after the laser pulse at a sampling frequency of 10 MHz, i.e., a 0.1  $\mu\text{s}$  spacing. The baseline is determined from the first 20  $\mu\text{s}$  and subtracted from the subsequently sampled points. The signal is then integrated from 3 to 40  $\mu\text{s}$  after the laser pulse, giving a numerical value proportional to the pulse energy. This procedure eliminates baseline problems, reduces high frequency noise by a factor of 10, and gives an effective 14 bit resolution.<sup>20</sup> For a single dark channel, we find shot to shot standard deviations of  $5 \times 10^{-5}$ . The photodiode detecting the pump pulse is read synchronously with a second ADC board (PCI-MIO-16E4; National Instruments).

### E. Data processing and noise suppression

The noise observed in a pump-probe spectrometer consists of three main components: laser excess noise, shot noise, and electronic noise of the detectors and the data acquisition device. The latter two contributions have been addressed in the preceding section. We will now show that the laser excess noise is the dominant part, and therefore discuss in detail our measures to decrease the influence of the laser fluctuations.

The output of a NOPA can have intensity noise as low as the pump laser (typically around 1% rms) if the amplification is driven properly into saturation.<sup>10</sup> The UV pump pulse generated in the SFM process has about twice the noise of the pump laser. Although in principle it should be possible to eliminate laser excess noise for the probe pulse by normalizing it to the reference channel, in practice it is difficult to reach the shot noise limit. Experimentally, we find that our shot to shot referencing procedure reduces the estimate for the normalized standard deviation (rms noise) by a factor of  $\beta=25$  (data not shown) and thus the laser excess noise remains the dominant noise source.

An analysis of the fluctuations of the laser system can help optimize the data acquisition and processing strategy. For kilohertz ultrafast laser systems, they are not purely statistical but typically dominated by low frequency contributions.<sup>21</sup> A signal processing that simply sums over a finite number of consecutive shots cannot average sufficiently over these frequencies. However, the dominant low frequency components imply that consecutive laser shots are strongly correlated.

We consider the normalized noise  $\{n_i\}$  given by the deviation  $n_i = (E_i - \langle E \rangle_N) / E_{\text{rms}}$  of the individual pulse energy from the average as displayed in Figs. 4(a) and 4(b) on a short and a long time scale.  $E_i$ ,  $i=1, \dots, N$ , are successively recorded pulse energies, and  $\langle E \rangle_N$  denotes the average and  $E_{\text{rms}}$  the quadratic mean value. For our laser system, the standard deviation of the normalized noise is in the long time limit less than 0.01, i.e., 1% rms. The Fourier transformation of the ensemble shown in Fig. 4(b) is displayed in Fig. 4(d). Figure 4(c) shows a scatter density plot of  $n_i$  vs  $n_{i+1}$  indicating a strong linear correlation between successive

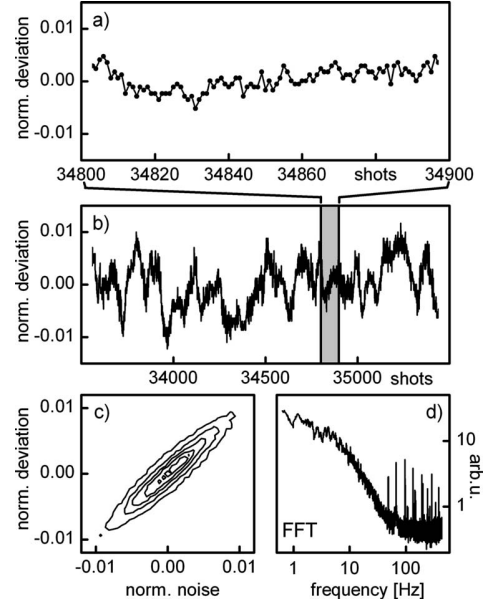


FIG. 4. Normalized shot to shot deviation of the pump laser system over (a) 0.1 s and (b) 5 s. (c) Scatter density plot of the pulse energy deviation vs energy deviation of the consecutive shot. (d) Fourier transform of the data shown in (b) plotted on a log-log scale.

pulses. The Pearson product moment correlation function  $r = \text{cov}(n_i; n_{i+1}) / \text{var}(n_i)$  (Ref. 22) is well suited to analyze our data and a perfect correlation would yield a value of +1 while a perfect anticorrelation would render  $-1$ . For our pump laser system we typically find a value of  $r > 0.93$ .

The high shot to shot correlation is exploited by a shot to shot referencing method with the pump beam blocked for every second laser shot (see Sec. II B). At one shot the probe signal (sig) and reference signal (ref) are recorded for the excited sample ( $\text{sig}_{2i}^*$ ,  $\text{ref}_{2i}^*$ ) and at the next shot without excitation ( $\text{sig}_{2i+1}^0$ ,  $\text{ref}_{2i+1}^0$ ). The signals for  $N$  pairs of laser shots are measured for every delay time  $\tau$  between the pump and probe, where typical values of  $N$  are 300–500. From these numbers, the excitation induced transmission change  $\Delta T$  is calculated relative to the transmission without excitation ( $T_0$ ):

$$1 + \frac{\Delta T(\tau)}{T_0(\tau)} = \left\langle \frac{\text{sig}_{2i}^*}{\text{ref}_{2i}^*} \right\rangle_N \left\langle \frac{\text{sig}_{2i+1}^0}{\text{ref}_{2i+1}^0} \right\rangle_N^{-1}, \quad (3)$$

$$\Delta \text{OD}(\tau) = -\log \left[ 1 + \frac{\Delta T(\tau)}{T_0(\tau)} \right]. \quad (4)$$

The difference in optical density  $\Delta \text{OD}$  can be computed with Eq. (4) from the normalized difference transmission signal given by Eq. (3). For the sufficiently small changes in the transmission observed in these studies,  $\Delta \text{OD}$  can be approximated quite well by

$$\Delta \text{OD} = -\frac{(\Delta T/T_0)}{\ln(10)} = -\frac{(\Delta T/T_0)}{2.3026}. \quad (5)$$

For further elucidation of the influence of the laser noise on the signal noise, we let  $P_i = P_0(1+n_i)$  and  $Q_i = Q_0(1+m_i)$  be the probe and pump pulse energies for the  $i$ th laser shot of the experiment, suffering from the normalized noises  $n_i$  and

$m_i$ , respectively. From Eq. (1) it follows for small signals that the pump induced transmission change of the sample is linear in the pump energy  $\Delta T_i \propto Q_i$ . Then the signal detected by the probe photodiode  $\text{sig}_{2i}^* \propto P_{2i}(T + \Delta T_{2i})$  can be expressed as

$$\text{sig}_{2i}^* \propto P_0 T(1 + n_{2i}) + P_0 \Delta T(1 + n_{2i} + m_{2i} + n_{2i} m_{2i}) \quad (6)$$

for the excited sample and as

$$\text{sig}_{2i+1}^0 \propto P_0 T(1 + n_{2i+1}) \quad (7)$$

for the sample without excitation (after Ref. 23). The reference channel suffers from a slightly different noise  $n'_i$ :  $\text{ref}_i^{0,*} \propto P_0(1 + n'_i)$ . With  $\delta_{2i} = (n_{2i} - n'_{2i}) - (n_{2i+1} - n'_{2i+1})$ , Eq. (3) can be rewritten to first order in terms of noise as

$$1 + \frac{\Delta T(\tau)}{T_0(\tau)} = 1 - \langle \delta_{2i} \rangle_N + \frac{\Delta T(\tau)}{T_0(\tau)} (1 + \langle m_{2i} \rangle_N - \langle \delta_{2i} \rangle_N). \quad (8)$$

Since  $\langle \delta_{2i} \rangle_N$  is a difference between different detectors and consecutive laser shots, it can be assumed to be mostly uncorrelated to  $\langle m_{2i} \rangle_N$ . The standard deviation for the pump-probe signal is thus given by

$$\hat{\sigma} \left[ \frac{\Delta T(\tau)}{T_0(\tau)} \right]^2 \approx \hat{\sigma}(\langle \delta_{2i} \rangle_N)^2 + \frac{\Delta T(\tau)}{T_0(\tau)} [\hat{\sigma}(\langle m_{2i} \rangle_N)^2 + \hat{\sigma}(\langle \delta_{2i} \rangle_N)^2]. \quad (9)$$

The second term  $\hat{\sigma}(\langle \delta_{2i} \rangle_N)$  determines the detection sensitivity whereas  $\hat{\sigma}(\langle m_{2i} \rangle_N)$  limits the signal-to-noise ratio of the transient transmission measurement. In the case of large transient transmission signals, the transmission change should be corrected for the pump noise. This can be done by dividing  $\Delta T(\tau)/T_0(\tau)$  by the ratio of the pump pulse energies averaged over the data point for the delay  $\tau$  and the long term average of the pump pulse energies.

We next want to go one step further and obtain an analytical expression for  $\hat{\sigma}(\langle m_{2i} \rangle_N)$  and  $\hat{\sigma}(\langle \delta_{2i} \rangle_N)$ . It can be shown that  $\hat{\sigma}(n_{2i} - n_{2i+1})^2 \approx 2(1-r)\hat{\sigma}(n)^2$  and therewith  $\hat{\sigma}(\delta_{2i})^2 \approx \beta^{-2}2(1-r)\hat{\sigma}(n)^2$ . From the shot to shot correlation  $r$ , the simplest estimate for a correlation over a  $k$ -shot distance is  $r^k$ . Using this relationship, one can estimate the correlation  $\text{cov}(\delta_{2i}; \delta_{2j}) \approx r^{|2j-2i|} \text{var}(\delta_{2i})$  and obtain a closed form expression for the total correlation within the sample. This gives an upper estimate for the standard deviations in Eq. (9):

$$\hat{\sigma}(\langle \delta_{2i} \rangle_N)^2 \leq \frac{2}{N} \frac{1+r^2}{1+r} \beta^{-2} \hat{\sigma}(n)^2, \quad (10)$$

$$\hat{\sigma}(\langle m_{2i} \rangle_N)^2 \leq \frac{1}{N} \frac{1+r^2}{1-r^2} \hat{\sigma}(m)^2. \quad (11)$$

With  $N=500$ ,  $\beta=25$ ,  $r=0.9$ ,  $\hat{\sigma}(n)=0.01$ , and  $\hat{\sigma}(m)=0.02$ , Eqs. (10) and (11) can be evaluated to  $\hat{\sigma}(\langle \delta_{2i} \rangle_N) = 2 \times 10^{-5}$  and  $\hat{\sigma}(\langle m_{2i} \rangle_N) = 3 \times 10^{-3}$ .

Comparing these values to the ones obtained experimentally (see Sec. III C), it can be seen that the probe induced noise as well as the signal-to-noise ratio match within a factor of 2. The following relation becomes apparent: When employing a shot to shot referencing procedure, a high shot to shot correlation is obviously advantageous for the referencing. On the other hand, a high correlation over many laser

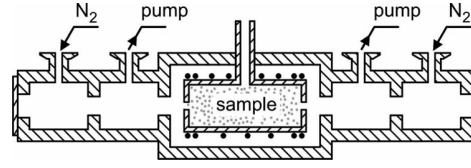


FIG. 5. Heatable gas cell with entrance and exit windows protected by a  $N_2$  gas flow.

shots reduces the number of uncorrelated shots in the sample, and averaging over the sample is less effective. For the probe induced noise [see Eq. (10)] these two effects fairly cancel out  $[(1+r^2)/(1+r) \approx 1]$ , whereas the pump induced noise [see Eq. (11)] is only reduced by the effective number of uncorrelated laser shots in the sample, which is about 10% of  $N$  since  $(1+r^2)/(1-r^2) \approx 10$ . This dilemma can be avoided by a fast scanning measurement scheme.<sup>24</sup> Our apparatus will be augmented in this way in the future.

In summary, the estimation in this section and the preceding one shows that the fluctuations and, in particular, the correlations of pump and probe pulses are the limiting factors for the signal-to-noise ratio and the sensitivity of the transient absorption signal. The detector shot noise and the precision of the data acquisition only contribute a small fraction. Therefore efforts aimed at reducing the laser noise will directly lead to a further improvement of the described setup.

## F. Gas cell

Medium sized molecules are typically obtained as crystalline samples at room temperature and have to be heated to achieve reasonable vapor pressures. If this is done in a cell, some of the substance condenses on the walls and windows and forms a thin layer. At the points where the light beams enter or exit the cell, they interact with this layer and eventually destroy the molecules. Since the molecules on the windows are immobile, the effect accumulates quickly and opaque spots appear that absorb the pump energy. We were not able to prevent this from happening by differentially heating the windows.

To circumvent this problem, a heatable gas cell has been constructed with windows protected by an inert gas flow (see Fig. 5). The cylindrical glass cell containing the sample is placed within an aluminum casing. Holes of 1.5 mm in diameter are drilled through the middle of the cell windows so the light beams can enter and exit the cell without passing through glass, and thereby through a layer of sample substance. A few windings of heating tape are wrapped around the cell and temperatures of up to 150 °C can be readily achieved. An extra winding of the heating tape is placed near each window to heat them slightly more than the central part of the glass cell. This prevents molecules from occluding the holes.

The light beams enter the aluminum casing via 1 mm thick fused silica windows at the endings of two 100 mm long tubes. A baffle with a 4 mm hole separates each tube into two chambers. The outer chamber is flushed with dry nitrogen from a cylinder while the inner one is pumped. In this way, a constant flow of nitrogen is adjusted through the baffle which efficiently keeps sample molecules from diffus-

ing to the windows and condensing there. The cell is operated at a pressure around 2 mbars, which is about ten times higher than the vapor pressure of the sample to avoid pumping a significant amount of sample out of the cell. Under these conditions the mean time between collisions is well above 10 ns, which is a factor of 100 longer than the time scale we examine with our pump-probe experiments.

### G. Determination of time zero

Especially for ultrafast processes, the exact onset of the pump induced photochemical reaction contains valuable information and should be determined as precisely as possible. To do so, we measure alternately (i) the cross correlation between pump and probe pulses in a 10  $\mu\text{m}$  thin BBO crystal and (ii) a short scan of the molecular dynamics around time zero. From consecutive measurements of the cross correlations, one can determine (see below for necessary corrections) the time zero during the actual molecular experiment. We find that the time zero drifts between consecutive measurements are less than 2 fs. Proper interpolation makes this small effect negligible.

A number of precautions have to be taken to ensure the desired precision in the determination of time zero.

- (1) All cross correlation measurements are performed with the crystal placed at the same physical position (focus) where the centers of the gas cell and flow cuvette are during the experiment.
- (2) To actually measure the cross correlation, the sample cell is replaced by a compensation window of the same material and nominal thickness as the entrance window of the cell. This window accounts for the dispersion and group velocity mismatch (GVM) of the pump and probe in the front cell window. The GVM is  $\sim 250$  fs/mm for fused silica. The dispersion influences the achieved temporal resolution and the compressors are adjusted accordingly.
- (3) The cross correlation determined by (2) has to be corrected for the difference in thickness of the compensation window and the cell window and for half the GVM induced by the sample.
- (4) To measure the difference in thickness of the compensation window and the sample cell entrance window, the cell is disassembled and only the front window is placed into the beam path. Alternate cross correlations with the cell window and the compensation window are then performed as described above. We found that the compensation window used for measurements with the gas cell introduces 20.3 fs more group delay than the sample cell window. In the case of the solution cell, the compensation is 3.8 fs too small (for 325 nm pump and 595 nm probe, see Fig. 6).
- (5) In experiments performed with the gas cell, the GVM of the pump and probe half way through the evacuated cell is smaller than through the additional air, which the beams transverse when the cell is taken out for cross correlation measurements. The shift of time zero due to the evacuation of the cell has been determined experimentally. For the experiments presented in Fig. 6, we

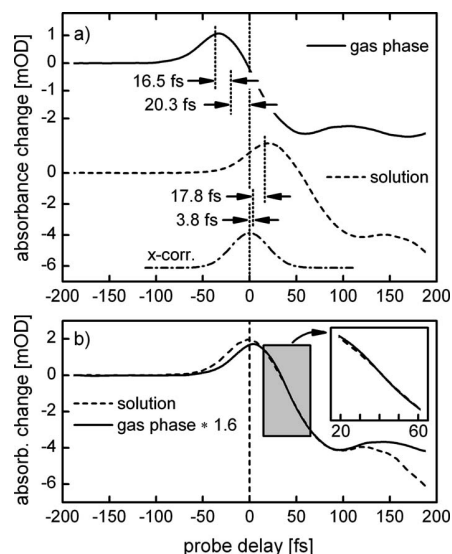


FIG. 6. (a) Initial dynamics of HBT in the gas phase and in solution compared to cross correlation measurements (dash-dotted line) with compensation window. The needed corrections to the time zero are indicated (for details see text). (c) Fully corrected dynamics of HBT in the gas phase and in solution. The rise of the emission occurs in both cases at the same delay time.

found that the cross correlation is shifted by 33 fs to smaller delays by evacuation of the cell. Since only half of the cell length enters into the spectroscopic measurement, we obtain a correction value of 16.5 fs.

- (6) For the solution experiments, the GVM of half of the thickness of the sample is computed from GVM data for solvents determined in our laboratory.<sup>17</sup> The flow cuvette used for the experiment presented in Sec. III has an optical path length of 120  $\mu\text{m}$ . For a layer of 60  $\mu\text{m}$  of cyclohexane, we obtain a cross correlation shift of 17.8 fs to later times for the wavelengths given above.

Although individual cross correlation measurements can be performed with a precision of better than 2 fs, due to concatenation of measurements the final accuracy is approximately 5 fs.

Figure 6(a) shows the initial dynamics for HBT measured in the gas phase and in solution. The cross correlation measurement obtained with the respective compensation window is taken as time zero [see dash-dotted line in the lower part of Fig. 6(a)]. As indicated, the gas phase signal appears too early and the solution phase one too late. The contributions to the deviation discussed above are shown to scale in the figure.

In Fig. 6(b) the experimental curves for HBT in the gas phase and in solution are displayed with proper correction of time zero. It turns out that within the precision of the measurement, the initial rise of the emission is in both cases equally fast. From such an observation we can deduce a detailed model of the influence of the solvent environment on the primary dynamics of the excited state intramolecular proton transfer.

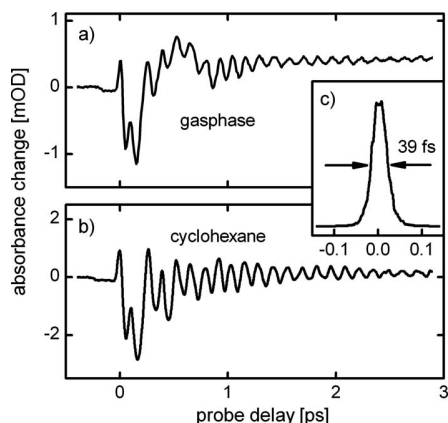


FIG. 7. Time dependent transient absorption of HBT (a) in the gas phase and (b) dissolved in cyclohexane, both probed at 490 nm. (c) Pump-probe cross correlation of 39 fs.

### III. PERFORMANCE OF THE SPECTROMETER: ULTRAFAST EXCITED STATE INTRAMOLECULAR PROTON TRANSFER

#### A. Transient absorption spectroscopy of 2-(2'-hydroxyphenyl)benzothiazole

As a first experiment with the new gas phase pump-probe spectrometer, the ultrafast intramolecular proton transfer in HBT is investigated. The process occurs on a time scale of 50 fs and is associated with rich wavepacket dynamics.<sup>7,13,25</sup> Since the transient absorption of HBT in the nonpolar and inert solvent cyclohexane is very well characterized,<sup>13,15</sup> a comparison to the transient absorption in the gas phase is ideal to identify gas phase specific features for the process. Here some results are presented to document the performance of the spectrometer. A detailed discussion of the molecular dynamics will be presented elsewhere.

Figure 7 shows a comparison of transient absorption curves of HBT in the gas phase and in cyclohexane solution excited at 325 nm and probed at 490 nm. The measured cross correlation was 39 fs and the UV pulses had an energy of 450 nJ. The gas cell was heated to  $\sim 110$  °C. To switch between the gas phase and solution experiments, the gas cell is replaced by a flow cuvette with an optical path length of 120  $\mu\text{m}$  and a 200  $\mu\text{m}$  thick fused silica entrance window. Additionally a compensation window is inserted in the beam to account for the different thicknesses of the gas and flow cell windows. Since no other adjustments are necessary, the setup is optimally suited to compare directly the dynamics in the gas phase and in the condensed phase. The solution measurements are in excellent agreement with previous experiments performed on a liquid jet.<sup>13</sup> The results show that the pump-probe spectrometer allows for the precise measurement of complex ultrafast dynamics in the isolated as well as in the soluted molecule.

#### B. Temporal resolution

The cross correlation trace presented in Fig. 7 has a width full width at half maximum of 39 fs. A conservative analysis shows that processes which are as fast as 20 fs can be reliably detected with deconvolution techniques or by fit-

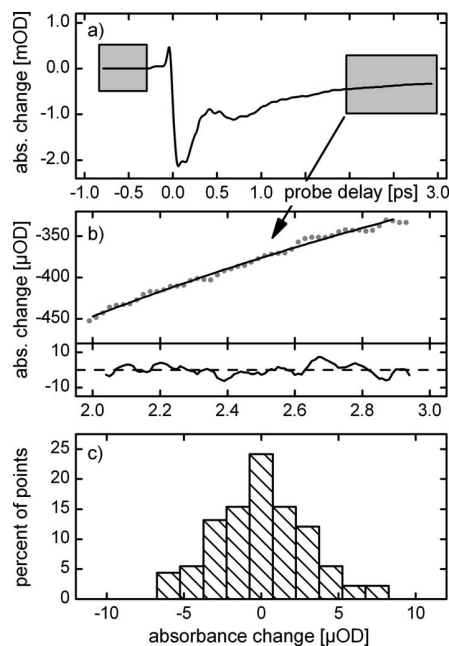


FIG. 8. Determination of the experimental noise: (a) Time trace of HBT in the gas phase measured at 350/570 nm. (b) Approximation of the data (dots) with a multiexponential decay (solid line) and noise contribution to the data obtained by subtracting the model function from the measured data. (c) Histogram of the noise with a standard deviation of  $2.9 \times 10^{-6}$  OD.

ting a model function that takes the cross correlation into account to the data. The achieved time resolution is also suitable to observe coherent motions in skeletal modes of molecules. These are seen as the oscillating signal contributions in both recordings shown in Fig. 7. In the first picoseconds they are dominant over the more common exponential signal decays. In the present configuration, the UV pump pulse with a length of 30 fs is mainly responsible for the cross correlation width. In the SFM process the spectral phase of the visible input beam is linearly transferred to the UV.<sup>26</sup> It is therefore possible to correct for higher order spectral phase distortions with chirped mirrors or adaptive optics in the visible beam path. This should allow for UV pump pulses with durations in the order of 10 fs,<sup>27</sup> further improving the time resolution by a factor of 4. It has already been demonstrated that the tuning range of the probe pulses can be readily extended into the near infrared while maintaining the time resolution.<sup>8</sup>

#### C. Sensitivity, signal-to-noise ratio, and dynamic range

To verify the sensitivity under realistic conditions and to determine the minimal detectable absorbance change, the noise of a typical pump-probe trace of HBT in gas phase is analyzed in Fig. 8. Five successive scans with an excitation wavelength of 350 nm and a probe wavelength of 570 nm were performed. Each data point of each scan is computed from 421 pairs of laser shots with and without excitation. The scan is recorded with a time step of 5 fs between successive data points. Afterward, the scans are averaged and the resulting curve is smoothed by adjacent averaging of five data points, corresponding to less than the ratio of the cross

correlation width over the time step, and thereby not deteriorating the temporal resolution. A statistical analysis of the signal before time zero returns a standard deviation, i.e., a detection sensitivity of the instrument of  $1.1 \times 10^{-6}$  OD, meaning that changes in the absorbance down to almost 1  $\mu$ OD can be detected on the  $1\sigma$  level. This is two orders of magnitude or more better than previous work; even so much less pump pulse energy is used.<sup>28,29</sup> The corresponding shot noise limit is less than a factor of  $\sim 10$  lower. With a maximum reasonable absorption change of 0.05 OD, the dynamic range, i.e., the ratio of the largest over the smallest detectable absorbance change within one scan is 45 000:1. For a pure exponential decay this would mean that it can be observed over ten decay time constants.

For the analysis of the signal after time zero, a multiexponential decay model function is fitted to a part of the measured trace which is expected to be a smooth decay without oscillatory contributions [see Fig. 8(b)]. Subtracting the fitted model function from the measured data gives the deviation of the measured data points from the smooth decay [see Fig. 8(b), lower panel] which can be identified to a good approximation with the noise of the data. Figure 8(c) shows a histogram of the deviations which exhibit roughly a Gaussian distribution. The standard deviation  $\sigma$  of the noise accounts to  $2.9 \times 10^{-6}$ . In addition to the fundamental noise of the setup, determined from the analysis of the data before time zero, the noise of the pump pulse is superimposed on the signal after time zero. Assuming that the noise components are independent, it can be computed to  $2.7 \times 10^{-6}$ . A detailed analysis of measurement traces at different signal amplitudes shows that the pump noise scales fairly linearly with the signal amplitude. This is in good agreement with the theory presented in Sec. II E. Comparing the pump noise to the average signal of  $0.36 \times 10^{-3}$  in the regime analyzed above, this gives a signal-to-noise ratio of 43 dB (140:1). The high signal-to-noise ratio allows us to detect weak oscillatory contributions to the signal, as they can originate from coherent nuclear wavepacket dynamics, and to observe these oscillations that typically decay faster than the population over a longer time scale, and thus determine frequency and damping time more accurately. The detection scheme presently does not correct for the fluctuations of the pump light. Precisely measuring the pump pulse energy and implementing such a correction might well push the signal-to-noise ratio up to 50 dB (300:1).

The demonstrated extremely high sensitivity and signal-to-noise ratio together with the superior temporal resolution allow for the first time the direct comparison of the ultrafast dynamics of chemical reactions proceeding in the isolated gas phase and in solution. It should therefore help further our fundamental understanding of the various contributions to the processes. Furthermore we believe that the setup does

allow the measurement of dynamics in single molecular layers which are most important in the rapidly developing field of molecular electronics and organic light emitting diodes.

## ACKNOWLEDGMENTS

This work was supported by the Austrian Science Fund within the framework of the Special Research Program F16 (Advanced Light Sources) and by the DFG-Cluster of Excellence: Munich-Centre for Advanced Photonics. D.J.N. would like to gratefully acknowledge support from the National Science Foundation and the Alexander von Humboldt Foundation.

- <sup>1</sup>A. H. Zewail, *J. Phys. Chem. A* **104**, 5660 (2000).
- <sup>2</sup>J. L. Herek, W. Wohlleben, R. J. Cogdell, D. Zeidler, and M. Motzkus, *Nature (London)* **417**, 533 (2002).
- <sup>3</sup>T. Brixner and G. Gerber, *ChemPhysChem* **4**, 418 (2003).
- <sup>4</sup>C. M. Tesch and R. de Vivie-Riedle, *J. Chem. Phys.* **121**, 12158 (2004).
- <sup>5</sup>T. Baumert, M. Grosser, R. Thalweiser, and G. Gerber, *Phys. Rev. Lett.* **67**, 3753 (1991).
- <sup>6</sup>S. Lochbrunner, J. J. Larsen, J. P. Shaffer, M. Schmitt, T. Schultz, J. G. Underwood, and A. Stolow, *J. Electron Spectrosc. Relat. Phenom.* **112**, 183 (2000).
- <sup>7</sup>A. J. Wurzer, S. Lochbrunner, and E. Riedle, *Appl. Phys. B: Lasers Opt.* **71**, 405 (2000).
- <sup>8</sup>C. Manzoni, D. Polli, and G. Cerullo, *Rev. Sci. Instrum.* **77**, 023103 (2006).
- <sup>9</sup>T. Wilhelm, J. Piel, and E. Riedle, *Opt. Lett.* **22**, 1494 (1997).
- <sup>10</sup>E. Riedle, M. Beutter, S. Lochbrunner, J. Piel, S. Schenkl, S. Spörlein, and W. Zinth, *Appl. Phys. B: Lasers Opt.* **71**, 457 (2000).
- <sup>11</sup>G. Cerullo and S. De Silvestri, *Rev. Sci. Instrum.* **74**, 1 (2003).
- <sup>12</sup>I. Z. Kozma, P. Baum, S. Lochbrunner, and E. Riedle, *Opt. Express* **11**, 3110 (2003).
- <sup>13</sup>S. Lochbrunner, A. J. Wurzer, and E. Riedle, *J. Phys. Chem. A* **107**, 10580 (2003).
- <sup>14</sup>We use the following definition of the optical density:  $OD = -\log_{10}(E_T/E_0)$ , with  $E_0$  the energy of the incident light pulse and  $E_T$  the transmitted energy.
- <sup>15</sup>S. Lochbrunner and E. Riedle, in *Recent Research Developments in Chemical Physics*, Vol. 4, Part I, edited by S. G. Pandalai, Transworld Research Network, Trivandrum, 2003, p. 31.
- <sup>16</sup>K. Ekvall, P. van der Meulen, C. Dhollande, L.-E. Berg, S. Pommeret, R. Naskrecki, and J.-C. Mialocq, *J. Appl. Phys.* **87**, 2340 (2000).
- <sup>17</sup>I. Z. Kozma, P. Krok, and E. Riedle, *J. Opt. Soc. Am. B* **22**, 1479 (2005).
- <sup>18</sup>A. E. Siegman, *Proc. SPIE* **1224**, 2 (1990).
- <sup>19</sup>A. E. Siegman, *Lasers* (University Science Books, Mill Valley, CA, 1986).
- <sup>20</sup>C. M. Lovejoy and D. J. Nesbitt, *J. Chem. Phys.* **86**, 3151 (1987).
- <sup>21</sup>D. von der Linde, *Appl. Phys. B: Photophys. Laser Chem.* **39**, 201 (1986).
- <sup>22</sup>W. Mendenhall and T. Sincich, *Statistics for Engineering and the Sciences*, 3rd ed. (MacMillan, London, 1988).
- <sup>23</sup>J. A. Moon, *Rev. Sci. Instrum.* **64**, 1775 (1993).
- <sup>24</sup>M. J. Feldstein, P. Vöhringer, and N. F. Scherer, *J. Opt. Soc. Am. B* **12**, 1500 (1995).
- <sup>25</sup>S. Lochbrunner, K. Stock, and E. Riedle, *J. Mol. Struct.* **700**, 13 (2004).
- <sup>26</sup>C. Schrieffer, S. Lochbrunner, M. Optiz, and E. Riedle, *Opt. Lett.* **31**, 543 (2006).
- <sup>27</sup>P. Baum, S. Lochbrunner, and E. Riedle, *Appl. Phys. B: Lasers Opt.* **79**, 1027 (2004).
- <sup>28</sup>T. R. Gosnell, A. J. Taylor, and J. L. Lyman, *J. Chem. Phys.* **94**, 5949 (1991).
- <sup>29</sup>H.-Y. Chen, I.-R. Lee, and P.-Y. Cheng, *Rev. Sci. Instrum.* **77**, 076105 (2006).





## Anhang 5

### **"Direct Observation of the Nuclear Motion during Ultrafast Intramolecular Proton Transfer"**

S. Lochbrunner, C. Schrieffer, and E. Riedle

in *Hydrogen-Transfer Reactions*, J. T. Hynes, J. P. Klinman, H.-H. Limbach,  
and R. L. Schowen, (Eds.), Wiley-VCH, Weinheim, pp. 349 – 375 (2006).

The full article can be obtained from the Wiley web site, or by using the DOI.

DOI: 10.1002/9783527611546.ch11



## Anhang 6

**"Can multidimensional wave packet dynamics be distinguished from tunneling?"**

C. Schrieffer, S. Lochbrunner, A. Ofial, and E. Riedle

Manuskript vorbereitet zur Einreichung an Phys. Rev. Lett. (2008)



## Can multidimensional wave packet dynamics be distinguished from tunneling?

C. Schrieber,<sup>1</sup> S. Lochbrunner,<sup>2</sup> A. Ofial,<sup>3</sup> and E. Riedle<sup>1,\*</sup>

<sup>1</sup>*Fakultät für Physik, Ludwig-Maximilians-Universität, Oettingenstr. 67, 80538 München, Germany*

<sup>2</sup>*Institut für Physik, Universität Rostock, Universitätsplatz 3, 18055 Rostock, Germany*

<sup>3</sup>*Department Chemie, Ludwig-Maximilians-Universität, Butenandt-Str. 11, 81377 München, Germany*

We investigate the reaction kinetics of ultrafast excited state intramolecular proton transfer (ESIPT) and discuss the kinetics of the process in terms of tunneling of the reactive proton, vibrational enhanced tunneling, and multidimensional wave packet dynamics of the entire system. Comparing the experimental results to numerical simulations allows us to ascribe the time constant of the ESIPT solely to a ballistic wavepacket motion of the molecule along skeletal coordinates that mainly affect the donor acceptor distance. Tunneling is not significantly involved.

PACS numbers: 82.39.Jn, 78.47.J-, 82.20.Tr, 82.53.\_k

Multidimensional dynamics involving several degrees of freedom simultaneously is a key aspect in understanding complex systems. It is very important and at the same time challenging to identify the mechanisms and parameters that determine the evolution of such a process. Here we consider the evolution of a wavepacket on a multidimensional potential energy surface which results in a photochemical reaction. Since a light hydrogen atom is involved the contribution of tunneling processes is highly likely. Barrier tunneling in multidimensional systems is a widespread phenomenon in molecular dynamics [1], however theoretically hard to tackle [2,3] leading to models with reduced dimensionality [4]. We discuss the interplay between the tunneling process and the multidimensional motion of the heavy atoms and tackle the question if an unambiguous signature of the tunneling process can be expected and its relevance for the dynamics can be determined from the deuterium isotope effect on the wavepacket evolution.

To experimentally elucidate if a multidimensional reaction path involving the rearrangement of molecular subcomponents can solely account for the kinetics of a chemical reaction, we choose the ESIPT model system 2-(2'-hydroxyphenyl)benzothiazole (HBT; see Fig. 1a) and tried to experimentally exclude a tunneling contribution to the ESIPT kinetics. ESIPT systems are especially suited to investigate the dynamics of hydrogen bonds since they provide a well defined reactant geometry and the PT can be triggered by photoexcitation with an ultrashort laser pulse resulting in a high time resolution [5]. For proton transfer (PT) in the electronic ground state it has been shown that the reaction mechanism is dominated by tunneling and largely depends on the separation of the proton donor and acceptor [6]. Deuterium isotope effects of 10 or larger have been reported. In many biological systems, temperature dependent proton transfer rates are observed. Even in the case of ultrafast excited state intramolecular proton transfer (ESIPT) with a PT time of typically a few tens of femtoseconds [7], the delay in product formation cannot solely be

accounted for by a simple switching of electronic orbitals. Various models have been discussed in the literature to explain the ESIPT time. They basically fall into two classes: (i) The reactant and the product tautomer are separated by an energy barrier on the reactive potential energy surface (PES). The tunneling of the proton through this barrier determines the speed of the transfer [8] (Fig. 1b). (ii) The ESIPT proceeds as a ballistic wavepacket motion along an essentially barrierless reaction path (Fig. 1c). An initial gating motion which comprises skeletal deformations leading to a reduction of the donor acceptor distance and the ESIPT time is given by the inertia of the heavy heteroatoms [7]. As a combination of (i) and (ii) there exists a variety of models where heavy atom vibrational effects [4,9] or solvent fluctuations [10] modulate the barrier and thus enhance the rates of the proton tunneling. The thermochemical classification in terms of ‘diabatic’ and ‘adiabatic’ proton transfer [11] applies to these pictures as follows. In case (i) the barrier splits the PES into an educt and product well with localized diabatic states, which are then coupled by the proton

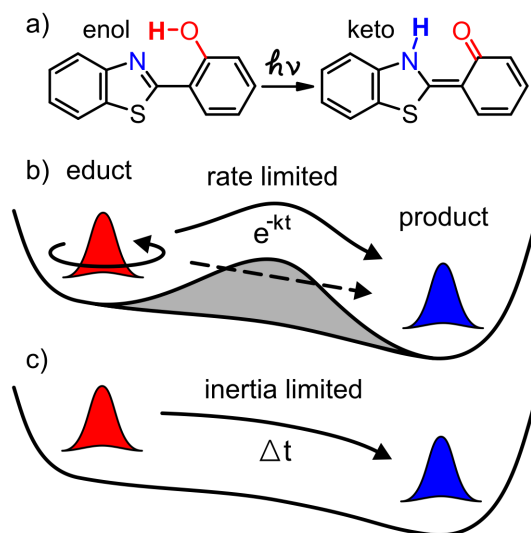


FIG. 1 (color online). (a) ESIPT of HBT. (b) Model PES for tunneling process. (c) Model PES for inertia limited process.

motion (diabatic PT). In case (ii) the high frequency quantum proton vibration adiabatically adjusts smoothly to the shifting proton potential as the backbone geometry changes (adiabatic PT).

We therefore perform a direct comparison of the ESIPT dynamics in HBT and deuterated HBT (DBT) where the reactive hydrogen atom is replaced by deuterium as suggested in ref. 12. If tunneling of the proton is relevant to the reaction kinetics, the larger mass of the deuterium should significantly increase the PT time. We discuss which changes in the kinetics are expected if tunneling is relevant for the transfer time. Then experimental results are presented which are obtained by transient absorption spectroscopy with a time resolution of 20 fs. From the comparison we finally conclude on the relevance of tunneling in ESIPT.

The expected effect of deuteration upon the ESIPT is estimated quantitatively as follows. In case the reactive coordinate is the position  $r$  of the proton along the equilibrium positions when bound to O and N, respectively (cf. Fig. 2), and the reaction path exhibits a substantial energy barrier, we can apply a one dimensional semiclassical model [9]. The transfer rate constant  $k$  out of the metastable enol into the bound keto state is calculated by Eq. (1) [13]. The semiclassical tunneling times [14,15] for the proton and deuterium are neglected, since they only contribute  $\sim 3$  fs and  $\sim 6$  fs, respectively.

$$k_x = \nu_x \exp[-S_x/\hbar] \quad (1)$$

$$S_x = 2(2m_x)^{1/2} \int dr \cdot (V(r) - E_x)^{1/2}$$

$\nu_x$  is the vibrational frequency of the local OH (OD) mode with  $x = H, D$ ,  $S_x$  the semi-classical action for a barrier penetration,  $m_x$  the mass of the hydrogen nucleus,  $V$  the potential barrier and  $E_x$  the energy of the proton in the educt well. Deuteration should reduce the transfer rate due to three effects: (i) The frequency  $\nu$  of the local stretch vibration is reduced by a factor of  $\sqrt{2}$ , (ii) the mass  $m$  of the tunneling particle doubles, and (iii) the zero point energy is reduced by a factor of  $\sqrt{2}$  resulting in an

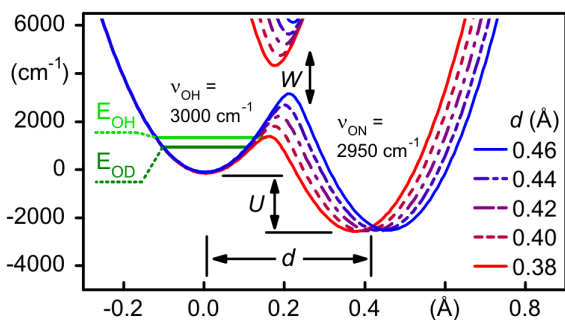


FIG. 2 (color online). Model potential as given by Eq. (2) for different separations  $d$  of the OH and ON local potential wells. Horizontal lines indicate the zero point energies of the proton and the deuterium in the OH educt well.  $U$ :  $2434 \text{ cm}^{-1}$ ,  $W$ :  $1500 \text{ cm}^{-1}$ .

effectively higher and broader barrier (see Fig. 2). Considering only the first two effects a proton transfer rate  $k_H = (50 \text{ fs})^{-1}$  should reduce upon deuteration to  $k_D = (131 \text{ fs})^{-1}$ . To take effect (iii) into account we follow the approach of Arthen-Engeland et al. [16] and design a model potential with the reactive coordinate being that of the mobile proton. A one dimensional potential energy surface  $V$  is obtained by coupling the two adiabatically interacting harmonic oscillator potentials of the enolic OH ( $\nu_{OH} = 3000 \text{ cm}^{-1}$ ) and ketonic NH stretch vibration ( $\nu_{NH} = 2950 \text{ cm}^{-1}$ ) [17]:

$$V = \frac{1}{2}(V_{OH} + V_{NH}) - \left[ \frac{1}{4}(V_{OH} - V_{NH})^2 + W^2 \right]^{1/2}$$

$$V_{OH} = \frac{1}{2}m_{OH}(2\pi \cdot \nu_{OH})^2 \cdot r^2 \quad (2)$$

$$V_{NH} = \frac{1}{2}m_{NH}(2\pi \cdot \nu_{NH})^2 \cdot (r-d)^2 + U$$

$W = 1500 \text{ cm}^{-1}$  [16] is the coupling matrix element,  $U = 2434 \text{ cm}^{-1}$  [18] the internal reaction energy and  $d$  the translocation distance of the proton. To obtain  $k_H = (50 \text{ fs})^{-1}$ ,  $d$  is set  $0.432 \text{ \AA}$ . With the given parameters the deuterium transfer rate is  $k_D = (306 \text{ fs})^{-1}$ . The change of the zero point energy leads to a pronounced additional decrease of the deuterium transfer rate. The value for the separation of the enolic and ketonic hydrogen equilibrium positions  $d$  obtained above is significantly smaller than recent geometry optimizations for HBT in the excited enol state reveal [18]. We therefore modify our model to account for two dimensional tunneling by allowing heavy atom vibrations [9,16,19]. According to ref. [18] an initial separation  $d = 0.8 \text{ \AA}$  is chosen. The translocation distance is then modulated periodically from the initial separation to a minimum  $d_{min}$ , mimicking the classical motion of a harmonic ON stretch vibration with the frequency  $\nu_{ON}$ . For the motion of heavy heteroatoms this is a quite good approximation. The transferred population  $p_x$  is computed by Eq. (3).

$$p_x(t) = 1 - \exp\left(-\int_0^t k_x(t') dt'\right) \quad (3)$$

Since the tunneling rate  $k_x$  strongly depends on the translocation distance  $d$ , the transfer dynamics is dominated by the ON vibration. Population transfer takes place virtually only nearby the inner turning point. For the given parameters and a minimal distance  $d_{min} = 0.377 \text{ \AA}$  the barrier for PT just vanishes at the turning point and 83 % of the protons are transferred within the first approach.  $\nu_{ON}$  is set  $254 \text{ cm}^{-1}$  according to the dominant oscillation frequency observed in the transient absorption experiments of HBT (see below). Fig. 3 shows the time dependent population in the educt state for this model. The inner turning point is then reached after  $\sim 50$  fs and the population transfer rate is maximal. For deuterons a drastic change of the dynamics is predicted. With the used parameters only 39 % of the

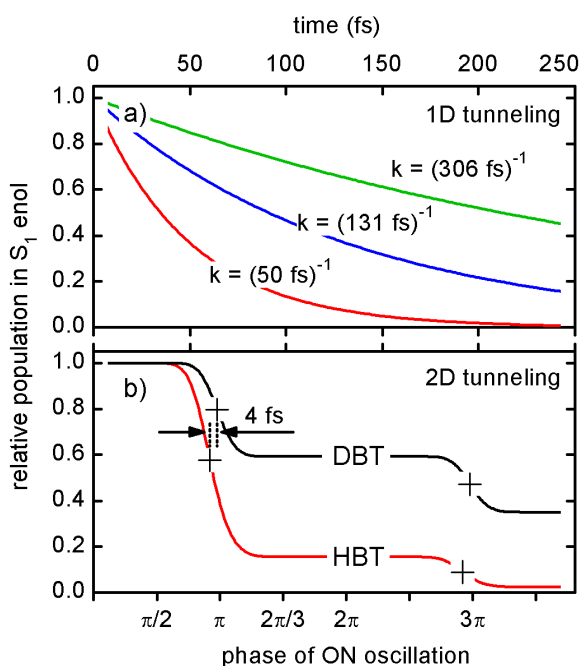


FIG. 3 (color online). (a) Population transfer in the one-dimensional model for several rate constants discussed in the text. (b) Time dependent population in the enol form calculated by a two dimensional transfer model for DBT (solid line) and HBT (dashed line).

deuterons are transferred within the first approach and at least two steps are necessary till most of the deuterated molecules are in the keto form (see Fig. 3). The center of the transfer steps for HBT and DBT are only separated by 4 fs. Thus for the 2D model no change in the initial rise time of the experimental keto\* signal would be expected for HBT and DBT, but in the case of DBT a pronounced second step should appear after  $\sim 195$  fs.

Increasing  $d_{min}$  results in a higher barrier and more than one ON approach is needed to transfer most of the protons. This would be an intermediate situation between the one dimensional model and the two dimensional case, and deuteration would lead to an even more pronounced multi-step like transfer than shown in Fig. 3. A further decrease of  $d_{min}$  reduces the barrier below the zero point energy of the proton in the enol form and results in a reaction path without a significant barrier.

For an examination of the models discussed above the following experiment was performed. HBT was deuterated in a mixture of  $\text{CDCl}_3$  and  $\text{D}_2\text{O}$  to a degree of  $> 99\%$  (for NMR data and details of the procedure see [20]). For the time-resolved pump-probe measurements, a 2 mM solution of the ESIPT molecules in cyclohexane (Merck, UVASOL) was prepared resulting in absorption of about 50 % of the pump light. For the measurements with DBT, the cyclohexane was previously saturated with  $\text{D}_2\text{O}$  to avoid H/D-exchange by residual  $\text{H}_2\text{O}$  traces in the solvent. After the pump-probe measurements, the degree of deuteration was  $> 65\%$ . The decrease is

mostly due to the recovery of the DBT from the sample for the characterization. It can therefore be assumed that during the pump-probe experiments  $> 80\%$  of the phenolic protons were exchanged for deuterium. As shown in [20], this is more than sufficient to detect an increase in the PT rate to  $(131 \text{ fs})^{-1}$  which is the most conservative estimation if tunneling is significantly involved. In fact, our measurements and analysis allow us to detect a change in the PT time constant of 10 fs (cf. Table 1S [20]).

A detailed description of the pump probe setup is given elsewhere [5]. Briefly, a fully tunable two color pump probe spectrometer based on two noncollinear optical parametric amplifiers (NOPAs) provides 35 fs long UV pump pulses at a center wavelength of 350 nm and 20 fs long probe pulses at around 500 nm. The pulses are focused into a flow cell with a channel thickness of 120  $\mu\text{m}$ . The transmitted probe light is measured with and without prior excitation and the relative transmission change is recorded as a function of the pump-probe delay time. The HBT and DBT samples are measured in direct succession.

We observe for DBT the same characteristic features of an ultrafast ESIPT as for HBT (Fig. 4a). The agreement between the DBT trace measured at 505 nm and the HBT trace measured at 502 nm is almost perfect (see Fig. 4). The agreement between traces measured at slightly different wavelengths for DBT and HBT can be explained by a small red shift of the emission of the DBT keto form compared to HBT (cf. Fig. 1S [20]). All time traces show an initial transmission decrease at time zero due to excited state absorption, contributing as soon as the molecule is in the  $S_1$  state. The subsequent transmission recovery and increase reflects the emission rise caused by the appearance of the electronically excited keto form. The short but distinct delay of about 50 fs is identified as the transfer time [5]. This delay is within the experimental precision of 5 fs the same for both HBT and DBT (see Fig. 4 b and c). The subsequent oscillations of the transmission signals are the signature of molecular vibrations coherently excited by the transfer (cf. Fig. 2S). They, too, do not change upon deuteration, neither in frequency nor in phase. Two dominant in-plane modes at  $113 \text{ cm}^{-1}$  and  $255 \text{ cm}^{-1}$  can be identified with normal modes from ab-initio calculations [5]. The slower one modulates the donor acceptor distance by a bending motion of the whole molecule while the second one changes this distance by a stretch motion of the complete skeleton.

We do not observe a delayed rise of the keto emission of DBT with respect to the rise for HBT contrary to the predictions of the one dimensional tunneling model (comp. Fig. 3S). There are also no indications that for DBT a second step of population transfer to the keto form appears as it is predicted by the two dimensional model assuming a significant barrier (comp. Fig. 3). This demonstrates that in both HBT and DBT no significant barrier exists for the

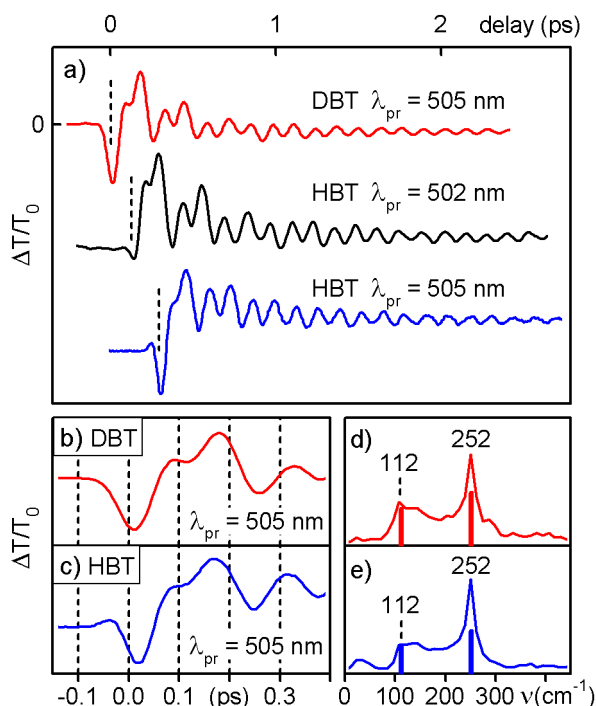


FIG. 4 (color online). (a) Time dependent transmission change of DBT measured at 505 nm probe wavelength and of HBT measured at 502 nm and at 505 nm. (b),(c) Enlarged view of initial ES IPT dynamics. (d), (e) Fourier transform spectra corresponding to (b) and (c), respectively.

ES IPT. We accordingly conclude that the ES IPT dynamics in HBT is a ballistic wavepacket motion along skeletal coordinates which involves a pronounced motion of the heavy atoms and leads to an efficient reduction of the donor acceptor distance. When this distance is short enough an electronic configuration change takes place and the bonds of the electronically excited product are formed. Thus the frequencies of the promoting normal modes, i.e. the inertia of the heavy atoms, dominate the ES IPT time. The findings can be cast into the two dimensional model if the contributing skeletal modes are combined to an effective coordinate and the transfer barrier at the turning point is located below the zero point energy of the proton and deuteron.

The results are not specific to HBT, however, in slightly larger molecules temperature dependent ES IPT rates and deuterium isotope effects have been reported. However previous investigations inferred deuterium isotope effects from fluorescence quantum yields, absorption line widths or transient absorption measurements with a time resolution slower than the ES IPT time [21]. We observe for the first time the effect of deuteration upon the ES IPT in real time and unambiguously see no change in the dynamics. The presented comparison between the model predictions and the measured kinetic traces shows that the coherent wavepacket motion provides clear observable signatures on the relevance of tunneling processes. We think the methodology can be applied to a wide range of ultrafast processes, for which

tunneling is discussed, and expect from its application a reliable identification of the relevant mechanisms.

Recent experimental and theoretical results on the ES IPT of 10-hydroxybenzo[h]quinoline (HBQ) [22], a molecule similar to HBT, but with a more rigid molecular skeleton and higher energetic normal modes, show that the ES IPT in HBQ follows the same mechanism, but the ES IPT time is about a factor of 2 shorter, corresponding to the higher frequencies of the promoting modes, supporting the wavepacket picture of the ES IPT.

Financial support by the German Science Foundation is gratefully acknowledged. We are thankful to Kai Stock and Brigitte Janker for support in the experiments.

\*Electronic address: riedle@physik.uni-muenchen.de

- [1] W. H. Miller, *Faraday Discuss. Chem. Soc.* **110**, 1 (1998).
- [2] K. Takahashi, and K.S. Ikeda, *Europhys. Lett.* **71**, 193 (2005).
- [3] S. Wiggins, L. Wiesenfeld, C. Jaffé, and T. Uzer, *Phys. Rev. Lett.* **86**, 5478 (2001).
- [4] A. Douhal, F. Lahmani, and A. H. Zewail, *Chem. Phys.* **207**, 477 (1996).
- [5] S. Lochbrunner, A. J. Wurzer, and E. Riedle, *J. Phys. Chem A* **107**, 10580 (2003)
- [6] C. Alhambra, M.L. Sanchez, J. Corchado, J.L. Gao, D.G. Truhlar, *Chem. Phys. Lett.* **355**, 388 (2002).
- [7] S. Lochbrunner, C. Schrieffer, and E. Riedle, in *Hydrogen-Transfer Reactions*, J. T. Hynes, J. P. Klinman, H.-H. Limbach, and R. L. Schowen, eds. (Wiley-VCH, Weinheim, 2006), 349.
- [8] A. N. Bader, V. G. Pivovarenko, A. P. Demchenko, F. Ariese, and C. Gooijer, *J. Phys. Chem. B* **108**, 10589 (2004).
- [9] D. Borgis and J. T. Heynes, *J. Phys. Chem.* **100**, 1118 (1996).
- [10] D. C. Borgis, S. Lee, and J. T. Heynes, *Chem. Phys. Lett.* **162**, 19 (1989).
- [11] B. Cohen, and D. Huppert, *J. Phys. Chem A* **105**, 2980 (2001).
- [12] A. Douhal, *Science* **276**, 221 (1997).
- [13] R. I. Cukier and J. Zhu, *J. Chem. Phys.* **110**, 9587 (1999).
- [14] E. H. Hauge, and J. A. Stovngren, *Rev. Mod. Phys.* **61**, 917 (1989).
- [15] M. Büttiker, and R. Landauer, *Phys. Rev. Lett.* **49**, 1739 (1982).
- [16] Th. Arthen-Engeland, T. Bultmann, N. P. Ernsting, M. A. Rodriguez and W. Thiel, *Chem. Phys.* **163**, 43 (1992).
- [17] T. Elsaesser and W. Kaiser, *Chem. Phys. Lett.* **128**, 231 (1986).
- [18] R. de Vivie-Riedle, V. De Waele, L. Kurtz, and E. Riedle, *J. Phys. Chem. A* **107**, 10591 (2003).
- [19] M. E. Tuckerman, and D. Marx, *Phys. Rev. Lett.* **86**, 4946 (2001).
- [20] See Supplementary Material.
- [21] W. Frey, F. Laermer, and T. Elsaesser, *J. Phys. Chem.* **95** (1991) 10391.
- [22] C. Schrieffer, M. Barbatti, K. Stock, A.J.A. Aquino, D. Tunega, S. Lochbrunner, E. Riedle, R. de Vivie-Riedle, and H. Lischka, *Chem. Phys.* (2007), doi:10.1016/j.chemphys.2007.10.021.



# Can multidimensional wave packet dynamics be distinguished from tunneling?

## Supplementary Material

*Christian Schrieffer<sup>a</sup>, Stefan Lochbrunner<sup>a</sup>, Armin Ofial<sup>b</sup>, and Eberhard Riedle<sup>a\*</sup>*

*<sup>a</sup>Department für Physik – Ludwig-Maximilians-Universität (LMU)*

*Oettingenstr. 67, 80538 München, Germany*

*<sup>b</sup>Department Chemie – Ludwig-Maximilians-Universität (LMU)*

*Butenandt-Str. 11, 81377 München, Germany*

\* corresponding author:

Phone: +49-89-2180-9210

Fax: +49-89-2180-9202

e-mail: [riedle@physik.uni-muenchen.de](mailto:riedle@physik.uni-muenchen.de)

In the following additional information are given on the steady state spectroscopy of HBT and DBT, the mechanism regarding the generation of signal oscillations by coherently excited vibrational modes, the sensitivity of the experiment regarding the degree of deuteration, and the preparation and characterization of the deuterated samples.

## Steady State Spectra and Mechanism of Oscillatory Signal Contributions

For 2-(2'-hydroxyphenyl)benzothiazole (HBT) in the electronic ground state the enol-form with the hydrogen atom bound to the donor oxygen of the H-chelate ring is the stable tautomer. If the molecule is promoted to the  $S_1$  electronic state, the hydrogen atom of the hydroxy group is transferred to the nitrogen atom. The excited state intramolecular proton transfer (ESIPT) leads to a strong Stokes shift between the UV absorption of the  $S_0$  enol-form and the  $S_1$  keto fluorescence at  $\sim 525$  nm. (see Fig. 1S). In protic solvents like ethanol, hydrogen bonds to the solvent can be formed, and the H-chelate ring breaks up. The intermolecular hydrogen bond inhibits the ESIPT and leads to a stabilization of the  $S_1$  enol form and to  $S_1$  enol fluorescence at  $\sim 380$  nm [1]. The traces of  $D_2O$  in cyclohexane that are needed to stabilize the deuteration of DBT lead in a small fraction of DBT molecules to the this effect (see Fig.1S). Assuming fluorescence quantum yields for the  $S_1$  enol ( $\phi_e=0.02$ ) and keto ( $\phi_k=0.002$ ) tautomer as reported for ethanol solution [Pot94], we estimate the fraction of molecules with a hydrogen bond to the solvent to  $< 2\%$ . Hence, their influence on the transient spectra can be neglected.

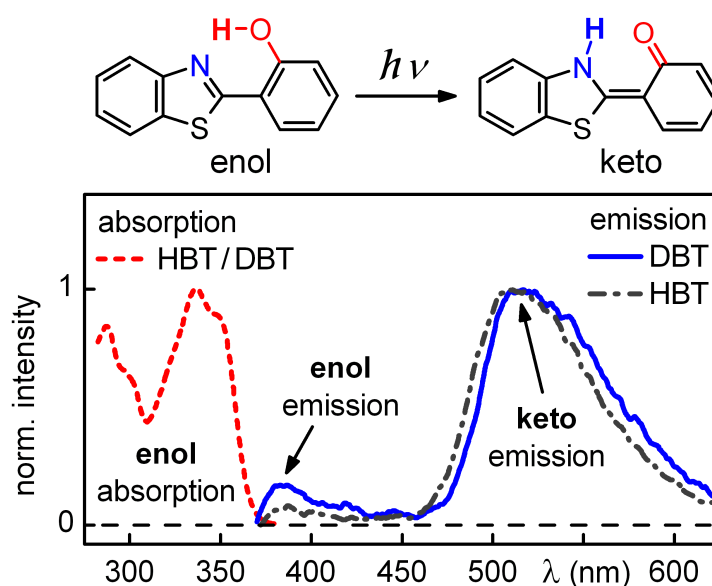


Fig. 1S: ESIPT scheme and steady state absorption (dashed line) and fluorescence spectra of HBT in cyclohexane (dash-dotted line) and fluorescence spectra of DBT in  $D_2O$  saturated cyclohexane (solid line)

The keto peak of the DBT fluorescence spectrum is slightly red shifted with respect to the HBT spectrum by  $\sim 4$  nm. This could be caused by the deuteration itself or the different polarity of the  $D_2O$  saturated cyclohexane. In time resolved measurements at a certain probe wavelength, the shift of the fluorescence spectrum results in a somewhat different

contributions of the stimulated emission to the transients for HBT and DBT. A transient recorded for HBT in cyclohexane at 500 nm probe wavelength should rather be compared to a transient recorded for DBT in D<sub>2</sub>O saturated cyclohexane at 504 nm.

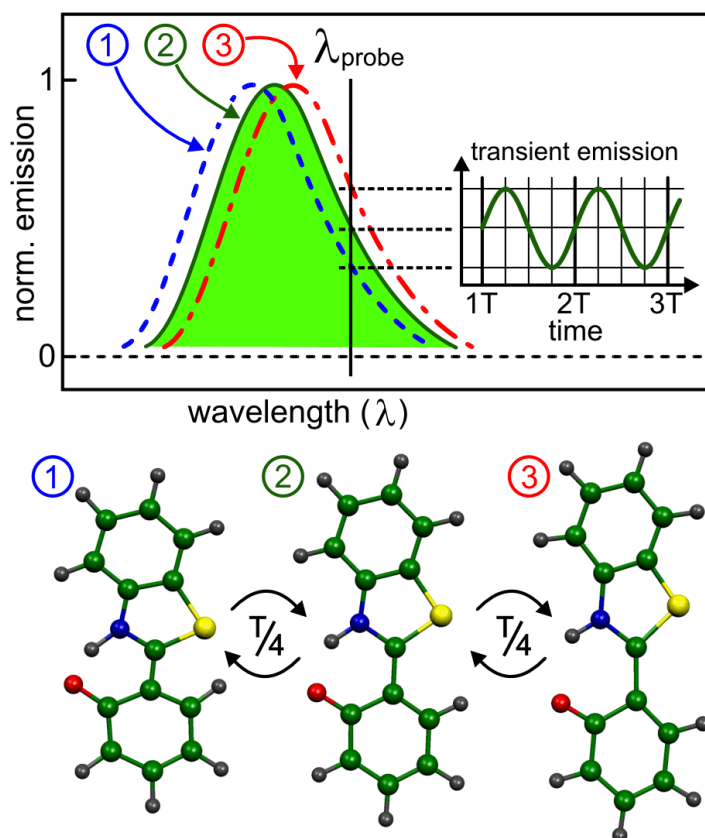


Fig. 2S: An oscillating wavepacket leads to periodic variations of the mean transition energy between two electronic states and thereby to an oscillatory shift of the spectrum. The amplitude of the oscillating signal is proportional to the slope of the spectrum.

The oscillatory signal contributions are due to vibrational wavepacket motions in the electronically excited product state and allow to identify the participating normal modes. As long as a wavepacket motion is observed the vibrational phase is still quite well defined. Although the electronic phase is scrambled in solution within some 10 fs due to the interaction with the solvent, the vibrational dephasing time is typically on the order of 1 ps. The vibrational wavepacket motion leads to a periodic variation of the optical transition energy and to an oscillatory spectral shift of the S<sub>1</sub> emission and the transient S<sub>n</sub>-S<sub>1</sub> absorption spectra as it is depicted in Figure 2S. It causes the characteristic oscillation of the HBT emission spectrum shown in Figure 3S. The amplitude of the oscillatory signal contributions has a dependence on the probe wavelength which reflects the slope of the emission spectrum.

The observation of the oscillatory signal contributions indicates that the oscillations are coherently excited in the ensemble of probed molecules.

## Estimation of the Experimental Sensitivity on the Degree of Deuteration

In the comparative time resolved measurements on 2-(2'-hydroxyphenyl)benzothiazole (HBT) and the deuterated form with the phenolic proton exchanged by deuterium (DBT), the degree of deuteration of DBT is not 100 % for reasons outlined below. The following estimation shall show what degree of deuteration is needed to see a difference in the transient transmission signals for HBT and partially deuterated HBT, i.e. mixtures of HBT and DBT, in case tunneling of the proton determines the transfer time. A model function  $f_H$  (based on Ref. 2) which accounts for an exponential population transfer from the enol to the keto configuration and subsequent oscillatory contributions is fitted to transient transmission data of HBT measured at 502 nm in cyclohexane. In this model a transfer rate of  $k_H = (\tau_H)^{-1} = (50 \text{ fs})^{-1}$  is obtained. The raw data and the fit are shown in Fig. 3S a). A model  $f_D$  for a tunneling dominated DBT time trace is generated by changing the transfer rate to  $k_D = (\tau_D)^{-1}$ . Since the low frequency oscillations in the data result from skeletal vibrations [2], their frequencies should not be altered significantly upon the deuteration. For partially deuterated DBT the experimentally determined transient transmission change is a superposition of signals from HBT and DBT. For a degree of deuteration  $p$  the expected trace  $f_p$  is obtained from the two traces  $f_H$  and  $f_D$  via

$$f_p = (1-p) \cdot f_H + p \cdot f_D.$$

For  $k_D = (131 \text{ fs})^{-1}$  and  $p = 0.5$  the mixed trace  $f_{0.5}$  is plotted in comparison to  $f_H$  and  $f_D$  in Fig. 3S b). Compared to pure HBT, the difference in the transfer time constants can clearly be seen by eye and re-fitting of  $f_{0.5}$  with the model function gives an effective rate of  $(74 \text{ fs})^{-1}$ . The re-fitting corresponds to the evaluation procedure applied to the experimental data. With a crosscorrelation of 40 fs and an experimental precision of 3 fs for time zero, a change of 10 fs in the proton transfer time constant should be unambiguously detectable. This is clearly the case for the parameters assumed in this example.

A more systematic investigation of the relationship between  $k_D$  and the degree of deuteration needed in the experiment to unambiguously prove the tunneling nature of the transfer is given in Tab. 1S. It can be seen that for the most conservative estimate of the deuterium transfer rate constant of  $k_D = (131 \text{ fs})^{-1}$  obtained in the main text, a degree of deuteration above 30 % should be sufficient to see a change in the experimentally determined rate. For a degree of

deuteration of 80 % (see below) we are able to see an effect on the experimentally determined rate if the deuterium transfer time constant  $\tau_D$  is 65 fs or longer (see Tab. 1S).

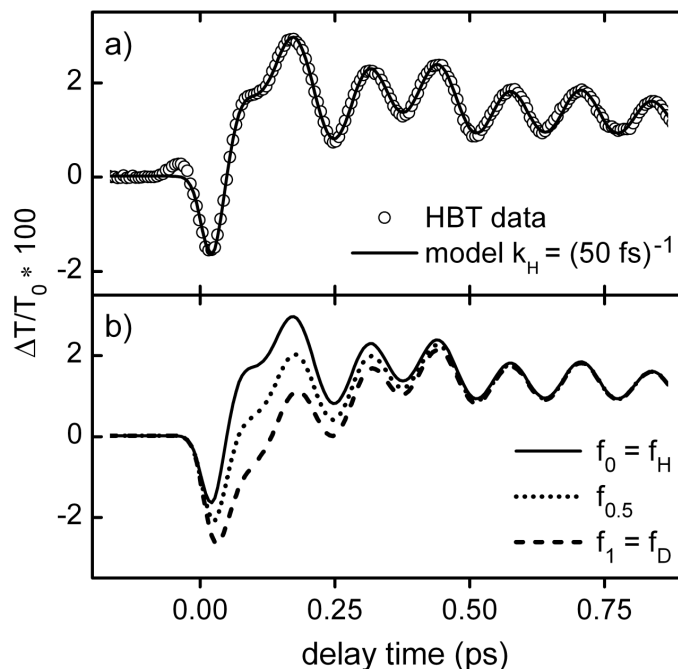


Fig. 3S: a) Transient transmission of HBT for  $\lambda_{\text{pump}} = 347 \text{ nm}$  and  $\lambda_{\text{probe}} = 502 \text{ nm}$  (open circles). Modeling of the HBT data with a function that has a 50 fs exponential rise for emission and oscillatory contributions (solid line) b) Simulations of the transient transmission for pure DBT (dashed line) and a 0.5:0.5 mixture of DBT and HBT are compared to pure HBT (solid line).

$\tau_D$	expected transfer time (fs)						
	p = 0.2	p = 0.3	p = 0.4	p = 0.5	p = 0.6	p = 0.7	p = 0.8
60 fs	52	53	54	55	56	57	58
65 fs	53	54	56	57	59	<b>60</b>	<b>62</b>
70 fs	53	55	57	59	<b>61</b>	<b>63</b>	<b>65</b>
80 fs	55	57	<b>60</b>	<b>63</b>	<b>66</b>	<b>69</b>	<b>73</b>
95 fs	56	<b>60</b>	<b>64</b>	<b>68</b>	<b>72</b>	<b>77</b>	<b>83</b>
110 fs	57	<b>61</b>	<b>66</b>	<b>71</b>	<b>77</b>	<b>84</b>	<b>91</b>
131 fs	57	<b>62</b>	<b>68</b>	<b>74</b>	<b>82</b>	<b>91</b>	<b>101</b>

Table 1S: Expected transfer times obtained by modeling time traces for samples with a DBT fraction p and a transfer time  $\tau_D$  for DBT and 50 fs for HBT. A transfer time of 60 fs or more would have been detected as a reduction of the transfer rate upon deuteration.

## Sample Preparation and Characterization of the Deuteration Degree

Deuteration of HBT can only be performed efficiently in a solvent with solubility both for water and HBT. However the time resolved experiments need to be performed in an aprotic, water free solvent [2,3]. This imposes the pursued procedure outlined in the following. HBT is deuterated in a chloroform solution, then recovered from chloroform, dissolved in cyclohexane for the transient absorption measurements and recovered from cyclohexane again to finally characterize the degree of deuteration after the transient absorption measurements.

The evolution of the H/D-exchange was monitored by analyzing samples of the reaction mixture by  $^1\text{H}$  NMR spectroscopy. The results are shown in Figure 4S - 6S. As integration standard the multiplet at  $\delta = 7.7$  ppm resulting from an single aromatic hydrogen is used. Its integral is set to 10.0 and all other integrals are given relative to this value. The O-H signal due to non deuterated HBT is found at  $\delta = 12.52$  ppm; the signal at 7.26 ppm originates from residual  $\text{CHCl}_3$ .

For the deuteration, a solution of HBT (1.00 g) in a mixture of  $\text{CDCl}_3$  (25 mL, Merck) and  $\text{D}_2\text{O}$  (10 mL, Merck, > 99.8 %) was stirred at room temperature. After 90 min the integral over the O-H signal in the NMR spectra showed that the deuteration was almost quantitative (> 99 %, Fig. 4S, after the references). The organic phase was separated and all volatile compounds were evaporated in vacuum ( $10^{-3}$  hPa, 50 °C). Analyzing the solid residue by  $^1\text{H}$  NMR spectroscopy showed a degree of deuteration of > 89 % (Fig. 5S). For the time-resolved pump-probe measurements, a 2 mM solution of the ESIPT molecules in cyclohexane (Merck, UVASOL) was prepared in order to achieve an absorption of ~50 % of the pump light. For the measurements with DBT, the cyclohexane was previously saturated with  $\text{D}_2\text{O}$  to avoid H/D-exchange by residual  $\text{H}_2\text{O}$  traces in the solvent. After the pump-probe measurements, the cyclohexane was partially evaporated, and the degree of deuteration was determined to be >65 % (see Fig. 6S).

Although water is basically not soluble in cyclohexane, it turned out, that even in dry cyclohexane the degree of deuteration decreases on the time scale of one hour quite rapidly. This is attributed to residual water in the solvent and on surfaces of the sample cell and flow system. It turned out, however, that when saturating cyclohexane with  $\text{D}_2\text{O}$  prior to dissolving DBT and flushing the apparatus with  $\text{D}_2\text{O}$  saturated cyclohexane, this initial decrease of deuteration can be avoided. The small amount of  $\text{D}_2\text{O}$  that dissolves in cyclohexane causes a slight change in the polarity of the solvent and shifts the emission spectrum by ~4 nm (see above). It has no influence on the dynamics observed in the femtosecond experiments since DBT must be in contact with a  $\text{D}_2\text{O}$  molecule during the laser excitation, which is highly

improbable at such low concentrations. The degree of deuteration however depends sensitively on the D<sub>2</sub>O content relative to the H<sub>2</sub>O content since only a couple of encounters during the experimental run are necessary to exchange deuterium with hydrogen.

### References

- [1] C. A. S. Potter, R. G. Brown, F. Vollmer, and W. Rettig, *J. Chem. Soc. Faraday Trans.* **90**, 59 (1994).
- [2] S. Lochbrunner, A. J. Wurzer, and E. Riedle, *J. Phys. Chem A* **107**, 10580 (2003).
- [3] M. Bräuer, M. Mosquera, J. L. Pérez-Lustres, and F. Rodríguez-Prieto, *J. Phys. Chem. A* **102**, 10736 (1998).

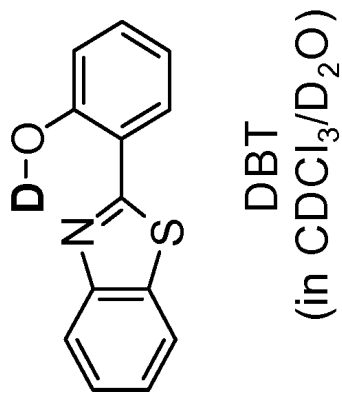
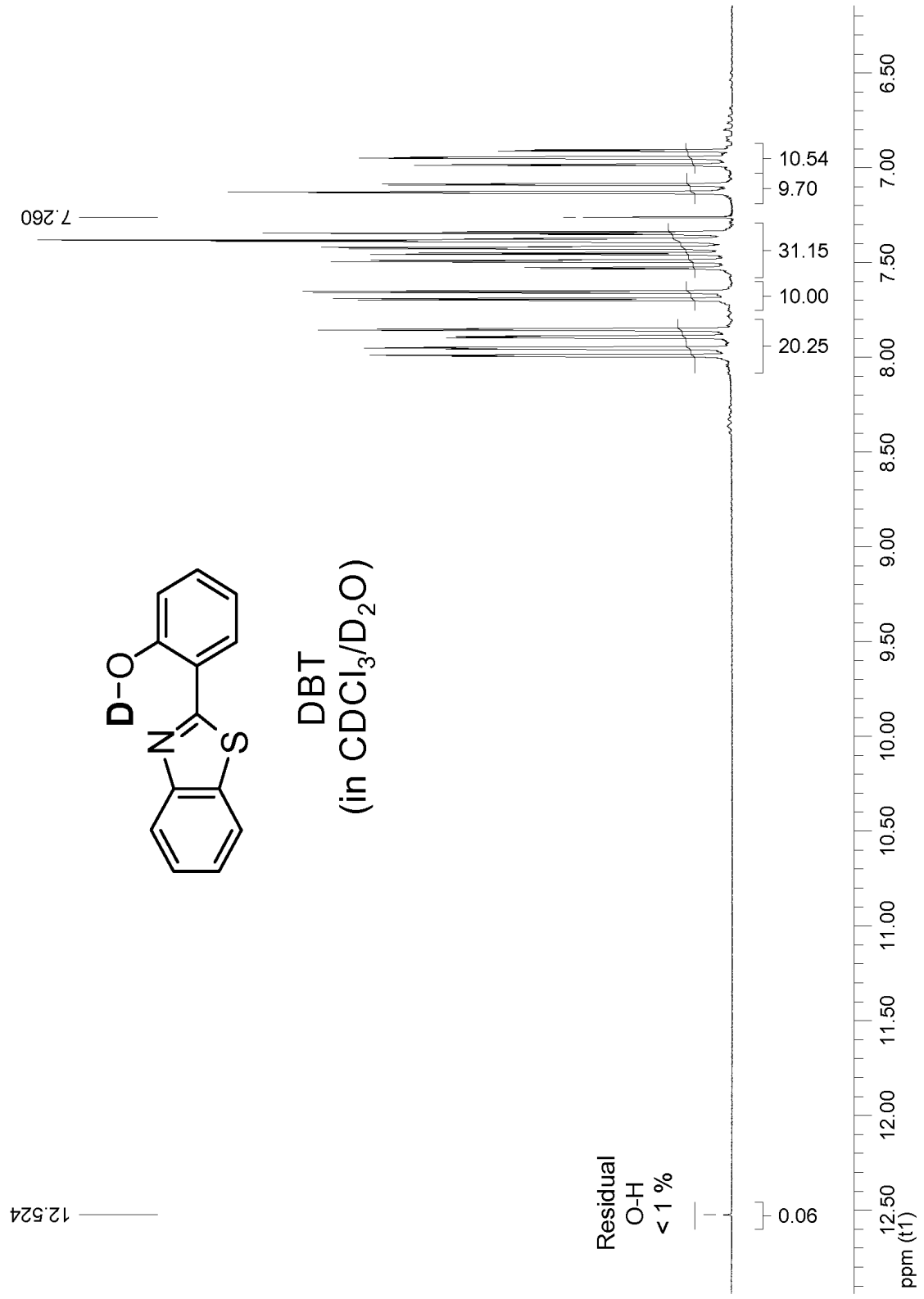


Fig. 4S: <sup>1</sup>H NMR spectroscopic monitoring of the deuteration of DBT by D<sub>2</sub>O in CDCl<sub>3</sub> (CDCl<sub>3</sub>/D<sub>2</sub>O, 200 MHz).



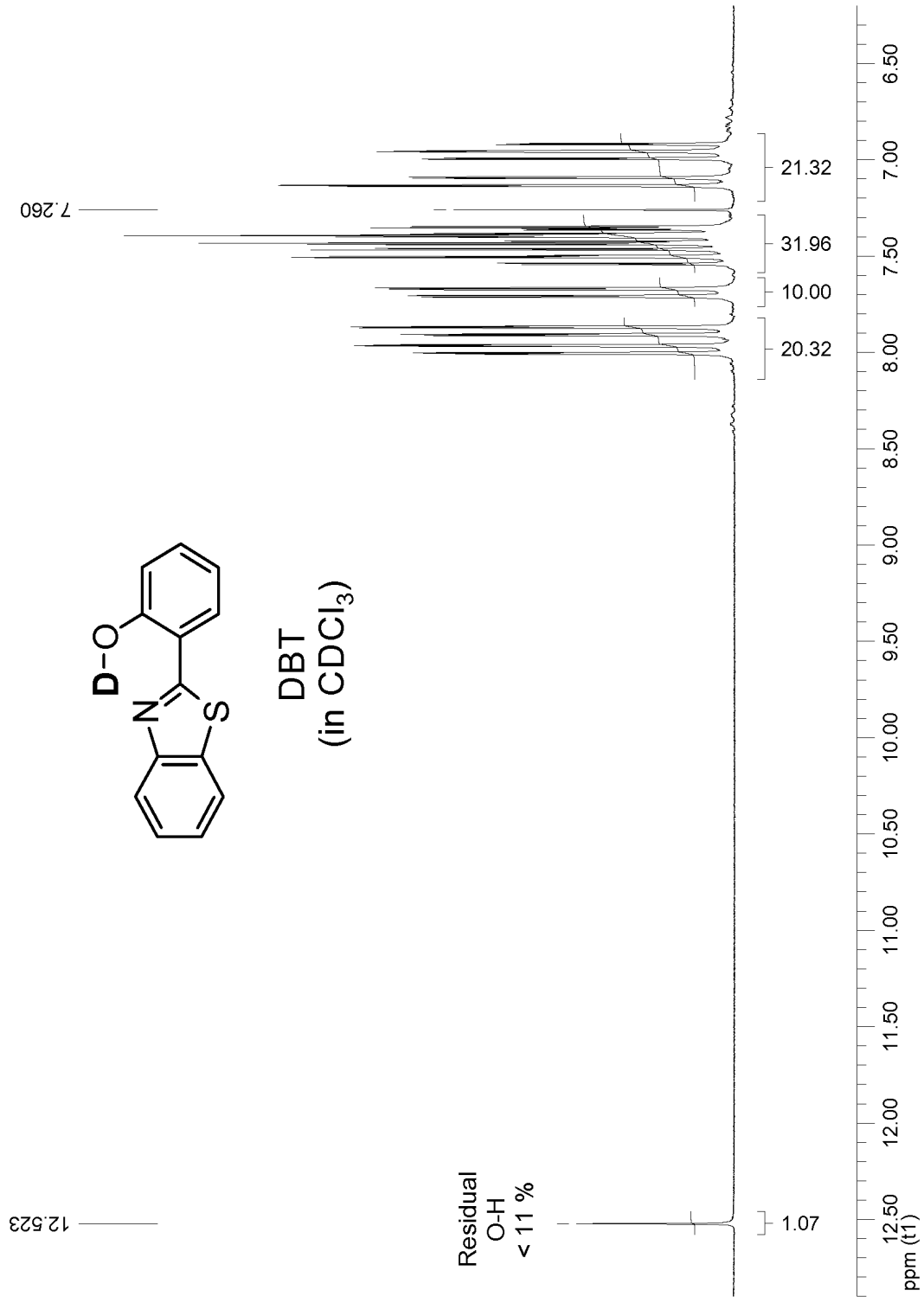


Fig. 5S: <sup>1</sup>H NMR spectroscopic determination of the deuteration degree in the isolated sample of DBT used for the ESIP experiment (CDCl<sub>3</sub>, 200 MHz).

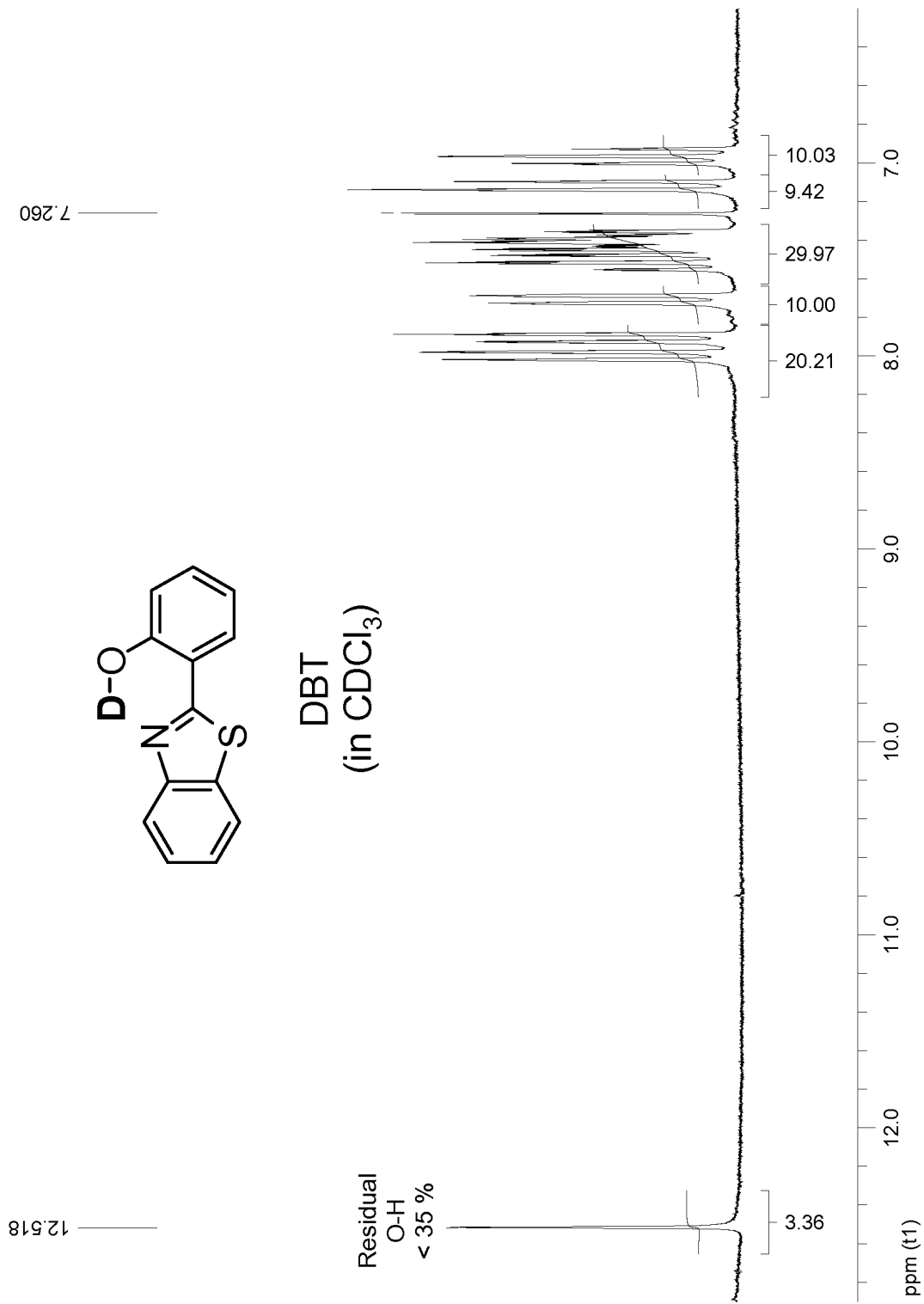


Fig. 6S: <sup>1</sup>H NMR spectroscopic determination of the deuteration degree in DBT after the ESIPT experiment (CDCl<sub>3</sub>, 200 MHz). An additional multiplet at  $\delta = 1.4$  caused by the presence of cyclohexane is not shown.

## Anhang 7

**"Reaction path dependent coherent wavepacket dynamics in  
excited state intramolecular double proton transfer"**

K. Stock, C. Schrieffer, S. Lochbrunner, and E. Riedle

Chem. Phys. 349, 197 – 203 (2008)





Contents lists available at ScienceDirect

## Chemical Physics

journal homepage: [www.elsevier.com/locate/chemphys](http://www.elsevier.com/locate/chemphys)

## Reaction path dependent coherent wavepacket dynamics in excited state intramolecular double proton transfer

Kai Stock, Christian Schrieber, Stefan Lochbrunner<sup>1</sup>, Eberhard Riedle\*

LS für BioMolekulare Optik, Fakultät für Physik, Ludwig-Maximilians-Universität (LMU), Oettingenstrasse 67, 80538 München, Germany

## ARTICLE INFO

## Article history:

Received 6 January 2008

Accepted 11 March 2008

Available online 15 March 2008

## Keywords:

Femtosecond molecular dynamics

ESIPT

ESIDPT

Parallel reaction paths

Wavepacket branching

Symmetry breaking

## ABSTRACT

The primary steps and the wavepacket dynamics of the ultrafast photoinduced double proton transfer in (2,2'-bipyridyl)-3,3'-diol are observed. A two-color pump probe spectrometer with 30 fs time resolution allows the variation of the vibrational excess energy. We find that the first step of the sequential proton transfer and the concerted double proton transfer both proceed in about 50 fs. We observe two types of coherently excited vibrational modes: (i) two symmetric stretching modes are closely associated with the concerted double proton transfer indicating that a simultaneous and symmetric reduction of the donor acceptor distances in both chelate rings takes place during the transfer; (ii) a nonsymmetric in-plane-bending mode is associated with the sequential proton transfer and provides evidence that the transient reduction of the donor acceptor distance occurs only in one chelate ring. This mode is exclusively excited by the reaction and cannot be excited optically according to symmetry selection rules. This constitutes a direct proof that a vibrational wavepacket can be excited by an ultrafast reaction itself.

© 2008 Elsevier B.V. All rights reserved.

## 1. Introduction

Molecules exhibiting excited state intramolecular proton transfer (ESIPT) are excellent model systems for studying ultrafast reactions. Many important aspects like the evolution of an initially prepared wavepacket and the role of skeletal motions in molecular reactions have been investigated using such systems [1–8]. In most cases considered so far the molecules exhibiting wavepacket dynamics proceed only along one distinct reaction channel without any branching. However, systems with parallel and branching reaction channels are highly interesting due to their chemical and biological relevance. The question arises if in this situation coherent wavepacket dynamics can be observed and if so, can it be used to characterize the different channels and get an improved understanding of the reaction mechanisms. Can the different path ways be treated on their own or do we observe a coupling between the branches and interference effects? Such molecules bear the possibility to choose one or the other reaction channel by an appropriate optical excitation similar to recent control experiments [9,10]. A good understanding of the wavepacket dynamics should lead

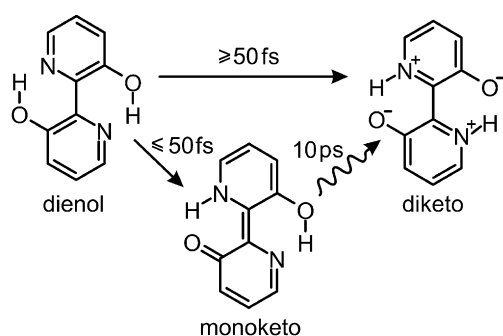
to a deeper insight in the underlying control mechanisms and to new control concepts. It is well established that ultrafast ESIPT is associated with coherent wavepacket motion and its analysis gives direct insight into the reaction mechanism [2–7,11–14]. Therefore, molecules exhibiting double proton transfer (PT) seem to be well suited model systems to investigate the aforementioned questions.

Molecules showing intramolecular as well as intermolecular double PT have been the subject of several experimental and theoretical studies [4,15–26]. In particular the question whether concerted or sequential PT occurs has been discussed for different systems. Since the mechanism of excited state intramolecular PT is now extremely well understood for molecules with a single H-chelate ring [5–8,14] a comparison with double PT will elucidate the typical features of a system with multiple reaction channels.

For our investigations (2,2'-bipyridyl)-3,3'-diol [BP(OH)<sub>2</sub>] is used. It has two H-chelate rings and exhibits intramolecular double PT in the electronically excited state [15,16,27,28]. The dienol ground state and the diketo form adopted after the double PT in the electronically excited state exhibit a centrosymmetric planar geometry [28,29]. This manifests itself in the lack of a detectable dipole moment in the ground state, at the Franck–Condon point, and at the diketo minimum of the electronically excited potential energy surface (PES) [28,30]. The symmetry leads also to strict selection rules for the optical excitation of vibrational modes

\* Corresponding author. Tel.: +49 89 2180 9210; fax: +49 89 2180 9202.

E-mail address: [eberhard.riedle@physik.uni-muenchen.de](mailto:eberhard.riedle@physik.uni-muenchen.de) (E. Riedle).<sup>1</sup> Present address: Institut für Physik, Universität Rostock, Universitätsplatz 3, 18055 Rostock, Germany.



**Scheme 1.** Concerted and sequential double proton transfer of BP(OH)<sub>2</sub> in the electronically excited state.

[31]. From fluorescence up-conversion studies [17,18] it is known that concerted and sequential double PT occur simultaneously (see Scheme 1). After optical excitation, part of the molecules transfer both protons of the chelate rings within a very short time forming directly the diketo tautomer. The other molecules shift in a first step only one proton and form the monoketo intermediate. Subsequently the second proton is transferred with a rate of (10 ps)<sup>-1</sup> leading again to the diketo form [17,18]. The branching ratio depends on the excess energy of the optical excitation, more monoketo is formed at shorter wavelengths [19]. Any significant involvement of triplet states in the PT process has been excluded [32]. Asymmetric substitution [31,33] and deuteration [18,31] have been used to further elucidate the PT. Despite all this work, the very initial steps, i.e., the concerted double PT and the first transfer in the sequential pathway have not yet been temporally resolved and the notion of the transfer mechanisms is still of somewhat hypothetical character.

In this paper we report on transient absorption measurements on BP(OH)<sub>2</sub> with a time resolution of 30 fs. The very initial steps of the process are resolved and pronounced oscillatory signal contributions are found indicating a coherent excitation of vibrational modes involved in the process. We utilize the dependence of the coherent dynamics on the excess energy to attribute the vibrational modes to one or the other channel and give a model for the reaction mechanism.

## 2. Experimental techniques

Transient absorption measurements were performed with two different setups. For the recording of transient spectra a fraction of the output of a home-built Ti:Sa regenerative amplifier (800 nm, 1 kHz repetition rate, 90 fs pulses) is used for third harmonic generation resulting in pulses at 267 nm with 500 nJ pulse energy for the excitation of the sample. With another part a continuum is generated in a CaF<sub>2</sub> disc to probe absorption changes. The beams are focused into the sample with a focus diameter of 200 μm for the pump beam and 80 μm for the probe beam. The sample is a cyclohexane solution of BP(OH)<sub>2</sub> in a fused silica cuvette with 500 μm optical path length. Spectra are recorded with a multichannel detector after dispersing the probe beam with a spectrograph. To avoid effects of orientational relaxation occurring on a time scale of about 10 ps all spectra were measured with the probe beam polarized in magic angle with respect to the pump beam. Further details of the setup are described elsewhere [34–36].

To resolve the wavepacket dynamics a two-color UV/Vis pump-probe spectrometer with a time resolution of 30 fs based on two noncollinearly phase matched optical parametric amplifiers (NOPAs) was used [3,6,37]. One NOPA uses a two stage setup with

an intermediate white light generation. Its output is frequency doubled in a 100 μm BBO crystal and compressed with a fused silica prism sequence. This allows to access the wavelength region between 310 nm and 380 nm that is required for covering the absorption band of the sample. Pulses (20 fs) in the visible region are generated with a second NOPA and a fused silica prism compressor. A part of this beam is split off and used as reference. Pump and probe beam are focused into the sample and detected by photodiodes. They are polarized parallel to each other.

To exchange the excited volume after each laser pulse the sample is pumped through a home made cell with 200 μm thick fused silica windows and an optical path length of 120 μm. BP(OH)<sub>2</sub> with a stated purity of 98% (Sigma Aldrich) is dissolved in cyclohexane (UVASOL; Merck) at a concentration of 2 × 10<sup>-3</sup> M. Absorption and fluorescence spectra of the samples used in the femtosecond experiments were taken regularly and compared to spectra measured for a small sample of high purity and also to published spectra [38]. No differences were observed and this was taken as indication for the lack of any relevant impurities. Experiments with neat solvent under the same conditions did not show significant solvent or window contributions to the signal.

To determine the time zero of the pump-probe delay the cross-correlation is measured at the sample position with the same amount of glass in the beam path. As crosscorrelation signal difference frequency mixing in a 100 μm BBO crystal is used. The width of the crosscorrelation was typically 40 fs and the time zero was determined with an accuracy better than 10 fs.

## 3. Results

Transient spectra at various delay times are presented in Fig. 1 for 267 nm excitation. Stimulated emission (SE) and excited state absorption (ESA), which dominates below 480 nm, contribute to the spectra. In the region of the fluorescence of BP(OH)<sub>2</sub> we observe a blue shift of the spectrum with increasing time. Between 400 nm and 460 nm only minor changes occur after the excitation. The ESA seems to be less strongly affected by the PT than the emission similar to the situation in 2-(2'-hydroxyphenyl)benzothiazole (HBT) [5,6] and signal changes due the PT process are dominated

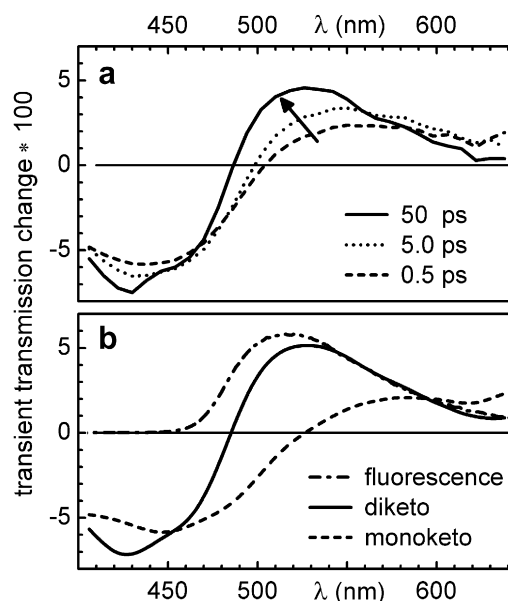


**Fig. 1.** (a) Transient absorption spectra of BP(OH)<sub>2</sub> dissolved in cyclohexane for different time delays. (b) Deduced absorption spectra of the electronically excited monoketo and diketo conformer.

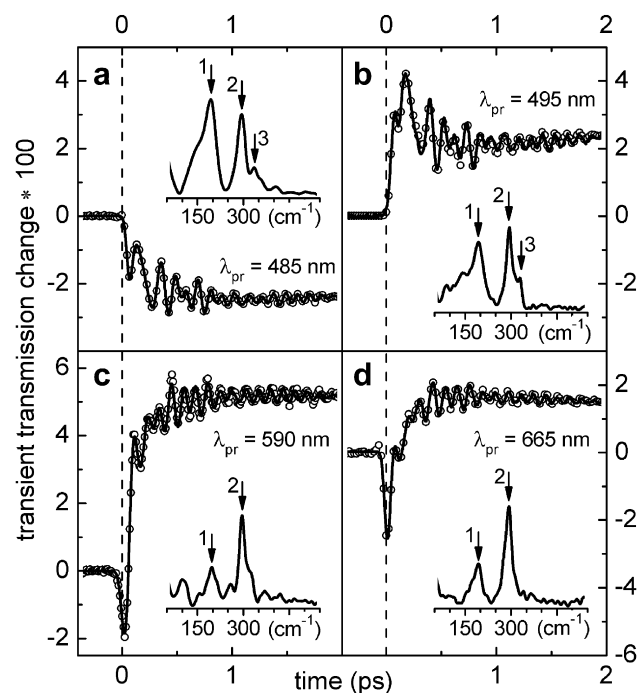
by variations in the emission spectra. The measurements can be fitted by a triexponential function with time constants (for discussion see below) of 200 fs, 10 ps, and about 3–4 ns. The latter two times agree very well with previous reports [17,18] and are attributed to the transition from the monoketo to the diketo form and to the fluorescence lifetime of BP(OH)<sub>2</sub> in cyclohexane. We did not find any indication that a  $n\pi^*$  state contributes significantly to the dynamics as proposed by others [24].

From the total transmission change we can reconstruct the transient absorption spectra for the different tautomers. The spectrum for the diketo tautomer is identical to the transient spectrum at long delay times. Shortly after optical excitation the ratio between monoketo to diketo is equal to 2 for the excitation at 267 nm [17,19] and the spectrum consists of 2/3 of the monoketo spectrum and 1/3 of the diketo. By suitable scaling and subtraction of the diketo spectrum (approximated by the transient spectrum after 200 ps) from the transient spectrum at 0.5 ps, we obtain the spectrum of the monoketo form (see Fig. 1b). The spontaneous emission spectra of both conformers were reconstructed in a similar way from fluorescence up-conversion measurements [17,38]. Our spectra are a combination of ESA and SE and describe the absorption properties of the individual conformers. The emission peaks at  $\sim 530$  nm for the diketo and at  $\sim 580$  nm for the monoketo form are in good agreement with the up-conversion measurements. As the PT reactions proceed, the fractions of monoketo and diketo evolve and the total transient spectrum changes accordingly.

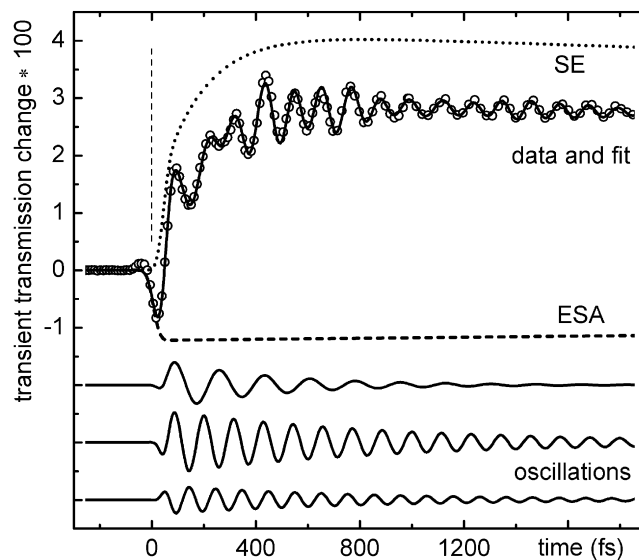
In accord with previous reports [17,19] we can conclude that the diketo tautomer is preferentially detected at short probe wavelengths and the monoketo at longer ones. This does, however, only apply to the total signal. Unfortunately the total transient absorption signal is a poor measure of the state population due to the opposing signal contributions from SE and ESA and the differing SE and ESA spectra for the two tautomers. In this work we are focused on the wavepacket dynamics and the coherent excitation of vibrational modes. A wavepacket oscillating in a vibrational coordinate causes periodic spectral shifts of the transient spectrum [5]. For time traces measured at a fixed probe wavelength this results in oscillatory signal contributions with the frequency of the vibration. Their amplitude scales with the slope of the spectrum [5] and we therefore expect the largest contribution of a wavepacket in the monoketo form in the wavelength region between 470 nm and 560 nm.

Fig. 2 shows transient transmission changes of BP(OH)<sub>2</sub> dissolved in cyclohexane with high temporal resolution at selected probe wavelengths. The center wavelength of the excitation pulses was 350 nm. We probe the transmission changes in the spectral region of the product state fluorescence [17]. The large Stokes shift ensures the observation of dynamics in the electronically excited state without any interference from ground state processes. All signals have contributions from SE and ESA. At a probe wavelength of 485 nm the ESA is dominant (see Fig. 2a) and the signal shows a transient transmission decrease. At the other presented probe wavelengths the SE is dominant resulting in a transmission increase. Note that this emission rise has a small but significant delay with respect to the excitation.

The transients in Fig. 2 show strong oscillations lasting more than 2 ps. These oscillations are due to vibronic wavepackets. Fourier transformation reveals the contributing frequencies (marked by arrows in Fig. 2). Independent of the probe wavelength we observe three oscillations at about 193  $\text{cm}^{-1}$ , 294  $\text{cm}^{-1}$  and 331  $\text{cm}^{-1}$ . These average values will be used below as labels for the three oscillations. The relative strength of the 193  $\text{cm}^{-1}$  mode decreases as the probe wavelength is tuned to the red. After the emission rise the nonoscillating components change with time constants of 200 fs and 10 ps.



**Fig. 2.** Transient absorption traces of BP(OH)<sub>2</sub> in cyclohexane excited at 350 nm and probed at (a) 485 nm, (b) 495 nm, (c) 590 nm and (d) 665 nm. Positive values indicate stimulated emission. The insets show the Fourier transformation of the time traces. The arrows and labels 1–3 indicate the oscillations termed 193, 294, and 331  $\text{cm}^{-1}$  (when present). The precise values of the experimental frequencies are given in Table 1.



**Fig. 3.** Transient absorption trace and the corresponding fit for BP(OH)<sub>2</sub> excited at 350 nm and probed at 625 nm. The data (open circles), the complete fit (solid line) and the components of the fit for SE (dotted), ESA (dashed) and the oscillations (solid lines in the lower part) are shown.

For a more detailed analysis a model function is fitted to the data sets analogous to the procedure described in Ref. [5]. Fig. 3 shows the transient at 625 nm together with the fitted model function and the various components. The oscillatory components are taken into account by exponentially damped cosine functions. The ESA occurs instantaneously with the excitation of the molecule to the S<sub>1</sub> state. It is modeled with a drop of the transmission at time

zero convoluted with the crosscorrelation. The SE is attributed to the  $S_1$  keto tautomers and indicates single or double proton transfer. The onset of the SE is modeled with a time delayed step function. The delay of the SE rise corresponds to the time, the wavepacket needs to reach a keto region of the  $S_1$  PES, i.e., the ES IPT to complete. It is therefore taken as a measure for the proton transfer time [14].

After the SE rise the nonoscillating components can be fitted by a biexponential function with a short time constant of about 200 fs and a longer one of  $\sim 10$  ps. The fast component is a decay at short probe wavelengths and a rise in the red. A similar effect has also been observed in HBT [3,5,11], 10-hydroxybenzo[h]quinoline [13,14] and other molecules exhibiting ES IPT [6,39]. It results from a red shift of the emission spectrum and is attributed to internal vibrational redistribution (IVR). Similar time constants of 350 fs and  $\sim 10$  ps were also found in fluorescence up-conversion measurements and the inferred anisotropies [38]. The 10 ps constant was attributed to the monoketo to diketo conversion, which is in good agreement with our findings.

The reported 350 fs time constant was explained as a demixing of the optically excited electronic wavefunction (dienol form) into the monoketo and diketo diabatic wavefunctions [38]. The analysis of our data implies that the initial splitting of the wavefunction into monoketo and diketo takes place within  $\sim 50$  fs. Since both experiments achieved different time resolutions and are of complementary nature, no clear conclusion can be drawn at present. Most likely, both IVR and electronic state demixing contribute to the observed signal kinetics.

The fit function reproduces the data very well (see solid lines in Figs. 2 and 3). The results for the proton transfer time and the oscillation frequencies are summarized in Table 1. We observe a proton transfer of about 50 fs. In the blue probing range there seems to be a tendency toward somewhat larger values while in the red the values are somewhat shorter. This contrasts to observations in HBT where longer times in the red spectral region were observed due to the time the wavepacket motion needs for transversing the observation region [5]. According to Fig. 1 the SE has large contributions from the diketo tautomer in the blue spectral region while in the red region the monoketo contributes stronger. Therefore the longer delay time in the blue could be taken as an indication that the formation of the diketo form is somewhat slower than the formation of the monoketo. A classical rate model would not allow such a distinction, since even differing rates for conversion

**Table 1**  
Fit results for the delay of the emission rise and for the frequencies of the oscillations at various pump and probe wavelengths

Pump (nm)	Probe (nm)	Delay (fs)	Frequencies ( $\text{cm}^{-1}$ )		
310	485	–	196	289	327
	560	64	180	301	332
	630	64	170	291	–
350	485	–	193	293	332
	495	(48)	194	293	332
	570	65	189	294	331
	590	57	195	295	333
	625	37	192	292	331
	665	40	192	294	330
375	485	59	195	294	330
	635	–	196	295	–
IR <sup>a</sup> /Raman <sup>b</sup> spectroscopy			203 (IR)	316 (Raman)	351 (Raman)
B3LYP/ 6-311+G(d,p)			198	304	343

At a probe wavelength of 485 nm the ESA is dominating and the time of the emission rise cannot be determined. Around 630 nm the contribution of the  $331 \text{ cm}^{-1}$  mode is very small and cannot be established for all pump wavelengths.

<sup>a</sup> Ref. [40].

<sup>b</sup> Ref. [31].

to the two keto states would still lead to an equal rise time of the two product signals. The situation is significantly different in the wavepacket picture. The optically prepared wavepacket can split very early in time and the resulting fragments need different times to reach the respective PES minima. These times do not have to correlate.

According to prior investigations [19] the branching ratio between the concerted and the sequential pathway depends on the vibrational excess energy deposited by the excitation. To explore this effect, excitation wavelengths of 375 nm at the low energy onset of the absorption spectrum, 350 nm and 310 nm were used. The results are depicted in Fig. 4. In line with the findings from the transient spectra (see Fig. 1) the net signal of the time traces is a delicate balance between ESA and SE. With the excitation wavelength the monoketo and diketo contributions to the signal change, and thus the net signal changes accordingly. The monoketo to diketo conversion on a 10 ps time scale leads in the blue and green spectral regions to a signal increase for long delay times, and in the red to a signal decrease (data not shown). For 375 and 350 nm excitation we find again pronounced oscillations in the signal with the same frequencies as in Fig. 2. At the highest excess energy only very weak oscillations can be found.

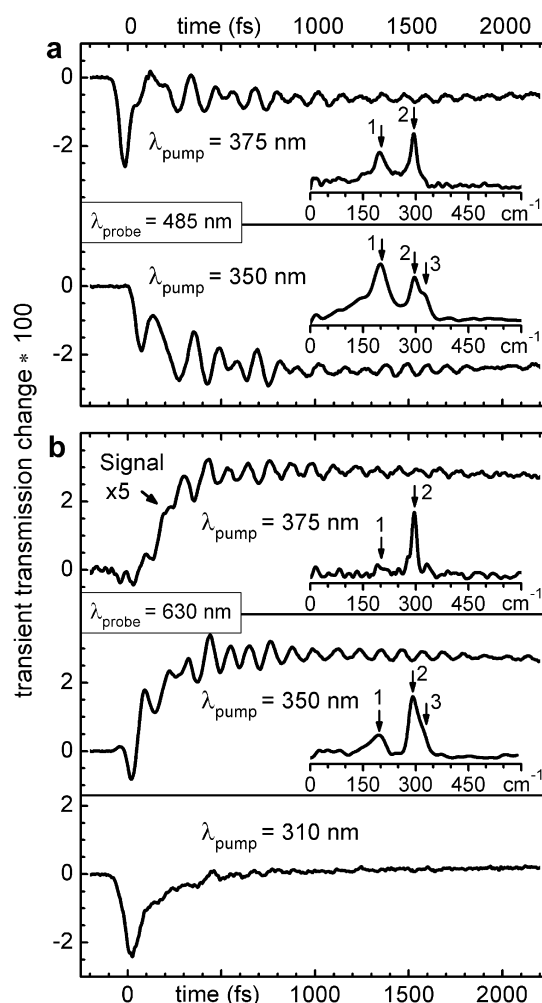


**Fig. 4.** Transient absorption of  $\text{BP(OH)}_2$  with Fourier transformations at different excitation wavelengths probed at (a) 485 nm and (b) nominally 630 nm. The signal at 375 nm excitation and 630 nm probing is multiplied by a factor of 5. The arrows and labels 1–3 indicate the oscillations termed 193, 294, and  $331 \text{ cm}^{-1}$  (when present). The precise values of the experimental frequencies are given in Table 1.



#### 4. Discussion

It has previously been established that BP(OH)<sub>2</sub> exhibits single proton transfer as well as double proton transfer on a sub-100 fs timescale in the first electronically excited state [17,18]. The measurements presented in this work allow us now to give a value of 50 fs or slightly less for the first step of the sequential transfer and 50 fs or slightly more for the concerted transfer. The additional observation of oscillatory signal contributions necessitates that a description of the processes in terms of wavepacket motion is used and a simple rate model does not seem suitable. Still, the principal mechanism for the first steps seems to be similar for both reaction channels. Obviously the presence of a second reaction channel does not significantly affect the process of the proton transfer itself.

The fast time scale for the double proton transfer and the step-like rise of the signal that has also been observed in other ESIPT molecules [8] suggests that the nature of this process is very similar to the single PT. It can be treated as a barrierless process and as motion of a well defined nuclear wavepacket on an excited PES. Due to momentum conservation the molecule performs after the PT oscillatory motions on the PES around the product minimum in normal modes which are correlated to the geometric changes of the molecules during the PT process. It leads to a periodic modulation of the transient spectrum that reflects the vibrational modes which have large projections on the reaction path. As

shown in Figs. 2–4 three vibrational modes are observed in our experiment.

To identify the molecular motions involved in the reaction we compare the observed frequencies with results from Raman and IR spectroscopy [31,40] and perform ab-initio calculations (cf. Table 1). The vibrational eigenmodes of BP(OH)<sub>2</sub> in the electronic ground state were calculated at the B3LYP/6-311+G(d,p) level using the GAUSSIAN 03 program package [41] and scaled by 0.9679 [42]. The point group C<sub>2h</sub> is assumed for the planar centrosymmetric BP(OH)<sub>2</sub> both in the ground and the excited state [30]. In the case of the ESIPT molecule HBT it was shown that the low frequency normal modes in the electronically excited state do not deviate much from those in the ground state [7]. This justifies the comparison of the observed S<sub>1</sub> with the ground state data. Fig. 5 shows results of the calculation. The three observed modes match with the calculated ones at 198 cm<sup>-1</sup>, 304 cm<sup>-1</sup> and 343 cm<sup>-1</sup>, all in-plane normal modes, which affect strongly the H-chelate rings of the molecule. The mode at 198 cm<sup>-1</sup> is assigned to the 20b<sub>u</sub> overall bending mode of BP(OH)<sub>2</sub> while the two higher frequencies correspond to symmetric in-plane-bending of the hydroxy groups (21a<sub>g</sub>) and an in-plane-shear deformation (20a<sub>g</sub>) of the molecule. There is no other calculated mode energetically close to the observed 193 cm<sup>-1</sup> vibration and the assignment to the mode 20b<sub>u</sub> is unambiguous. An additional out-of-plane mode 8b<sub>g</sub> is calculated at 304 cm<sup>-1</sup>. A visual inspection of the corresponding molecular deformation shows no change in the chelate rings. We therefore consider it highly unlikely that it is this mode that we observe experimentally.

The overall bending of the molecule by the 20b<sub>u</sub> mode decreases the O–N distance at one side of the molecule while it increases it on the other side (see Fig. 5a). For a number of ESIPT molecules it has been demonstrated that such low frequency bending modes strongly affecting the chelate ring are crucial for the PT since they cause the initial reduction of the donor acceptor distance necessary for the enol to keto change [5–7,12,39]. For BP(OH)<sub>2</sub> this suggests a connection of the bending mode to the first step of the sequential proton transfer. According to the selection rules in the C<sub>2h</sub> point group, only total symmetric (a<sub>g</sub>) modes can be directly excited in the allowed electronic dipole transition. The observation of the 20b<sub>u</sub> mode at 193 cm<sup>-1</sup> is in contradiction to this rule and indicates an excitation by a reactive process, in this case by the ESIPT.

The observed symmetric modes change both O–N distances simultaneously and conserve the C<sub>2h</sub> symmetry of the molecule. This suggests that these molecular vibrations are associated with the concerted proton transfer. Similar proposals can also be found in the literature [18,31,40], however, direct experimental evidence was not yet available.

To verify this claim we analyze the measurements with the same probe wavelength and different excess energies in the excitation (see Fig. 4). The excitation wavelength changes the branching ratio between the generation of the diketo and monoketo tautomer [19]. If there is indeed the proposed coupling between the two reaction pathways and the observed wavepacket dynamics, a change of the branching ratio should affect the observed amplitudes of the modes. In Fig. 4 the Fourier transforms of traces with 350 and 375 nm excitation and probe wavelengths of 485 nm and 630 nm are compared. According to Ref. [19] about 30% of the excited molecules are transferred to the monoketo form after excitation at 350 nm compared to 16% at 375 nm. Because the amount of the monoketo form is changed by a factor of about 2 and the amount of diketo formation only slightly, we expect much larger changes in the oscillation amplitudes assigned to the single proton transfer. The Fourier analysis clearly shows a significantly higher amplitude for the 193 cm<sup>-1</sup>-bending mode at higher excess energy. The observed dependence of the oscillation amplitudes on

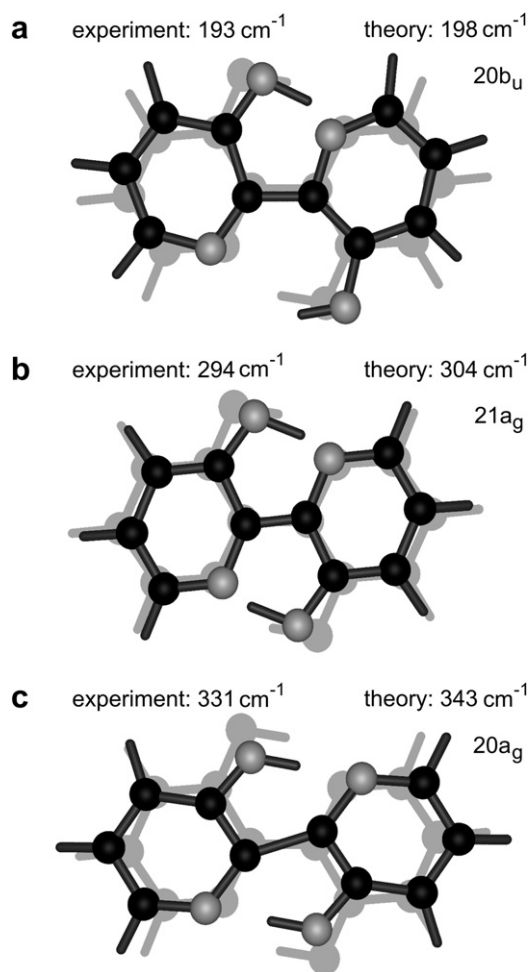


**Fig. 5.** Calculated normal modes of BP(OH)<sub>2</sub> [DFT, B3LYP/6-311+G(d,p)] that are assigned to the ones observed in the experiment. The particular modes shown are the 20b<sub>u</sub>, 21a<sub>g</sub> and 20a<sub>g</sub> (top to bottom).

the excitation wavelength corroborates the assignment of the wavepacket dynamics to the different reaction channels.

Excitation at 310 nm results in only weak oscillatory signal components (see Fig. 4b – lower panel). The molecule is prepared with a very high excess energy. A large number of vibronic states is populated and significant coupling between the vibrational modes is expected. This leads to a fast broadening of the wavepacket and a loss of contrast in the signal oscillations as it is observed.

## 5. Summary and conclusions

The nature of the primary steps in the photodynamics of BP(OH)<sub>2</sub> and the associated wavepacket evolution have been revealed by UV–Vis transient absorption spectroscopy with 30 fs time resolution. It is found that both the concerted double proton transfer and the initial step of the sequential transfer proceed in about 50 fs. The former is associated with a symmetric shortening of the donor acceptor distances and the latter with an asymmetric one. The molecular deformations are observed as characteristic wavepacket motions. In all these respects, the double proton transfer is extremely similar to the previously investigated single proton transfers. The two reaction channels seem to evolve independently from each other.

The ultrafast concerted process can well be rationalized by an appropriate gradient of the S<sub>1</sub> PES at the Franck–Condon (FC) point. Pronounced normal modes might not be developed in the dienol excited state due to its rapid decay to the keto tautomers, and hence a normal mode picture is not informative, however a projection of the ground state wavepacket to the FC point should be a suitable description. From the FC point the wavepacket accelerates toward the diketo minimum. An acceleration towards one of the monoketo minima is less obvious as it has to spontaneously break the symmetry of the molecule. We have to keep in mind, however, the thermal excitation of the molecules before the optical excitation. This is equivalent to rapid fluctuations from the symmetric geometry and the ultrafast excitation will catch the molecule in such a deformed geometry. It is therefore placed on the S<sub>1</sub> PES off the symmetric FC point and free to break into an asymmetric reaction. Similarly, solvent fluctuations will contribute to a loss of symmetry. To substantiate these ideas, a PES from high level quantum chemical calculations is dearly needed.

It is worth noting that the experimental observation of the excitation of the 20b<sub>u</sub>-bending mode in the PT product is a direct proof that a wavepacket can be generated by the ultrafast reaction itself. We consider it quite likely that such a mechanism contributes considerably to all vibrations that are active in the PT. We furthermore expect that the reaction induced creation of a wavepacket, i.e., a coherent vibrational excitation in the product, is possible for many ultrafast photochemical processes. It can happen when the reaction time is shorter than the relevant vibrational periods. This situation should occur for processes proceeding on an adiabatic PES without an effective potential barrier.

The observed wavepacket dynamics in BP(OH)<sub>2</sub> is characteristic for each reaction channel and can also be used for the distinction between the two paths. This is not only true for the analysis of the process, but even more interestingly it might provide a unique chance for coherent control experiments [40]. If the symmetric vibrations – that can be accessed optically – are constructively enhanced, more diketo production is expected. If, on the other hand, the symmetric vibrations are destructively superimposed, the monoketo tautomer should be preferentially formed. This scheme could be combined with a suitable choice of the excitation wavelength.

Beyond the present example of BP(OH)<sub>2</sub> the new insight into the mechanism of double proton transfer might also aid the under-

standing of other systems displaying such multidimensional dynamics. The relatively slow progressing double proton transfer in porphycene does show clear vibrational activity [43,44]. For related systems with vanishing barriers, the reactions will most likely proceed on an ultrafast time scale as wavepacket motion. For the well known example of dimers of 7-azaindole it is still an open debate whether only stepwise double proton transfer or also a concerted one occurs [22,25,26]. We expect that an experiment with sufficient temporal resolution should render wavepacket signatures on the experimental curves that can be interpreted similarly to the present work to determine whether there is a symmetric or an asymmetric approach of the two 7-azaindole moieties.

## Acknowledgements

We thank Helmut Satzger and Christopher Root for valuable help with the white light absorption measurements and Anna Grabowska for the fruitful discussion and helpful comments. Funding by the Deutsche Forschungsgemeinschaft is gratefully acknowledged. The work was supported by the DFG-Cluster of Excellence: Munich-Centre for Advanced Photonics and by the Austrian Science Fund within the Special Research Program F16 (Advanced Light Sources).

## References

- [1] T. Arthen-Engeland, T. Bultmann, N.P. Ernsting, M.A. Rodriguez, W. Thiel, *Chem. Phys.* 163 (1992) 43.
- [2] C. Chudoba, E. Riedle, M. Pfeiffer, T. Elsaesser, *Chem. Phys. Lett.* 263 (1996) 622.
- [3] A.J. Wurzer, S. Lochbrunner, E. Riedle, *Appl. Phys. B* 71 (2000) 405.
- [4] N.P. Ernsting, S.A. Kovalenko, T. Senyushkina, J. Saam, V. Farztdinov, *J. Phys. Chem. A* 105 (2001) 3443.
- [5] S. Lochbrunner, A.J. Wurzer, E. Riedle, *J. Phys. Chem. A* 107 (2003) 10580.
- [6] S. Lochbrunner, E. Riedle, *Recent Res. Dev. Chem. Phys.* 4 (2003) 31.
- [7] R. de Vivie-Riedle, V. de Waele, L. Kurtz, E. Riedle, *J. Phys. Chem. A* 107 (2003) 10591.
- [8] S. Lochbrunner, K. Stock, E. Riedle, *J. Mol. Struct.* 700 (2004) 13.
- [9] A. Assion, T. Baumert, M. Bergt, T. Brixner, B. Kiefer, V. Seyfried, M. Strehle, G. Gerber, *Science* 282 (1998) 919.
- [10] J.L. Herek, W. Wohlleben, R.J. Cogdell, D. Zeidler, M. Motzkus, *Nature* 417 (2002) 533.
- [11] S. Lochbrunner, A.J. Wurzer, E. Riedle, *J. Chem. Phys.* 112 (2000) 10699.
- [12] K. Stock, T. Bizjak, S. Lochbrunner, *Chem. Phys. Lett.* 354 (2002) 409.
- [13] S. Takeuchi, T. Tahara, *J. Phys. Chem. A* 109 (2005) 10199.
- [14] C. Schrieffer, M. Barbatti, K. Stock, A.J.A. Aquino, D. Tunega, S. Lochbrunner, E. Riedle, R. de Vivie-Riedle, H. Lischka, *Chem. Phys.*, 2007, doi:10.1016/j.chemphys.2007.10.021.
- [15] H. Bulska, *Chem. Phys. Lett.* 98 (1983) 398.
- [16] A.L. Sobolewski, L. Adamowicz, *Chem. Phys. Lett.* 252 (1996) 33.
- [17] H. Zhang, P. van der Meulen, M. Glasbeek, *Chem. Phys. Lett.* 253 (1996) 97.
- [18] D. Marks, H. Zhang, M. Glasbeek, P. Borowicz, A. Grabowska, *Chem. Phys. Lett.* 275 (1997) 370.
- [19] D. Marks, P. Proposito, H. Zhang, M. Glasbeek, *Chem. Phys. Lett.* 289 (1998) 535.
- [20] M. Chachivili, T. Fiebig, A. Douhal, A.H. Zewail, *J. Phys. Chem. A* 102 (1998) 669.
- [21] S. Takeuchi, T. Tahara, *Chem. Phys. Lett.* 277 (1997) 340.
- [22] S. Takeuchi, T. Tahara, *Chem. Phys. Lett.* 347 (2001) 108.
- [23] J. Weiß, V. May, N.P. Ernsting, V. Farztdinov, A. Mühlpfordt, *Chem. Phys. Lett.* 346 (2001) 503.
- [24] F.V.R. Neuwahl, P. Foggi, R.G. Brown, *Chem. Phys. Lett.* 319 (2000) 157.
- [25] O.-H. Kwon, A.H. Zewail, *Proc. Natl. Acad. Sci.* 104 (2007) 8703.
- [26] S. Takeuchi, T. Tahara, *Proc. Natl. Acad. Sci.* 104 (2007) 5285.
- [27] A. Grabowska, Ł. Kaczmarek, *Pol. J. Chem.* 66 (1992) 715.
- [28] P. Borowicz, A. Grabowska, R. Wortmann, W. Liptay, *J. Lumin.* 52 (1992) 265.
- [29] J. Lipkowski, A. Grabowska, J. Waluk, G. Calestani, B.A. Hess Jr., *J. Cryst. Spectrosc. Res.* 22 (1992) 563.
- [30] R. Wortmann, K. Elich, S. Lebus, W. Liptay, P. Borowicz, A. Grabowska, *J. Phys. Chem.* 96 (1992) 9724.
- [31] P. Borowicz, O. Faurskov-Nielsen, D.H. Christensen, L. Adamowicz, A. Les, J. Waluk, *Spectrochim. Acta Part A* 54 (1998) 1291.
- [32] A. Grabowska, P. Borowicz, D.O. Mártire, S.E. Braslavsky, *Chem. Phys. Lett.* 185 (1991) 206.
- [33] D. Marks, H. Zhang, P. Borowicz, A. Grabowska, M. Glasbeek, *Chem. Phys. Lett.* 309 (1999) 19.
- [34] R. Huber, H. Satzger, W. Zinth, J. Wachtveitl, *Opt. Commun.* 194 (2001) 443.

- [35] H. Satzger, S. Spörlein, C. Root, J. Wachtveitl, W. Zinth, P. Gilch, *Chem. Phys. Lett.* 372 (2003) 216.
- [36] M. Seel, E. Wildermuth, W. Zinth, *Meas. Sci. Technol.* 8 (1997) 449.
- [37] E. Riedle, M. Beutter, S. Lochbrunner, J. Piel, S. Schenk, S. Spörlein, W. Zinth, *Appl. Phys. B* 71 (2000) 457.
- [38] P. Toebe, H. Zhang, M. Glasbeek, *J. Phys. Chem. A* 106 (2002) 3651.
- [39] S. Lochbrunner, C. Schrieber, E. Riedle, in: J.T. Hynes, J.P. Klinman, H.-H. Limbach, R.L. Schowen (Eds.), *Hydrogen-Transfer Reactions*, Wiley-VCH, Weinheim, 2006, p. 349.
- [40] P. Borowicz, A. Leś, L. Adamowicz, J. Waluk, *Photochem. Photobiol. Sci.* 4 (2005) 143.
- [41] M.J. Frisch, G.W. Trucks, H.B. Schlegel, G.E. Scuseria, M.A. Robb, J.R. Cheeseman, J.A. Montgomery Jr., T. Vreven, K.N. Kudin, J.C. Burant, J.M. Millam, S.S. Iyengar, J. Tomasi, V. Barone, B. Mennucci, M. Cossi, G. Scalmani, N. Rega, G.A. Petersson, H. Nakatsuji, M. Hada, M. Ehara, K. Toyota, R. Fukuda, J. Hasegawa, M. Ishida, T. Nakajima, Y. Honda, O. Kitao, H. Nakai, M. Klene, X. Li, J.E. Knox, H.P. Hratchian, J.B. Cross, V. Bakken, C. Adamo, J. Jaramillo, R. Gomperts, R.E. Stratmann, O. Yazyev, A.J. Austin, R. Cammi, C. Pomelli, J.W. Ochterski, P.Y. Ayala, K. Morokuma, G.A. Voth, P. Salvador, J.J. Dannenberg, V.G. Zakrzewski, S. Dapprich, A.D. Daniels, M.C. Strain, O. Farkas, D.K. Malick, A.D. Rabuck, K. Raghavachari, J.B. Foresman, J.V. Ortiz, Q. Cui, A.G. Baboul, S. Clifford, J. Cioslowski, B.B. Stefanov, G. Liu, A. Liashenko, P. Piskorz, I. Komaromi, R.L. Martin, D.J. Fox, T. Keith, M.A. Al-Laham, C.Y. Peng, A. Nanayakkara, M. Challacombe, P.M.W. Gill, B. Johnson, W. Chen, M.W. Wong, C. Gonzalez, and J.A. Pople, *Gaussian 03, Revision D.01*, Gaussian, Inc., Wallingford CT, 2004.
- [42] M.P. Andersson, P. Uvdal, *J. Phys. Chem. A* 109 (2005) 2937.
- [43] J. Waluk, *Acc. Chem. Res.* 39 (2006) 945.
- [44] M. Gil, J. Waluk, *J. Am. Chem. Soc.* 129 (2007) 1335.



## Anhang 8

**"The interplay of skeletal deformations and ultrafast excited-state intramolecular proton transfer: Experimental and theoretical investigation of 10-hydroxybenzo[h]quinoline"**

C. Schriever, M. Barbatti, K. Stock, A. J. A. Aquino, D. Tunega,  
S. Lochbrunner, E. Riedle, R. de Vivie-Riedle, and H. Lischka

Chem. Phys. 347, 446 – 461 (2008)





# The interplay of skeletal deformations and ultrafast excited-state intramolecular proton transfer: Experimental and theoretical investigation of 10-hydroxybenzo[*h*]quinoline

Christian Schriever<sup>a,\*</sup>, Mario Barbatti<sup>b,\*</sup>, Kai Stock<sup>a</sup>, Adélia J.A. Aquino<sup>b</sup>,  
Daniel Tunega<sup>b</sup>, Stefan Lochbrunner<sup>a,1</sup>, Eberhard Riedle<sup>a,\*</sup>,  
Regina de Vivie-Riedle<sup>c,\*</sup>, Hans Lischka<sup>b,\*</sup>

<sup>a</sup> Fakultät für Physik – Ludwig-Maximilians-Universität (LMU), Oettingenstrasse 67, 80538 München, Germany

<sup>b</sup> Institute for Theoretical Chemistry – University of Vienna, Waehringer Strasse 17, 1090 Vienna, Austria

<sup>c</sup> Department Chemie – Ludwig-Maximilians-Universität (LMU), Butenandt-Strasse 11, 81377 München, Germany

Received 30 August 2007; accepted 20 October 2007

Available online 1 November 2007

---

## Abstract

The excited-state intramolecular proton transfer in the aromatic polycycle 10-hydroxybenzo[*h*]quinoline is investigated by means of transient absorption experiments with 30 fs time resolution, classical dynamics and wavepacket dynamics. The experiments establish the ultrafast transfer after UV excitation and show signatures of coherent vibrational motion in the keto product. To elucidate details of the proton transfer mechanism, the classical dynamics is also performed for 2-(2'-hydroxyphenyl)benzothiazole and the results are compared. For both systems the proton transfer takes place on the ultrafast scale of 30–40 fs, with good agreement between the theoretical investigations and the measurements. The dynamics simulations show that for both molecules the proton is handed over by means of skeletal deformation of the molecule. Due to the more rigid structure of 10-hydroxybenzo[*h*]quinoline the hydrogen migration mode participates more actively than in 2-(2'-hydroxyphenyl)benzothiazole.

© 2007 Elsevier B.V. All rights reserved.

**Keywords:** Photodynamics; Ultrafast proton transfer; Transient spectroscopy; Wavepacket dynamics; On-the-fly classical dynamics; TD-DFT

---

## 1. Introduction

Excited-state intramolecular proton transfer (ESIPT) is an important topic for the understanding of photoreactions in organic systems [1–9]. Due to the large body of work the

overall energetics and kinetics are now well understood (for an overview see [10]). We now want to address the more general question, whether we can understand not only the overall energetics or kinetics, but the detailed dynamics of a reactive molecular process from the combination of state of the art experiments and first principle calculations. For this purpose ESIPT is unique for the following reasons. It can be directly initiated by excitation with an ultrashort laser pulse, allowing for experiments on the time scale of the nuclear motion, and it provides as an intramolecular process a well defined starting geometry [5]. Previous femto-second experiments have already shown that multidimensional dynamics can be observed and a detailed picture about the reaction path can be obtained. Even more important, the ultrafast time scale on which the ESIPT takes place

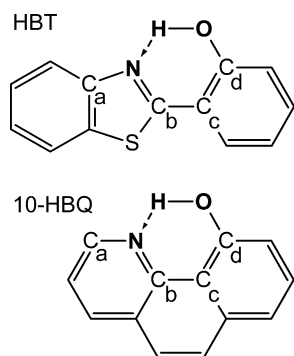
\* Corresponding authors. Tel.: +43 1 4277 52752; fax: +43 1 4277 9527 (M. Barbatti); tel.: +43 1 4277 52757; fax: +43 1 4277 9527 (H. Lischka); tel.: +49 89 2180 9210; fax: +49 89 2180 9202 (E. Riedle); tel.: +49 89 21 80 77533; fax: +49 89 21 80 77133 (R. de Vivie-Riedle).

E-mail addresses: christian.schriever@physik.uni-muenchen.de (C. Schriever), mario.barbatti@univie.ac.at (M. Barbatti), eberhard.riedle@physik.uni-muenchen.de (E. Riedle), regina.de\_vivie@cup.uni-muenchen.de (R. de Vivie-Riedle), hans.lischka@univie.ac.at (H. Lischka).

<sup>1</sup> Present address: Institut für Physik Universität Rostock, Universitätsplatz 3, 18055 Rostock, Germany.

makes it especially well suited for dynamics simulations. In addition, it turns out that the whole transfer process proceeds on one adiabatic potential energy surface (PES) [11,12] and displays a multidimensional character [13].

ESIPT has been studied in several compounds containing a H-chelate ring like 2-(2'-hydroxyphenyl)benzoxazole (HBO) [4], 2-(2'-hydroxyphenyl)benzothiazole (HBT) [2,3], 2-(2'-hydroxyphenyl)benzotriazole (TINUVIN P) [7,14] and 10-hydroxybenzo[h]quinoline (10-HBQ) [15–17] (compare Scheme 1). The large and characteristic Stokes shift between the UV absorption of the ground state enol-form and the visible fluorescence (see Fig. 1) already indicates that after excitation to the  $S_1$ -state, a reactive process takes place that significantly decreases the energy gap between the ground and excited-state. In the electronic ground state the enol-form with the hydrogen atom bound to the donor oxygen of the H-chelate ring is the stable tautomer. If the molecule is promoted to the  $S_1$  excited-state



Scheme 1. Geometric structure of HBT and 10-HBQ before the proton transfer. The carbon atoms that are most relevant to the proton transfer reaction are labeled.

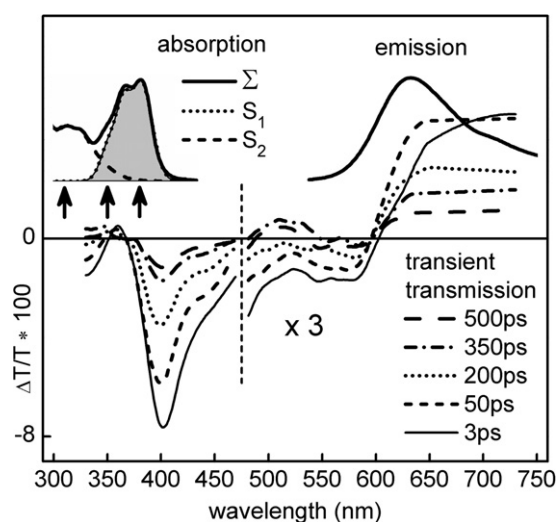


Fig. 1. Upper panel: steady state absorption and emission spectrum of 10-HBQ in cyclohexane (solid lines). For the absorption spectrum ( $\Sigma$ ) the decomposition into the  $S_2$ - $S_0$  and  $S_1$ - $S_0$  bands is shown (dashed lines). The wavelengths chosen for the fs-excitation are indicated. Lower panel: transient transmission of 10-HBQ after excitation with 370 nm pulses for selected delay-times.

the hydrogen atom of the hydroxy group is transferred to the nitrogen at the opposite side of the ring. Already in the seminal work of Weller the fluorescence is attributed to this reaction product [18]. The breaking of the OH-bond and the formation of a keto bond were unequivocally proven for the ESIPT of HBT by time resolved infrared spectroscopy [3,19]. It was found that the absorption band of the OH stretching vibration disappears upon UV excitation of HBT, and the C=O stretching band arises due to the ESIPT. After the ESIPT the molecules return by internal conversion (IC) or radiative decay to the electronic ground state of the enol-form. In the absence of any associated conformational changes a very fast ground state proton transfer brings the molecule back to its enol-form [14].

Numerous femtosecond absorption and emission studies have been performed on various ESIPT compounds. They show that for many systems the transfer of the proton is extremely fast with durations in the order of typically 50 fs and that the molecule exhibits subsequently a coherent wavepacket motion in skeletal vibrational modes associated with deformations of the H-chelate ring. Various models have been discussed in the literature to rationalize the observed dynamics. Arthen-Engeland et al. [4] proposed that the proton transfer in HBO – a system analogous to HBT but with an oxygen atom replacing the sulfur atom – proceeds through tunneling mediated by skeletal motions. Lochbrunner et al. [5], based on the experiments with HBT in cyclohexane, have proposed that the process takes place by means of the contraction of the donor-acceptor distance, with a completely passive role of the proton and without tunneling. This model was supported by detailed quantum chemical studies [12] using normal mode analysis (NMA). This latter model is able to explain the irreversibility of the proton transfer on the short time scale as well as the role of the low-frequency motions that appear as vibronic progression in the fluorescence spectra [4]. Corroboration for the non-tunneling ESIPT model comes also from recent theoretical investigations, which show the existence of a barrierless path for proton transfer in HBT (Aquino et al. [6]) and in the closely related system TINUVIN P (Sobolewski et al. [7]).

In the present work, we investigate the excited-state intramolecular proton transfer of 10-HBQ and HBT (see Scheme 1). For 10-HBQ the signatures of a coherent wavepacket motion have already been reported [16], indicating that the compound is suitable for the intended investigations. In HBT an in-plane bending of the entire skeleton allows for an efficient reduction of the donor-acceptor-distance. In 10-HBQ such a mode is not expected to exist in the low-frequency region because of the geometric restrictions imposed by the quinoline rings. These restrictions can be used to probe how the skeletal deformations mediating the proton transfer change in comparison to HBT and whether the barrierless path is a special feature of HBT or general to ESIPT.

The present investigations were conducted by means of pump-probe experiments on 10-HBQ, quantum dynamics



simulations on 10-HBQ, and classical dynamics simulations on 10-HBQ and HBT. The femtosecond experiments reveal the transfer time, the wavepacket dynamics, and the vibrational modes coherently excited by the ESIPT. By using quantum and classical approaches in parallel we expect to utilize the advantages of either method. The quantum-propagation approach allows the investigation of the vibrational structure of the optically prepared wavepacket evolving in the excited-state. This approach, however, is limited in general to few internal degrees of freedom due to limitations in the computation and utilization of the required grids for the potential energy and the time-dependent wave function. On the other side, the classical approach in the form of on-the-fly dynamics [20] allows straightforward inclusion of all internal degrees of freedom, but misses the non-local features of the dynamics. The combination of all three approaches on a single molecule should allow an unprecedented degree of insight into the ESIPT process.

## 2. Experimental details

The two-color pump-probe spectrometer used in our experiments is a versatile tool providing both the necessary resolution to observe the ultrafast dynamics in real time and the tunability to investigate all compounds of interest. It is described in detail elsewhere [21]. Briefly, a home-built Ti:sapphire regenerative amplifier (100 fs, 1 kHz, 800 nm) pumped a single- and a double-stage noncollinear optical parametric amplifier (NOPA) [22]. The output of the two-stage NOPA was pre-compressed with a pair of chirped mirrors and a prism sequence and frequency-doubled in a 100  $\mu\text{m}$  thin BBO crystal. The generated ultraviolet (UV) pulse was compressed using a double-pass Brewster angled prism sequence. The UV pulse was focused into a flow cell with a 120  $\mu\text{m}$  thick layer of the sample solution and had an energy of 80 nJ. It was tuned to excite 10-HBQ to the  $S_1$  and  $S_n$  states (385 nm, 350 nm, and 310 nm, see Fig. 1). The visible output of the single-stage NOPA was split into two beams ( $\sim 1$  nJ) which were used as probe and reference for measuring the time resolved transmission change in a magic-angle polarization geometry. The energies of the probe and reference pulses were detected integrally by home-built photodiode detectors, avoiding coherent artifacts that tend to mask the dynamics around time zero in dispersed measurements.

Both the pump and probe pulses were close to Gaussian in temporal shape and within about 20% of the transform limit. The 350 and 385 nm pulses had a width (FWHM) of 25–35 fs, depending on the daily alignment, at 310 nm the pulse width increased to 50 fs. The resulting cross correlation width varied between 33 fs and 60 fs, also depending on the probe wavelength.

Transient absorption spectra covering the whole visible and near UV range were measured with a time resolution of 200 fs. In this setup, a Ti:sapphire amplifier system (CPA-2001, Clark-MXR; 150 fs, 1 kHz, 775 nm) pumped

a two-stage NOPA. A Brewster prism sequence was used to imprint negative chirp on the NOPA pulse such that it had a duration of about 100 fs at the place of the 100  $\mu\text{m}$  thin BBO doubling crystal. The UV pulse (370 nm, 100 nJ) was compressed using a sequence of prisms anti-reflection coated for the UV with an apex angle of 45° and delayed by on a motorized delay line with respect to the probe pulses. A fraction of the CPA pulse was focused with a numerical aperture adopted for a low continuum generation threshold into a 4 mm thick rotating calcium fluoride crystal [23]. The whitelight continuum typically spanned from 300 nm to 750 nm and was used as probe pulse. A short pass filter blocked the remainder of the pump pulses. A sample cell with 1 mm optical path length was used. After passing the sample, the continuum was dispersed with an imaging grating spectrograph ( $f = 200$  mm) and detected with an integrating photodiode module (PDI-400-1-P-UV; Becker & Hickl GmbH). The transient spectra were obtained by synchronously scanning the spectrograph and the delay line to correct for the shift of time zero imposed by the group velocity dispersion (GVD) of the continuum. Thus GVD corrected spectra were obtained directly from the measurement without further post-processing.

10-Hydroxybenzo[h]quinoline was obtained from Prof. Hans Langhals (Department Chemie, Ludwig-Maximilians-Universität München). It was dissolved in cyclohexane (UVASOL; Merck) with a concentration of  $10^{-2}$ – $10^{-3}$  M, resulting in an absorption of about 50% of the pump light.

## 3. Experimental results

### 3.1. Steady state and transient spectra of 10-HBQ

The absorption spectrum of 10-HBQ in cyclohexane is found in the near UV (see Fig. 1). The first band at around 380 nm can be safely assigned to the  $S_1 \leftarrow S_0$  ( $\pi\pi^*$ ) transition [15,16]. The second one located below 340 nm is most likely the absorption to the  $S_2$  state, where the exact character of this state is not yet clear. To quantify the contribution of the two states for excitation at different wavelengths, we modeled the absorption spectrum as a sum of five Gaussian spectral features (see Fig. 1S of the Supplementary data). This simple decomposition suggests that at 380 nm only the  $S_1$  state is excited, at 350 nm 75%  $S_1$  and 25%  $S_2$  and at 310 nm nearly exclusively  $S_2$ .

The  $S_1 \leftarrow S_0$  band displays a characteristic vibronic structure with the first two peaks separated by about 1200  $\text{cm}^{-1}$ . This means that vibrational excess energy is most likely deposited in normal modes around this value. The normal mode analysis of the geometric distortions upon electronic excitation (see discussion in Section 4.3) indeed identifies a large number of Franck-Condon (FC) active modes in the range between 1000 and 1600  $\text{cm}^{-1}$ . A lesser part of the excess energy will go to the low-frequency modes that are found to be active in the ESIPT.

The emission spectrum peaks around 630 nm, a large Stokes shift typical for proton transfer. The transient transmission spectrum (lower part of Fig. 1) is the sum of ground state bleach (below 400 nm), stimulated emission (around 650 nm) and a very pronounced excited-state absorption peaked at 400 nm. This leads to a zero crossing of the signal at about 600 nm. When inferring population numbers of the states involved in the ESIPT cycle from the transient signal, this superposition has to be kept in mind.

The major features of the transient spectrum are already apparent after 1 ps and only increase slightly up to 20 ps. Afterwards all features decrease simultaneously, indicating no further excited-state processes, but instead the relaxation to the  $S_0$  state. Any involvement of triplet states or conformational changes would be seen as differing time behavior of the ground state bleach and the stimulated emission.

### 3.2. Electronic and nuclear relaxation

The detailed kinetics of the photo initiated processes in 10-HBQ are best investigated with a pump-probe setup with a freely tunable probe wavelength. Typical traces of the transient transmission changes after excitation of the  $S_1$  state (370 nm) are shown in Fig. 2a. Nearly identical results were obtained after excitation with 325 nm pulses. Regardless of the probe wavelength and thereby the specific signature considered, we find an exponential decay at longer times with a time constant of  $292 \pm 20$  ps in excellent agreement with the value  $260 \pm 30$  ps reported before [16]. This is the  $S_1$  relaxation dominated by internal conversion. The same behavior is found after excitation with 325 nm pulses in accord with the expected rapid internal conversion from the  $S_2$  to the  $S_1$  state.

In the range up to 30 ps an additional exponential component with a time constant of 10.5 ps is found independent of the pump and probe wavelength. Very similar observations were reported in previous time resolved investigations of 10-HBQ with a value of 8–10 ps [15] and 8.3 ps [16]. Our measurements (compare Fig. 2b and c) show that for all combinations of pump and probe wavelengths this component appears as a transmission rise, i.e. a decrease of the transient absorption. In the transient spectra we find no reshaping of the spectral features in the first 50 ps and a general increase of the transmission throughout the observed range from 330 to 730 nm.

From the NOPA–NOPA experiments (Fig. 3) we find a third exponential component at very early times. Due to the strongly modulated signal (see below) the exact value of the decay time depends very much on the fitting model. Such a signal contribution has already been reported before and the values of 330 fs [15] and 350 fs [16] fall within the range observed by us. We will refer to it as “350 fs” component in the following.

The 350 fs time constant was attributed by Chou et al. [15] to vibronic relaxation from the keto  $S'_2(L_b)$  state orig-

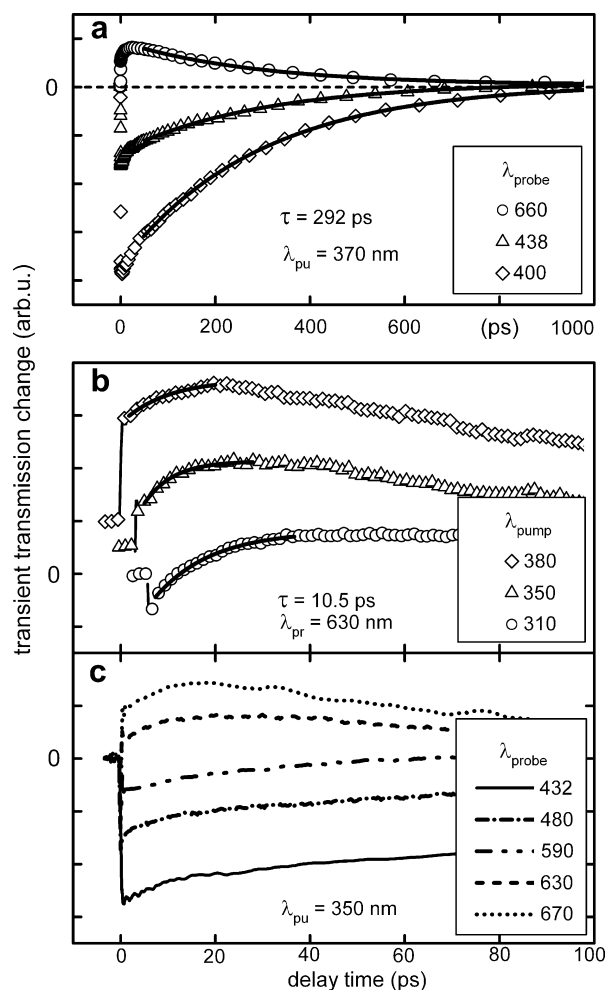


Fig. 2. (a) Transient whitelight transmission of 10-HBQ in cyclohexane after excitation with 370 nm pulses. The curves at all detection wavelengths can be modeled (solid lines) with a single exponential relaxation and the same time constant of 292 ps. (b) For varying pump wavelengths and a probe wavelength of 630 nm a 10.5-ps transmission increase (solid lines) with a varying relative amplitude is found in two-color measurements. (c) Transmission change for 350 nm excitation and selected whitelight wavelengths.

inally populated by ultrafast ESIPT to a supposedly lower lying  $S'_1(L_a)$  state. Takeuchi and Tahara [16] argue convincingly that such a 350 fs vibronic relaxation would destroy the vibrational coherence and is therefore in contradiction to the clear observation of wavepacket motion (see below). In addition, our own quantum chemical calculations followed the evolution of the system from the FC point to the keto minimum and show no evidence for a lower lying electronic state (see Fig. 4S of the Supplementary data). In conclusion, we follow Ref. [16] and assign the 350 fs component to internal vibrational redistribution. We found a similar contribution also for the ESIPT in HBT [5].

The previous reports assign the 10.5 ps relaxation component to vibrational cooling of 10-HBQ by the solvent [15,16]. This is certainly a process that is frequently observed in similar sized molecules and solvents and we agree that it contributes to the experimental signals. A

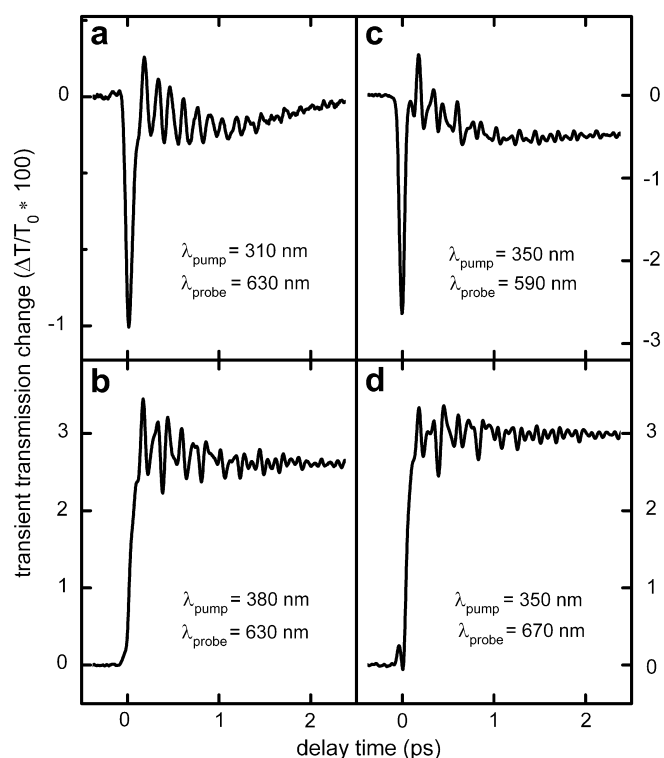


Fig. 3. Transient transmission changes for 10-HBQ in cyclohexane for various excitation and detection wavelengths. All curves were recorded for a temporal resolution of about 40 fs. The pronounced oscillatory contributions are due to vibronic wavepackets in keto-10-HBQ.

cooling process should, however, lead to narrowing and shifting of transient bands. We do not find large enough restructuring of the spectra to match the sizable amplitudes of the 10.5 ps relaxation contribution. The same arguments would hold for a possible electronic process in 10-HBQ. Therefore we have to identify an additional contribution to the decrease of the transient absorption observed over the range from 330 to 730 nm.

In addition to the electronic excitation of 10-HBQ the pump pulse also ionizes some solvent molecules via multiphoton absorption. The resulting free electrons are rapidly solvated [24]. For cyclohexane the spectrum of the solvated electron extends from the middle of the UV to the NIR with a weak peak at around 450 nm and only a variation of the transient absorption by a factor of two over the range from 330 to 730 nm. In the pure solvent the lifetime of the solvated electron is in the sub-nanosecond range. For various solutions investigated in our laboratory we have found that the lifetime is drastically reduced. This is in accord with reports by other groups [25,26], and times in the low picosecond range are quite frequent. We therefore tentatively attribute the major part of the 10.5 ps absorption decay to the decay of the solvated electron concentration.

Further experimental evidence for this assignment stems from two observations contained in Fig. 2. The decrease of the pump wavelength leads to a drastic change of the transmission observed at 630 nm right after the excitation. The net signal changes from transmission to absorption (see

Fig. 2b). Since the ionization of the solvent is a multiphoton process, it is easily rationalized that the higher pump photon energy will lead to a higher yield of solvated electrons. Moreover, comparison of the experimental curves shows that in the NOPA–NOPA experiments (Fig. 2b) the 10.5 ps contribution is more pronounced than in the whitelight measurements (Fig. 2c). Since the latter were recorded with a tenfold lower concentration, the influence of the solute on the electron kinetics is less pronounced. Whether the decay corresponds to a direct geminate recombination or a solute mediated process, is not yet understood and needs further investigation. For the present context of ESIPT it is only relevant that we do not have to consider an additional 10.5 ps process in 10-HBQ.

### 3.3. Proton transfer and wavepacket motion

The NOPA–NOPA measurements with a temporal resolution of better than 30 fs allow the direct observation of the ESIPT and the associated wavepacket dynamics in addition to the slower exponential components discussed above. Selected traces are shown in Fig. 3, a number of further ones were recorded and evaluated and will be used for the discussion. Close to zero delay-time between pump and probe, we either find an increased transmission (Fig. 3b and d) or a pronounced negative spike (Fig. 3a and c). For HBT we have previously discussed this behavior in great detail [5]. The pump pulse promotes the molecules into the  $S_1$  state and the excited-state absorption sets in instantaneously as a negative transient transmission over the whole observation wavelength range. With a short delay the stimulated emission out of the keto  $S_1$  state can be seen in the range of the spontaneous emission spectrum as positive contribution that signals the ESIPT. The two opposite signal contributions partially cancel afterwards, but cause the characteristic spike of Fig. 3a and c in the first tens of femtoseconds. At some detection wavelengths the excited-state absorption of the enol 10-HBQ is weak and the spike is not detected. The originally generated vibronic wavepacket moves ballistically along the adiabatic PES and the delayed rise of the transmission results instead of the more usual exponential increase. As discussed in Section 3.1, the net signal after the initial 350 fs IVR relaxation is dependent on the probe wavelength (see Fig. 1) and through the solvated electron contribution also on the pump wavelength.

In addition to the population kinetics discussed so far, very pronounced oscillatory contributions are found in all curves of Fig. 3, in accord with earlier reports [16]. These can be safely attributed to wavepacket motion in the keto  $S_1$  state [5]. As the probe wavelength is tuned down to 480 nm the oscillations rapidly disappear. This is due to the nearly flat spectral dependence of the transient spectrum [27]. The fact that the slope of the total transient spectrum and not of the stimulated emission spectrum determines the strength of the oscillatory contribution is an indication that the excited-state absorption spectrum is also periodically shifted by the vibronic motion.

The variation of the pump wavelength down to 310 nm results in excitation mainly to the  $S_2$  state (see Section 3.1 and Fig. 1). Even in this case there are strong indications of wavepacket motion following the ESIPT. The lack of any significant changes in the transient spectrum after 325 nm excitation and all the NOPA–NOPA measurements with 310 nm excitation lead us to conclude that the internal conversion  $S_2 \rightarrow S_1$  must proceed extremely fast and most probably directly feeds the ESIPT channel. Due to this high speed, the nuclear wavepacket does not spread dramatically and an oscillatory component amounting to at least 50% of that observed after 350 or 380 nm excitation is seen (compare Fig. 3a and b).

The analysis of the NOPA–NOPA traces was performed by fitting a model function to the data that accounts for the ballistic proton transfer (instantaneous excited-state absorption and time delayed onset of emission) [5] and up to three exponential contributions. The delay-time of the rise of about 24 fs is identified as the time the molecular wavepacket needs to reach the product region of the potential energy surface: the proton transfer time. The oscillating signal contributions are modeled by four damped cosine functions to extract the frequencies of the oscillations. With appropriately fitted parameters, the model function can accurately reproduce the experimental data. The consistency of the parameters is checked by their dependence on the probe wavelength [5]. The fitted values are compiled in Table 1.

The fitted frequencies of the oscillations and their amplitudes can be compared with Fourier transform spectra of the experimental curves (Fig. 4). There is an excellent match between the two ways of analyzing the data. The three higher frequencies (235, 393 and 545  $\text{cm}^{-1}$ ) agree with the ones seen previously [16]. Our temporal resolution does not allow us to uniquely identify the 692  $\text{cm}^{-1}$  mode

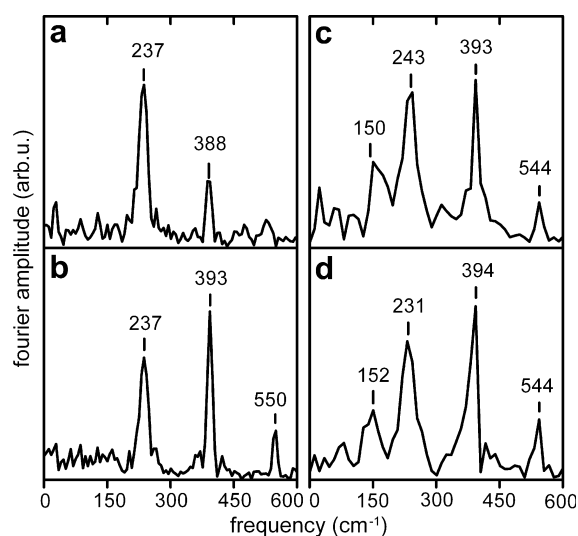


Fig. 4. Fourier transformations of the oscillatory contributions of the pump-probe traces shown in Fig. 3. The labels indicate the frequency positions of the major peaks. (a)  $\lambda_{\text{pump}} = 310$  nm,  $\lambda_{\text{probe}} = 630$  nm; (b)  $\lambda_{\text{pump}} = 380$  nm,  $\lambda_{\text{probe}} = 630$  nm; (c)  $\lambda_{\text{pump}} = 350$  nm,  $\lambda_{\text{probe}} = 590$  nm; (d)  $\lambda_{\text{pump}} = 350$  nm,  $\lambda_{\text{probe}} = 670$  nm.

reported in Ref. [16]. Both the fit and the Fourier analysis do, however, show a low-frequency mode at 149  $\text{cm}^{-1}$  not reported before. Takeuchi and Tahara point out, that the beating between higher modes can easily be seen at the difference frequency [16]. Indeed, the difference between 393 and 235  $\text{cm}^{-1}$  amounts to 158  $\text{cm}^{-1}$ , close to the 149  $\text{cm}^{-1}$ , but the long damping times and the large amplitude of the low-frequency mode still leave the possibility open that we do observe true wavepacket motion in an additional mode. As will be shown in Section 4.3, there is no appropriate in-plane mode in 10-HBQ, instead the fundamental or the overtone of an out-of-plane mode might be observed.

For a more detailed understanding of the experimental observations and the underlying ESIPT process a microscopic model has to be developed. This is best based on first principle calculations for electronic structure and the nuclear dynamics associated with the electronic rearrangement constituting the proton transfer. To this end we employed *ab initio* methods, classical molecular dynamics and 2D wavepacket propagation.

## 4. Computational details

### 4.1. Geometry optimizations and vertical excitation energies

The calculations of equilibrium geometry, vertical and adiabatic excitations for the ground state ( $1^1A'$ ) and the  $\pi\pi^*$  ( $2^1A'$ ) state of HBT and 10-HBQ were performed at DFT/TDDFT [28–30] and RI-CC2 [31,32] levels using the TURBOMOLE package [33]. The B3LYP [34] functional and the SVP [35] basis were used.  $C_s$  symmetry of the nuclear framework has been imposed in all cases. The stationary points were characterized by harmonic analysis. The computational level was systematically tested in terms

Table 1

Experimentally determined proton transfer times  $t_{\text{PT}}$ , wavepacket frequencies  $\tilde{\nu}_i$ , and corresponding amplitudes  $A_i$  and damping times  $\tau_i$  for 10-HBQ

$\lambda_{\text{pump}}$ [nm]	310	350	350	380
$\lambda_{\text{probe}}$ [nm]	630	590	670	630
$t_{\text{PT}}$ [fs]	27.4	23.9	46.6	44.8
$A_{\text{resid.}}$	−0.30	−0.91	2.98	2.63
$\tilde{\nu}_1$ [ $\text{cm}^{-1}$ ]		155	144	148
$A_1$		0.42	0.15	0.09
$\tau_1$ [ps]		0.73	0.97	0.85
$\tilde{\nu}_2$ [ $\text{cm}^{-1}$ ]	234	238	229	237
$A_2$	0.23	0.20	0.49	0.59
$\tau_2$ [ps]	0.61	0.48	0.53	0.61
$\tilde{\nu}_3$ [ $\text{cm}^{-1}$ ]	393	395	391	394
$A_3$	0.04	0.11	0.24	0.24
$\tau_3$ [ps]	1.18	0.94	1.49	1.32
$\tilde{\nu}_4$ [ $\text{cm}^{-1}$ ]		547	541	547
$A_4$		0.03	0.07	0.05
$\tau_4$ [ps]		3.98	1.53	1.80

$A_{\text{Resid.}}$  is the residual signal amplitude after 350 fs.

of methods and basis set for HBT and other systems undergoing ES IPT [6].

#### 4.2. Potential energy surface for the wavepacket dynamics

Potential energy surfaces were calculated for the ground state  $S_0$  ( $1^1A'$ ) and the first singlet excited-state  $S_1$  ( $2^1A'(\pi\pi^*)$ ) state for 10-HBQ and HBT using a grid in the  $R_{OH}$  and  $R_{ON}$  distances (see Scheme 1) consisting of 408 points. Values of  $R_{OH}$  were chosen in the interval of 0.85–2.50 Å with a step size of 0.05 Å and for  $R_{ON}$  ranged from 2.1 to 3.2 Å with a step size of 0.1 Å. At each grid point (fixed values of  $R_{OH}$  and  $R_{ON}$ ) the remaining coordinates were optimized for the  $S_1$  state. The  $S_0$  surface was calculated using these optimized geometries. This is meaningful, since the  $S_0$  surface is only needed to calculate the ground state vibrational wave function used as starting condition for the description of the pump pulse interaction. The calculations for the ground state were carried out at the DFT(B3LYP)/SVP level and the excited-state was calculated using the TD-DFT(B3LYP)/SVP approach. A contour plot of the excited-state surface is shown in Fig. 5 for 10-HBQ. Similar plots are shown for the ground and excited-states of 10-HBQ and HBT (Figs. 2S and 3S of the Supplementary data). Cuts along the proton transfer coordinate of both systems are also shown in Supplementary data (Fig. 4S).

#### 4.3. Normal mode analysis along the reaction path in the $S_1$ state

The potential energy surface computed for 10-HBQ (see previous subsection) has been used to determine a reaction path (minimum energy path = MEP) starting from the

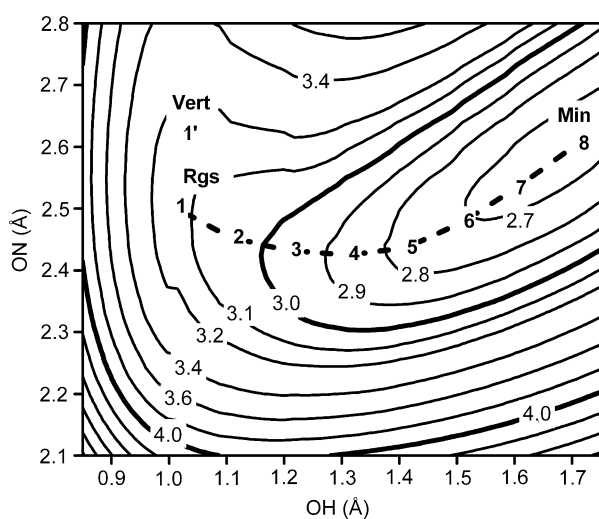


Fig. 5. Excited-state potential energy surface for 10-HBQ in terms of the ON and OH coordinates. Selected points along the minimum energy path are labeled 1–8. 1' Vert indicates the approximate position of the Franck-Condon point. 1 Rgs is obtained by keeping the ground state OH distance at the enol minimum and relaxing all other coordinates in the  $S_1$ . Energies are given in eV relative to the minimum of the ground state.

point labeled “Rgs/1” (Fig. 5). This point has been obtained using the OH distance of the ground state minimum and optimizing the remaining coordinates in the  $S_1$  state. For comparison, the vertical excitation and its approximate position are also depicted in Fig. 5 (Vert/1'). This point, however, is not contained in the geometry space of our two-dimensional energy surface since its geometry has been optimized for the ground state and not for the excited-state. The variation of the ON and OH values along the reaction path are collected in Table 1S of the Supplementary data.

In order to perform the normal mode analysis (NMA) along the reaction path [36], selected geometries belonging to the path (see the PES and the points  $j \in \{1, \dots, 8\}$  in Fig. 5) are projected onto the normal mode basis obtained at the excited-state keto minimum ( $K^*$ ). We then analyze how much of each eigenmode must be added to an equilibrium configuration to result in the molecular structure found at the point of interest on the reaction path. The NMA follows the path indicated in Fig. 5 from the FC (= Rgs)-region where the molecule is still close to the geometric structure of the enol ground state, crosses the “transition region” approximately at point 3, and proceeds towards point 8 where the geometry is close to the excited keto 10-HBQ tautomer.

Combining the positions of all nuclei in 10-HBQ in a 72-dimensional vector  $X = (q_1^T, q_2^T, \dots, q_{24}^T)^T$  and introducing a solution vector  $C = (C_i)$  of equal dimension this analysis is stated as the matrix problem:

$$X_{\text{ref}} - X_j = \Theta_{\text{ref}} C. \quad (1)$$

In Eq. (1),  $X_{\text{ref}}$  is the equilibrium geometry  $K^*$  of the excited-state.

For the equilibrium configuration  $X_{\text{ref}}$  the  $72 \times 72$  matrix  $\Theta_{\text{ref}}$  comprises all 66 eigenvectors of vibration as well as the translation of the center of mass and the rotation of the entire molecule to satisfy the Eckart conditions [36]. It is crucial to minimize the influence of relative translation and rotation between  $X_{\text{ref}}$  and  $X_j$  to ensure solution vector entries  $C_i$  that describe only vibrational contributions. A detailed outline of the method can be found in Ref. [36].

#### 4.4. Wavepacket dynamics

Wavepacket propagations on the 2D PES spanned by the coordinates  $R_{OH}$  and  $R_{ON}$  in 10-HBQ have been performed for the first 300 fs. The change in the ON distance reflects the contraction of the chelate ring, one prominent feature for the proton transfer as shown in our previous work on HBT [12]. Earlier wavepacket studies on different proton transfer systems [37,38] as well as our NMA analysis for HBQ (see Sections 4.3 and 5.2) further support this choice of coordinates. The system Hamiltonian reads

$$H = \begin{pmatrix} T_{\text{nuc}} + V_{S_0} & -\mu_{01} \cdot \varepsilon(t) \\ -\mu_{01} \cdot \varepsilon(t) & T_{\text{nuc}} + V_{S_1} \end{pmatrix} \quad (2)$$

with the kinetic part of the Hamiltonian

$$T_{\text{nuc}} = -\frac{1}{2M_{\text{OHN}}} \Delta(R_{\text{OH}}) - \frac{1}{2M_{\text{ON}}} \Delta(R_{\text{ON}}) \quad (3)$$

and

$$M_{\text{OHN}} = \frac{m_{\text{H}}(m_{\text{O}} + m_{\text{N}})}{m_{\text{H}} + m_{\text{O}} + m_{\text{N}}} \quad (4)$$

$$M_{\text{ON}} = \frac{m_{\text{O}} \cdot m_{\text{N}}}{m_{\text{O}} + m_{\text{N}}}$$

where  $V_{S_0/S_1}$  denotes the 2D potential energy surfaces of the  $S_0$  and  $S_1$  state, respectively. The off diagonal elements represent the laser coupling with  $\mu_{01}$  the transition dipole moment and  $\varepsilon(t)$  the electric field of the laser pulse. The transition dipole moment  $\mu_{01}$  between  $S_0$  and  $S_1$  is set to 1 Debye and the laser field  $\varepsilon(t)$  is treated semi-classically, as the size of the molecule is much smaller than the wavelength of the pump pulse. Transform limited 30 fs Gaussian pulses (FWHM of the intensity) were used in all wavepacket propagations, corresponding to the experimental pulse length at 350 and 385 nm excitation.

The time-dependent Schrödinger equation

$$i \frac{\partial}{\partial t} \begin{pmatrix} \Psi_{S_0}(t) \\ \Psi_{S_1}(t) \end{pmatrix} = H \begin{pmatrix} \Psi_{S_0}(t) \\ \Psi_{S_1}(t) \end{pmatrix} \quad (5)$$

with the system Hamiltonian described by Eq. (2) is solved applying the split-operator method (SPO) [39] for the propagator.

The initial wave function is the lowest vibrational eigenfunction of the ground state potential  $S_0$  which has been determined by a relaxation method, using propagation in imaginary time plus an additional diagonalization step [40]. In the same way we obtained the vibrational energy levels of the  $S_0$  and the  $S_1$  state for the reduced 2D model.

#### 4.5. Classical dynamics

Classical dynamics simulations were performed for HBT and 10-HBQ on the first singlet-excited-state ( $S_1$ ) energy surface. For each system, 35 trajectories have been simulated during 100 fs with time step 0.5 fs. The Velocity–Verlet algorithm [41] was applied to solve the Newton's equations of nuclear motion. The Born–Oppenheimer energies and gradients were obtained by means of the TD-DFT(B3LYP) approach. The SV(P) basis set [35] was used for all atoms except the migrating hydrogen atom, to which the polarization functions of the full SVP basis set were added. The initial conditions for each trajectory were generated by sampling the coordinates and momenta so as to reproduce the ground-vibrational quantum harmonic distribution of the electronic ground state. Only initial conditions for which the  $S_0$ – $S_1$  excitation energy was within a window of  $\pm 0.25$  eV of the calculated vertical excitation energy of the ground state equilibrium geometry (HBT: 3.68 eV, 10-HBQ: 3.36 eV) were accepted. This corresponds to a temperature of the molecule of 0 K. The ground-state geometry and velocity were used as initial

conditions for the trajectory in the excited-state. The classical dynamics simulations were performed with the NEWTON-X program package [20,42] using TD-DFT calculations performed with the TURBOMOLE program package.

## 5. Computational results

### 5.1. Vertical excitation energies and the potential energy surfaces

For HBT, geometry optimizations, vertical excitation energies and proton transfer curves have been already presented in Ref. [6]. For 10-HBQ, TDDFT and RI-CC2 vertical and adiabatic excitations relative to the ground state energy are shown in Table 2. The calculated values agree well with the experimentally observed values for the maximum of the absorption and emission spectrum. In the ground state an energy minimum has been found only for the enol-form of HBT and 10-HBQ. Searches for ground state minima on the keto side have been carried out also starting from the keto structure of the excited-state. Nevertheless, geometry optimizations always led back to the enol-form. In the excited-state no energy minimum was found for the enol structure. The keto structure is a true energy minimum for 10-HBQ. The total Stokes shift (B3LYP/SVP) is the sum of the energy difference of the  $S_1$  minimum (keto) and the FC point of  $5660 \text{ cm}^{-1}$  and the corresponding energy difference in the  $S_0$  state of  $5499 \text{ cm}^{-1}$ .

HBT shows one imaginary frequency corresponding to torsion around the CC bond connecting the phenyl ring and the benzothiazole ring. This coordinate is found to be not of importance for the ultrafast ESIPT discussed here, but it is relevant for the internal conversion on a picosecond time scale.

As can be seen in the contour plots of the 10-HBQ and HBT  $S_1$  surfaces (Fig. 5 and Figs. 2S, 3S and 4S of the Supplementary data), the FC region is connected to the minimum in the  $S_1$  state by a barrierless path. This path is, however, curved and a one dimensional trajectory just along the OH coordinate encounters a substantial barrier.

Table 2

TD-DFT and RI-CC2 vertical (vert.) and minimum-to-minimum (m.-m.), absorption energies (eV) for 10-HBQ relative to the ground-state energy minimum

Geometry	Transition	B3LYP/SVP	RI-CC2/SVP	exp.
gr.st.	vert. ( $\pi\pi^*$ )	3.35	3.64	3.26
gr.st.	vert. ( $n\pi^*$ )	4.57	4.86	
$\pi\pi^*$ (keto)	m.-m. ( $\pi\pi^*$ )	2.66	2.57	
$n\pi^*$ (enol)	m.-m. ( $n\pi^*$ )	4.16	4.38	
$n\pi^*$ (keto)	m.-m. ( $n\pi^*$ )	3.18	2.92	
$\pi\pi^*$ (keto)	fl. ( $\pi\pi^*$ )	1.97	1.71	1.98
$n\pi^*$ (enol)	fl. ( $n\pi^*$ )	3.66	3.81	
$n\pi^*$ (keto)	fl. ( $n\pi^*$ )	2.23	1.50	

(fl.) denotes vertical fluorescence transitions from the excited-state to  $S_0$ .

For the dynamic process it becomes immediately clear, that the actual reaction path has to be multi-dimensional. There is a strong gradient of the PES in the FC region that constitutes the driving force for the molecular deformation that leads to the ESIPT.

### 5.2. Normal mode analysis along the reaction path

The comparison of the results from the transient transmission measurements in the  $S_1$  state and a normal mode analysis reveals that at least four low-frequency modes are involved in the ESIPT of 10-HBQ. To fully understand their dynamical interplay and relative significance we investigated the connection between the normal modes and the structural changes along the  $S_1$  MEP on the calculated 2D  $S_1$  PES. To this end NMA [36] is performed for selected points on the  $S_1$  reaction path (see Fig. 5).

The absolute values of the solution coefficients  $C_i$  for  $X_{\text{ref}} = X_{K^*}$  in Eq. (1) are displayed in Fig. 6. At the bottom of the figure we show the position of the calculated frequencies, in-plane modes are displayed as upward sticks, out off plane modes as downward ones. For clarity, we restrict the graphical presentation to  $<1000 \text{ cm}^{-1}$ .

The modes in the range below  $1000 \text{ cm}^{-1}$  predominantly belong to vibrations involving the entire molecular backbone. Modes in the fingerprint region ( $1000\text{--}1600 \text{ cm}^{-1}$ ) start to behave increasingly local with rising frequency until they are restricted around  $3000 \text{ cm}^{-1}$  to the motion of a few hydrogen atoms only. Among the highest modes, the mode at  $3060 \text{ cm}^{-1}$  is highly localized in the NH relative motion and does not involve the remaining structure. Nearly all modes in the fingerprint region contribute mod-

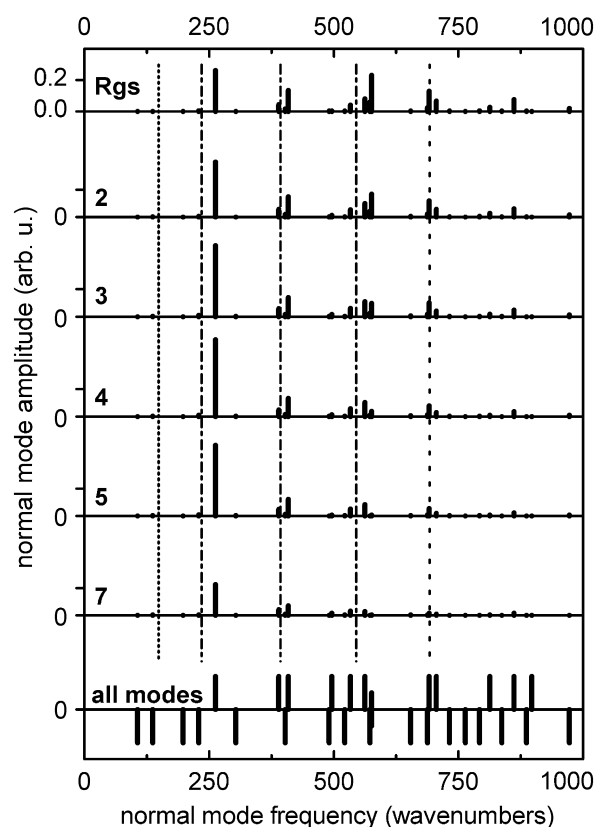


Fig. 6. Absolute values of the coefficients of the normal mode analysis for 10-HBQ. The points along the minimum energy path are chosen according to Fig. 5. In the bottom panel all normal modes are displayed, the in-plane modes as upward sticks, the out-off plane modes as downward sticks. The dash-dotted lines indicate the frequencies of the experimentally observed oscillations both by us and in Ref. [16]. The dashed line is observed only in Ref. [16], the dotted line only in the present experiment.

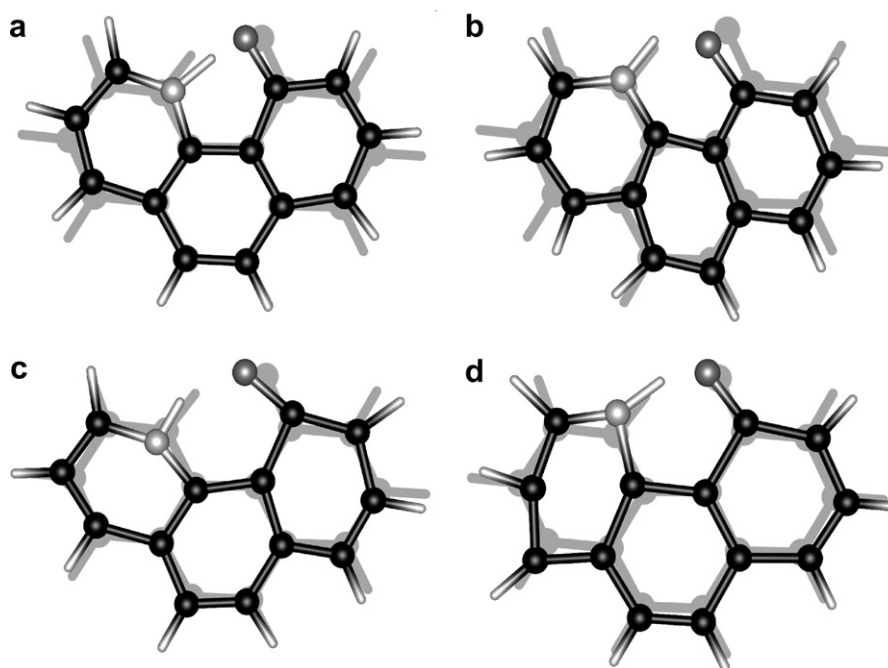


Fig. 7. Selected normal modes for the  $S_1$  state of keto-10-HBQ (N atom in light color) that are relevant for the ESIPT process. The undistorted geometry is shown shaded in each part of the figure. (a)  $262 \text{ cm}^{-1}$  mode, (b)  $409 \text{ cm}^{-1}$  mode, (c)  $576 \text{ cm}^{-1}$  mode, (d)  $690 \text{ cm}^{-1}$  mode.

erately to the molecular distortion at the FC point. They are, therefore, FC active in the electronic transition and can explain the observed vibronic structure of the absorption spectrum (Fig. 1 and Section 3.1).

Four  $K^*$  normal modes in the frequency range below  $1000\text{ cm}^{-1}$  contribute significantly along the minimum energy path. The three energetically higher ones each belong to a group of similar vibrations. Their contributions are large near the FC-region and constantly decrease progressing to the keto minimum in accordance with the nuclear rearrangement from the enol to the keto tautomer. In the energy range between  $1000$  and  $1600\text{ cm}^{-1}$  the mode contributions follow the same pattern. All these vibrations are in-plane motions with contributions involving the NH bending motion.

Only the low energy vibrations can contribute to the experimentally observed wavepacket dynamics. In the NMA we find four dominant contributions shown in Fig. 7: (a) the  $262\text{ cm}^{-1}$  mode is a bending motion of the two outer phenyl rings leading to the contraction of the chelate ring, (b) the group of modes at  $389$  and  $409\text{ cm}^{-1}$ , which are asymmetric stretching modes of the central phenyl ring, (c) the group at frequencies of  $533$ ,  $562$ ,  $572$  and  $576\text{ cm}^{-1}$  and (d) the pair of frequencies at  $690$  and  $705\text{ cm}^{-1}$ . Groups (c) and (d) comprise asymmetric stretching vibrations in all three phenyl rings. All these modes are in-plane motions and strongly modulate the ON distance. The most prominent mode at  $262\text{ cm}^{-1}$  is the only mode that passes through an amplitude maximum

along the reaction path (compare Fig. 6) and can be regarded as the driving coordinate of the ESIPT.

To summarize the vibrational analysis: We identified four in-plane low-frequency normal modes, more precisely groups of modes, that match the experimental findings of  $235$ ,  $393$ ,  $545$  and  $692\text{ [16] cm}^{-1}$  within the approximations made in the calculation. The small deviations may also arise from solvent effects, as the calculations are pure gas phase simulations while the experiments are performed in solution. The  $262\text{ cm}^{-1}$  mode is the dominant contribution, reinforcing the idea that it is the driving mode in the ESIPT. All other contributing modes have decreasing amplitude coefficients  $C_i$  along the MEP starting near the FC-point versus the keto minimum.

### 5.3. Nuclear wavepacket dynamics associated with the proton transfer

To obtain a detailed insight into the short time dynamics of the first 300 fs of the ESIPT in 10-HBQ, we performed wavepacket propagations on the 2D PES spanned by the coordinates  $R_{\text{OH}}$  and  $R_{\text{ON}}$ . The ON coordinate describes the contraction of the chelate ring promoting the proton transfer. The wavepacket propagation starts in the vibrational ground state of  $S_0$  ( $T = 0\text{ K}$ ) and explicitly takes into account the interaction with the exciting femtosecond pulse.

Two different pump pulse intensities were tested in close connection to the experiment. For the pump pulse duration

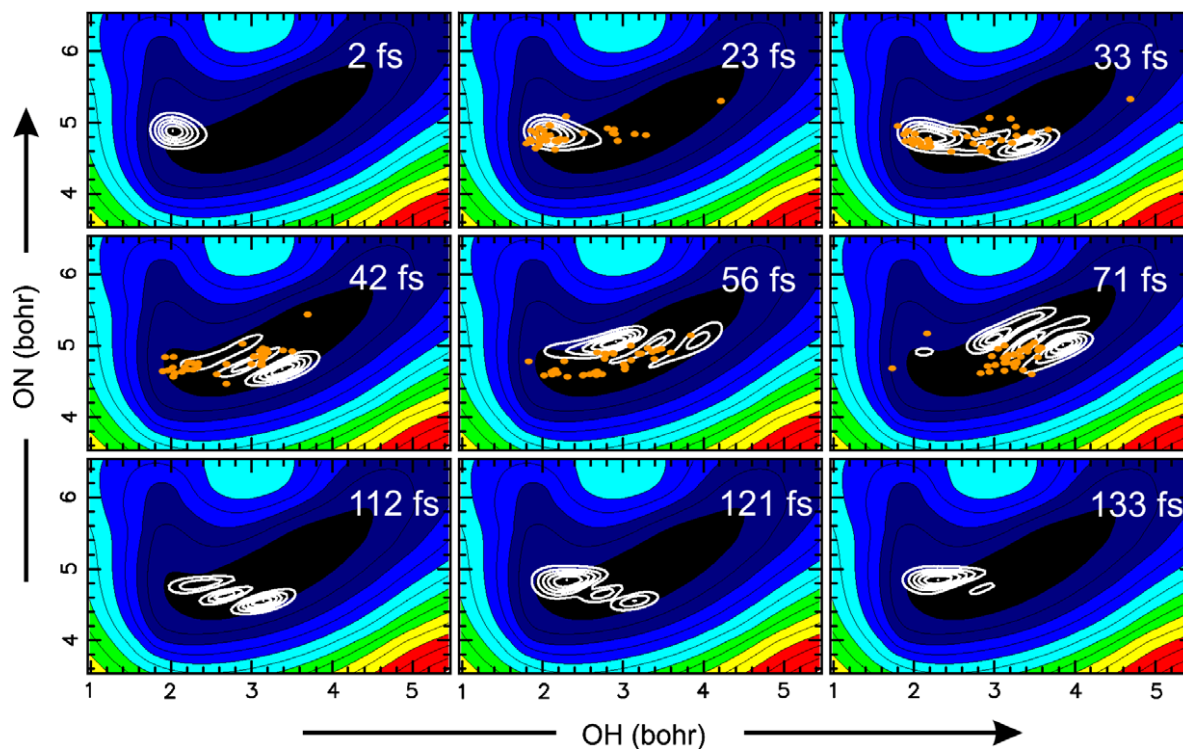


Fig. 8. Snapshots of the wavepacket propagation in the ON–OH space during the first 133 fs. The superimposed orange dots show the values of these coordinates for all classical trajectories at the same time.



of 30 fs FWHM the experimental conditions amount to an intensity of 34 GW/cm<sup>2</sup> and this peak intensity renders a quantum efficiency for absorption of around 1%, i.e. it guarantees that multi-photon excitation does not occur. Changing the intensity to 1720 GW/cm<sup>2</sup> increased the absorption efficiency in the 2D model to above 70%, yet the wavepacket dynamics stayed the same. The latter value was therefore taken to visualize the dynamics. The center frequency of the pump pulse was either tuned to the vertical excitation energy or to 0.1 eV below. This again produced identical wavepacket dynamics. For the figures shown in this work, the vertical excitation energy was chosen.

Snapshots of the wavepacket dynamics are depicted in Fig. 8 for the first 133 fs. Additional snapshots up to 376 fs are shown in Fig. 5S of the Supplementary data. The time zero (0 fs) corresponds to the maximum of the pump pulse. A localized wavepacket is prepared at the coordinates of the enol ground state minimum and immediately starts to evolve along the OH coordinate. Simultaneously it develops a nodal structure along this mode. The amplitudes in the wave function oscillate on the time scale of the vibrational period  $T_{\text{OH}} = 21$  fs. The center of gravity moves somewhat slower to the keto minimum at  $R_{\text{OH}} = 3.21$  bohr. To interpret the wavepacket dynamics, we have to look at the vibrational eigenfunctions.

The calculated vibrational levels of the 2D model used for the description of the S<sub>1</sub> state correspond to the vibrational motion along the OH and ON coordinates and their combinations. Selected eigenfunctions are shown in Fig. 9; the nodal structure of the OH modes is seen from upper left to lower right, the one of the ON modes from lower left to upper right. We use the notation ( $\nu_{\text{OH}}, \nu_{\text{ON}}$ ) for a detailed description and the index  $\nu = 0, 1, \dots$  to label the combination levels according to their energetic order. The fundamental of the OH mode lies at 1592 cm<sup>-1</sup> and the fundamental of the ON mode at 390 cm<sup>-1</sup>. The ON mode lies in the range of the skeletal normal modes involving the central phenyl ring and induces the contraction of the chelate ring. The OH vibration responds to the wide keto potential and is therefore significantly reduced from the value of the enol-form. The spectral width (FWHM of the electric field) of the pump pulse corresponds to about 1000 cm<sup>-1</sup> and is sufficient to superimpose 3 or 4 quanta of ON vibration, but only one OH vibrational level. We thus expect a localized wavepacket that evolves along the ON direction.

Comparison of the wavepacket with the eigenfunctions shows a strong similarity of the wavepacket at later times with the  $\nu = 12$  state, the first overtone of the OH vibration ( $\nu_{\text{OH}} = 2, \nu_{\text{ON}} = 0$ ). This means that a major part of the vibrational energy that is generated by the relaxation from the enol FC point to the keto minimum is transferred to the OH mode. Since the nodal structure of the wavepacket is already quite similar to that of the  $\nu = 12$  state in the snapshots at 33, 42 and 56 fs (see Fig. 8), we can deduce that the wavepacket reaches the equilibrium geometry of the keto tautomer after approximately 40 fs.

Due to its kinetic energy, the wavepacket oscillates further – dominantly along the OH coordinate, changing and regaining its nodal structure. Although the total energy is conserved, the wavepacket does not return to its starting geometry. The wavepacket has spread and it is now trapped in the wide keto potential.

For a detailed analysis and in particular to understand the unexpected motion of the wavepacket in the OH coordinate and not the ON coordinate that could be coherently excited by the pump pulse, we project the wavepacket onto the vibrational eigenfunctions (see Fig. 9 top). Only selected vibrational states contribute – pure ON states do not contribute, only states with OH character participate. The limited spectral width of the pump pulse only makes a single OH excitation accessible ( $\nu_{\text{OH}} = 2$ ) the remaining contributions are combination modes with  $\nu_{\text{ON}} = 1-3$ . Thus the wavepacket dynamics for the ESIPT follow the OH coordinate with small but necessary deviations in the direction of the ON coordinate.

The determination of the 40 fs transfer time that is in close agreement with the experimental finding allows us to justify the choice of the particular form of the S<sub>1</sub> PES used. As discussed in Section 4.2 the coordinates beyond  $R_{\text{OH}}$  and  $R_{\text{ON}}$  were relaxed for the S<sub>1</sub> state. In an independent study, molecular dynamics calculations were used to estimate the time needed for the geometrical relaxation from the FC point to the nearby potential minimum to be slightly below 10 fs. For the unrelaxed geometry the gradient of the PES can be expected to be slightly larger leading to an even faster acceleration of the wavepacket. So our conclusion of the ultrafast time scale of the PT is certainly valid. At the time the wavepacket reaches the crossing to the keto region, where the unrelaxed PES might potentially display a barrier, the geometric relaxation has already been completed and the use of the relaxed geometry is fully justified.

#### 5.4. Classical dynamics associated with the proton transfer

Fig. 10 shows the time evolution of the distances  $R_{\text{OH}}$  and  $R_{\text{NH}}$  averaged over all trajectories for HBT (a) and 10-HBQ (b). The standard deviations for the average values are shown by the shaded areas. In the analysis of the classical dynamics, we have defined the time for the proton transfer as the average time for which the OH and NH distances equal. This time is 36 fs for HBT and 30 fs for 10-HBQ (Fig. 10 and Table 3). The time evolution of several other internal coordinates is given in Figs. 6S and 7S of the Supplementary data.

The decisive feature of the proton transfer for both systems is the decrease of the ON distance before the OH distance starts to increase significantly. This kind of motion is related to low-frequency skeletal modes of the system, as discussed in the previous sections. An analysis of the time evolution of the distances  $R_{\text{ON}}$  and  $R_{\text{OH}}$  (Fig. 11a) shows that for HBT the process takes place in four steps as illustrated in Fig. 11b. (1) The proton transfer starts with an

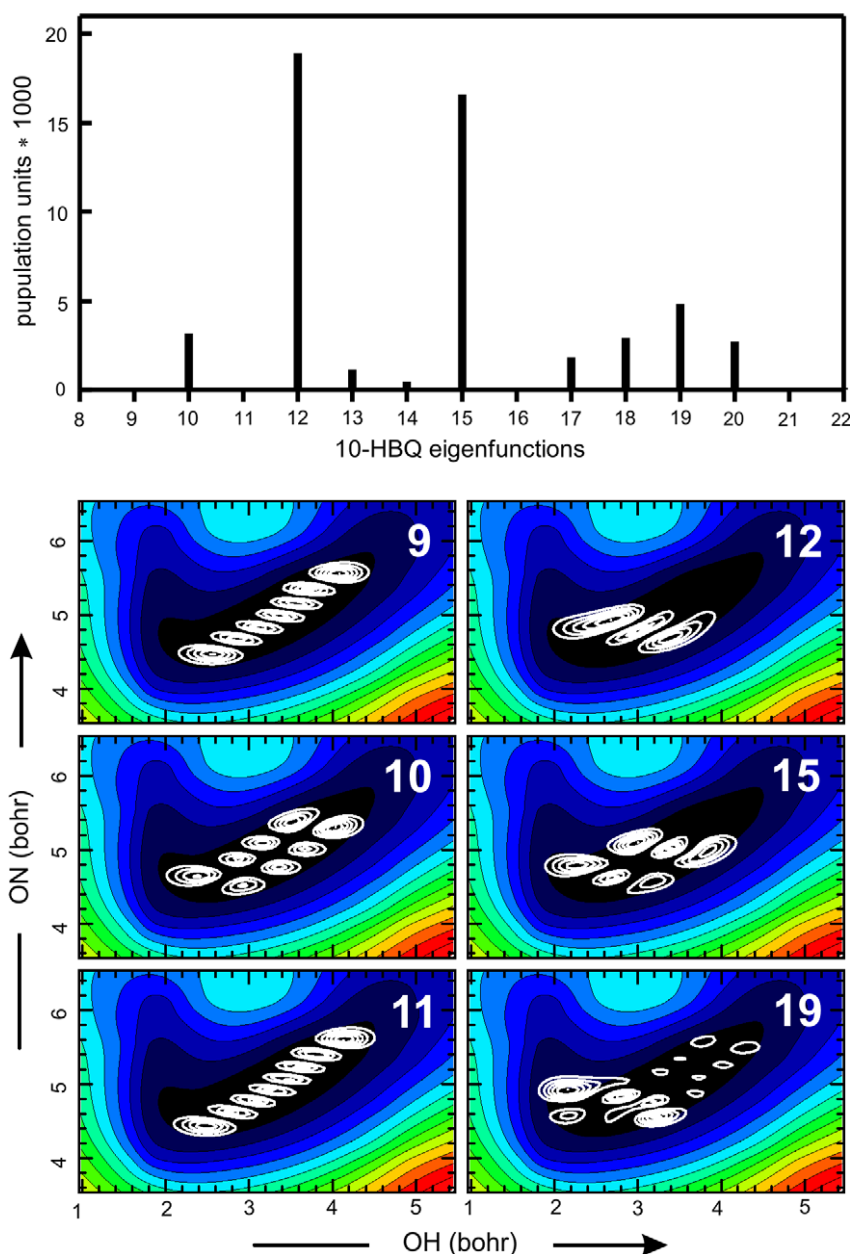


Fig. 9. Vibrational modes contributing to the wavepacket of 10-HBQ. Upper panel: Projection of the pump pulse induced wavepacket onto the 2D vibrational eigenmodes. Exclusively, vibrational modes with nodal modes along the OH coordinate are populated. Lower Panel: Plots of selected vibrational eigenfunctions, the mode number is given as label. Vibrational contributions in OH and ON direction are: mode 9 ( $\nu_{\text{OH}} = 0, \nu_{\text{ON}} = 6$ ), mode 10 ( $\nu_{\text{OH}} = 1, \nu_{\text{ON}} = 3$ ), mode 11 ( $\nu_{\text{OH}} = 0, \nu_{\text{ON}} = 7$ ), mode 12 ( $\nu_{\text{OH}} = 2, \nu_{\text{ON}} = 0$ ), mode 15 ( $\nu_{\text{OH}} = 2, \nu_{\text{ON}} = 1$ ), mode 19 mainly ( $\nu_{\text{OH}} = 3, \nu_{\text{ON}} = 0$ ) character.

OH-bond stretching of about  $0.2 \text{ \AA}$ . (2) After that, the ON distance is reduced while the OH distance stays almost constant. (3) As soon as the ON distance is reduced to  $\sim 2.52 \text{ \AA}$ , the OH-bond starts to increase simultaneously with the reduction of the ON distance. (4) When the OH distance reaches  $\sim 1.5 \text{ \AA}$ , the ON distance increases again and the transfer is complete. Moreover, a few oscillations in the ON and OH distances are observed in the last stage of the proton transfer. It is remarkable that in 10-HBQ a quite similar proton transfer mechanism seems to be in effect (see Fig. 11c) even though this molecule is much more

rigid than HBT. This enhanced rigidity leads to a significantly smaller change of the ON distance. The motions for HBT and 10-HBQ are compared in a schematic way in Fig. 11b.

In principle, the ESIPT can proceed in three different ways as illustrated in Fig. 12: (i) the hydrogen stretching mode plays an active role in the entire process (Fig. 12a), with the transfer depending only on the OH stretching without involving any skeletal distortion (active mode), (ii) the skeletal distortion described by the initial approach of the O and N atoms triggers the hydrogen migration

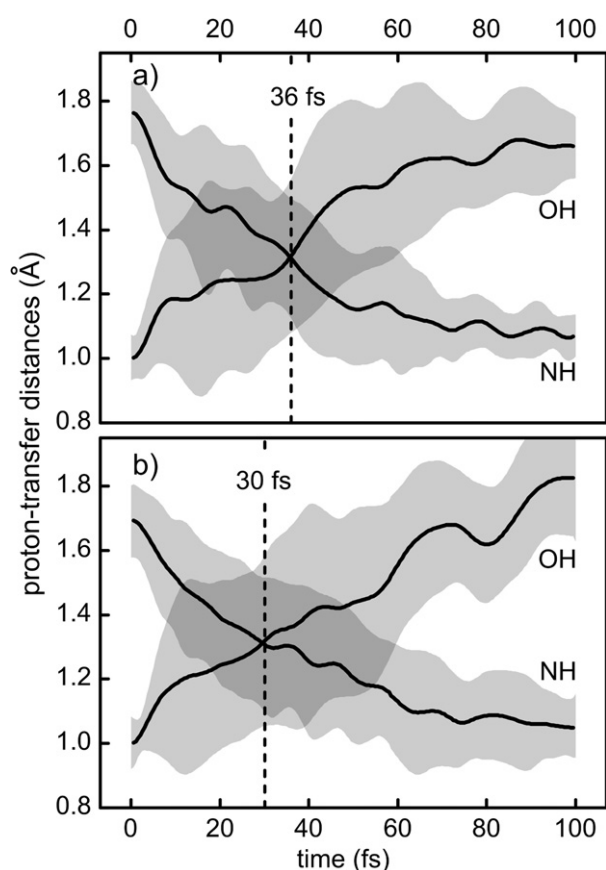


Fig. 10. Time evolution of the OH and NH distances averaged over all trajectories for (a) HBT and (b) 10-HBQ. The solid curves correspond to the average values and the shaded areas give the standard deviation.

Table 3

Proton transfer time according to the several methods employed in this and previous works

	Time (fs)	
	HBT	10-HBQ
Experimental	33	25
Wavepacket dynamics	–	40
Classical dynamics	36	30

mode (semi-passive mode) (Fig. 12b), and (iii) the proton transfer can be completely dominated by the skeletal distortion, without any substantial contribution of the hydrogen migration mode (passive mode) (Fig. 12c). Comparing Fig. 11b) with Fig. 12 it is clear that while for 10-HBQ the ESIPT corresponds to the semi-passive case, the V shape in HBT is clearly passive.

The difference between HBT and 10-HBQ can be understood in terms of the flexibility of their structures. The steric hindrance restricts the ON approach considerably more in 10-HBQ than in HBT, explaining why the OH stretching is more pronounced in 10-HBQ than in HBT. This difference in the geometrical restrictions can be seen, for example, in the time evolution of the  $C_bN$  coordinate (Figs. 6S and 7S in the Supplementary data). During the proton transfer, the

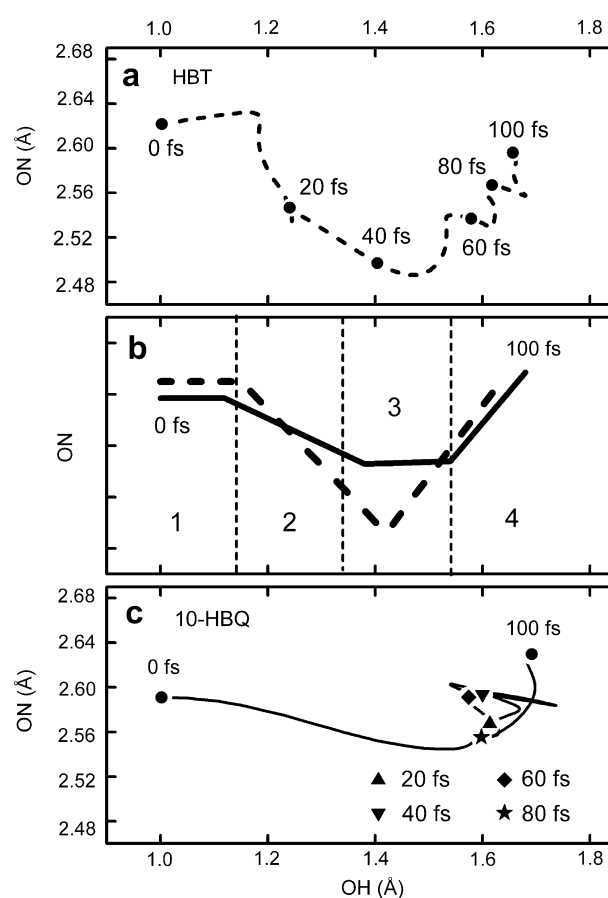


Fig. 11. Average trajectory (100 fs) projected onto the OH and ON coordinates for (a) HBT and (c) 10-HBQ. (b) Scheme illustrating the steps in the proton transfer for both systems (HBT: dashed line, 10-HBQ: solid line).

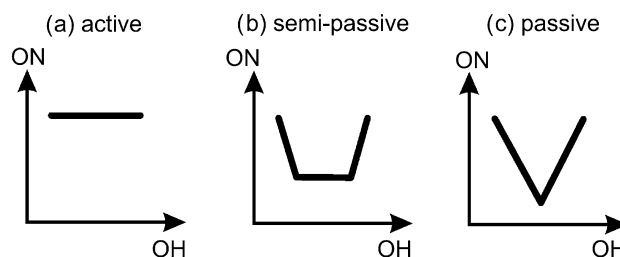


Fig. 12. Three qualitatively different courses of the ESIPT reaction regarding behavior of the O(donor)H...N(acceptor) moiety. Depending on the change of the OH and ON distances, the role of the proton can be described as (a) active, (b) semi-passive, and (c) passive.

mean value of this coordinate has a maximum variation of 0.07 Å for HBT and of only 0.04 Å for 10-HBQ.

As a result of the structural isomerization, a  $C=O$  double bond should form. The detection of the vibrational band corresponding to this bond has been a main experimental evidence for the formation of the keto structure after the photoexcitation [3]. This effect can be seen in the classical trajectories by monitoring the CO bond length during the trajectories (see Figs. 6S and 7S of the Supplementary data). At the beginning of the dynamics, the aver-

age of the CO bond length is 1.34 Å for both, HBT and 10-HBQ. As soon as the proton transfer takes place, the CO bond length drops to an average value of 1.28 Å in the case of HBT and 1.30 Å in 10-HBQ. On the other hand, the standard deviation from these averages increases with time, which has an important implication for the determination of the energy-receptor modes, as we shall discuss in the Section 5.5.

Hynes and coworkers discussed proton transfer in the adiabatic and nonadiabatic limit [43,44]. If we consider the enol and keto regions of the PES as separate electronic configurations, such an approach might be useful. The calculations for both 10-HBQ and HBT and the ultrafast transfer time clearly show that effectively there is no barrier for the ESIPT. This means that the coupling is extremely strong and along the MEP the transfer has to be considered as adiabatic. For 10-HBQ the small degree of ON approach is responsible for the fact that even for the direct connection from the FC point to the keto minimum no significant barrier is found. The flexibility of HBT leads to a fairly large barrier that is circumvented on the MEP. In this sense the ESIPT of HBT would seem to show increased nonadiabaticity, but the correct consideration of the involvement of the skeletal motion leads back to the adiabatic regime.

### 5.5. Comparison between wavepacket and classical dynamics

Both the wavepacket dynamics and the classical trajectories aim at modeling the ultrafast ESIPT observed in the experiment. The classical calculation is able to consider all 66 vibrational degrees of freedom, but neglects the wave character of the nuclei, i.e. the delocalization and the nodal structures. The wavepacket propagation on the other hand is restricted to few selected coordinates for technical reasons, in the present case to 2D. Still it is most interesting to compare the respective results.

The corresponding values of the OH and ON bond lengths computed for all classical trajectories are displayed as orange dots in the snapshots for the wavepacket motion of 10-HBQ (Fig. 8). At the beginning of the dynamics, before the proton transfer takes place, the classical trajectories for 10-HBQ spread somewhat faster than the quantum wavepacket, spanning a much wider region of the ON–OH space. After the transfer (see snapshots between 42 and 71 fs in Fig. 8) the quantum wavepacket strongly spreads on the surface, due to its vibrational components of the wide keto potential (see Section 5.3), while the classical distribution becomes more localized.

The localization of the classical trajectories in a restricted region of the ON–OH space indicates that an energy flow exists from the ON and OH vibrations to other modes. If the standard deviation of the distances is taken as an approximate measure for the available kinetic energy contained in the respective bond, the search for receptor modes in the classical trajectories can be done by looking for correlations between the standard deviation of the active modes (ON or OH) and the standard deviation of

other modes. From the analysis of the time evolution of the coordinates shown in Figs. 6S and 7S of the Supplementary data, the  $C_dO$  and  $C_bN$  stretching modes emerged as the best candidates for receptor modes. In Fig. 13 the standard deviation of the  $C_dO$  and  $C_bN$  distances as functions of the standard deviation  $\delta$  for the ON distance is plotted in the course of the dynamics. Starting at approximately 45 fs (therefore, just after the proton transfer) there is an overall negative correlation between the standard deviations of the ON and the  $C_dO$  average distances. This means that during this time, the reduction in the ON distribution of amplitudes corresponds directly to the increase of the  $C_dO$  distribution. Starting approximately at the same time, the negative correlation is also observed between the ON and  $C_bN$  standard deviations. The quantum results do not show the same reduction of the ON distribution as they are restricted to two-dimensions and no energy dissipation is included. The wavepacket oscillates in the keto potential spreading and refocusing (see e.g. Fig. 8, snapshot at 133 fs) according to its revival times. The steric hindrance for the ON motion, which leads to a pronounced hydrogen migration in the classical trajectory calculations, is reflected in the wavepacket dynamics in the exclusive participation of OH and OH combination modes. It is worth noting that mainly in the  $C_dO$  curve, the negative correlation at 80 fs turns into an opposite but attenuated pattern, indicating back-transfer of energy to the ON mode. This may well correspond to the long lasting vibrational coherences observed in the experiment, which can not yet be reproduced by the calculations because of the limited time range investigated.

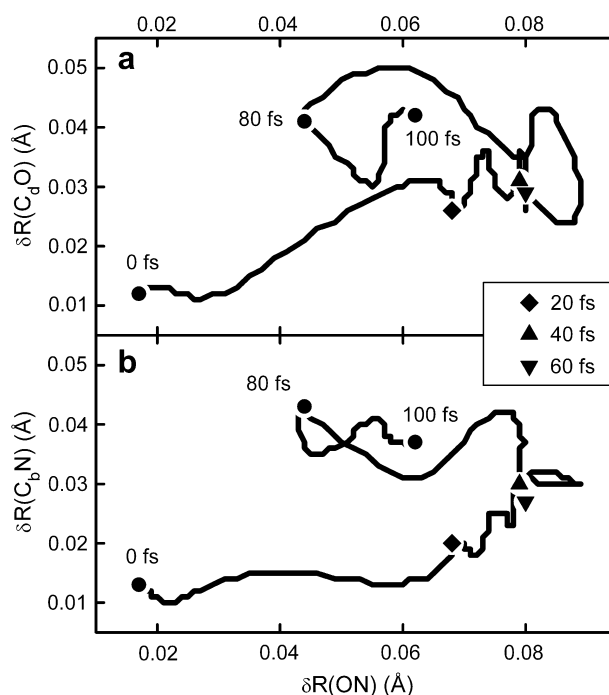


Fig. 13. (a) 10-HBQ: Standard deviation of the  $C_dO$  and (b)  $C_bN$  average distances in function of the standard deviation of the ON average distance plotted in the course of the dynamics.

## 6. Comparison between theoretical and experimental results

The first and most direct question that the combined experimental and theoretical efforts can answer is the speed of the proton transfer. Usually a rate model is assumed for such a process, implying a probability that is directly proportional to the educt state population. This concept does not hold for processes that are equally fast as the nuclear motions. In the case of the ESIPT in both 10-HBQ and HBT the optically prepared nuclear wavepacket evolves on the adiabatic  $S_1$  PES to the point where the switching from the electronic enol configuration to the keto one happens with unity probability.

As a consequence, it is not trivial to define a unique proton transfer time. In the experiment the first appearance of stimulated emission from the keto form is taken as a measure for the completion of the ESIPT. Depending on the choice of probe wavelength the time varies between 24 and 45 fs for 10-HBQ. In the wavepacket calculation the emergence of the nodal structure at  $\sim 40$  fs seems to be a good signature. In the trajectories an equal OH and NH distance is used to signal the ESIPT. We believe that this time of 30 fs for 10-HBQ corresponds to the switch of the electronic configuration.

Despite the differing criteria, the three methods render a very consistent picture for the ESIPT time. As soon as the molecule is sufficiently deformed, the actual proton transfer can happen. Since there is no barrier in the PES, the deformation and the ESIPT happen on the time scale of the nuclear motions at  $\sim 35$  fs.

After the ESIPT a fraction of  $\sim 6000\text{ cm}^{-1}$  of the electronic excitation energy is converted to vibrational energy. The experiment clearly shows that a major part of this energy ends up as coherent vibrational motion. The dynamic calculations show first indications of such behavior, but more extensive work is needed to explicitly reproduce the 350 fs IVR time and the picosecond dephasing of the wavepacket motion. In this context it is important to note that the experiment was performed at 297 K, while both sets of calculations assumed  $T = 0$  K. The significant thermal population of the many low-frequency modes at room temperature might explain some of the remaining differences. In particular thermally excited out-of-plane modes might be the cause of the experimentally observed  $149\text{ cm}^{-1}$  motion. Simulations of the pump-probe signal would be most helpful to decide, whether the lowest frequency oscillatory signal is indeed a vibrational mode or rather due to a nonlinear coupling of the contributions of higher frequencies with a frequency difference equal to the observed one.

## 7. Conclusions

The excited-state proton transfer in 10-HBQ was investigated in this work by means of different theoretical and experimental methodologies, namely quantum wavepacket propagation, classical dynamics simulation, and transient

absorption experiments. All results converge to a scenario in which the proton transfer takes place in the ultrafast time scale of 30–40 fs by means of skeletal deformation, rather than by simple hydrogen migration. Very similar conclusions were derived from earlier work on HBT [5,12] and the additional evidences presented in this work. In both systems these skeletal deformations display as main effect the shortening of the ON distance in such a way that the hydrogen atom can barrierlessly form the new bond to nitrogen, moving to its final position. In HBT, the skeletal deformations are the main responsible modes for the transfer, with the proton having only a passive role. On the other hand, in 10-HBQ, the hydrogen migration mode is only activated by the skeletal deformation modes and the OH stretch plays a more active role. The agreement between the quantum and classical results is additional evidence that the ESIPT process takes place in 10-HBQ without tunneling. In particular, if the tunneling was a dominant process, the classical time for proton transfer should be much longer than the quantum time.

Although classical and quantum dynamics agree on the time scale of the process and in the role of the skeletal deformation, the limitations of each approach are illustrated by direct comparison of the results. It is not surprising to find that the classical approach is unable to describe the nodal structure of the wavepacket in higher vibrational levels, a feature that is nicely revealed by the quantum approach. The limitation of the quantum-propagation to a 2D potential energy surface makes the wavepacket spread into regions of this surface that probably would not be visited at all if all internal degrees were included and the dissipation of energy to receptor modes were allowed. The analysis of the classical trajectories indicates that the  $C_dO$  and  $C_bN$  bond lengths are the main candidates as receptor modes.

Starting from the earlier interpretation of the ESIPT dynamics in HBT it is actually surprising that the much stiffer 10-HBQ undergoes ultrafast proton transfer. According to our calculated  $S_1$  PES this is due to the strong gradient in the FC point and the lack of any barrier on the minimum energy path to the keto type minimum. As a consequence of the stiffer geometry, the relevant skeletal modes are up-shifted in frequency and this actually yields the somewhat faster ESIPT in 10-HBQ. In both cases the role of the proton itself is rather passive.

In 10-HBQ the typical constriction of the chelate ring that was found to dominate the molecular deformation in HBT [5,12] is hindered and therefore does not contribute strongly. As a consequence the distribution of the vibrational energy available after the ESIPT is quite different for 10-HBQ as compared to HBT and related compounds like TINUVIN-P and HBO. In HBT we argued that most of the energy goes to the low-frequency modes [5,12] and this view agrees with the observed lack of high mode excitation seen in IR measurements [19,45]. For TINUVIN-P a low-frequency proton transfer promoting mode was found as a major accepting mode of the proton transfer cycle [46].

Even more directly, For HBO it was found that high-frequency modes are not directly excited by the ESIPT, while for modes below  $1000\text{ cm}^{-1}$  substantial excess populations were observed [47]. For 10-HBQ, in contrast, we have found from the combined investigations of this work that a high-frequency mode with OH character is populated and only a comparatively small amount of the vibrational excess energy goes to the low-frequency modes. In this way the rigid structure of 10-HBQ influences the vibrational activity much more than the ESIPT process itself.

### Acknowledgements

This work was supported by the Austrian Science Fund within the framework of the Special Research Program F16 (Advanced Light Sources), Project P18411-N19 and by the DFG-Cluster of Excellence: Munich-Centre for Advanced Photonics. We are grateful for technical support and computer time at the Linux PC cluster Schrödinger III of the computer center of the University of Vienna. Support from the Fonds der Chemischen Industrie and the Deutsche Forschungsgemeinschaft (SPP Femtosekunden-Spektroskopie elementarer Anregungen in Atomen, Molekülen und Clustern) is gratefully acknowledged. The authors thank Hans Langhals for providing the sample used in the experimental work.

### Appendix A. Supplementary data

Supplementary data associated with this article can be found, in the online version, at [doi:10.1016/j.chemphys.2007.10.021](https://doi.org/10.1016/j.chemphys.2007.10.021).

### References

- [1] A.L. Sobolewski, W. Domcke, Chem. Phys. Lett. 211 (1993) 82.
- [2] P.F. Barbara, L.E. Brus, P.M. Rentzepis, J. Am. Chem. Soc. 102 (1980) 5631.
- [3] T. Elsaesser, W. Kaiser, Chem. Phys. Lett. 128 (1986) 231.
- [4] T. Arthen-Engeland, T. Bultmann, N.P. Ernstring, M.A. Rodriguez, W. Thiel, Chem. Phys. 163 (1992) 43.
- [5] S. Lochbrunner, A.J. Wurzer, E. Riedle, J. Phys. Chem. A 107 (2003) 10580.
- [6] A.J.A. Aquino, H. Lischka, C. Hättig, J. Phys. Chem. A 109 (2005) 3201.
- [7] A.L. Sobolewski, W. Domcke, C. Hättig, J. Phys. Chem. A 110 (2006) 6301.
- [8] A.L. Sobolewski, W. Domcke, in: D. Heidrich (Ed.), The Reaction Path in Chemistry: Current Approaches and Perspectives, Kluwer, 1995, p. 257.
- [9] A.L. Sobolewski, W. Domcke, Phys. Chem. Chem. Phys. 8 (2006) 3410.
- [10] J.T. Hynes, J.P. Klinman, H.-H. Limbach, R.L. Schowen (Eds.), Hydrogen-Transfer Reactions, Wiley-VCH, Weinheim, 2006.
- [11] A.L. Sobolewski, W. Domcke, Phys. Chem. Chem. Phys. 1 (1999) 3065.
- [12] R. de Vivie-Riedle, V. De Waele, L. Kurtz, E. Riedle, J. Phys. Chem. A 107 (2003) 10591.
- [13] A.L. Sobolewski, W. Domcke, Chem. Phys. 184 (1994) 115.
- [14] C. Chudoba, S. Lutgen, T. Jentzsch, E. Riedle, M. Woerner, T. Elsaesser, Chem. Phys. Lett. 240 (1995) 35.
- [15] P.-T. Chou, Y.C. Chen, W.S. Yu, Y.H. Chou, C.Y. Wei, Y.M. Cheng, J. Phys. Chem. A 105 (2001) 1731.
- [16] S. Takeuchi, T. Tahara, J. Phys. Chem. A 109 (2005) 10199.
- [17] M.L. Martinez, W.C. Cooper, P.-T. Chou, Chem. Phys. Lett. 193 (1992) 151.
- [18] A. Weller, Z. Elektrochem. 60 (1956) 1144.
- [19] M. Rini, A. Kummrow, J. Dreyer, E.T.J. Nibbering, T. Elsaesser, Faraday Discuss. 122 (2002) 27.
- [20] M. Barbatti, G. Granucci, M. Persico, M. Ruckebauer, M. Vazdar, M. Eckert-Maksic, H. Lischka, J. Photochem. Photobiol. A: Chem. 190 (2007) 228.
- [21] A.J. Wurzer, S. Lochbrunner, E. Riedle, Appl. Phys. B 71 (2000) 405.
- [22] E. Riedle, M. Beutter, S. Lochbrunner, J. Piel, S. Schenkl, S. Spörlein, W. Zinth, Appl. Phys. B 71 (2000) 457.
- [23] M. Raytchev, E. Pandurski, I. Buchvarov, C. Modrakowski, T. Fiebig, J. Phys. Chem. A 107 (2003) 4592.
- [24] T.W. Kee, D.H. Son, P. Kambhampati, P.F. Barbara, J. Phys. Chem. A 105 (2001) 8434.
- [25] J.A. Kloepfer, V.H. Vilchiz, V.A. Lenchenkov, A.C. Germaine, S.E. Bradforth, J. Chem. Phys. 113 (2000) 6288.
- [26] C. Xia, J. Peon, B. Kohler, J. Chem. Phys. 117 (2002) 8855.
- [27] W.T. Pollard, S.-Y. Lee, R.A. Mathies, J. Chem. Phys. 92 (1990) 4012.
- [28] R. Bauernschmitt, R. Ahlrichs, Chem. Phys. Lett. 256 (1996) 454.
- [29] R. Bauernschmitt, M. Haser, O. Treutler, R. Ahlrichs, Chem. Phys. Lett. 264 (1997) 573.
- [30] F. Furche, R. Ahlrichs, J. Chem. Phys. 11 (2002) 7433.
- [31] C. Hättig, J. Chem. Phys. 118 (2003) 7751.
- [32] A. Kohn, C. Hättig, J. Chem. Phys. 119 (2003) 5021.
- [33] R. Ahlrichs, M. Bär, M. Häser, H. Horn, C. Kölmel, Chem. Phys. Lett. 162 (1989) 165.
- [34] A.D. Becke, J. Chem. Phys. 98 (1993) 5648.
- [35] A. Schafer, H. Horn, R. Ahlrichs, J. Chem. Phys. 97 (1992) 2571.
- [36] L. Kurtz, A. Hofmann, R. de Vivie-Riedle, J. Chem. Phys. 114 (2001) 6151.
- [37] N. Doslic, O. Kühn, J. Manz, K. Sundermann, J. Phys. Chem. A 102 (1998) 9645.
- [38] N. Doslic, K. Sundermann, L. Gonzalez, O. Mó, J. Giraud-Girard, O. Kühn, Phys. Chem. Chem. Phys. 1 (1999) 1249.
- [39] C. Leforestier, R.H. Bisseling, C. Cerjan, M.D. Feit, R. Friesner, A. Guldberg, A. Hammerich, G. Jolicard, W. Karrlein, H.D. Meyer, N. Lipkin, O. Roncero, R. Kosloff, J. Comput. Phys. 94 (1991) 59.
- [40] J. Manz, K. Sundermann, R. de Vivie-Riedle, Chem. Phys. Lett. 290 (1998) 415.
- [41] W.C. Swope, H.C. Andersen, P.H. Berens, K.R. Wilson, J. Chem. Phys. 76 (1982) 637.
- [42] M. Barbatti, G. Granucci, H. Lischka, M. Ruckebauer, M. Persico, NEWTON-X: a package for Newtonian dynamics close to the crossing seam, version 0.13b, 2007, <<http://www.univie.ac.at/newtonx>>.
- [43] D. Borgis, J.T. Hynes, J. Phys. Chem. 100 (1996) 1118.
- [44] P.M. Kiefer, J.T. Hynes, Solid States Ionics 168 (2004) 219.
- [45] M. Rini, J. Dreyer, E.T.J. Nibbering, T. Elsaesser, Chem. Phys. Lett. 374 (2003) 13.
- [46] V. Kozich, J. Dreyer, W. Werncke, Chem. Phys. Lett. 399 (2004) 484.
- [47] V. Kozich, J. Dreyer, A. Vodchits, W. Werncke, Chem. Phys. Lett. 415 (2005) 121.

The interplay of skeletal deformations and ultrafast excited state  
intramolecular proton transfer: experimental and theoretical  
investigation of 10-hydroxybenzo[h]quinoline

## Supplementary Material

Christian Schrieber<sup>a</sup>, Mario Barbatti<sup>b</sup>, Kai Stock<sup>a</sup>, Adélia J. A. Aquino<sup>b</sup>, Daniel Tunega<sup>b</sup>,  
Stefan Lochbrunner<sup>a</sup>, Eberhard Riedle<sup>a</sup>, Regina de Vivie-Riedle<sup>c</sup>, Hans Lischka<sup>b</sup>

<sup>a</sup>*Department für Physik – Ludwig-Maximilians-Universität (LMU)  
Oettingenstr. 67, 80538 München, Germany*

<sup>b</sup>*Institute for Theoretical Chemistry – University of Vienna  
Währinger Strasse 17, 1090 Vienna, Austria*

<sup>c</sup>*Department Chemie – Ludwig-Maximilians-Universität (LMU)  
Butenandt-Str. 11, 81377 München, Germany*

Corresponding Authors:

Dr. Mario Barbatti  
Tel.: +43 1 4277 52752  
Fax.: +43 1 4277 9527  
*E-mail address:*  
mario.barbatti@univie.ac.at

Prof. Dr. Hans Lischka  
Tel.: +43 1 4277 52757  
Fax.: +43 1 4277 9527  
*E-mail address:*  
hans.lischka@univie.ac.at

Prof. Dr. Eberhard Riedle  
Tel.: +49 89 2180 9210  
Fax.: +49 89 2180 9202  
*E-mail address:*  
eberhard.riedle@physik.uni-muenchen.de

Prof. Dr. Regina de Vivie-Riedle  
Tel.: + 49 89 21 80 77533  
Fax.: +49 89 21 80 77133  
*E-mail address:*  
regina.de\_vivie@cup.uni-muenchen.de

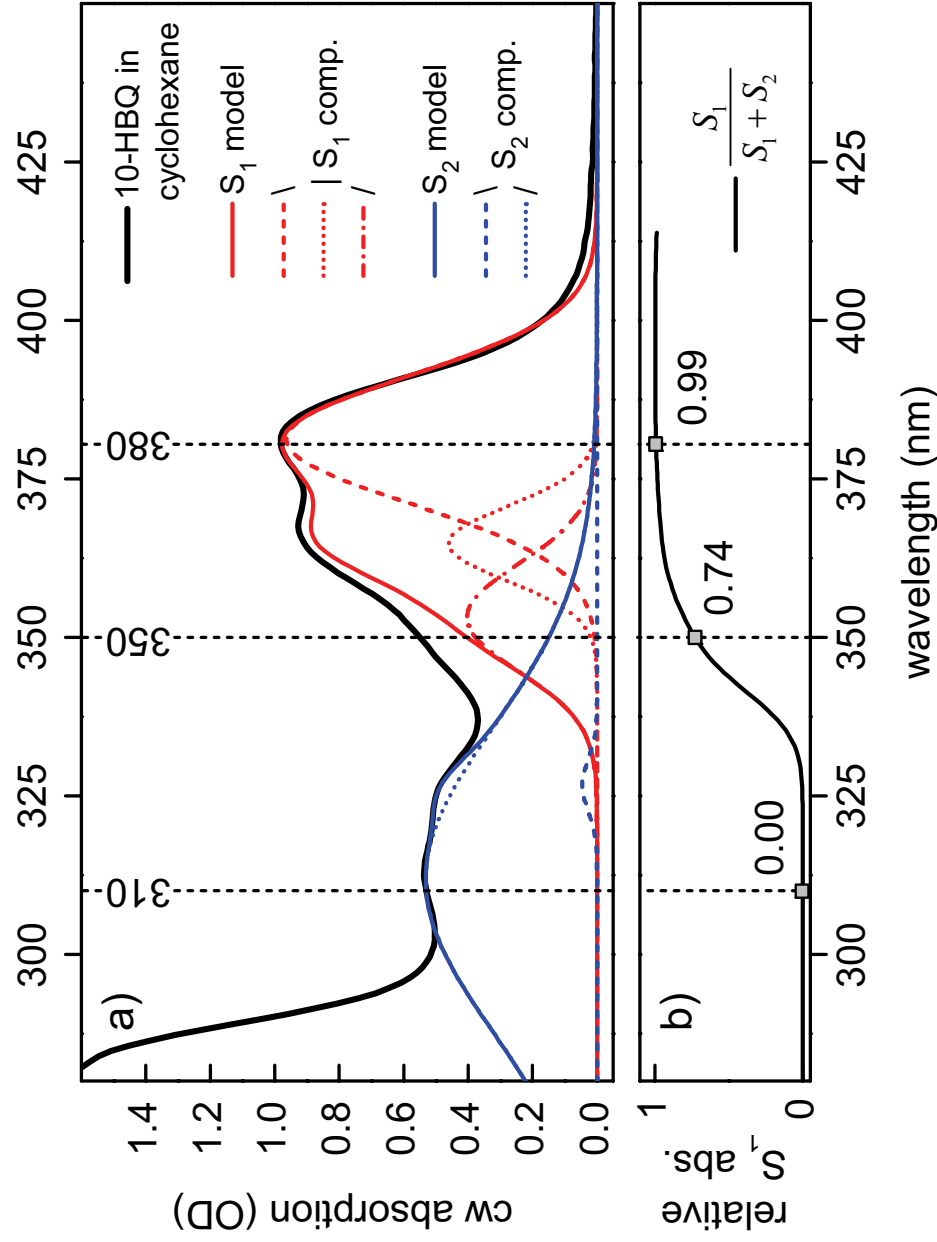


Fig. 1S: a) The 10-HBQ absorption spectrum recorded in cyclohexane (black line) is modeled by a sum of five Gaussian curves ( $S_1$  comp. and  $S_2$  comp.). The sum of the  $S_1$  components is displayed by the red solid trace ( $S_1$  model). The sum of the  $S_2$  components is displayed by the blue solid trace ( $S_2$  model). b) The fraction of the  $S_1$  absorption over the total absorption is computed from the model functions for  $S_1$  and  $S_2$  derived in a). The labels indicate the values of the fraction at the wavelength 310, 350 and 380 nm.



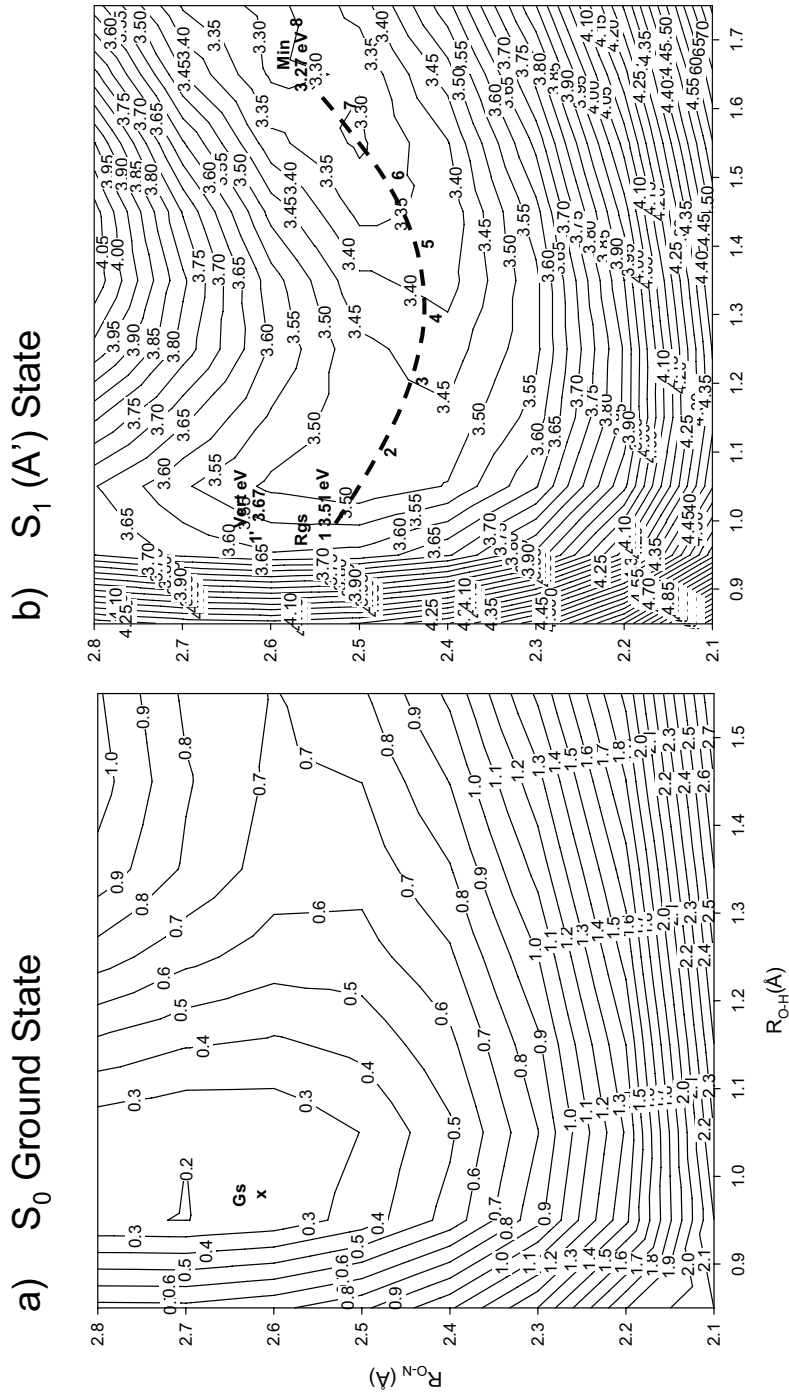


Fig. 2S: 2D potential energy surfaces (PES) of HBT calculated for  $R_{O-H}$  and  $R_{O-N}$ , i.e. the distances between the mobile proton (H) and oxygen (O) and between the nitrogen (N) and oxygen (O), respectively. Energies are given in eV relative to the minimum of the ground state.

a) PES of the ground state calculated at DFT(B3LYP)/SVP level as described in Sec. 4.2 of the manuscript. Gs indicates the ground state minimum calculated for the excited state. b) PES of the excited  $S_1$  ( $2^1A'$  ( $\pi\pi^*$ )) state calculated using the TD-DFT(B3LYP)/SVP approach. Selected points along the minimum energy path are labeled 1-8. 1' Vert indicates the approximate position of the Franck-Condon point. 1 Rgs (=Relaxed ground state) is obtained by keeping the ground state OH distance fixed at the enol minimum and relaxing all other coordinates in the  $S_1$ .

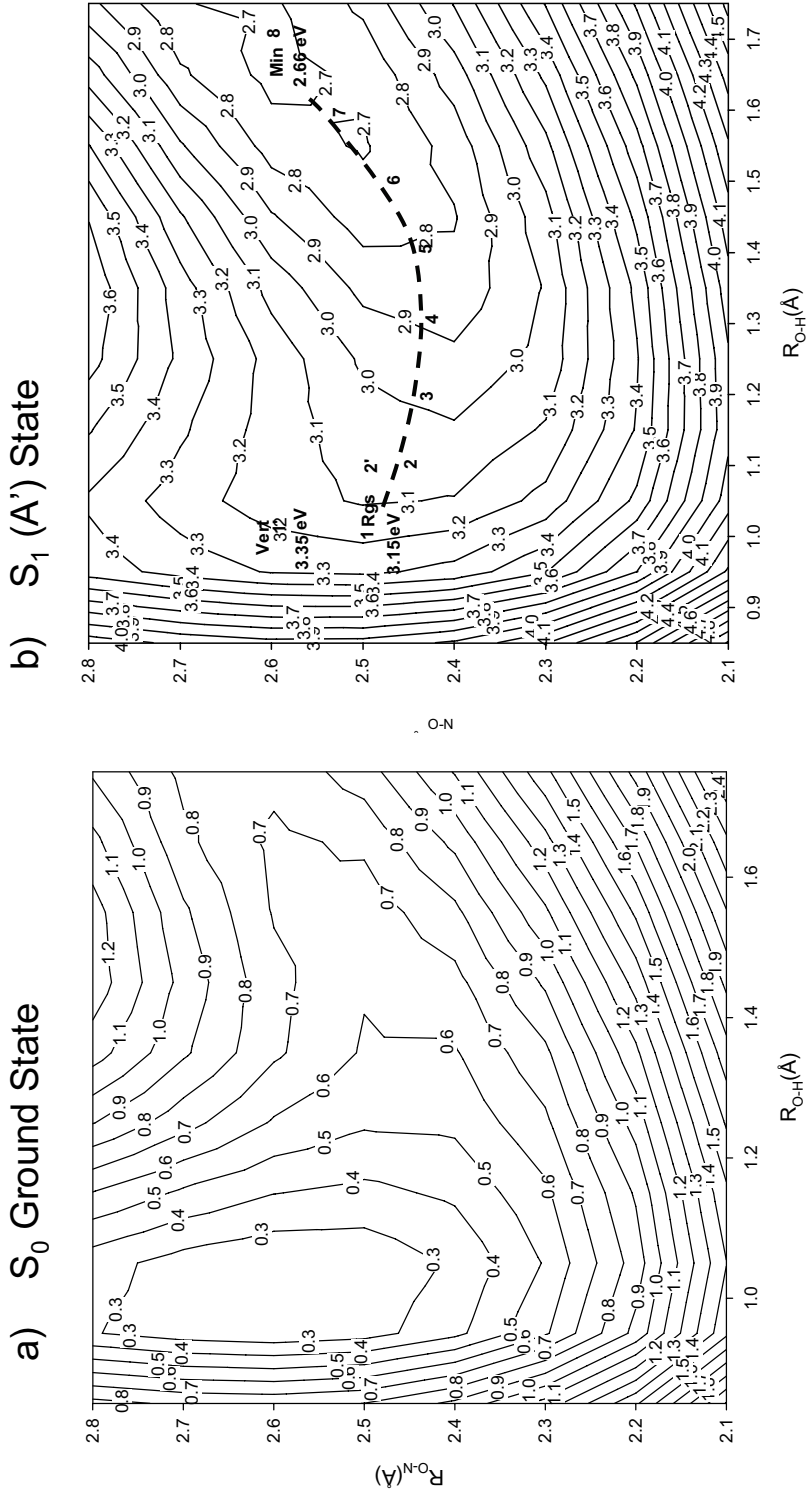


Fig. 3S: a) 2D potential energy surfaces (PES) of 10-HBQ calculated for  $R_{O-H}$  and  $R_{O-N}$ , i.e. the distances between the mobile proton (H) and oxygen (O) and between the nitrogen (N) and oxygen (O), respectively. Energies are given in eV relative to the minimum of the ground state.

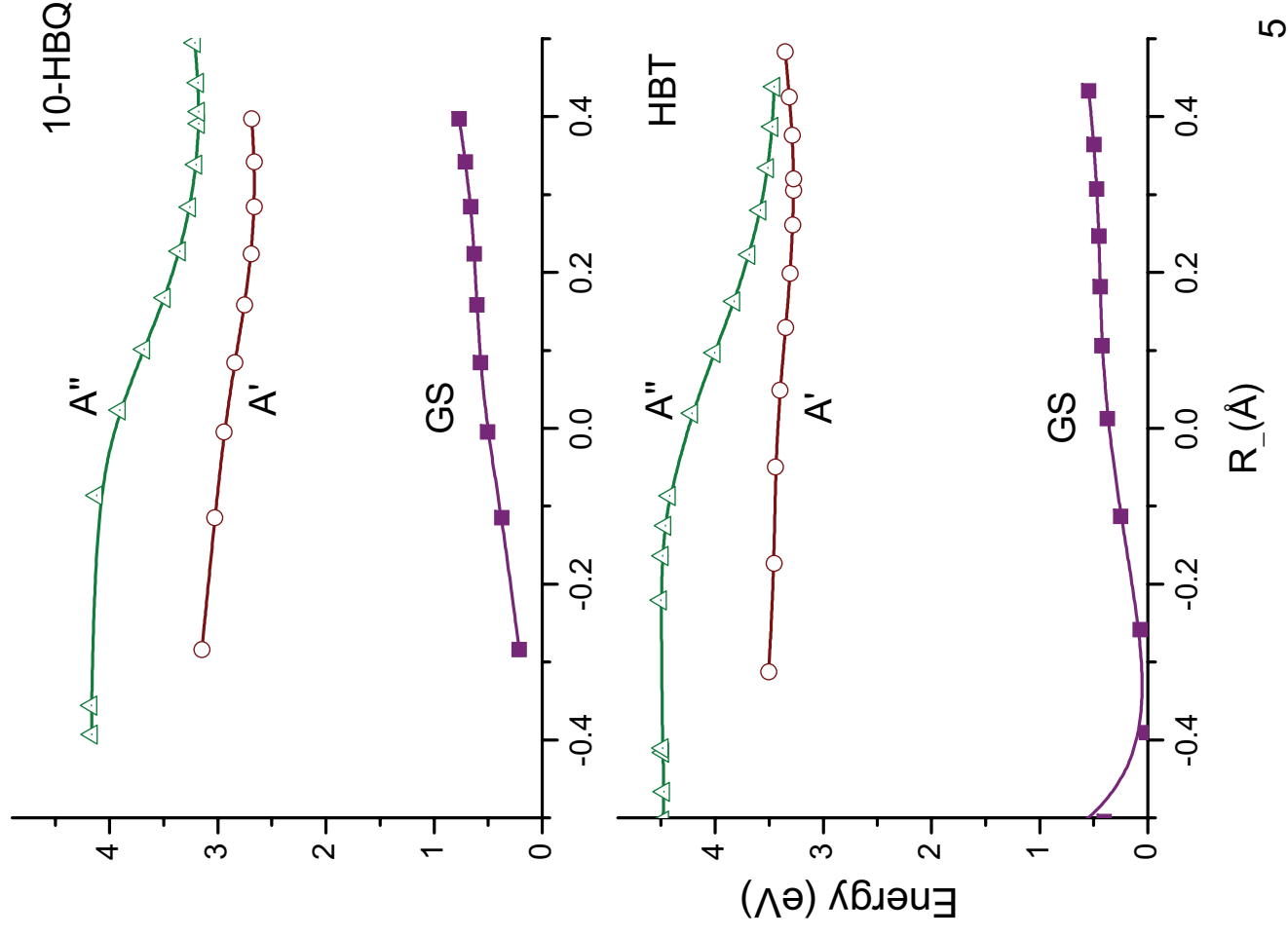
a) PES of the ground state calculated at DFT(B3LYP)/SVP level as described in Sec. 4.2 of the manuscript. b) PES of the excited  $S_1$  ( $2^1A'$  ( $\pi\pi^*$ )) state calculated using the TD-DFT(B3LYP)/SVP approach. Selected points along the minimum energy path are labeled 1-8. 1' Vert indicates the approximate position of the Franck-Condon point. 1 Rgs (=Relaxed ground state) is obtained by keeping the ground state OH distance fixed at the enol minimum and relaxing all other coordinates in the  $S_1$ .

Point	10-HBQ			HBT		
	OH (Å)	ON (Å)	ON (Å)	OH (Å)	OH (Å)	ON (Å)
1' (Vert)	1.000	2.590	2.590	0.995	0.995	2.614
1 (Rgs)	1.000	2.499	2.499	0.995	0.995	2.541
2	1.200	2.489	2.489	1.100	1.100	2.467
2'	1.100	2.489	2.489	-	-	-
3	1.200	2.428	2.428	1.200	1.200	2.433
4	1.300	2.422	2.422	1.300	1.300	2.417
5	1.400	2.439	2.439	1.400	1.400	2.422
6	1.500	2.467	2.467	1.500	1.500	2.467
7	1.600	2.522	2.522	1.600	1.600	2.500
8 (Min)	1.678	2.594	2.594	1.733	1.733	2.569

Table 1S: Bidimensional minimum energy path in the  $S_1$  state of 10-HBQ and HBT. The explicit values for the variation of the ON and OH distances along the reaction path ways are listed for the selected points which were introduced in Fig. 2S and 3S. (Min) stands for the  $S_1$  keto minimum.

Fig. 4S: For every point of the 2D OH – NH potential energy surface the value  $R_- = \frac{1}{2}(R_{\text{OH}^-} + R_{\text{NH}})$  is defined. Along the minimum path for  $R_-$  cuts through the potential energy surfaces are calculated. For negative values of  $R_-$  the distance between the donating oxygen and the proton is smaller than between the accepting nitrogen and the proton, meaning the proton transfer has not taken place yet.

The cuts through the ground (GS), first (A') and second (A'') excited state potential energy surfaces for 10-HBQ (top graph) and HBT (bottom graph) show that the two excited states do not cross, but come very close in case of HBT.



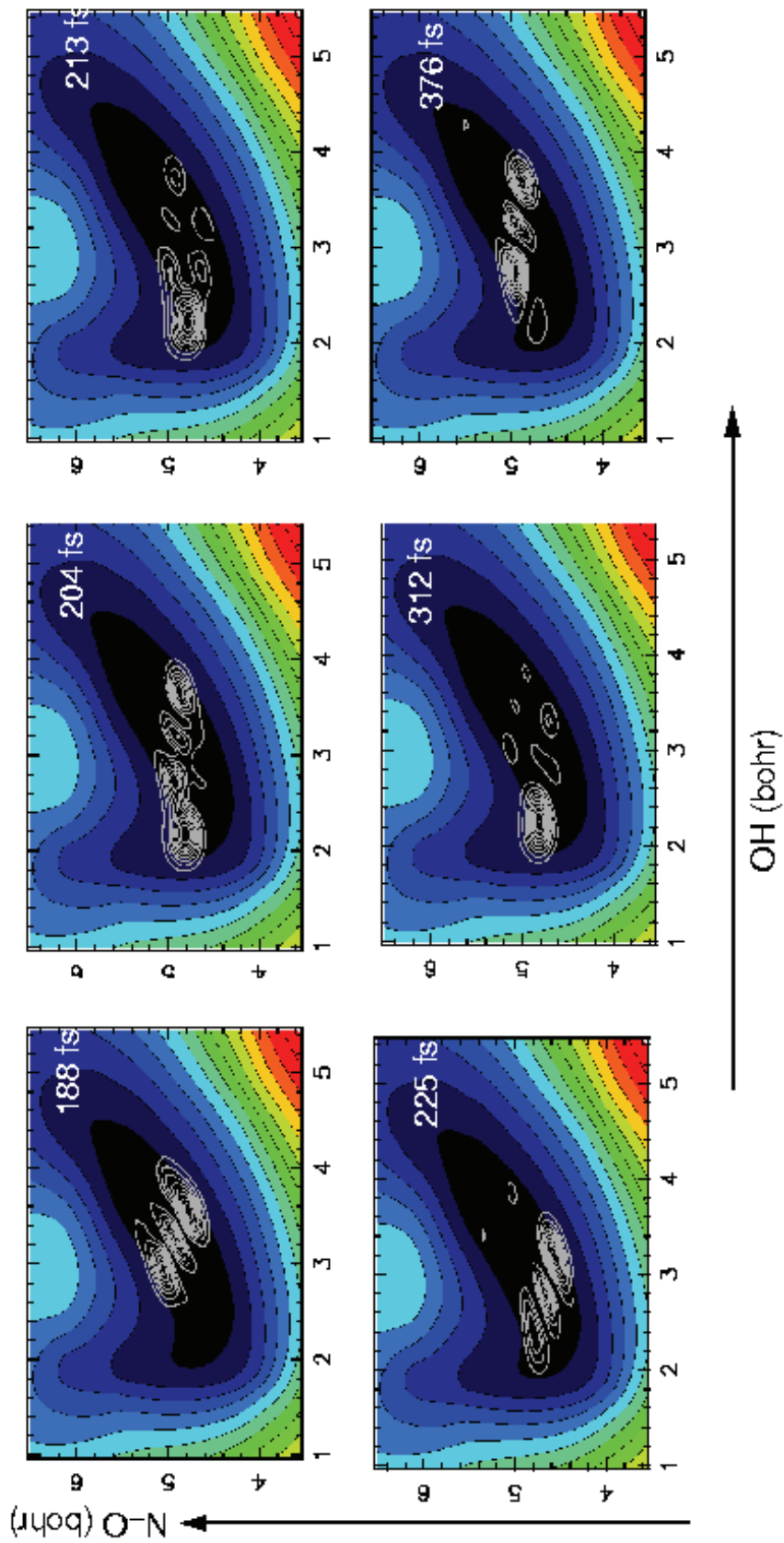


Fig. 5S: Snapshots of the wavepacket propagation in the ON-OH space during the time interval from 188 to 376 fs. For details see Sec. of the manuscript. 5.3.

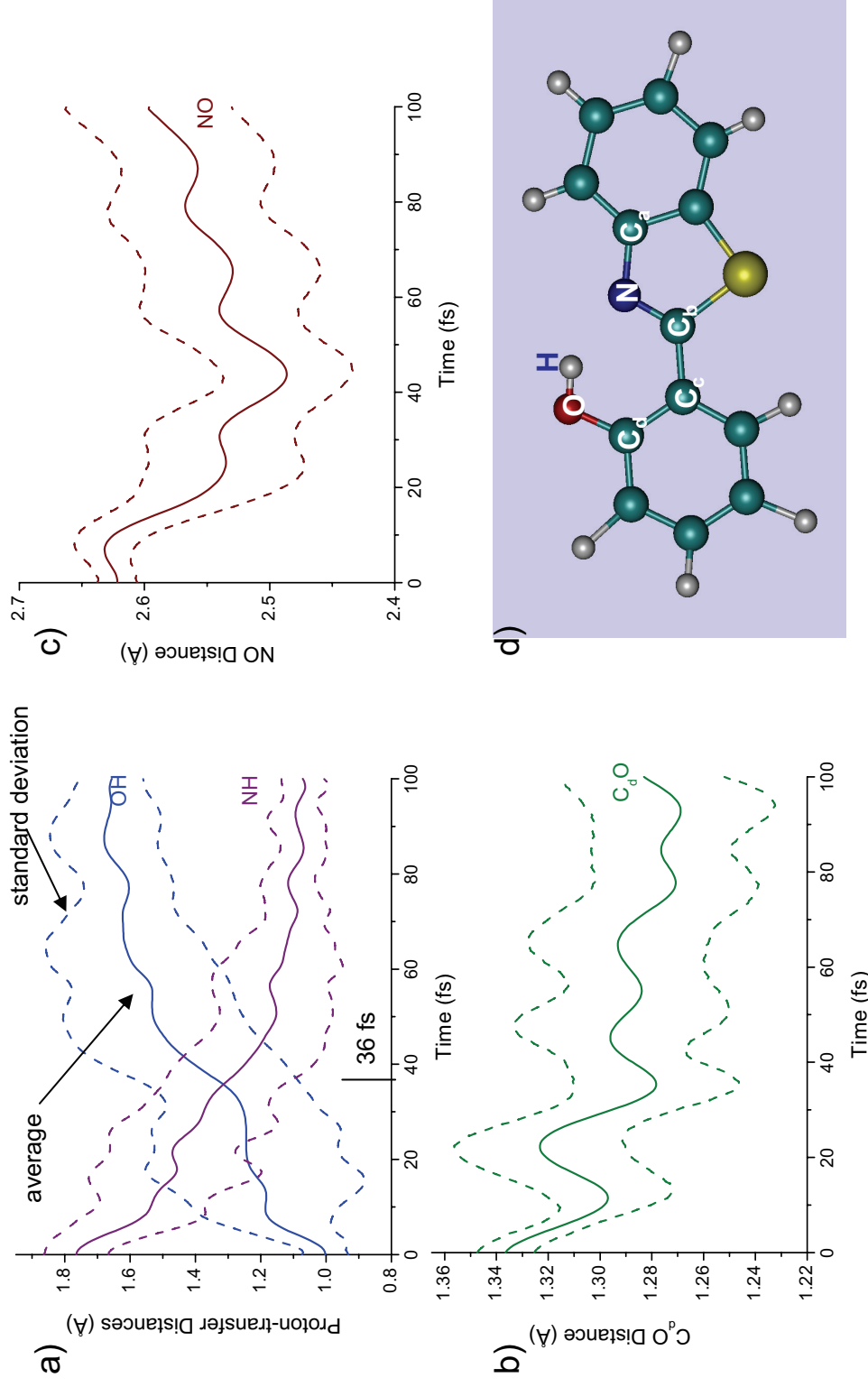


Fig. 6S: a) Time evolution of the OH and NH distances averaged over all trajectories for HBT. The standard deviations for the average values are shown by the dashed lines. In the analysis of the classical dynamics, we have defined the time for the hydrogen-transfer as the average time for which the OH and NH distances equal. This time is 36 fs for HBT. b), c) Time evolution of the internal coordinates C<sub>O</sub> and NO and their standard deviations. d) Geometric structure of HBT before the proton transfer. The carbon atoms that are most relevant to the proton transfer reaction are labeled.

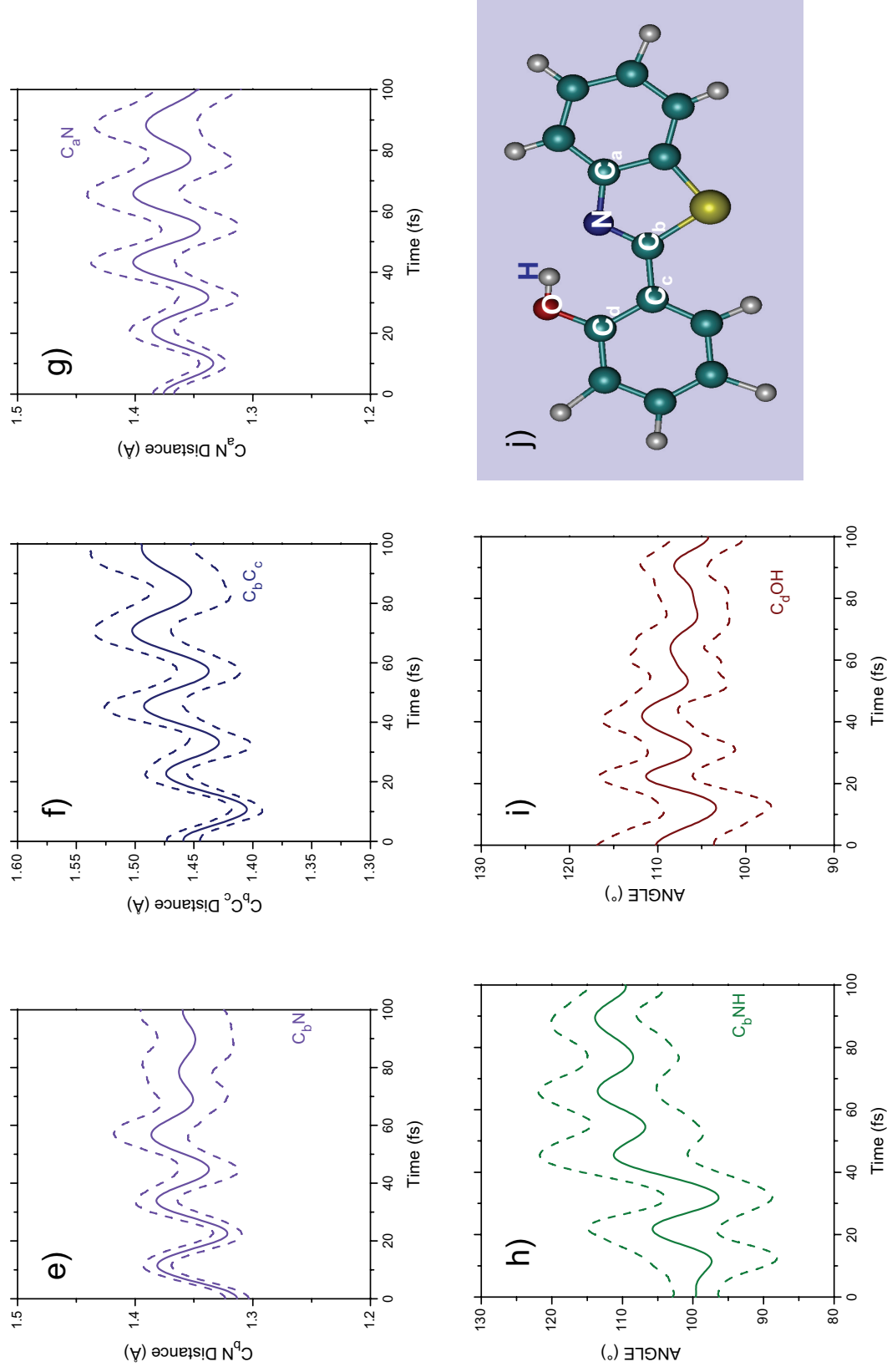


Fig. 6S-continued: e), f), g) Time evolution of the internal coordinates  $C_bN$ ,  $C_bC_c$ ,  $C_aN$ , respectively. h), i) Time evolution of the internal angles  $C_bNH$  and  $C_dOH$ , respectively. The standard deviations for all trajectories are indicated as dashed lines. j) Geometric structure of HBT before the proton transfer. The carbon atoms that are most relevant to the proton transfer reaction are labeled.

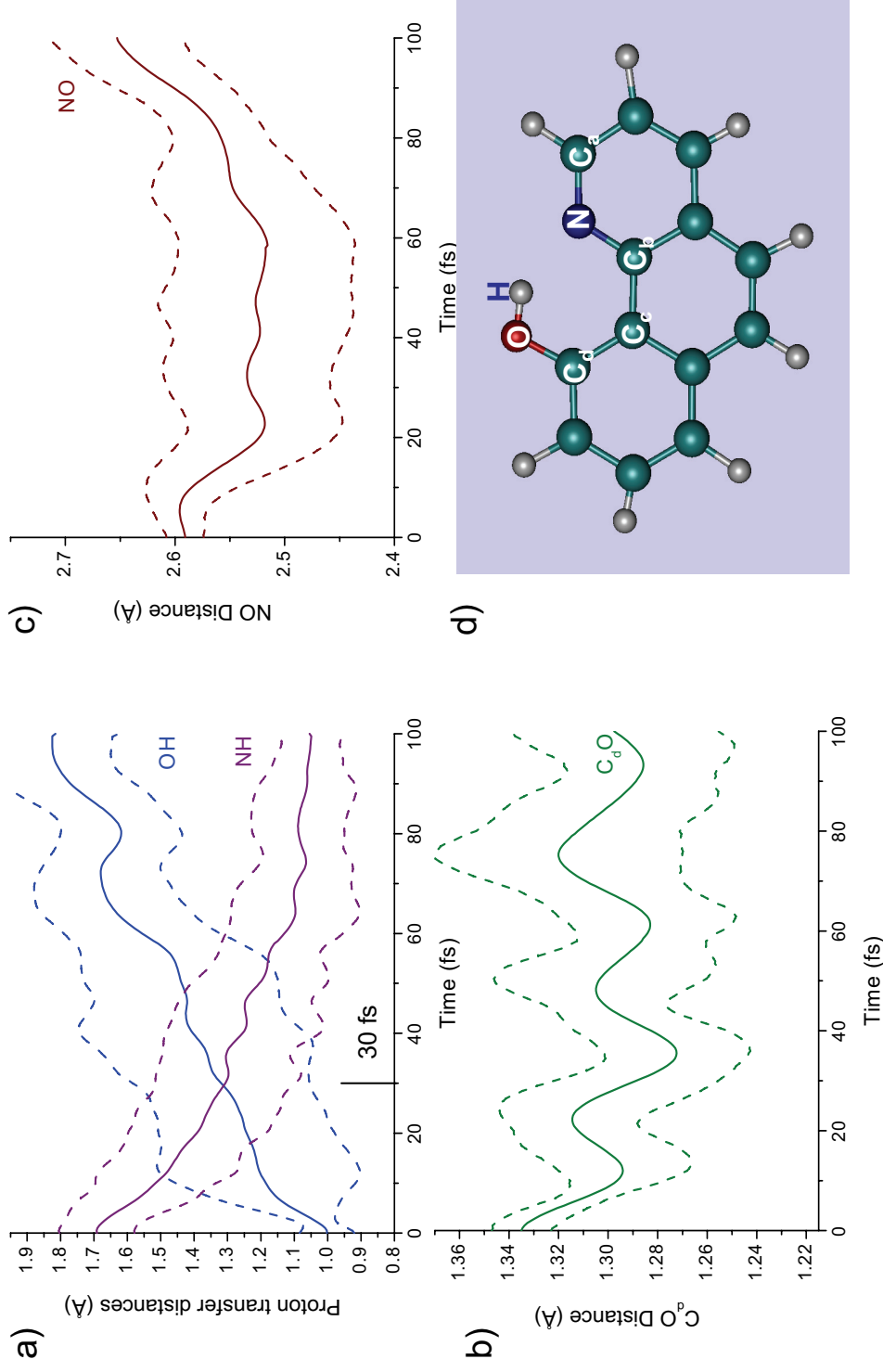


Fig. 7S: a) Time evolution of the OH and NH distances averaged over all trajectories for 10-HBQ. The standard deviations for the average values are shown by the dashed lines. In the analysis of the classical dynamics, we have defined the time for the hydrogen-transfer as the average time for which the OH and NH distances equal. This time is 30 fs for 10-HBQ. b), c) Time evolution of the internal coordinates C<sub>6</sub>O and NO and their standard deviations. d) Geometric structure of 10-HBQ before the proton transfer. The carbon atoms that are most relevant to the proton transfer reaction are labeled.



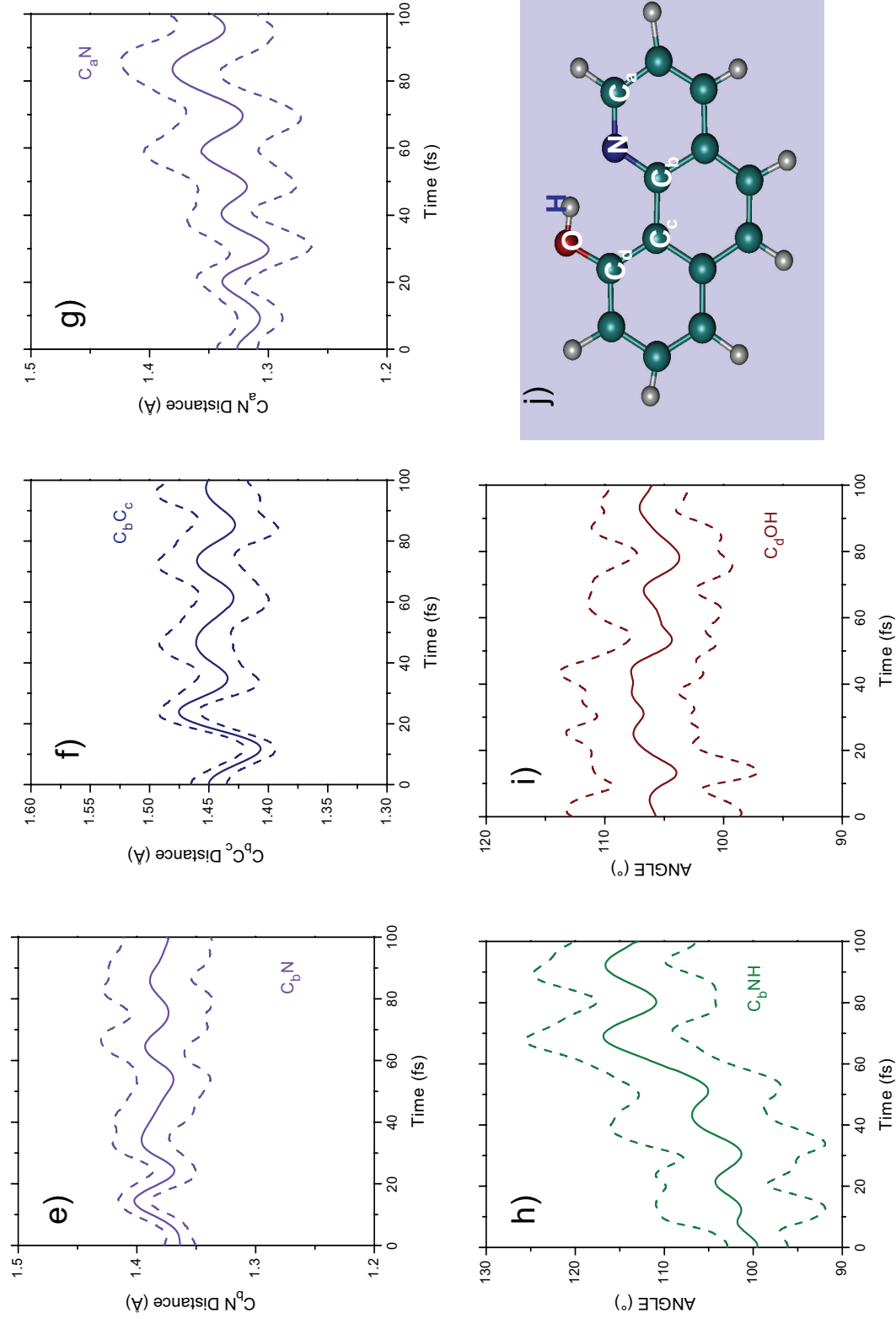


Fig. 7S-continued: e), f), g) Time evolution of the internal coordinates  $C_bN$ ,  $C_bC_c$ ,  $C_aN$ , respectively. h), i) Time evolution of the internal angles  $C_bNH$  and  $C_dOH$ , respectively. The standard deviations for all trajectories are indicated as dashed lines. j) Geometric structure of 10-HBQ before the proton transfer. The carbon atoms that are most relevant to the proton transfer reaction are labeled.



## Anhang 9

**"Comparison of the intramolecular proton transfer cycle  
in the gas phase and in solution"**

C. Schriever, S. Lochbrunner, D. J. Nesbitt, and E. Riedle

Manuskript vorbereitet zur Einreichung an J. Chem. Phys. (2008)



## Comparison of the intramolecular proton transfer cycle in the gas phase and in solution

Christian Schrieber,<sup>1</sup> Stefan Lochbrunner,<sup>2</sup> David J. Nesbitt,<sup>3,a)</sup> and Eberhard Riedle<sup>1,b)</sup>

<sup>1</sup>Fakultät für Physik, Ludwig-Maximilians-Universität, Oettingenstr. 67, 80538 München, Germany

<sup>2</sup>Institut für Physik, Universität Rostock, Universitätsplatz 3, 18055 Rostock, Germany

<sup>3</sup>Joint Institute for Laboratory Astrophysics, NIST, Department of Chemistry and Biochemistry, University of Colorado, Boulder, Colorado 80309-0040, USA

The excited state intramolecular proton transfer (ESIPT) of 2-(2'-hydroxyphenyl)benzothiazole (HBT) and 10-hydroxybenzo[h]quinoline (10-HBQ), the associated wavepacket dynamics and the internal conversion in the gas phase as well as in cyclohexane solution are investigated by femtosecond absorption spectroscopy. Both the isolated molecule in the gas phase and the solvated molecule show the identical initial ESIPT mechanism, i.e. the same proton transfer time and the same skeletal deformations that reduce the proton donor-acceptor distance to facilitate a barrierless adiabatic reaction path. However, the subsequent dynamics varies strikingly with the environment. For the isolated molecule we observe an excited state lifetime of the ESIPT product of 2.6 ps for excitation at 325 nm and 4.2 ps for excitation at 350 nm, which is almost two orders of magnitude faster than in a cyclohexane solution. The ESIPT induced wavepacket dynamics in the gas phase show the same frequency components as observed in cyclohexane solution. For HBT we find an additional low frequency torsional mode, for 10-HBQ two additional out-of-plane modes. Along the torsional coordinate in HBT, a conical intersection with the electronic ground state allows for a fast internal conversion (IC). The coherent excitation of the torsional mode indicates that for the isolated molecule the internal conversion is associated with wavepacket dynamics. In solution, friction damps the wavepacket dynamics, removes kinetic energy from the torsional mode and changes the character of the motion along the potential energy surface from ballistic to diffusive. We propose that along the IC path a barrier exists. In solution the friction afflicted diffusive motion and the friction induced energy loss in combination with the barrier result in a strongly reduced IC rate. After the IC a significant population of the transketo tautomer in the electronic ground state is observed. This supports the suggestion that the torsion is the promoting mode of the IC. In 10-HBQ we also find a 10-fold faster internal conversion in the gas phase than in solution. From the coherent excitation of out-of-plane normal modes that do not contribute to the reaction path, we tentatively propose an out-of-plane conical intersection as the pathway for the internal conversion. However, the out-of-plane motion has a much smaller amplitude as in HBT due to the rigid geometry of the molecular skeleton. Correspondingly, the differences between the dynamics of 10-hydroxybenzo[h]quinoline in the gas phase and in solution are less pronounced.

### INTRODUCTION

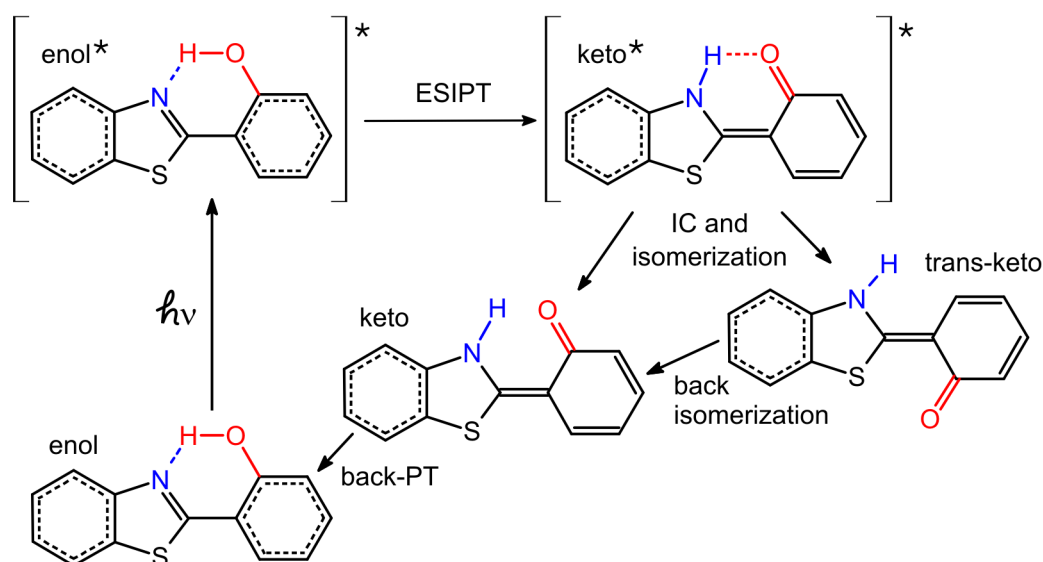
Many ultrafast molecular processes are governed by intramolecular motions at the speed of skeletal vibrations as well as by the interaction with the surrounding medium [1-15]. For complex molecules only little is known about the influence of the environment on the coherent wavepacket motions and how environmentally induced variations of the wavepacket motion change the outcome of the process. To understand the interplay between intra- and intermolecular contributions to the dynamics, we disentangle them by studying the same photoreaction both in the solvated and in the isolated molecule. It is essential to use the same probe process for both experiments; otherwise the wavefunction will be projected onto different manifolds of final states, resulting in different signatures even if there are no changes in the molecular dynamics [16].

Ultrafast excited state intramolecular proton transfer (ESIPT) is the prototype of a chemical reaction since it comprises the breaking of a bond and the simultaneous formation of a new one. ESIPT systems show rich wavepacket dynamics [17-19] and are especially suited to investigate the dynamics of hydrogen bonds, since they provide a well defined reactant geometry and the transfer of the hydrogen atom can be triggered by photoexcitation with an ultrashort laser pulse.

2-(2'-hydroxyphenyl)benzothiazole (HBT) is a prototype ESIPT molecule and has been subject to detailed studies in the past [17-29]. The proton transfer cycle of HBT in solution [24,25] is summarized in scheme 1. In the  $S_0$  electronic ground state, the enol tautomer with the reactive proton bonded to the oxygen atom in the H-chelate ring is the stable form. After excitation to the  $S_1$  state, the mobile proton is transferred to the accepting nitrogen atom, forming the keto tautomer. In unpolar, aprotic solvents like cyclohexane, this initial step takes less than 50 fs [17]. Real-time observations of the ESIPT process show strong oscillatory signal contributions subsequent to the proton transfer which have been identified with coherently

<sup>a)</sup> Staff Member, Quantum Physics Division, National Institute of Standards and Technology

<sup>b)</sup> Electronic mail: riedle@physik.uni-muenchen.de



SCHEME 1. (color online) Proton-transfer cycle of HBT. Conformers in the  $S_1$  state are indicated by \*.

excited normal modes of the molecule. They originate from the initial deformation of the molecule that reduces the donor-acceptor distance [17,30]. This contraction allows for a barrierless reaction path and an efficient mixing between the electronic configurations of the enol and the keto form [23,31,32]. The reported dephasing time of the oscillations in cyclohexane solution is on the order of 1 ps [17]. The lifetime of the  $S_1$  keto tautomer formed by the ESIPT varies strongly with solvent and temperature and lies in the range between several ten to several hundred picoseconds [22,29,33,34]. It has been proposed that a torsional motion around the phenyl-thiazole bond promotes the internal conversion [22,33]. Recent ab-initio calculations indicate that an energetically favorable conical intersection of the  $S_1$  with the  $S_0$  state at a torsional angle of  $90^\circ$  exists, which can provide the pathway for a fast internal conversion (IC) to the electronic ground state [21]. The  $S_0$  cis-keto tautomer shows ultrafast reverse proton transfer and in cyclohexane solution it has not yet been observed spectroscopically. However, a cis-trans isomerization might occur in the electronically excited state [35] or with the IC process [21,24]. Experimentally, it was found that a significant fraction of the molecules end up in the  $S_0$  state as trans-keto tautomer which is a metastable configuration with a live time of microseconds [35-37] (cf. Table 1). The sensitivity of the HBT dynamics, in particular the IC, on the environment indicates that a microscopic understanding of the mechanisms is only possible if the influence of the environment can be determined. This is the goal of the present study.

In this context one important question is, if the torsional coordinate plays indeed the key role the above mentioned studies ascribe it to. Here the comparison to a molecule which has no such torsional degree of freedom should be most helpful. The ESIPT compound 10-hydroxybenzo[h]quinoline (10-HBQ) fulfills this

requirement due to its structure of basically three condensed benzene rings. Comparative studies of the dynamics of 10-HBQ on a short and long time scale are given in ref.s [19,18]. Due to the more rigid molecular skeleton of 10-HBQ, the low frequency normal modes involved in the deformation of the H-chelate ring are shifted to higher frequencies, and in cyclohexane solution, 10-HBQ shows a slightly faster proton transfer than HBT. The experimentally observed IC is somewhat slower than for HBT; the mechanism has not been resolved yet.

In this paper we investigate the proton transfer cycle of HBT and 10-HBQ for the isolated molecule in the gas phase and compare it to the one found in solution phase environments. Transient absorption is used as probe signal both in the gas phase and in solution since it allows for a time resolution superior to most other techniques, and in solution phase experiments, it has proven to provide a rich amount of spectroscopic information revealing detailed insight into the dynamics [16,17,38-40]. The purpose of this investigation is (1) to identify the species involved in the proton transfer cycle in the gas phase and obtain their kinetic data, (2) to elucidate the mechanism for the internal conversion of the  $S_1$  keto form in the gas phase, (3) to determine the proton transfer time in the gas phase, and (4) to evaluate the ESIPT induced wavepacket dynamics in terms of the ESIPT mechanism. In the gas phase structural changes are not hindered by a solvation shell and the comparison of HBT and 10-HBQ directly shows the influence of the geometric restrictions on the ESIPT and IC.

## Experiment

ESIPT molecules exhibit a large Stokes-shift due to the reactive process that significantly lowers the energy of the  $S_1$  excited state. To establish the ESIPT of HBT in the gas phase, steady state absorption and emission

spectra are recorded.

The absorption spectrum is measured in a 50 mm long glass cell that was heated with several windings of electrical heat tape. An additional winding of heat tape was placed on each cell window to prevent the condensation of thin layers of molecules. The temperature of the cell was measured with a NTC thermocouple. The steady state fluorescence spectrum was recorded after cw excitation of the sample by a 8 mW, 325 nm HeCd Laser. An X-type glass cell geometry was chosen to minimize stray light from the entrance and exit windows of the pump laser. The cell was heated by electrical heat tape and evacuated at times to check contributions from non-gaseous HBT contributing to the fluorescence signal. These contributions were found negligible.

To resolve the signatures of the proton transfer in real time, i.e. with a time resolution on the order of the fastest steps involved in the ESIPT, two color pump probe measurements are performed. The fully tunable two-color pump-probe spectrometer used in our experiments provides a time resolution of 20 fs and a sensitivity of  $1.1 \times 10^{-6}$  OD. It is optimized for gas phase absorption experiments and supports long sample lengths and high excitation energies. Gas phase and solution phase samples can be measured in direct succession without changes to the setup. It is described in detail elsewhere [16]. Briefly, a Ti:sapphire amplifier system (CPA-2001, Clark-MXR; 150 fs, 1 kHz, 775 nm) pumped a single- and a double-stage noncollinear optical parametric amplifier (NOPA) [41]. The output of the two-stage NOPA was mixed with a fraction of the fundamental to generate high intensity UV pump pulses [42]. The NOPA was tuned to excite the  $S_1$  states of HBT (325 nm and 350 nm; see Fig.1) and 10-HBQ (350 nm). The ultraviolet (UV) pump pulse was collinearly overlapped with the probe pulse and weakly focused to obtain good spatial overlap over a path length of  $\sim 50$  mm. For the solution phase experiments a flow cell with a 120  $\mu\text{m}$  thick layer of the sample solution was placed in the focus. For the gas phase measurements, a sample cell with a path length of 50 mm was used [16]. Typically a cross correlation of 40 fs was achieved, allowing to resolve dynamics on the 20 fs time scale.

To obtain transient spectra of HBT in the gas phase, the probe pulses were tuned to 22 different wavelengths in the spectral region from 450 to 695 nm. To maintain the same experimental conditions throughout the measurement series, the probe pulses were not compressed individually and the time resolution was 100 – 150 fs throughout the spectral scanning range.

For solution phase samples, transient absorption spectra covering the whole visible and near UV range were recorded with a broadband probe resulting in an effective time resolution of  $\sim 200$  fs [18]. In this setup, the pump pulses (325 and 368 nm) were generated by frequency doubling of the output of the two-stage NOPA. A whitelight continuum generated in a 4 mm thick rotating calcium fluoride crystal was used as probe

pulse. Its spectrum typically spanned from 300 to 750 nm. A sample cell with 1 mm optical path length was used. After passing through the sample, the continuum was dispersed for spectrally resolved single channel detection. The transient spectra were obtained by synchronously scanning the detection wavelength and the delay line to correct for the shift of time zero imposed by the group velocity dispersion (GVD) of the continuum.

The results presented below show the dynamics under magic angle configuration of pump and probe pulses [43]. Measurements with parallel and perpendicular polarization reveal that the orientational relaxation in the gas phase occurs on a time scale of  $\sim 2$  ps, whereas in solution it takes  $\sim 50$  ps [17]. For measurements with parallel polarization, a method to segregate the molecular dynamics in the gas phase from the rotational depolarization is given in Appendix B.

HBT (CAS 3411-95-8) was obtained from Aldrich and purified by recrystallization. 10-HBQ (CAS 33155-90-7) was obtained from TCI. The solvents used for the experiments were spectroscopic grade (Uvasol; Merck). HBT and 10-HBQ were dissolved with a concentration of  $10^{-3}$  –  $10^{-4}$  M, to give an absorption of typically 50 % at the excitation wavelength.

## EXPERIMENTAL RESULTS AND DISCUSSION

In Sections I – VIII the experimental findings for HBT in the gas phase and in cyclohexane solution are presented and discussed. Steady state spectroscopy is used to establish the ESIPT in the gas phase (Sec. I). From transient spectra the species and time scales involved in the proton transfer cycle are identified (Sec. II and III). The low frequency oscillatory contributions unique to the gas phase transients are assigned to the wavepacket motion of the IC (Sec. IV). Their absence in the condensed phase is discussed in terms of friction induced by the environment (Sec. V). The ESIPT in the gas phase and in solution is compared with respect to the proton transfer time (Sec. VI) and the associated wavepacket dynamics (Sec. VII). Finally, the influence of the environment on the vibrational dephasing (Sec. VIII) and the impact of a rigid molecular backbone, like in 10-HBQ, on the dynamics are discussed (Sec. IX).

### I. $S_1$ enol and keto fluorescence

The absorption spectrum of HBT is found in the near UV (see Fig. 1). The first absorption band of HBT in the gas phase peaks at 327 nm and is blue shifted by  $\sim 900$   $\text{cm}^{-1}$  with respect to cyclohexane solution (337 nm). While the absorption in cyclohexane at ambient room temperature shows a shoulder at 347 nm, this feature is significantly less pronounced in the absorption of isolated molecules in the gas phase at 400 K. The fluorescence of HBT in cyclohexane peaks at 542 nm and is Stokes-shifted by  $\sim 7650$   $\text{cm}^{-1}$ . The fluorescence peak is assigned to the  $S_1$  keto tautomer [22,34]. In ethanol solution, the fluorescence of HBT has a major

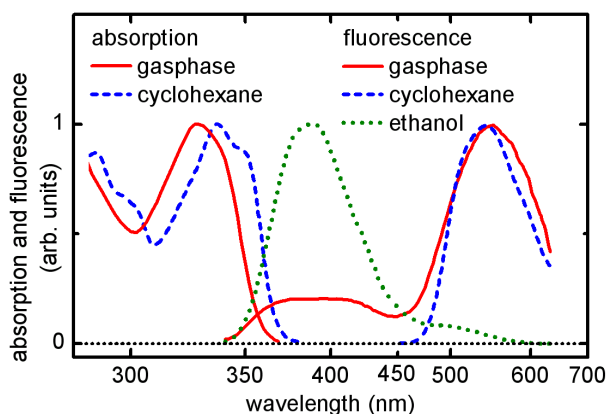


FIG 1. (color online) Steady state absorption and fluorescence spectra of HBT in the gas phase, cyclohexane and ethanol solution. The absorption spectra in ethanol (data not shown) is almost identical to the one in cyclohexane solution. The gas phase absorption spectrum was recorded at  $\sim 400$ K, the fluorescence spectrum at  $\sim 420$ K.

contribution which is not Stokes-shifted. It peaks at 390 nm and is assigned to the  $S_1$  enol tautomer. Hydrogen bridges to the solvent partially break the H-chelate ring of HBT and inhibit the ESIPT reaction [26,37,44].

In the gas phase, the fluorescence has two contributions: (1) a major contribution peaking at 546 nm which almost coincides with the keto fluorescence of HBT in cyclohexane and (2) a significantly less pronounced contribution at around 390 nm which is in the same spectral region as the enol fluorescence observed in ethanol. Adding ethanol vapor to the heated fluorescence cell causes the 390 nm peak to increase in intensity whereas the 546 nm peaks almost remains unchanged (data not shown). For ethanol solution it is known that the fluorescence quantum yield of the stabilized  $S_1$  enol form is about a factor of 10 higher than of the  $S_1$  keto product [37]. Due to the even faster IC of isolated HBT in the gas phase (see below) it can be safely assumed that more than 98% of the excited molecules undergo ultrafast ESIPT. This finding is also supported by the absence of sharp structures on the  $S_1$  absorption band. The ultrafast depopulation of the  $S_1$  enol form by the ESIPT leads to a homogeneous broadening of any possible gas phase line structure. The enol fluorescence results from molecules for which the ESIPT is inhibited probably due to water molecules from various surfaces bonding to the H-chelate ring or impurities in the sample. Their contribution to the time resolved measurements, however, can be neglected due to their small fraction in population.

Assuming the same molar extinction coefficient in the absorption maximum in the gas phase and in cyclohexane solution ( $\epsilon = 16500 \text{ M}^{-1} \text{ cm}^{-1}$  [24]), the density of HBT molecules at 400 K is  $3.6 \times 10^{-6} \text{ M}$ , corresponding to a vapor pressure of 0.12 hPa. For the NOPA-NOPA experiments the sample was buffered with  $\text{N}_2$  at an ambient pressure of  $\sim 4$  hPa, leading to a time between collisions of  $\sim 15$  ns, which is significantly longer than the spectroscopically observed time scale. Thus, we do not expect any effects from collisions

between  $\text{N}_2$  and HBT molecules, or even HBT and HBT molecules.

## II. Transient spectra in solution: IC and transketo signature

The transient transmission spectrum of HBT in cyclohexane after optical excitation at 325 nm (see Fig. 2) is the sum of ground state bleach below 350 nm, stimulated emission around 575 nm and a pronounced absorption component peaked at 400 nm. The major features of the transient spectrum are fully developed after 1 ps and decrease from then on. After 1.8 ns only a transient absorption at  $\sim 470$  nm and a fraction of the ground state bleach remains.

For a systematic analysis, the method of decay-associated spectra is utilized [45,46]. Three major components with exponential time constants of 12 ps, 143 ps and  $\sim 6.2$  ns are found (Fig 2b). The spectrum associated with the 143 ps time is the major contribution both to the emission at 575 nm and the absorption at 400 nm. By comparison to the steady state spectra, the 575 nm emission can be safely assigned to the  $S_1$  keto tautomer. Consequently, the major part of the 400 nm absorption is the excited state absorption (ESA) of the  $S_1$

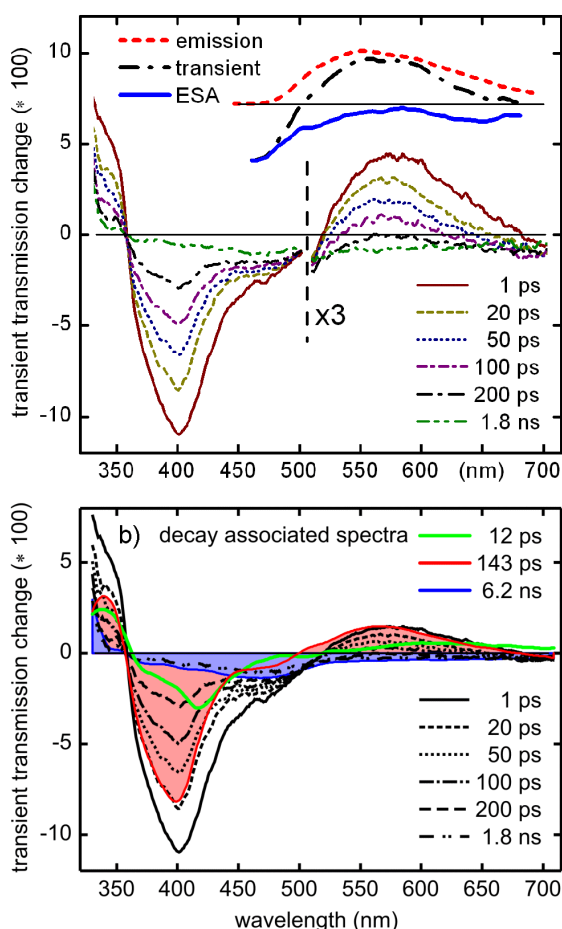


FIG. 2. (color online) (a) Transient spectra of HBT in cyclohexane solution for various delay times of pump and probe. The transient spectrum at 200 ps is decomposed into emission (scaled cw-fluorescence) and absorption component (upper right). (b) Decay associated spectra.



keto form and the 143 ps decay corresponds to the time constant of the IC. The rate of 143 ps observed for 325 nm excitation is significantly faster than the value of 580 ps found for 368 nm excitation (data not shown; cf. Tab. 1). This agrees with other ES IPT compounds in which the IC also accelerates with increasing excess energy [47]. It indicates that a significant energy barrier has to be overcome for the IC. Temperature dependent studies of the fluorescence lifetime and quantum yield in HBT support this finding [22,37,44]. The spectrum associated with the 12 ps time constant resembles the 143 ps component, but is a factor of  $\sim 3$  smaller in amplitude and somewhat red-shifted. The decay of the 12 ps component causes a blue shift of the composed/total transient spectrum, and is tentatively assigned to solvation and cooling [17].

The 6.2 ns component corresponds to an absorption peaking at  $\sim 470$  nm and tailing somewhat into the red spectral region and a residual ground state bleach below 350 nm. The time constant is not precisely determined since the maximum experimental time delay was 1.8 ns; it can be assumed that it is significantly longer. This component is tentatively assigned to the absorption of the  $S_0$  transketo tautomer formed upon IC of the  $S_1$  keto, originating from the ES IPT. Brewer [35] et al. have observed with two pulse laser excitation and nanosecond time resolution an almost identical absorption band for HBT in chloroform solution. It shows a biexponential decay with 13.4  $\mu$ s and 59.5  $\mu$ s and was attributed to the  $S_0$  transketo tautomer undergoing a slow back-isomerization to the stable  $S_0$  enol configuration. At 368 nm pump we hardly observe any  $S_0$  transketo formation (data not shown).

### III. Transient spectra in the gas phase: IC and proton back transfer

A direct recording of transient spectra in the gas phase via a broadband probe pulse which is then spectrally dispersed, was experimentally not feasible. Instead, 22 time traces with probe wavelength ranging from 450 – 695 nm were recorded and transient spectra reconstructed. An intensity plot and the corresponding time traces are depicted in Figure 3 to give an overview of the dynamics of HBT in the gas phase. Figure 4 a) shows a set of transient spectra for HBT in the gas phase. Within the time resolution of the experiment an emission band rises, peaking at 575 nm. The emission shows a fast initial red shift within the first 0.5 ps and then decays within a few picoseconds. Comparing the emission component to the steady state spectra for HBT in the gas phase (Fig. 4b) and to the kinetics of HBT in cyclohexane solution, we assign the emission to the  $S_1$  keto tautomer.

Around 460 nm a transient absorption is found which appears within the time resolution of 100 fs and increases up to 20 ps with a time constant equal to the decay of the emission band. Directly after the excitation, the whole spectroscopically accessible population is in the  $S_1$  keto state, and the initial absorption in the blue is

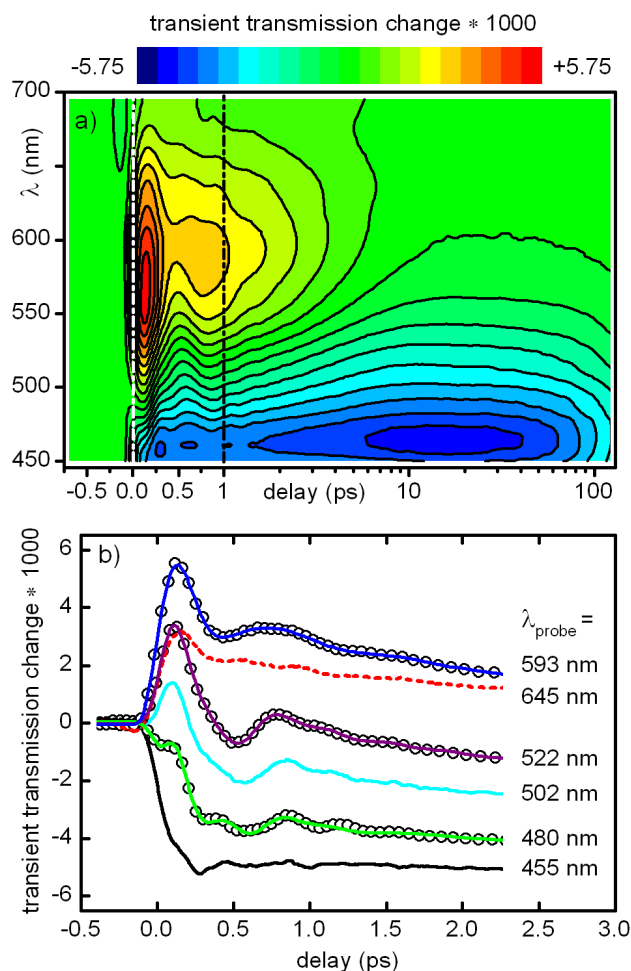


FIG. 3. (color online) (a) Color coded 2D plot of transients in the gas phase. (b) Cuts of the 2D data at various wavelengths. For the 480, 522 and 593 nm transients the data (open circles) as well as the fit results (solid lines) are displayed.

the excited state absorption of the  $S_1$  keto tautomers corresponding to the long wavelength tail of the strong ESA band observed in cyclohexane (Fig. 2). The fast decay of the emission indicates a fast IC of HBT to the ground state. The synchronous absorption increase in the blue is then associated with the appearance of a product of the IC. From the spectral position of the absorption increase and in analogy to the cyclohexane solution, we conclude that upon the IC a fraction of the molecules form the metastable  $S_0$  transketo tautomer. For long delay times, only  $S_0$  transketo tautomers are observed which show a slow back-isomerization to the  $S_0$  enol form that does not absorb in the observed spectral region.

The decay associated spectra (Fig. 4b) show three major components with time constants of 2.5, 30 and 120 ps. The spectrum of the 2.5 ps component closely resembles the emission cross-section derived from the steady state spectrum. Accordingly, the 2.5 ps is the time constant of the IC.

The spectra for the 30 and 120 ps components have opposite sign, but are almost identical in shape and have a fixed amplitude ratio (30:70) in the spectral region where their amplitudes contribute significantly to the

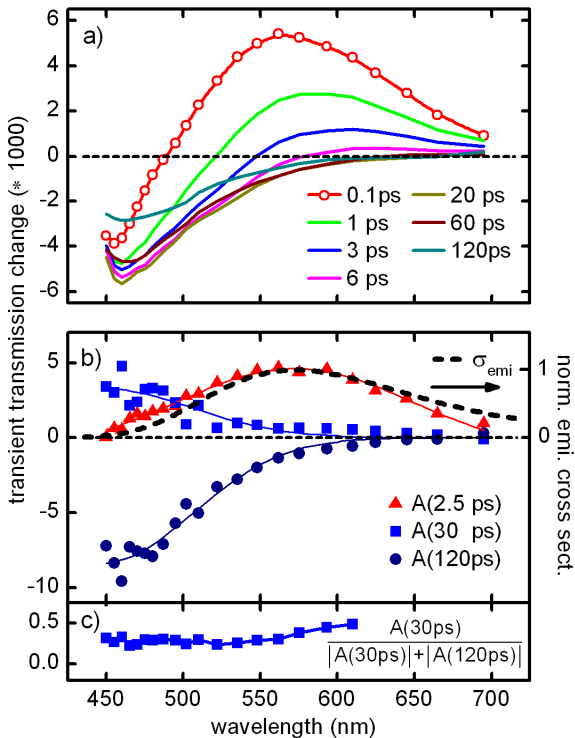


FIG. 4. (color online) (a) Transient spectra of HBT in the gas phase for various delay times. (b) Decay associated spectra and emission cross-section (scaled cw fluorescence). (c) Relative amplitude of the  $\tau = 30$  ps decay associated spectrum.

total spectrum (Fig. 4c). Therefore we do not think, they reflect two subsequent steps between three different species or states. The identical shape of the amplitudes points rather to a non-exponential kinetics which is parameterized by the sum of two exponentials. Even though the exponential model might not be intrinsically linked to the mechanism of the relevant process, it provides a convenient parameterization and will be used to characterize the relevant time scales. The values of the 30 and 120 ps time constants are not the result of a completely free fitting procedure, because the coupled kinetics and the opposite sign of the associated amplitude spectra lead to two time constants of similar magnitude. Instead, they have been chosen carefully to yield best fit results and to be well separated from each other. A variation of  $\pm 10$  ps in the 30 ps time constant is found to have negligible effect on the 2.5 ps time constant and does not influence the results obtained for the IC (Table 1).

The amplitude spectrum of the 30/120 ps component closely resembles the transient spectra at later times. Based on these findings, we identify the two time constants with the non-exponential kinetics of the  $S_0$  transketo back-isomerization. It is interesting to note that the transketo decay in chloroform, which occurs on a time scale of tens of microsecond, was also fitted with a biexponential function and the resulting time constants of 13.4  $\mu$ s and 59.5  $\mu$ s [35]. For solution experiments the double exponential behavior was explained with a second order process involving the encounter of two HBT transketo molecules [29]. However, in our gas phase experiments the density on HBT molecules is

TABLE 1:  $S_1$  IC ( $\tau_{IC}$ ) and  $S_0$  transketo back-isomerization time constants ( $\tau_{ISO}^{fast}, \tau_{ISO}^{slow}$ ).

mol.	environment	$\lambda_{pump}$	$\tau_{IC}$	$\tau_{ISO}^{fast}$	$\tau_{ISO}^{slow}$
HBT	gas	325 nm	2.6 ps	30 ps	120 ps
	gas	350 nm	4.2 ps		
	CHX. sol.	325 nm	143 ps	13.4 $\mu$ s <sup>[a]</sup>	59.5 $\mu$ s <sup>[a]</sup>
	CHX. sol.	368 nm	580 ps		
10-HBQ	gas	350 nm	3 ps (20%) 42 ps (80%)	-	-
	CHX. sol.	380 nm	300 ps	-	-

much too low in order to have encounters within the observed time window. Thus the reason for the nonexponential behavior remains unclear.

#### IV. Wavepacket motion associated with the IC in the gas phase

While the analysis of the transient spectra established a picosecond IC and the transketo formation, more information is needed to clarify the IC mechanism. Valuable evidence can be derived from the time traces shown in Fig. 3b) that deviate at short times quite strongly from the exponential behavior assumed up to now. For a more detailed analysis a model function is fitted to the time scans which is the sum of exponential decays and damped cosine oscillations (for details see Appendix A). Due to the restricted time resolution of these measurements only low frequency oscillatory contributions to the transients can be observed and the ES IPT and high frequency oscillations are not resolved. A fast exponential decay component with a positive valued amplitude and an average time constant of 2.6 ps is found in all transients for 325 nm excitation. It matches the value of 2.5 ps obtained for the IC via the decay associated spectra very well.

The fits reveal a pronounced oscillatory component with a frequency of 41  $cm^{-1}$  (corresponding to an oscillation period of 0.81 ps) and a damping time of 0.32 ps. For probe wavelengths in the very blue and red, an additional oscillatory component with a frequency of 87  $cm^{-1}$ , the same damping time of 0.32 ps, but a significantly lower amplitude is observed. Applying the same analysis to data recorded for excitation at 350 nm (cf. Sec. VII) we find a somewhat slower IC time constant of 4.2 ps and the same low frequency oscillatory contributions with a slightly longer damping time of 0.43 ps (see Table 1 and 2).

The signal oscillations provide strong evidence for a coherently excited wavepacket in a vibrational mode. The observed wavepacket dynamics can be safely attributed to the  $S_1$  keto tautomer since a ground state wavepacket in the enol form cannot contribute in the visible spectral range. A comparison to vibrational modes calculated for the electronic ground state (B3LYP/6-311+G(d,p) level [48,49]) shows that the

TABLE 2: HBT: Frequencies and dephasing times of oscillatory contributions to the transients. The dephasing times given brackets have a large uncertainty due to the small amplitude of the oscillation.

assign.	gas phase		CHX sol.		
	$\lambda_{\text{pump}}$ (nm)	325	350	325	350
IC	$\nu_1$ ( $\text{cm}^{-1}$ )	41	40		
	$\tau_1$ (ps)	0.32	0.43		
	$\nu_2$ ( $\text{cm}^{-1}$ )	87	89		
	$\tau_2$ (ps)	0.31	0.43		
ESIPT	$\nu_3$ ( $\text{cm}^{-1}$ )			110	112
	$\tau_3$ (ps)			0.41	0.40
	$\nu_4$ ( $\text{cm}^{-1}$ )	251	247	250	249
	$\tau_4$ (ps)	1.33	1.60	1.29	1.24
	$\nu_5$ ( $\text{cm}^{-1}$ )	285	282	286	
	$\tau_5$ (ps)	(1.71)	(5.35)	1.32	

observed mode should be a torsion around the central phenyl-thiazole-bond, involving the entire molecular skeleton. The torsion is with  $40 \text{ cm}^{-1}$  the lowest frequency normal mode followed by the butterfly mode at  $60 \text{ cm}^{-1}$ . Even if quite strong frequency variations between the  $S_0$  and the  $S_1$  state are assumed, no other mode can reasonably be considered.

Several authors argued that a torsional motion should be associated with the IC [22,33,35]. A small energy gap or even a conical intersection of the  $S_1$  keto potential energy surface (PES) and the  $S_0$  PES was postulated along this coordinate [24,26,36]. Recently, multireference calculations on the CASSCF and MRCI+Q levels indicated that along the torsional coordinate around the phenyl-thiazole bond characterized by the angle  $\phi$ , a conical intersection of the  $S_0$  and  $S_1$  state exists at an angle of about  $\phi = 90^\circ$  [21]. This model is backed up by our transients that show a transketo formation synchronous with the decay of the stimulated emission and thereby with the IC. Directly after passing the intersection at  $\phi = 90^\circ$  the pathways branch and the molecule can continue to twist and form the  $S_0$  transketo tautomer ( $\phi \approx 180^\circ$ ) or reverse the twist and end up as  $S_0$  cisketo tautomer ( $\phi = 0^\circ$ ).

To rationalize the wavepacket dynamics in this mode we have to consider the following. The calculations find that the planar  $S_1$  cisketo tautomer is a maximum along the torsional coordinate [21]. The characterization of the PES along the torsion by means of optimizing the remaining coordinates for a fixed torsional angle revealed a flat but barrierless  $S_1$  curve towards the intersection [21]. However, from the dependence of the IC rate on the temperature in solution [22,29,37,44] and on the excess energy in the gas phase (see above) we propose that a small barrier exists along the torsional coordinate (Fig. 5). This is in line with our observation that the keto emission shows no shift towards the

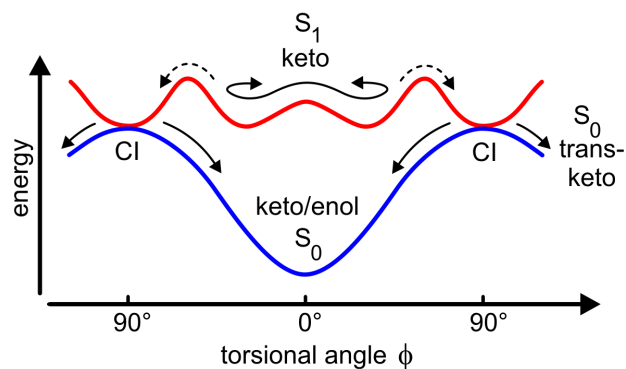


FIG. 5. (color online) Model potential for the internal conversion of HBT in the gas phase.

infrared. An extreme red shift should be expected if the wavepacket can propagate towards the intersection without any hindrance as the  $S_0$  and  $S_1$  state approach each other more and more. A potential barrier implies the existence of a potential minimum at some torsional angle  $0^\circ < \phi < 90^\circ$  (Fig. 5) around which a wavepacket can oscillate. At 400 K the expected thermally occupied level of the torsional mode ( $40 \text{ cm}^{-1}$ ) in the  $S_0$  state is  $\langle n \rangle = 6.5$ . However, the relatively high reduced torque of inertia will cause a rather narrow initial distribution along the torsional coordinate. After the optical excitation and the ultrafast ESIPT this wavepacket propagates along the torsional coordinate to the barrier where at least a fraction of it is reflected and starts to oscillate. It is also possible that a large fraction transverses the barrier already at the first attempt. This would result in a very pronounced first signal maximum and indirectly to a fast damping, in line with our observations. However, also spreading and dephasing of the wavepacket due to strong anharmonicities and population of high vibrational levels can lead to the fast decay of the coherent oscillatory signal contributions. This one dimensional model is still crude and needs more experimental and theoretical evidence for elaboration. Most likely, additional coordinates are involved and need to be considered.

The  $41 \text{ cm}^{-1}$  mode does not show a phase shift between probe wavelengths in the blue and red wing of the emission spectrum, as one might expect if the emission spectrum oscillates in frequency space due to a periodic variation of the average transition energy [17]. A dependence of the Einstein B coefficient on the torsional angle can explain a spectrally uniform periodic variation of the emission intensity. And indeed classical mechanics trajectories find that the Einstein B coefficient for stimulated emission strongly decreases for torsional angles  $\phi > 30^\circ$  [21].

The frequency of the  $87 \text{ cm}^{-1}$  oscillation is about two times the frequency of the torsional mode within our experimental accuracy. We assign it therefore tentatively to the second harmonic of the torsional mode. It can result from deformations of the wavepacket during the propagation and deviations of the time dependent signal from an ideal cosine form.

Both the coherent excitation of the  $41\text{ cm}^{-1}$  mode and the very fast IC in the gas phase are in contrast to the behavior in solution. The notion that the mode can be identified with a torsional motion and with the path to the CI links both phenomena in a natural way. This indicates that in the gas phase at least the first step of the IC is associated with a coherent wavepacket dynamics.

### V. The key role of frictional forces in solution

The  $41\text{ cm}^{-1}$  mode is associated with a large amplitude twisting of the entire molecular skeleton and therefore should in solution it should be subject to frictional forces which cause efficient dissipation of kinetic energy. In the condensed phase, the wavepacket motion along this coordinate is overdamped and no oscillatory signal contributions linked to this mode are observed. Instead of a ballistic propagation a diffusive motion biased by the weak slope of the potential towards the intersection results. Because of the friction induced energy dissipation, much less energy is available to cross the barrier and to approach the conical intersection in solution than in the gas phase. The diffusive motion towards the intersection will change from a directed motion to a spreading of the population density when the local minimum before the barrier is reached. This should dramatically reduce the IC rate and is in line with our observations.

Recently time resolved Raman measurements on the ESIPT of substituted (amino)anthraquinones in solution showed that a large amount of energy is deposited in the first solvation shell during the first 200 fs [12]. This should correspond to the first approach to the barrier during which a large fraction of the excess energy is transferred to the solvent. Our femtosecond absorption studies on HBT in solution revealed a red shift of the emission spectrum with a time constant of 250 fs [17]. It is quite natural to argue that this red shift reflects a change of the average transition frequency when the population distribution moves from the planar geometry along the torsional coordinate to the local minimum. In the gas phase this red shift is replaced by the damped oscillation and therefore no exponential 250 fs component appears in the corresponding time traces.

The dependence of the IC rate on viscosity and temperature [22,29] supports the notion that a diffusive large amplitude motion along a rather flat PES with a small but significant effective barrier leads to the conical intersection. The existence of a barrier is evident from the variation of the IC with the excitation wavelength in the gas phase. A temperature dependent study under constant viscosity revealed a barrier of  $60\text{ cm}^{-1}$  for 2-(2'-hydroxy-5'-methylphenyl)-3,3-dimethylindole, a compound similar to HBT [50]. Also in 1'-hydroxy-2'-acetonaphthone, a temperature dependent cis-trans isomerization yield and rate were reported [51]. In solution the temperature dependence is to a large extent caused by the variation of the solvent viscosity and the friction with temperature. This can lead to an effective Arrhenius activation energy that is several times higher

than the intrinsic barrier height [36,50]. All this points to large amplitude motions with small driving force.

### VI. Identical ESIPT mechanism and proton transfer time

The strong impact of the environment on the IC raises the question if this influence already affects the preceding ultrafast proton transfer. To observe directly the ESIPT and the associated wavepacket dynamics in addition to the slower components discussed above, NOPA-NOPA measurements with a temporal resolution of 20 fs [16] are performed. Figure 6 a) compares the transients recorded after excitation at 350 nm and probed at 510 nm (magic angle configuration) for the gas phase and solution sample. Together with the experimental data the results of the fitting procedure are shown. Both traces have a common transmission decrease close to zero delay time between pump and probe pulse. The pump pulse promotes the molecules into the  $S_1$  state and the ESA sets in instantaneously as a negative transient transmission over the whole observation wavelength range. With a short delay the

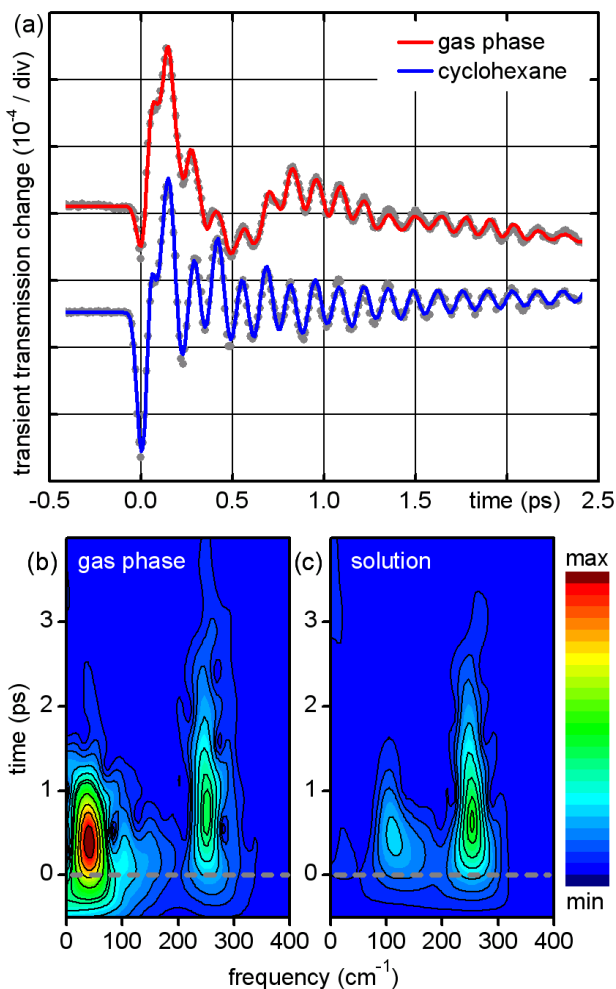


FIG. 6. (color online) (a) Transient transmission change of HBT in the gas phase and in cyclohexane solution for  $\lambda_{\text{pump}} = 350\text{ nm}$  and  $\lambda_{\text{probe}} = 510\text{ nm}$ . (b), (c) Sliding window Fourier transforms of the transients shown in (a).

stimulated emission from the keto  $S_1$  state can be seen as positive contribution to the transient transmission that signals the ESIPT. The delay of the emission rise is therefore taken as a measure of the proton transfer time [17,18]. A detailed comparison with a precision of better than 5 fs has shown [16] that the delay of the emission rise, i.e. the proton transfer time, is identical in gas phase and solution. For 325 nm pump and 595 nm probe a proton transfer time of  $35 \pm 5$  fs was found [16]. A slight increase in the proton transfer time towards longer probe wavelengths is observed. This is due to the fact that the wavepacket needs more time to reach this region of the  $S_1$  keto PES and has been observed in other ESIPT molecules as well [17,18,20,31]. Figure 6 clearly shows the similarity of the oscillatory contributions to the transients in the two environments. From the similarity of the proton transfer time and the identical phase of the subsequent signal signatures which result from the coherent wavepacket motion during and after the proton transfer we conclude that the ESIPT proceeds in the same way in the gas phase and in solution and the environment has only a negligible influence on the ultrafast intramolecular reaction.

## VII. Wavepacket dynamics associated with the ESIPT

Sliding window Fourier transforms with a windows length of 1 ps (Hanning window, effective frequency

resolution  $\sim 33$   $\text{cm}^{-1}$ ) of the transients are shown in Fig 6 b) and c) on a common intensity scale. For the transient recorded in cyclohexane solution we find dominant modes at 110  $\text{cm}^{-1}$  and 250  $\text{cm}^{-1}$ . In the gas phase we observe the 250  $\text{cm}^{-1}$  oscillation with the same frequency and relative phase as in solution (Fig. 6 a). The 41  $\text{cm}^{-1}$  oscillation is very strong and obscures other contributions in the low frequency range. Therefore it is not possible to provide clear evidence for the coherent excitation of the 110  $\text{cm}^{-1}$  mode.

Selected traces for 325 and 350 nm excitation in the gas phase and 350 nm excitation in cyclohexane solution are shown in Fig. 7. Fourier transforms of the oscillatory components (Fig. 8) exhibit the following frequency components: (1) exclusively in the gas phase, a 41  $\text{cm}^{-1}$  component, (2) dominantly in solution a 110  $\text{cm}^{-1}$  component, both in gas phase and solution (3) a strong 250  $\text{cm}^{-1}$  and (4) a weak  $\sim 284$   $\text{cm}^{-1}$  component, and (5) a  $\sim 530$   $\text{cm}^{-1}$  component which cannot be established for all probe wavelengths. The decay times of the oscillatory contributions obtained by the fitting procedure are listed in Table 2. The damping of the oscillations occurs with a time constant somewhat slower than 1 ps for the 250  $\text{cm}^{-1}$  mode both in the gas phase and in solution. The damping times in the gas phase slightly increase with decreasing excess energy, in cyclohexane solution there is no significant change between 325 and 347 nm [17] excitation.

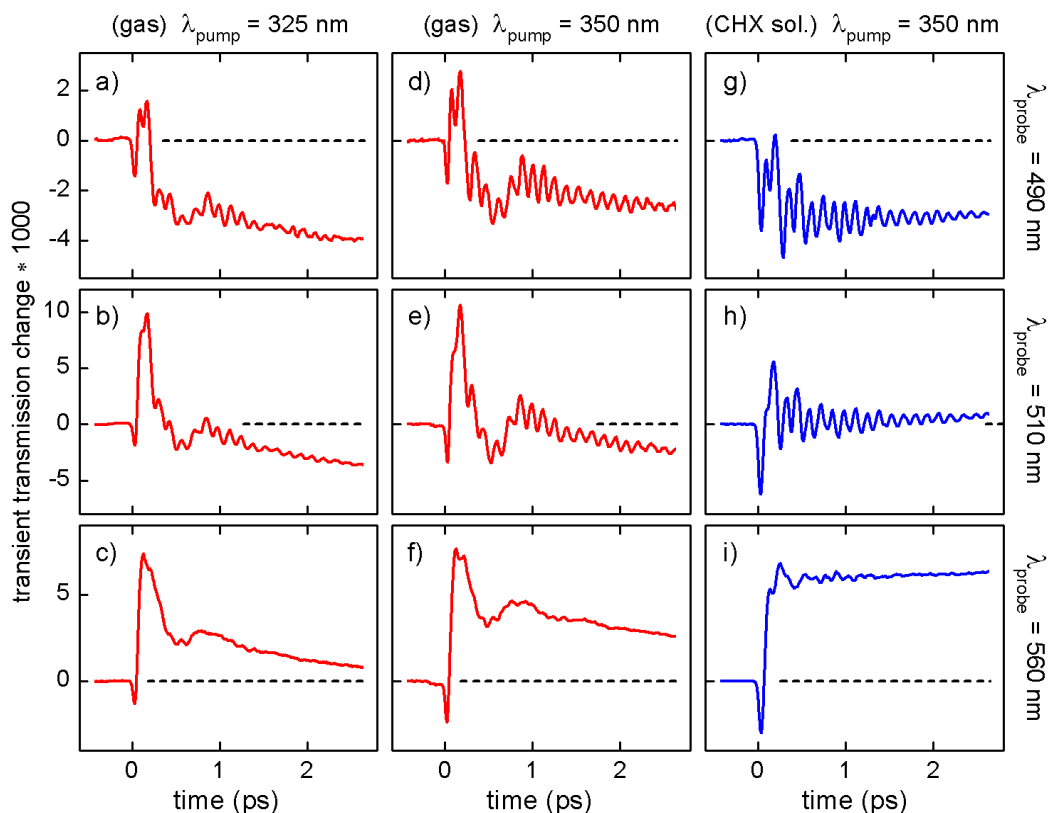


FIG. 7. (color online) Comparison of short time dynamics of HBT in the gas phase and in cyclohexane solution for various pump and probe wavelength. First and second col.: gas phase; third col.: cyclohexane solution. First col.  $\lambda_{\text{pump}} = 325$  nm; second and third col.:  $\lambda_{\text{pump}} = 350$  nm. First row:  $\lambda_{\text{probe}} = 490$  nm; second row:  $\lambda_{\text{probe}} = 510$  nm; third row:  $\lambda_{\text{probe}} = 560$  nm.

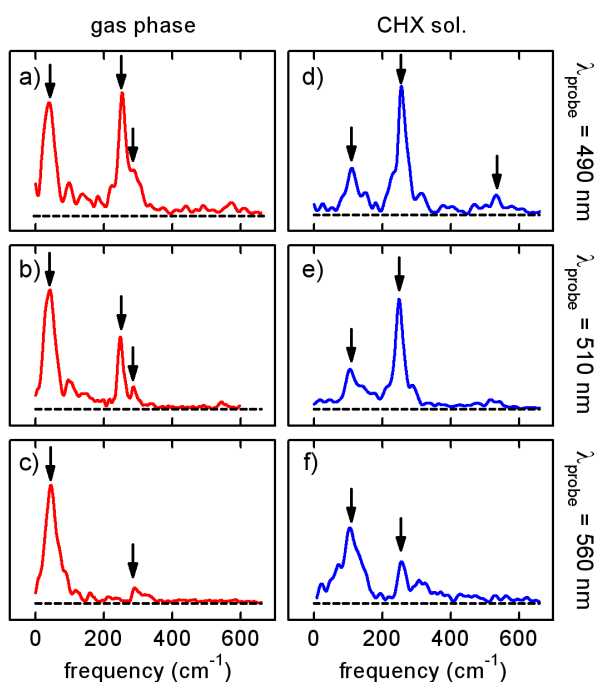


FIG. 8. (color online) Fourier transforms of the part of the transients shown in Fig. 7. The arrows indicate the frequencies found by fitting a model function (cf. Table 2).  $\lambda_{\text{pump}} = 350$  nm. First col.: gas phase; second col.: cyclohexane solution. First row:  $\lambda_{\text{probe}} = 490$  nm; second row:  $\lambda_{\text{probe}} = 510$  nm; third row:  $\lambda_{\text{probe}} = 560$  nm.

The oscillatory contributions at 110, 250, and 284  $\text{cm}^{-1}$  are in accord with earlier reports for HBT in cyclohexane solution [17]. Comparing the frequencies to ab-initio calculations [23] reveals that the modes are in-plane deformations of the molecular skeleton which reduce the donor acceptor distance in the H-chelate ring. This contraction dominates the ES IPT reaction path since it reduces the distance between the reactive hydrogen and the accepting nitrogen atom without increasing the potential energy due to an elongation of the OH-bond. It allows for an efficient mixing between the electronic configurations of the enol and the keto form and a barrierless transition. The ultrafast ES IPT proceeds as a ballistic wavepacket motion and results in a coherent excitation of modes in the  $S_1$  keto form that contribute strongly to the reaction coordinate [17,30]. At 560 nm probe wavelength the contribution of the 250  $\text{cm}^{-1}$  mode in the gas phase (and in solution) is very small, since this probe wavelength is very close to the emission maximum of the  $S_1$  keto tautomer. The 41  $\text{cm}^{-1}$  mode, however, is equally prominent for all probe wavelengths in the gas phase. This is due to different mechanisms causing the oscillations. While along the 250  $\text{cm}^{-1}$  mode the Franck-Condon factors change [17] (proportional to the slope of the emission spectrum), along the 41  $\text{cm}^{-1}$  mode the Einstein B coefficient changes [21] (not correlated to the slope of the emission). The 41  $\text{cm}^{-1}$  component observed in the gas phase does not contribute to the ES IPT reaction path as discussed above.

## VIII. Origin of the oscillatory dephasing

The observed damping times of the higher frequency normal modes in solution (325 nm excitation) are comparable to the ones found with 347 nm excitation [17]. In the gas phase these damping times show a slight decrease with increasing excess energy, but are overall slightly longer than in cyclohexane solution (cf. Table 2). The decay of the oscillation amplitudes in the gas phase is partially due to the dephasing of the vibronic wavepacket and partially due to the decay of the  $S_1$  population; our model function (cf. Appendix A) disentangles the two effects. The damping times in solution and in the gas phase are fairly the same for modes with frequencies above 200  $\text{cm}^{-1}$ . Their vibrational dephasing is largely intrinsic to the molecule and only to a small degree induced by the interaction with the solvent. Due to the energy released by the ES IPT, vibrational levels with several quanta of vibrational energy should be populated [17]. Because of anharmonicities of the PES at  $S_1$  keto minimum these levels are not equally spaced in energy and efficient broadening of the wavepacket occurs without the need for additional dephasing processes [52]. In addition, coupling to other modes might also contribute. In solution, the damping of the bending mode at 110  $\text{cm}^{-1}$  is much faster than the damping of other coherently excited modes with higher frequencies. At shorter excitation wavelengths more excess energy is deposited in the molecule and higher vibrational levels are populated in the product potential. In the gas phase this results in a slightly faster dephasing of the wavepacket (325 vs. 350 nm excitation, Table 2). In solution friction can remove some of this energy and the excess energy dependence of the dephasing times are less pronounced.

The vibrational dephasing is thus in striking contrast to the electronic dephasing which is accelerated by many orders of magnitude via the solvent interaction. In line with the minor influence of the solvent on the dephasing times, the vibrational frequencies are also not affected by the environment.

## IX. Wavepacket dynamics and internal conversion in 10-HBQ

To establish the importance of large amplitude torsional motions for a fast IC in ES IPT molecules, a comparison to compounds like 10-HBQ is quite instructive. The fully conjugated system of both the enol and keto configuration enforces a planar geometry and thus does not allow for a large amplitude out-of-plane deformations. A diluted gas phase sample of 10-HBQ was excited at 350 nm, close to the absorption maximum in the gas phase (data not shown). The transient transmission was recorded at selected wavelengths in the red spectral region, where the signal is dominated by the stimulated emission (Fig. 9). The gas phase transients are compared to previously performed measurements in cyclohexane solution [18] recorded with excitation at 380 nm (Fig. 9b), which is the absorption maximum in

solution [18]. On longer time scales we observe a biexponential decay of the stimulated emission signal of the gas phase transients with time constants of 3 ps (20%) and 42 ps (80 %) (Fig. 9a), resulting in an average time constant of 34 ps. In cyclohexane solution the time constant for the IC is  $\sim 300$  ps for 370 nm excitation [18]. The IC in the gas phase is about a factor of 10 faster than in cyclohexane solution.

On the short time scale, we find pronounced oscillatory contributions to the transients in both environments. Within the first 200 fs the dynamics look very similar; then the gas phase signatures are dominated by a beating structure that is not present in the cyclohexane transients. Fig. 9 d) and e) show sliding window Fourier transforms (cf. Sec. VII) of the transients. For the transient recorded in cyclohexane solution we find dominant modes at 235 and 393  $\text{cm}^{-1}$

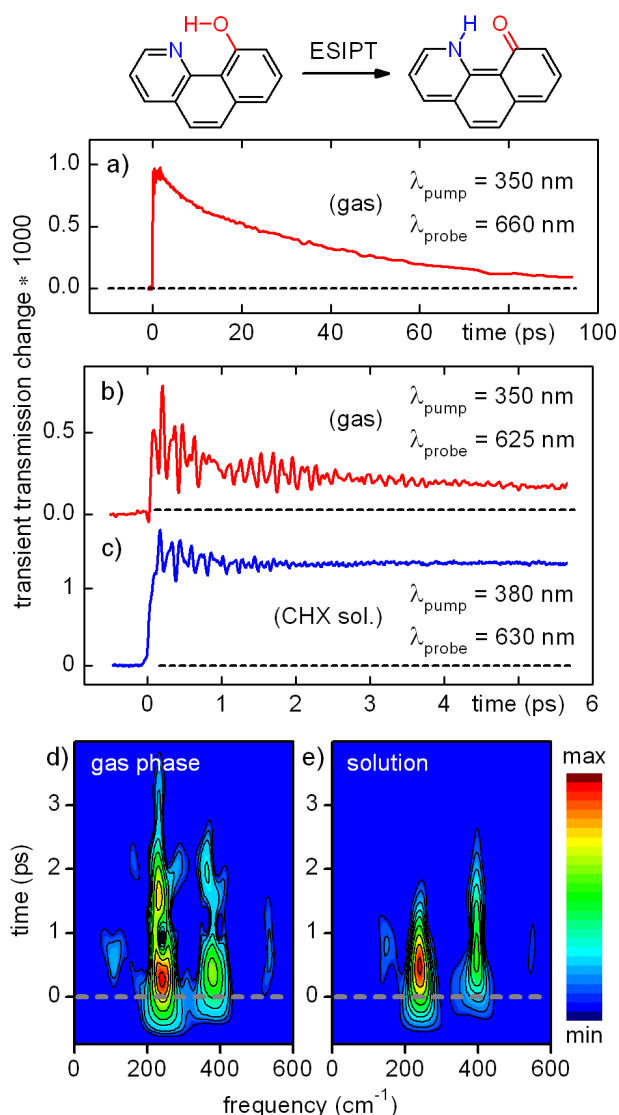


FIG. 9. (color online) ES IPT and IC of 10-HBQ. (a) Emission decay of 10-HBQ in the gas phase. (b) Transient transmission of 10-HBQ in the gas phase for  $\lambda_{\text{pump}} = 350$  nm and  $\lambda_{\text{probe}} = 625$  nm. (c) Transient transmission of 10-HBQ in cyclohexane solution for  $\lambda_{\text{pump}} = 380$  nm and  $\lambda_{\text{probe}} = 630$  nm. (d), (e) Sliding window Fourier transforms of the transients shown in (b) and (c).

TABLE 3: 10-HBQ: Frequencies and dephasing times of oscillatory contributions to the transients.

assign.	gas phase		CHX sol.
	$\lambda_{\text{pump}}$ (nm)	350	380
ES IPT	$\nu_1$ ( $\text{cm}^{-1}$ )	229	235
	$\tau_1$ (ps)	2.0	0.6
IC	$\nu_2$ ( $\text{cm}^{-1}$ )	249	
	$\tau_2$ (ps)	1.0	
ES IPT	$\nu_3$ ( $\text{cm}^{-1}$ )	378	393
	$\tau_3$ (ps)	0.8	1.2
IC	$\nu_4$ ( $\text{cm}^{-1}$ )	404	
	$\tau_4$ (ps)	1.0	
ES IPT	$\nu_5$ ( $\text{cm}^{-1}$ )	530	545
	$\tau_5$ (ps)	1.9	1.3

and a very weak contribution at 545  $\text{cm}^{-1}$ . The Fourier spectrum of the gas phase transient also shows three regions with significant contributions. However, the gas phase Fourier spectrum shows several peaks where in solution only a single peak is observed. Oscillatory contributions are observed at 229, 249, 378, 404 and 530  $\text{cm}^{-1}$  (cf. Table 3). The frequency groups 229/249  $\text{cm}^{-1}$  and 378/404  $\text{cm}^{-1}$  cause the beating structures in the transients.

A more detailed analysis by fitting a model function (cf. Appendix A) to the data confirms these assignments. The fit results are summarized in Table 3. The modes that are common to gas phase and solution show in the gas phase a frequency that is reduced by about 3 % with respect to solution. This might be an effect of the higher sample temperature in the gas phase. The dephasing time of the 378/404  $\text{cm}^{-1}$  modes in the gas phase and the 393  $\text{cm}^{-1}$  mode in solution are  $\sim 1$  ps. The dephasing time for the 229  $\text{cm}^{-1}$  mode is  $\sim 2$  ps and about twice as long as for the 235  $\text{cm}^{-1}$  mode in solution (Table 3).

In the groups 229/249  $\text{cm}^{-1}$  and 378/404  $\text{cm}^{-1}$  the lower frequency modes are the more intense ones. Therefore we can exclude that the lower frequencies reflect the excitation of high vibrational levels of modes with fundamental frequencies corresponding to the higher frequencies in the pairs. For HBT such a splitting of the 250 or 284  $\text{cm}^{-1}$  mode has not been observed either.

The  $S_0$  enol and  $S_1$  keto tautomer of 10-HBQ have been reported to have planar geometry [18]. The modes with 235, 393, 545  $\text{cm}^{-1}$  contributing to the ES IPT of 10-HBQ in cyclohexane solution were identified with in-plane deformations reducing the proton donor-acceptor distance [18]. By comparison of the observed frequency components to *ab-initio* calculations [18], we tentatively propose that the additional frequency components (249 and 404  $\text{cm}^{-1}$ ) in the gas phase correspond to out-of-plane normal modes of 10-HBQ. These two modes have a dephasing time of 1 ps, which is significantly shorter than for the other observed modes in the gas phase ( $\sim 2$  ps), indicating large amplitude deformations. In analogy to the mechanism of the IC in HBT, we

tentatively propose an out-of-plane conical intersection for the accelerated IC of 10-HBQ in the gas phase. The large amplitude out-of-plane motions would be strongly damped in solution and thus do not show up as coherent oscillations in the transients. However, further studies of the PES are required to substantiate this suggestion and to find the exact location of the conical intersection and the corresponding minimum energy path.

## SUMMARY AND CONCLUSIONS

In this work we characterized the influence of the environment on the ESIPT cycle of HBT and 10-HBQ. From the evolution of the transient absorption measured after photoexcitation at 325 and 350 nm in the gas phase and in cyclohexane solution we obtained the following findings.

The proton transfer in the electronically excited state of HBT takes the same time of 35 fs in the gas phase and in solution. It proceeds as a ballistic wavepacket motion along a path which results in an in-plane bending of the molecular skeleton and a transient shortening of the donor-acceptor-distance. Vibrational in-plane modes which reflect these geometry changes are coherently excited by the transfer independently of the environment. Subtle changes are only seen regarding the subsequent dephasing of the wavepacket motion. The same observations are made for 10-HBQ. These findings can be understood from the fact that the transfer path proceeds in the plane of the molecular skeleton. In this case the surrounding solvent molecules have hardly to move and frictional forces are only due to sliding of the HBT moieties along the inner solvation shell. The associated frictional forces should be substantially smaller than in cases where the solvent molecules have to change their site to let a moving moiety pass. The ESIPT is associated with a decrease of potential energy of about 0.3 eV and the slope of the PES along the reaction paths provides a reasonably strong driving force [17,23]. The interaction with the environment is therefore only a small perturbation with respect to the ESIPT. This holds as long as the polarity of the solvent is not too large and the solvent does not give rise to intermolecular hydrogen bonds. Protic or polar solvents are known to break the intramolecular hydrogen bond and to disrupt the ESIPT path or to change the energetics of specific species. This can lead to a different proton transfer cycle [33,37,53].

Wavepacket dynamics which involves large amplitude displacements of molecular moieties can be efficiently damped by the solvent. The  $110\text{ cm}^{-1}$  mode is strongly damped in cyclohexane solution. The  $41\text{ cm}^{-1}$  torsional mode is overdamped in solution and only observed in the gas phase. The initial  $\sim 250$  fs red shift of the emission found in cyclohexane solution [17] is tentatively interpreted as the remainder of the overdamped low frequency wavepacket motion associated with the torsion. Exponential signal contributions in the time range of a few hundred femtoseconds are often observed [52,54] and might be in

many cases the signatures of an overdamped vibrational wavepacket motion in low frequency modes.

The rapid damping of large amplitude vibrations goes in hand with a rapid dissipation of energy to the solvent which proceeds on a much faster time scale than the actual "cooling". This damping can completely change the character of a molecular process. The coherent wavepacket motion in the gas phase transforms to a rate like process in solution and the energy release to the solvent leads to a reduced transition probability at energy barriers. Since both effects reduce the speed of a process in solution, a dramatic deceleration compared to the isolated molecule can result. This happens in the case of the IC of HBT. The appearance of the  $S_0$  transketo tautomer with a significant yield indicates that in both environments the IC is associated with a large amplitude torsion around the central phenyl-thiazole bond. However, the IC and the back-isomerization of the  $S_0$  transketo tautomer proceed in the gas phase orders of magnitude faster than in solution. In addition, the gas phase transients show a coherent excitation of the normal mode corresponding to the torsional motion. This clearly indicates that at least the first step of the IC in the gas phase proceeds as a ballistic wavepacket motion whereas in solution friction does not allow for such a wavepacket evolution. For the ESIPT compound ortho-hydroxyacetophenone in the gas phase femtosecond ionization studies found an oscillatory signal contribution with a period of about 600 fs and a quite fast internal conversion with a time constant in the order of 5 ps that shortens with increasing excess energy [55]. We propose that the signal oscillations reflect a wavepacket motion in a torsional coordinate and that the IC mechanism is quite similar to HBT. This indicates that the IC due to a conical intersection along a torsional coordinate is a general feature of medium sized ESIPT compounds. The strong impact of friction on the torsion and thus on the IC explains also the results of our earlier studies on ortho-hydroxybenzaldehyde [47,56]. There a prolongation of the  $S_1$  lifetime by a factor of 13 was found in solution compared to the gas phase.

The transients for 10-HBQ in the gas phase show a  $\sim 10$ -fold accelerated IC compared to cyclohexane solution. We again find that in the gas phase additional normal modes are excited. They are assigned to out-of-plane deformations that do not contribute to the reduction of the proton donor-acceptor distance initiating the ESIPT, but lead to an out-of-plane conical intersection. The rigid molecular backbone of 10-HBQ does not allow for large amplitude torsional motions. The effect of the solvent is weaker than in HBT where the  $S_1$  lifetime changes by about two orders of magnitude. We think this reflects the fact that the torsion of HBT by  $90^\circ$  needs more distinct rearrangements of the solvation shell and stronger frictional forces apply than for the partial pyramidalization of 10-HBQ. This is in line with our main conclusion that frictional forces change the character of the dynamics completely if a large amplitude motion is involved that makes a proper rearrangement of the solvation shell necessary.



## ACKNOWLEDGMENT

This work was supported by the Austrian Science Fund within the framework of the Special Research Program F16 (Advanced Light Sources) and by the DFG-Cluster of Excellence: Munich-Centre for Advanced Photonics. D.J.N. would like to gratefully acknowledge support from the National Science Foundation and the Alexander von Humboldt Foundation.

## APPENDIX A:

### Model Function for Fitting Procedure

To extract the individual signal components in detail, every experimental trace was fitted with the model function  $S$  (Eq. A.1). The model function previously used [17] for the analysis of the molecular dynamics in cyclohexane solution was modified to account for the transketo formation and the low frequency torsional motion associated with the IC.

$$S = CC \otimes [S_{ESA} + (S_{SE} + D_{tor}) \cdot (1 + D_{WP}) + S_{ABS}] \quad (\text{A.1})$$

The total transient transmission signal  $S$  is given by the sum of the molecular response functions convoluted with the Gaussian cross correlation  $CC$ . The dynamics comprise ESA from the  $S_1$  state ( $S_{ESA}$ ), SE from the  $S_1$  keto tautomer ( $S_{SE}$ ),  $S_0$  transketo absorption ( $S_{ABS}$ ), and coherent wavepacket dynamics in the  $S_1$  keto tautomer  $D_{WP}$  and  $D_{tor}$ . The analytical expression for these contributions are given in Eq. (A.2).

$$\begin{aligned} S_{ESA}(t) &= A_{ESA} \cdot \exp(-t/\tau_{IC}) \cdot \Theta(t) \\ S_{SE}(t) &= A_{SE} \cdot \exp(-t/\tau_{IC}) \cdot \Theta(t - t_{PT}) \\ S_{ABS}(t) &= A_{ABS} \left[ a \exp(-t/\tau_{ISO}^{slow}) + (1-a) \exp(-t/\tau_{ISO}^{fast}) \dots \right. \\ &\quad \left. - \exp(-t/\tau_{IC}) \right] \cdot \Theta(t - t_{PT}) \\ D_i(t) &= A_i \cos(2\pi\nu_i t + \varphi_i) \cdot \exp(-t/\tau_i) \cdot \Theta(t - t_{PT}) \end{aligned} \quad (\text{A.2})$$

$D_{WP}$  and  $D_{tor}$  are both modeled by means of the oscillations  $D_i$ . The torsional motion leading to the conical intersection is identified with a strongly damped low frequency wavepacket motion  $D_{tor}$ . It has been shown that along the torsional coordinate, the Einstein B coefficient for stimulated emission varies significantly. This variation has the same effect on the stimulated emission intensity as a modulation of the  $S_1$  population. For the high-frequency oscillations such an effect has not been observed; they simply cause a periodic shift of the emission spectrum, and for probe wavelengths in the slope of the emission spectrum a periodic modulation of the simulated emission intensity. We describe the total signal contribution from  $S_1$  keto emission as the product of the population dynamics and the high-frequency wavepacket dynamics:  $(S_{SE} + D_{tor}) \cdot (1 + D_{WP})$ . In absence of the torsional motion and for a  $S_1$  lifetime

much longer than the oscillatory dephasing time (e.g. in cyclohexane), the product ansatz can be simplified to a sum of the stimulated emission and amplitude-scaled dynamics  $S_{SE} + D_{WP}^*$ .

The instantaneous excited state absorption  $S_{ESA}$  is taken into account by an exponential component with a negative valued amplitude  $A_{ESA}$ . The non oscillating part of the stimulated emission  $S_{SE}$  is modeled with a positive valued exponential component  $A_{SE}$  delayed by  $t_{PT}$  and describes the emission from the  $S_1$  keto tautomer. The delay  $t_{PT}$  is the proton transfer time. The ESA and SE signal both decay with the population in the  $S_1$  state, i.e. the time constant of the internal conversion  $\tau_{IC}$ . The excited state absorption sets in with a step at time zero modeled by the Heavyside function  $\Theta(t)$ , the delayed onset of the stimulated emission is modeled with a delayed Heavyside function  $\Theta(t - t_{PT})$ .

The rise of the  $S_0$  transketo absorption  $S_{ABS}$ , corresponding to the formation of the  $S_0$  transketo tautomer, occurs with the same time constant  $\tau_{IC}$  as the  $S_1$  population decays. Combined with the subsequent transketo decay [ $f(t)$ ] back to the  $S_0$  keto form which does not absorb in the investigated spectral region we obtain the following expression.

$$A_{ABS} [f(t) - \exp(-t/\tau_{IC})] \quad (\text{A.3})$$

A detailed analysis shows that the decay of the  $S_0$  transketo tautomer is non exponential (cf. Sec. III). A specific model function  $f(t)$  for the kinetics could not be derived, due to lack of knowledge about the exact mechanism of the back-isomerization and the  $S_0$  potential energy surface in the relevant coordinates. We find, however, that two coupled exponentials with rate constants of  $\tau_{ISO}^{fast} = 30$  ps and  $\tau_{ISO}^{slow} = 120$  ps describe the kinetics very well (cf. Sec. III).

$$f(t) = a \exp(-t/\tau_{ISO}^{slow}) + (1-a) \exp(-t/\tau_{ISO}^{fast}) \quad (\text{A.4})$$

The coherent wavepacket oscillations  $D_{WP}$  and  $D_{tor}$  are characterized by their frequencies  $\nu_i$ , amplitudes  $A_i$ , phases  $\varphi_i$  and dephasing times  $\tau_i$ . The oscillating components are due to wavepacket dynamics in the keto region of the  $S_1$  PES and therefore their emergence is modeled by the same time shift  $t_{PT}$  as the emission.

The convolution of the exponential functions with the Gaussian crosscorrelation can be expressed as the product with an appropriate error function. For practical reasons, the convolution of the oscillatory cos function with the Gaussian crosscorrelation was omitted since it only influences the amplitude of the cos function.

Best fits were judged from minimization of the quadratic error and visual inspection of the fit residuals. A Gauss-Newton or Levenberg-Marquart algorithm with numerical derivatives was used. While the Gauss-Newton iterations are faster and more convenient for iterative fitting, the Levenberg-Marquart algorithm tends to produce better fit results in case of many parameters. The quality of the fit, measured by the coefficient of

determination  $r^2 = 1 - \sigma^2(\text{data} - \text{fit}) / \sigma^2(\text{data})$  was typically  $> 0.9985$ .  $\sigma$  denotes the standard deviation.

When modeling the oscillations with damped cosine functions, often a slight mismatch of the fit function and the molecular dynamics for long delay times is found. The fit is more sensitive to the transient signal at earlier times due to the quadratic measure of the goodness of the fit and the decreasing amplitudes at later times. The dephasing of fit function and data is due to a slight change in the frequency of the molecular oscillation, which is probably caused by IVR and relaxation. We typically observe a reduction of the  $250 \text{ cm}^{-1}$  mode by about  $4 \text{ cm}^{-1}$  on a time scale of 2 ps. The visual inspection of the fit is very sensitive to these phase shifts, since  $\Delta\nu$  of  $4 \text{ cm}^{-1}$  over  $\Delta t$  2 ps corresponds to a phase shift of  $\sim 90^\circ$ . These changes in frequency were only minor and will not be discussed in detail. The tabulated frequencies are the values found without accounting for a frequency shift, to be comparable to previous analysis [17].

For transients recorded with a time resolution that is significantly slower than the typical proton transfer time of 35 fs, the delayed onset of ESA and SE can be neglected and no high frequency normal modes  $D_{WP}$  are resolved. The fit function can then be simplified to:

$$S = CC \otimes [S_{ESA/SE} + S_{ABS} + D_{tor}] \quad (\text{A.5})$$

This model has been applied to the time traces discussed in Sec. IV.

## APPENDIX B: Correction of anisotropy decay

The rotational depolarization of HBT and 10-HBQ molecules in the gas phase takes place within about 2 ps depending on the (rotational) temperature of the sample and is therefore more than one order of magnitude faster than in cyclohexane solution (50ps) [17]. For the recording of the wavepacket dynamics in solution, typically parallel polarization of pump and probe light is used since it yields larger signals and a higher modulation depth for the wavepacket oscillations. In the gas phase the fast rotational depolarization masks both the population and wavepacket dynamics. To disentangle them either the magic angle configuration of pump and probe polarizations can be used, or for a known anisotropy, measurements obtained for parallel polarization can be freed from the rotational dynamics. This method has been used to evaluate ‘‘early’’ measurements for 325 nm pump wavelength that were recorded with parallel polarization.

The signals of the transient transmission measurements for parallel ( $S_{\parallel}(t)$ ), perpendicular ( $S_{\perp}(t)$ ) and magic angle ( $S_{\ast}(t)$ ) polarization of pump and probe are related by  $S_{\ast}(t) = [S_{\parallel}(t) + 2S_{\perp}(t)]/3$  [43]. Measurements under magic angle configuration and parallel polarization are related by

$$S_{\parallel}(t) = S_{\ast}(t)[1 + 2r(t)], \quad (\text{B.1})$$

with  $r(t) = [S_{\parallel}(t) - S_{\perp}(t)] / [S_{\parallel}(t) + 2S_{\perp}(t)]$  depicting the anisotropy. A theoretical description of the anisotropy can be obtained from the theory of Felker et al. [57] for the rotation of free molecules using ab-initio data (B3LYP/6-311+G(d,p) [48,49]) for the rotational constants (HBT: 1.37, 0.283, 0.235 GHz; 10-HBQ: 1.19, 0.556, 0.380 GHz). The calculations we performed are based on a prolate symmetric top approximation, with the transition moment lying along the A axis. In this case, the coherences are of J-type, which means that  $\Delta K = 0$ , and therefore there are only three states coherently excited ( $J-1, J, J+1$ ) from an initial  $|J, K\rangle$  state. Summing over 1500 J states was found sufficient even for temperatures up to 500 K, i.e. the result did not change when summing over considerably more states. The time scale of the anisotropy is found to change with temperature, but the overall shape remains almost unchanged over a wide temperature range from 200 to 500 K. In this temperature regime, the calculated anisotropy can be perfectly modeled as a sum of three Gaussians. This allows to separate the rotational dynamics from the proton transfer dynamics for measurements obtained for parallel polarization, to convert parallel polarization measurements to magic

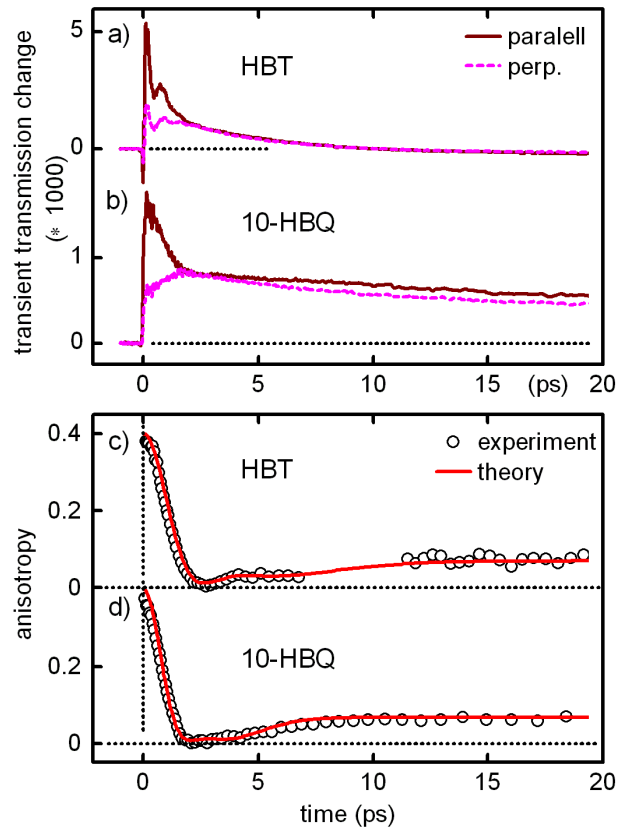


FIG. 10. (color online) Transient transmission change of (a) HBT and (b) 10-HBQ in the gas phase recorded with parallel and perpendicular polarization of pump and probe. The anisotropy calculated from the experimental data is compared to the theoretical prediction for the anisotropy decay from the free rotation of large molecules in the gas phase.

angle, and to obtain a fit value for the temperature from parallel polarization measurements, i.e. an internal gauge for the rotational temperature of the  $S_1$  excited state molecules.

The result of the calculations for 400 K are compared in Fig. 10 to the experimentally obtained anisotropy for 350 nm excitation and 560 nm probe, and match both for HBT and 10-HBQ very nicely. The appropriate description by the theory indicates that the initial assumption about the transition dipole moment fits very well. It can be concluded that both in HBT and 10-HBQ the transition dipole moments of  $S_0$  enol,  $S_1$  keto and  $S_0$  keto are very much oriented along the A axis of the molecules. This is even true for the  $S_0$  transketo tautomer of HBT. These findings are supported by the fact that the anisotropy starts at 0.4.

## REFERENCES

- [1] J. T. Hynes, J. P. Klinman, H.-H. Limbach, and R. L. Schowen, eds., *Hydrogen-Transfer Reactions* (Wiley-VCH, Weinheim, 2006).
- [2] E. T. J. Nibbering and T. Elsaesser, *Chem. Rev.* 104, 1887 (2004).
- [3] M. Pfeiffer, K. Lenz, A. Lau, T. Elsaesser, and T. Steinke, *J. Raman Spectrosc.* 28, 61 (1997).
- [4] T. Arthen-Engeland, T. Bultmann, N.P. Ernsting, M.A. Rodriguez, W. Thiel, *Chem. Phys.* 163 (1992) 43.
- [5] M. Gühr, M. Bargheer, M. Fushitani, T. Kiljunen, and N. Schwentner, *Phys. Chem. Chem. Phys.* 9, 779 (2007).
- [6] J. L. Herek, S. Pedersen, L. Bañares, and A. H. Zewail, *J. Chem. Phys.* 97, 9046 (1992).
- [7] E. T. J. Nibbering, J. Dreyer, O. Kühn, J. Bredenbeck, P. Hamm and T. Elsaesser, in *Analysis and Control of Ultrafast Photoinduced Reactions*, Springer Series in Chemical Physics 87, O. Kühn and L. Wöste, eds., Chapter 7 (Springer, Berlin, Germany, 2007).
- [8] A. Douhal, *Acc. Chem. Res.* 37, 349 (2004).
- [9] D. Madsen, J. Stenger, J. Dreyer, E. T. J. Nibbering, P. Hamm and T. Elsaesser, *Chem. Phys. Lett.* 341, 56 (2001).
- [10] M. Scherl, D. Haarer, J. Fischer, A. DeCian, J.-M. Lehn, and Y. Eichen, *J. Phys. Chem.* 100, 16175 (1996).
- [11] U. Schmidhammer, V. De Waele, S. Mintova, E. Riedle, and T. Bein, *Adv. Funct. Mater.* 15, 1973 (2005).
- [12] S. J. Schmidtke, D. F. Underwood, and D. A. Blank, *J. Phys. Chem. A* 109 7033 (2005).
- [13] S. Hammes-Schiffer and J. C. Tully, *J. Phys. Chem.* 99, 5793 (1995).
- [14] J. Waluk, *Acc. Chem. Res.* 39, 945 (2006).
- [15] H. Hosoi, H. Mizuno, A. Miyawaki, and T. Tahara, *J. Phys. Chem. B* 110, 22853 (2006).
- [16] C. Schrieffer, S. Lochbrunner, E. Riedle, and D.J. Nesbitt, *Rev. Sci. Instrum.* 79, 013107 (2008).
- [17] S. Lochbrunner, A. J. Wurzer, and E. Riedle, *J. Phys. Chem. A* 107, 10580 (2003).
- [18] C. Schrieffer, M. Barbatti, K. Stock, A. J. A. Aquino, D. Tunega, S. Lochbrunner, E. Riedle, R. de Vivie-Riedle, and H. Lischka, *Chem. Phys.* (2007), doi:10.1016/j.chemphys.2007.10.021.
- [19] S. Takeuchi, and T. Tahara, *J. Phys. Chem. A* 109, 10199 (2005).
- [20] S. Lochbrunner, K. Stock, and E. Riedle, *J. Mol. Struct.* 700, 13 (2004).
- [21] M. Barbatti, A. J. A. Aquino, H. Lischka, C. Schrieffer, S. Lochbrunner, and E. Riedle, in preparation for *J. Am. Chem. Soc.* (2008).
- [22] P. F. Barbara, L. E. Brus, and P. M. Rentzepis, *J. Am. Chem. Soc.* 102, 5631 (1980).
- [23] R. de Vivie-Riedle, V. De Waele, L. Kurtz, and E. Riedle, *J. Phys. Chem. A* 107, 10591 (2003).
- [24] M. Ikegami and T. Arai, *J. Chem. Soc., Perkin Trans.* 2 7, 1296 (2002).
- [25] T. Höfer, P. Kruck, T. Elsaesser, and W. Kaiser, *J. Phys. Chem.* 99, 4380 (1995).
- [26] R. S. Becker, C. Lenoble, and A. Zein, *J. Phys. Chem.* 91, 3509 (1987).
- [27] T. Elsaesser and W. Kaiser, *Chem. Phys. Lett.* 128, 231 (1986).
- [28] W. Frey, F. Laermer, and T. Elsaesser, *J. Phys. Chem.* 95 10391 (1991).
- [29] W. Al-Soufi, K.-H. Grellmann, and B. Nickel, *Chem. Phys. Lett.* 174, 609 (1990).
- [30] K. Stock, C. Schrieffer, S. Lochbrunner, and E. Riedle, *Chem. Phys.* (in print, 2008).
- [31] S. Lochbrunner, C. Schrieffer, and E. Riedle in *Hydrogen-Transfer Reactions*, J. T. Hynes, J. P. Klinman, H.-H. Limbach, and R. L. Schowen, eds., Chapter 11 (Wiley-VCH, Weinheim, 2006).
- [32] A. J. A. Aquino, H. Lischka, and C. Hättig, *J. Phys. Chem. A* 109, 3201 (2005).
- [33] T. Elsaesser and B. Schmetzer, *Chem. Phys. Lett.* 140, 293 (1987).
- [34] F. Laermer, T. Elsaesser, and W. Kaiser, *Chem. Phys. Lett.* 148, 119 (1988).
- [35] W. E. Brewer, M. L. Martinez, and P.-T. Chou, *J. Phys. Chem.* 94, 1915 (1990).
- [36] S. R. Vázquez, M. C. R. Rodríguez, M. Mosquera, and F. Rodríguez-Prieto, *J. Phys. Chem. A* 111, 1814 (2007).
- [37] C. A. S. Potter, R. G. Brown, F. Vollmer, and W. Rettig, *J. Chem. Soc. Faraday Trans.* 90, 59 (1994).
- [38] D. Polli, L. Lüer, and G. Cerullo, *Rev. Sci. Instrum.* 78, 103108 (2007).
- [39] L. Lüer, C. Manzoni, G. Cerullo, G. Lanzani, and M. Meneghetti, *Phys. Rev. Lett.* 99, 027401 (2007).
- [40] C. Kolano, J. Helbing, M. Kozinski, W. Sander, and P. Hamm, *Nature* 444, 469 (2006).
- [41] E. Riedle, M. Beutter, S. Lochbrunner, J. Piel, S. Schenkl, S. Spörlein, and W. Zinth, *Appl. Phys. B* 71, 457 (2000).
- [42] Z. Kozma, P. Baum, S. Lochbrunner, and E. Riedle, *Opt. Express* 11, 3110 (2003).
- [43] H. E. Lessing, A. von Jena, *Chem. Phys. Lett.* 42, 213 (1976).
- [44] M. Itoh, and Y. Fujiwara, *J. Am. Chem. Soc.* 107, 1561 (1985).
- [45] P. Fita, E. Luzina, T. Dziembowska, C. Radzewicz, and A. Grabowska, *J. Chem. Phys.* 125, 184508 (2006).
- [46] I. H. M. van Stokkum, D. S. Larsen, and R. van Grondelle, *Biochim. Biophys. Acta* 1657, 82 (2004).
- [47] K. Stock, T. Bizjak, and S. Lochbrunner, *Chem. Phys. Lett.* 354, 409 (2002).
- [48] Gaussian 03, Revision D.01, M. J. Frisch et al, Gaussian, Inc., Wallingford CT, 2004.

- [49] M. P. Andersson, and P. Uvdal, *J. Phys. Chem. A* 109, 2937 (2005).
- [50] A. Mordziński, J. Lipkowski, G. Orzanowska, and E. Tauer, *Chem. Phys.* 140, 167 (1990).
- [51] J. A. Organero and A. Douhal, *Chem. Phys. Lett.* 381, 759 (2003).
- [52] P. Vöhringer, R. A. Westervelt, T.-S. Yang, D. C. Arnett, M. J. Feldstein, and N. F. Scherer, *J. Raman Spectrosc.* 26, 535 (1995).
- [53] C. A.S. Potter, and R. G. Brown, *Chem. Phys. Lett.* 153, 7 (1988).
- [54] M. H. Vos, F. Rappaport, J.-C. Lambry, J. Breton, and J.-L. Martin, *Nature* 363, 320 (1993).
- [55] C. Su, J.-Y. Lin, R.-M. R. Hsieh, and P.-Y. Cheng, *J. Phys. Chem. A* 106, 11997 (2002).
- [56] S. Lochbrunner, T. Schultz, M. Schmitt, J. P. Shaffer, M. Z. Zgierski, and A. Stolow, *J. Chem. Phys.* 114, 2519 (2001).
- [57] P.M. Felker, J.S. Baskin, and A.H. Zewail, *J. Phys. Chem.* 90, 724 (1986).

## Anhang 10

**"The ultrafast internal conversion of 2-(2'-hydroxyphenyl)benzothiazole  
in the gas phase"**

M. Barbatti, A. J. A. Aquino, H. Lischka, C. Schrieffer, S. Lochbrunner, and E. Riedle

Manuskript eingereicht an J. Am. Chem. Soc. (2008)



## The ultrafast internal conversion of 2-(2'-hydroxyphenyl)benzothiazole in the gas phase

Mario Barbatti,<sup>1</sup> Adélia J. A. Aquino,<sup>1</sup> Hans Lischka,<sup>1</sup>  
Christian Schrieber,<sup>2</sup> Stefan Lochbrunner,<sup>2,†</sup> and Eberhard Riedle<sup>2</sup>

<sup>1</sup>*Institute for Theoretical Chemistry, University of Vienna, Waehringerstrasse 17, A-1090 Vienna, Austria*

<sup>2</sup>*Fakultät für Physik, Ludwig-Maximilians-Universität, Oettingenstr. 67, 80538 München, Germany*

<sup>†</sup>*Present address: Institut für Physik, Universität Rostock, Universitätsplatz 3, D-18055 Rostock, Germany*

Submitted July 13, 2007

E-mail: Mario.Barbatti@univie.ac.at, Hans.Lischka@univie.ac.at, Eberhard.Riedle@physik.uni-muenchen.de

**Abstract:** In a joint approach excited-state time-dependent density functional theory (TD-DFT) dynamics simulations (supported by second-order approximate coupled-cluster (RI-CC2) and multireference configuration interaction (MRCI) calculations) and transient absorption measurements in gas phase were performed for 2-(2'-hydroxyphenyl)benzothiazole (HBT) with the goal to understand its ultrafast internal conversion (IC) process. The results show that the reason for this ultrafast IC is due to the torsional isomerization taking place on a picosecond time scale. A S1/S0 conical intersection exists at a twisted-pyramidalized geometry and practically coincides with the twisted minimum in the S1 state. The dynamics simulations show that after electronic excitation to the S1 state and after fast excited state proton transfer (30-50 fs), HBT reaches the region of the S1/S0 crossing within about 500 fs, which will lead to ultrafast deactivation to the ground state. The measured IC time of 2.6 ps is about 40 times shorter in the gas phase than in cyclohexane solution, confirming the theoretical predictions. After the IC, HBT branches in two populations, one that rapidly closes the proton transfer cycle and another (trans-keto) that takes ~100 ps for that step.

### I. INTRODUCTION

Molecules exhibiting intramolecular proton transfer in the electronically excited state (ESIPT) are intensively studied to gain insight into fundamental photophysical and photochemical processes and to explore their potential to applications e.g. as dyes and sunscreens.<sup>1-8</sup> Detailed experimental and theoretical investigations for cases such as HBT (2-(2'-hydroxyphenyl)benzothiazole), 10-HBQ (10-hydroxybenzo[h]quinoline), and BP(OH)<sub>2</sub> (2,2'-bipyridyl)-3,3'-diol) show that the photo-initiated proton transfer proceeds as a ballistic wavepacket motion on a timescale of less than 50 fs and involves skeletal deformations that modulate the donor acceptor distance.<sup>7,9-13</sup> Although the ESIPT is very similar in all these molecules striking differences in the internal conversion (IC) rates are found. The IC times vary by almost four orders of magnitude from 150 fs for TINUVIN-P<sup>14</sup> to 0.86 ns for 2-(2'-hydroxyphenyl)-4-methylthiazole in methylcyclohexane.<sup>15</sup> The fluorescence spectra indicate that the energy gap between the ground and excited state varies only by a factor of 1.5 among the considered molecules and thus cannot account for such variations in the IC rate. For most investigated ESIPT molecules, the IC accelerates with increasing temperature<sup>1,5,15</sup> and a strong influence of the solvent has been observed.<sup>1,9</sup>

HBT (see Fig. 1) has served as a basic example for many ESIPT studies.<sup>1,6,10,12,16,17</sup> The proton transfer causes a substantial rearrangement in the electronic

structure, which leads to a strong Stokes shift of about 9000 cm<sup>-1</sup> in non-polar solvents.<sup>10</sup> Recently, we applied transient absorption experiments with 30 fs time resolution in combination with classical and wavepacket dynamics simulations to understand in detail how the proton transfer process takes place in HBT and in the related system 10-HBQ.<sup>12</sup> These investigations confirmed the ultrashort time scale (30-50 fs) of the ESIPT and gave a detailed picture of structural and mechanistic aspects of that process. The subsequent IC had not been the subject of those investigations.

In all these studies of HBT the molecule was considered as planar. The photoexcitation of HBT and the consequent biradical character connected with the thiazole and hydroxyphenyl rings due to the proton transfer could, however, trigger a torsional motion around the CC-interring bond (Fig. 1) in the same way as it occurs upon the photoexcitation of systems like ethylene,<sup>18</sup> stilbene<sup>19,20</sup> or azobenzene.<sup>21</sup> Recent theoretical investigations<sup>8</sup> on 2-(2'-hydroxyphenyl)benzotriazole (TIN-H), closely related to HBT, and our own preliminary theoretical investigations on HBT show that such a torsion actually occurs. This kind of motion plays a key role in photochemistry since it may lead to an avoided crossing or even to a conical intersection between the excited state and the ground state after twisting by 90° (see Refs. <sup>22-26</sup>), leading to ultrafast IC rate in the latter case. The measured fluorescence spectra (and consequently the long excited-state life time) show that this is not the

case for HBT in solution, at least not in the solvents that have been used so far.

In this work we again join experimental and theoretical efforts in order to study the dynamics of the IC process occurring in HBT and to investigate in particular the actual possibilities for ultrafast decay to the ground state along the lines discussed in the previous paragraph. In order to work out the effect of the torsional motion and separate it from environmental effects the pump-probe experiments with 20 fs time resolution have to be performed in the gas phase. Such measurements could be carried out successfully recently and the technical details have been reported.<sup>27</sup> The quantum chemical calculations are not less demanding because of the size of the HBT molecule and the occurrence of intersections between different energy surfaces. Moreover, it is our goal to simulate the dynamics of the IC process, which increases computational demands drastically. We want to show that this combination of state-of-the-art experimental and theoretical investigations reveals details of the photodynamical processes at a so far unprecedented level.

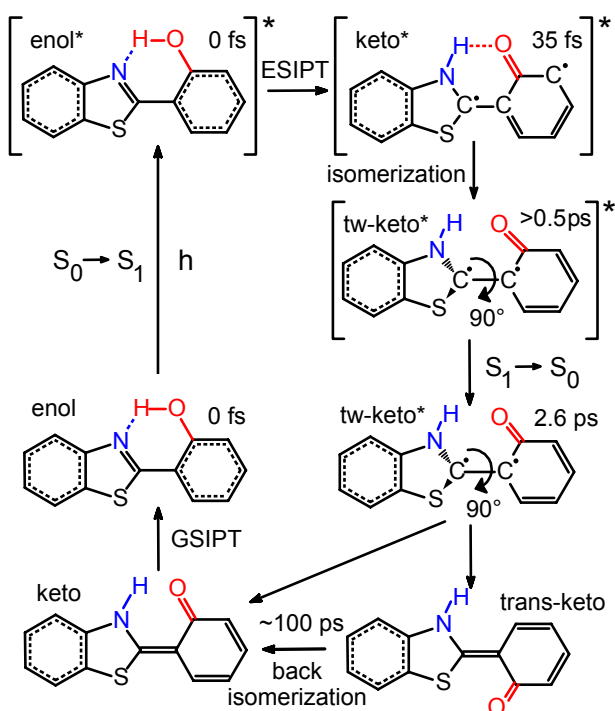


FIG.1: Schematic representation of the internal conversion in HBT in the gas phase. After the photo-excitation, excited state proton transfer (ESIPT) triggers the isomerization, which brings the system to a conical intersection. HBT returns to the ground state by internal conversion. The ground state relaxation, which includes the back proton transfer (GSIPT), completes the cycle. A long-lived population of trans-keto is also observed. The timings added to selected structures indicate their clock time starting with the absorption process of a photon in the enol form of HBT.

## II. COMPUTATIONAL DETAILS

Classical dynamics simulations were performed for HBT on the first singlet excited state ( $S_1$ ) energy surface. Thirty trajectories were simulated up to a maximum of 500 fs with a time step of 1 fs. The Velocity-Verlet algorithm<sup>28</sup> was applied to solve Newton's equations of nuclear motion. The Born-Oppenheimer energies and gradients were obtained by means of the TD-DFT approach<sup>29-31</sup> using the B3-LYP functional.<sup>32</sup> The SV(P) basis set<sup>33</sup> was applied for all atoms except the migrating hydrogen atom, to which the polarization functions of the full SVP basis set were added. Throughout this work, this basis set choice will be referred as SV(P)\*. Test calculations comparing the full SVP, the SV(P) and the SV(P)\* basis sets had shown that the p functions on the migrating hydrogen are important. Furthermore, comparison of results obtained with the SVP and TZVP basis sets<sup>6</sup> showed very good agreement in vertical and adiabatic excitation energies and optimized geometries, meaning that the SV(P)\* basis is an efficient candidate to be used in the extended on-the-fly dynamics calculations. The initial conditions for each trajectory were generated by sampling the coordinates and momenta so as to reproduce the ground-vibrational quantum harmonic distribution of the electronic ground state by means of a Wigner distribution. The ground-state geometries and velocities were used as initial conditions for the trajectories in the excited state.

The trajectory dephasing discussed in Section 0 was calculated in the following way. The  $S_1$ - $S_0$  transition energy as a function of time was collected from the trajectories. For each time interval  $i$  of 10 fs in the course of the dynamics the number  $n_i$  of trajectories with energy lying in the range  $E_{av} \pm \Delta E$  was counted, where  $E_{av}$  is the average transition energy in the interval  $i$  and  $\Delta E$  was set to 0.2 eV. The number  $n_i$  was normalized by the total number of points in the interval. Finally, the dephasing function  $\Phi(t)$  is defined by these values  $n_i$  normalized by their average value between 100 and 200 fs. During this period, the width only fluctuates around a constant value.

Additional calculations were performed for stationary points and cuts on the potential energy surface at the resolution-of-identity second-order approximate coupled-cluster (RI-CC2),<sup>34-36</sup> multireference configuration interaction (MRCI), and complete active space self-consistent field (CASSCF) methods. In the CASSCF calculations an active space composed of two electrons in two  $\pi$  orbitals was used (CASSCF(2,2)). State-averaging was performed over the ground state and the first singlet excited state (SA-2). The same CAS(2,2) was used as the reference space for the MRCI calculations, which included single and double excitations (MR-CISD). Higher-order excitation effects were taken into account by means of the Pople correction (+Q).<sup>37-39</sup> The main purpose of these calculations was the demonstration



of the existence of the  $S_1/S_0$  crossing for which the use of true multireference methods is crucial. In view of the size of HBT the 3-21G basis set<sup>40</sup> was selected for the MRCI and CASSCF calculations. In spite of the small size of this basis set it is expected that the main features of the  $S_1$  and  $S_0$  energy surfaces on torsion are reproduced correctly. The SV(P)\* was used in the RI-CC2 calculations.

Stationary points were obtained at the SA-2-CASSCF level with the routines for analytical energy gradient computation<sup>39,41,42</sup> as implemented in the COLUMBUS program package.<sup>43-45</sup> COLUMBUS was also used for the MRCI calculations. The excited-state dynamics simulations were performed with the NEWTON-X program<sup>46,47</sup> using TD-DFT energy gradients<sup>48</sup> provided by the TURBOMOLE program package.<sup>49</sup> All additional TD-DFT and RI-CC2 calculations were performed with the TURBOMOLE program package as well.

### III. EXPERIMENTAL DETAILS

The transient absorption of HBT in the gas phase and in cyclohexane solution is measured with a pump-probe spectrometer based on two noncollinearly phase matched optical parametric amplifiers (NOPAs). The spectrometer is able to detect changes in the optical density as small as  $10^{-6}$ .<sup>27</sup> In brief, two NOPAs<sup>50</sup> are pumped by a regenerative Ti:sapphire amplifier system (CPA 2001; Clark-MXR, Inc.). Chirped sum frequency mixing of the output of one NOPA with a fraction of the Ti:sapphire beam results in ultraviolet (UV) pump pulses at 325 nm.<sup>51</sup> The output of the second NOPA serves as probe beam. To obtain a sufficient sensitivity for low density gas phase samples a collinear focusing geometry with a long Rayleigh range and an interaction length of 50 mm is applied. For the gas phase experiments, HBT is heated to about 125°C in an evacuated cell to increase the vapor pressure. For measurements on HBT in cyclohexane a  $3 \cdot 10^{-3}$  M solution is pumped through a cuvette with an optical path length of 120  $\mu\text{m}$ . This allows us by just exchanging the cells to directly compare the molecular dynamics in the gas phase and in solution.

## IV. RESULTS AND DISCUSSION

### IV. A Experimental results

To understand the influence of the environment on the IC of HBT, we compare the photoinduced dynamics of the solvated and the isolated molecule. The steady state absorption and emission spectra in the gas phase are blue shifted by about 800  $\text{cm}^{-1}$  and 500  $\text{cm}^{-1}$  relative to the spectra in cyclohexane (not shown). The 325 nm pump pulses promote HBT both in solution and in the gas phase into the  $S_1$  state. The induced transmission change measured at 560 nm is shown in 0a for both cases. The initial transmission rise is due to the emission from the keto form in the electronically excited state, populated by the ultrafast

ESIPT.<sup>10</sup> In solution, only wavepacket dynamics but no change of the average signal is observed on the picosecond time scale and the stimulated emission decays with a time constant of  $\sim 100$  ps in good agreement with previous reports.<sup>1,52</sup> It reflects the deactivation to the electronic ground state. The weak oscillatory feature due to 108  $\text{cm}^{-1}$  wavepacket dynamics is observed in good agreement with values reported previously<sup>10</sup> (see 0c). It results from the coherent excitation of an in-plane bending vibration promoting the ESIPT.

The transient absorption of HBT in the gas phase also exhibits an initial transmission rise due to stimulated emission from the keto form (see 0a). The emission decays quite rapidly and vanishes within 5 ps. Contrary to the solution data a large but strongly damped low frequency oscillation is found in addition. A model function with a fast and a slow decay is fitted to the data giving time constants of 2.6 ps and 100 ps. The fast time describes the emission decay and characterizes the IC rate.

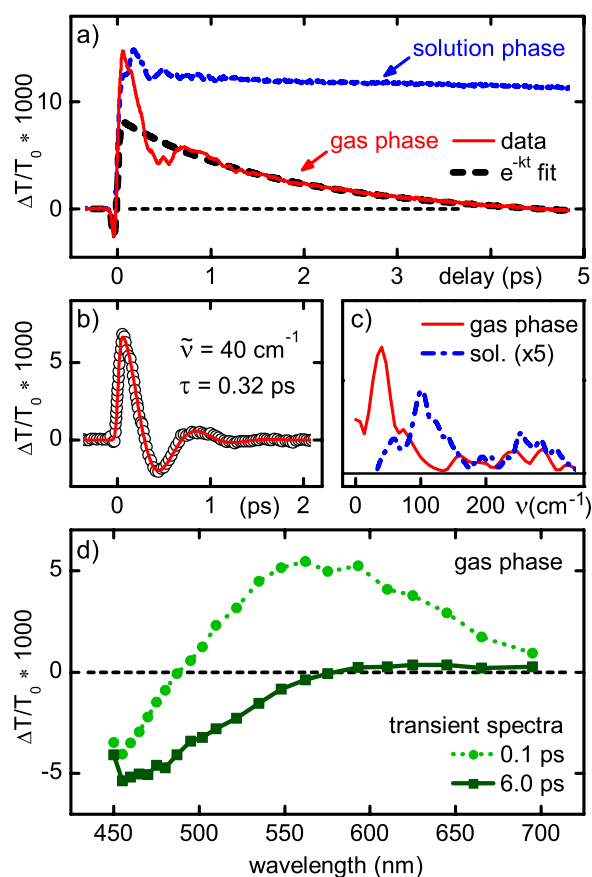


FIG.2: a) Time-resolved transmission change of HBT in cyclohexane (dotted) and in the gas phase (solid) at 560 nm after excitation at 325 nm. An exponential fit (dashed) to the gas phase data reveals an IC time of 2.6 ps. b) Residuum (circles) of the exponential fit modeled with a damped cosine function (solid). c) Fourier transformations of the gas phase (solid) and solution phase (dash dotted, scaled by a factor of 5) residuum. d) Transient spectra at a delay time of 0.1 ps and 6 ps reconstructed from time traces measured at different probe wavelengths.

Obviously, the IC in the gas phase is about 40 times faster than in the cyclohexane solution. After the emission decay a small residual absorption (negative going signal) remains which can be seen from the crossing of the experimental trace with the zero line at 4.5 ps. This absorption disappears on a time scale of 100 ps according to the fit. We tentatively assign it to a *trans*-keto tautomer in the electronic ground state. This tautomer was observed after photoexcitation of HBT dissolved in chloroform and has a broad absorption band around 460 nm.<sup>53</sup> Measurements at probe wavelengths between 450 and 690 nm were combined to reconstruct the transient spectrum at 0.1 and 6.0 ps (see Fig. 2d). The initial stimulated emission signal around 560 nm and the excited state absorption starting in the blue is changed within this time delay to a purely absorptive signal increasing toward 450 nm. The spectral shape suggests that we see the above mentioned 460 nm band and supports the proposed assignment to the *trans*-keto tautomer.

0b displays the residuum of the gas phase data after subtracting the exponential contributions, which exhibits a pronounced and strongly damped oscillatory behavior. Fitting an exponentially damped cosine function to the residuum reveals a frequency of 40 cm<sup>-1</sup> and a damping time of 0.32 ps in agreement with the residuum's Fourier transformation (see 0c).

#### IV. B Discussion of the experimental results

The femtosecond experiments find for HBT an acceleration of the IC in the gas phase by a factor of 40 compared to the cyclohexane solution. Also for *o*-hydroxybenzaldehyde (OHBA) a 13 times faster IC was observed in the gas phase compared to a cyclohexane solution.<sup>9,54</sup> This indicates that the faster IC in the gas phase may be a wide spread feature of ESIPT compounds. Viscosity is a rate limiting factor that is only present in solution. A reduction of the IC rate with increasing viscosity has already been observed for several ESIPT compounds like HBT<sup>1,52,55</sup>, 1'-hydroxy-2'-acetonephthone,<sup>5</sup> and (1-hydroxy-2-naphthyl)-s-triazine.<sup>56</sup> This was interpreted as a strong indication that a *cis*-*trans* isomerization promotes the IC.<sup>1,5,52,55,56</sup> In our femtosecond experiments this motion is for the first time directly observed. They show that after the ESIPT a wavepacket motion along the torsional coordinate exists leading to the region of the PES where a conical intersection should be located. This strongly supports the results of the trajectory calculations (see below), which find that the torsional mode is dominant on the picosecond scale and that a conical intersection does indeed exist near the 90° twisted structure. At the twisted conformation a branching can occur to the *cis*-keto or the *trans*-keto ground state (Fig. 1). The latter one cannot undergo fast proton back-transfer and is long lived.<sup>53</sup> This is in line with our observation of a 100 ps transient absorption which can be assigned to the *trans*-keto tautomer.

The large difference between the gas and solution phases can be rationalized as follows. In the gas phase the molecule propagates in a ballistic way directly to the region of very efficient IC. This motion is associated with a large-amplitude twisting of the entire molecular skeleton. In solution, it is strongly damped by friction due to interaction with the solvent molecules. Thereby the ballistic motion is stopped and the torsion evolves in a statistical fashion, similar to a Brownian motion.

#### IV. C Torsional coordinate and conical intersection

The discussion above shows that the torsional motion around the interring bond between the benzthiazole and hydroxyphenyl moieties plays a crucial role. Previous TDDFT/B3LYP calculations have shown<sup>6</sup> that for the keto form in the S<sub>1</sub> state one imaginary vibrational frequency existed, which was characterized by the interring torsion (note a corresponding misprint in Table 10 of Ref 6 where the value in brackets for the ππ\*(keto) form should be one instead of zero). Therefore, extensive investigations have been performed using several quantum chemical methods in order to establish the reliability of the obtained results. Such tests are especially important for the verification of the TD-DFT method for two reasons: first, this method may predict a wrong charge distribution for biradicaloid states, which would result in a wrong description of the potential energy along the torsional coordinate,<sup>57</sup> second, during the excited state relaxation the system may reach geometries with strong multireference character, which obviously cannot be adequately described with single-reference methods. Nevertheless, the computational efficiency and the availability of analytical gradients make TD-DFT one of the few methods available to perform on-the-fly excited-state dynamics simulations for systems as large as HBT and for simulation times as long as 500 fs. In view of these potential drawbacks, we have performed comparisons between relevant cuts on the HBT potential energy surfaces calculated with TD-DFT and other single- and multireference methods, in order to validate the theoretical level used in the dynamics calculations.

Four different theoretical methods have been employed for the characterization of the potential energy of HBT along the torsional coordinate. The resulting curves are displayed in Fig. 3a and b, and characteristic points are collected in Table 1. For each fixed torsional angle  $\theta$  the remaining coordinates were optimized for the S<sub>1</sub> state. The figure shows for all employed methods a similar flat but effectively barrierless S<sub>1</sub> curve. Due to the single-reference character of the TD-DFT and RI-CC2 methods, it was not possible to compute the energies for torsional angles larger than 70° and 60°, respectively. As will be discussed below, this is also true for the dynamics calculations. For both methods, however, the same trend of drastically reducing the S<sub>1</sub>-S<sub>0</sub> energy gap at

large torsions is observed. In Fig. 3c the torsional dependence of the Einstein coefficient  $B(\theta)$  for stimulated emission<sup>58</sup> is shown. It is calculated from the transition dipole moment  $\mu_{10}(\theta)$  (CASSCF values) as

$$B(\theta) = \frac{1}{6\epsilon_0\hbar^2} |\mu_{10}(\theta)|^2 \quad (1)$$

where  $\epsilon_0$  is the vacuum permittivity and  $\hbar$  is Planck's constant divided by  $2\pi$ . This torsional behavior will be discussed below.

The vertical excitation energies computed at the CASSCF and MRCI+Q levels are too high by 1.8 and 1.3 eV, respectively. This is a typical behavior of these methods already found for smaller molecules such as ethylene and butadiene<sup>59,60</sup> and extensive MRCI calculations have to be performed (see e.g. Ref.<sup>59,61</sup>) which are out of reach for molecules of the size of HBT. The performance of MRCI+Q improves considerably for the minimum to minimum and fluorescence transitions. For the conical intersection it provides the correct multireference character and is generally applicable in contrast to the TDDFT and RI-CC2 methods. Therefore, we use these methods especially for the direct proof of the existence of a conical intersection at a strongly twisted HBT structure.

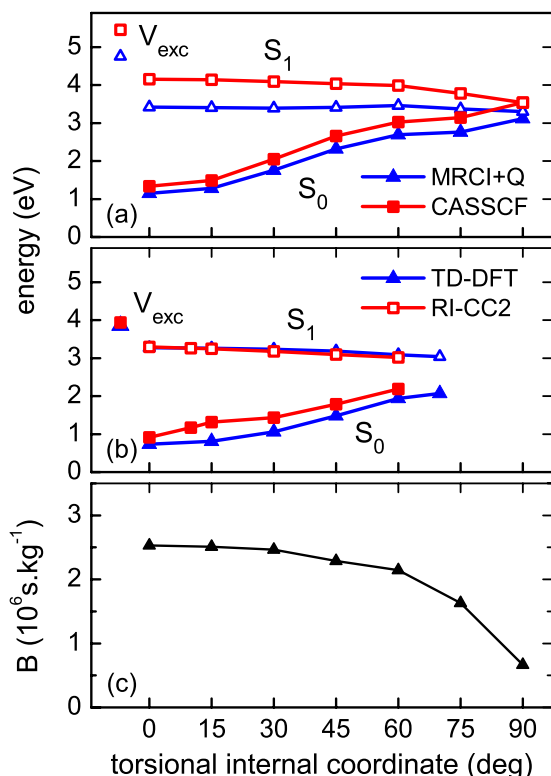


FIG.3: Potential energy curves along the relaxed torsional coordinate for HBT. (a) SA-2-CASSCF(2,2)/3-21G and MR-CISD+Q/SA-2-CASSCF(2,2)/3-21G. (b) TD-DFT(B3-LYP)/SV(P)\* and RI-CC2/SV(P)\*. (c) Einstein coefficient B for stimulated emission obtained at the SA-2-CASSCF(2,2)/3-21G level.

The complete torsional CASSCF and MRCI curves until 90° are displayed in Fig. 3a. The MRCI curves have been computed using the optimized CASSCF geometries. In the last point (90°), the restricted optimization at CASSCF level resulted in the degeneracy between S<sub>1</sub> and S<sub>0</sub> indicating the conical intersection. The CASSCF and the MRCI results using the CASSCF geometries showed that the effect of inclusion of dynamic electron correlation basically leads to a vertical shift in all points, producing almost parallel torsional curves.

The structure of HBT at the conical intersection at 90° is shown in Fig. 4c. Note that the reaction path was calculated in terms of natural internal coordinates<sup>62</sup> where the natural torsional internal coordinate is defined as the average of the four dihedral angles NCCC (cis), NCCC (trans), SCCC (cis), and SCCC (trans). Although this average coordinate is kept constant during the optimization procedure, each individual dihedral angle can change, as can be seen from the values of the NCCC (cis) and SCCC (cis) dihedral angles in Fig. 4c, 109° and 71°, respectively. This means that twisted structure also shows some degree of pyramidalization at the bridge carbon of the thiazole ring after the optimization. The optimization starting at this geometry but without any restriction does not significantly change this result. Fig. 4 shows the geometries optimized at the CASSCF level of the ground-state (enol, Fig. 4a) and the excited-state (keto, Fig. 4b). Geometries optimized at TD-DFT and RI-CC2 levels using triple- $\zeta$  quality basis set have been reported previously.<sup>6</sup> The change in the geometrical parameters indicates that the excited state relaxation affects mostly the hydroxyphenyl and the thiazole rings. In the twisted geometry, the biradical structure localizes across the CC bridge analogous to what also happens in TIN-H.<sup>8</sup>

#### IV. D Excited-state dynamics simulations

The barrierless path connecting the Franck-Condon region to the S<sub>1</sub>/S<sub>0</sub> conical intersection is a good indication for the possibility for HBT to display an ultrafast decay in the gas phase. The flatness of the excited state potential energy curve, however, could imply that HBT will not preferentially follow the torsional motion or if it does, it might take a relatively long time. This question can be addressed directly by performing excited-state dynamics calculations. As already mentioned above, thirty trajectories were computed at the TD-DFT(B3-LYP)/SV(P)\* level for a maximum of 500 fs. Most of trajectories (25) run at least 400 fs, but only six of them completed 500 fs without finishing by an error in the TD-DFT section of the calculation. This error was a consequence of the fact that the multireference character becomes important between 400 fs and 500 fs and it was not possible to continue the simulation using TD-DFT. Despite the fact that the simulations could not be completed at the TD-DFT level, the current results.

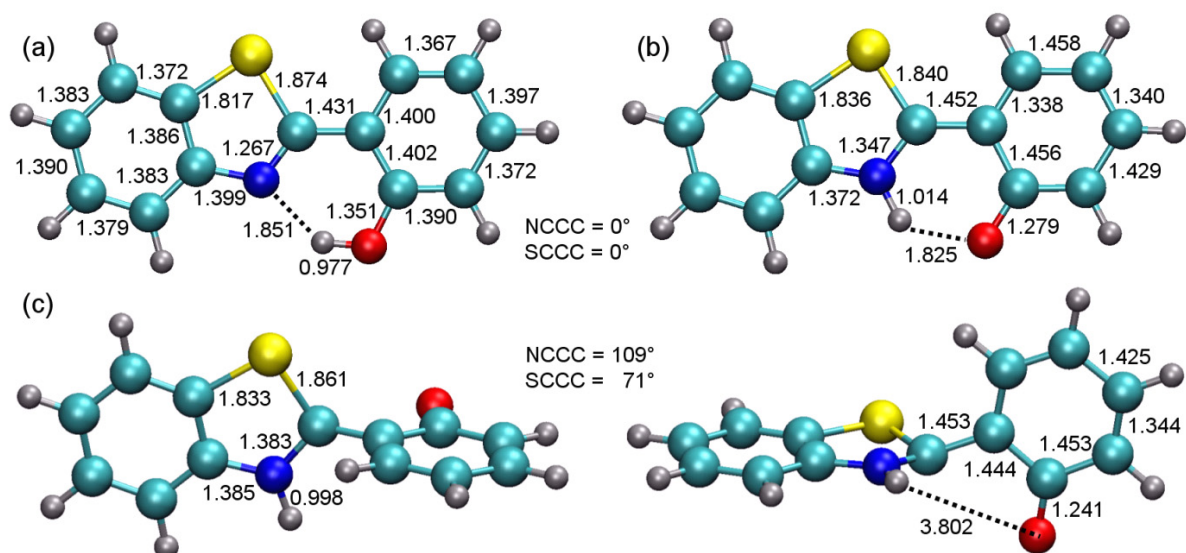


FIG.4: (a) Ground state (enol), (b) planar excited state (keto), and (c) twisted excited state optimized geometries at the CASSCF level. In (b) and (c) the bond lengths are given only for those bonds that change more than 0.01 Å in comparison to the ground state structure (a). (c) shows two different views of the same structure. All bond lengths in Å.

still show quite conclusively some interesting features that can help to understand the IC of HBT in the gas phase.

0 shows the excited-state potential energy as a function of time for one of the trajectories that completed 500 fs. The ground-state potential energy for the same geometries and the  $S_1$ - $S_0$  energy gap are shown as well. A quite similar general behavior is found for all trajectories. The fast oscillation in the potential energy corresponds to the hydrogen stretching motions. The dynamics starts in an approximately planar structure depending on the initial conditions and after 30 fs the proton transfer is observed. This first part of the dynamics has already been described in detail.<sup>12</sup> In the trajectory shown in 0, HBT remains essentially planar after the proton transfer for about 250 fs until the torsional motion starts to become effective. At 500 fs, the  $S_1$ - $S_0$  energy gap is reduced to 0.8 eV. Along the trajectory, the migrating hydrogen atom is moved out of the thiazole ring plane, indicating that the NH...O hydrogen bond still persists. At 500 fs this hydrogen has a dihedral angle of 41° with the thiazole ring and its distance to

the oxygen atom is 2.20 Å. The pyramidalization occurs simultaneously to the torsional motion, which is far from being rigid, as can be inferred from the values 62° and 84° of the NCCC (*cis*) and SCCC (*cis*) dihedral angles at 500 fs.

The analysis of the complete set of trajectories shows similar features. The average value of the  $S_1$ - $S_0$  energy gap is reduced from 3.6 eV to 1.1 eV between 0 fs and 500 fs (0b). As mentioned above, the pyramidalization causes an asymmetry between the NCCC (*cis*) and SCCC (*cis*) dihedral angles, as shown in 0a. While the SCCC angle reaches 68° at 500 fs, the NCCC angle is only 36° at the same time.

The overall motion is simply following the torsional potential depicted in 0b. This can be seen by investigating the average  $S_1$ - $S_0$  energy gap not as a function of time, as in 0b, but as function of the natural torsional internal coordinate. The average  $S_1$ - $S_0$  energy gaps as obtained from the dynamics and from the potential energy curve are plotted in 0. This figure shows a fast decrease of the gap from 3.64 eV to around 2.5 eV taking place in less than 100 fs, while HBT is still essentially planar.

Table 1. Energies of optimized structures and conical intersection of HBT.

Geometry	State	Energy (eV)				Exp <sup>c</sup>
		CASSCF	MRCI+Q	TD-DFT	RI-CC2	
Min $S_0$ (enol)	$S_0$	0.00	0.00	0.00	0.00	0.00
	$S_1$	5.46	4.76	3.86	3.94	3.68
Min $S_1$ (keto)	$S_0$	1.34	1.15	0.73	0.92	-
	$S_1$	4.16	3.42	3.28	3.30	-
Fluorescence	$S_1 \rightarrow S_0$	2.82	2.27	2.55	2.38	2.29
Conical intersection	$S_1/S_0$	3.54/3.54	3.11/3.30	~2.6 <sup>a</sup>	~2.6 <sup>b</sup>	-

<sup>a</sup> Average between the energies of the  $S_1$  and  $S_0$  states at 70°.

<sup>b</sup> Average between the energies of the  $S_1$  and  $S_0$  states at 60°.

<sup>c</sup> Experimental data from Ref. [53].

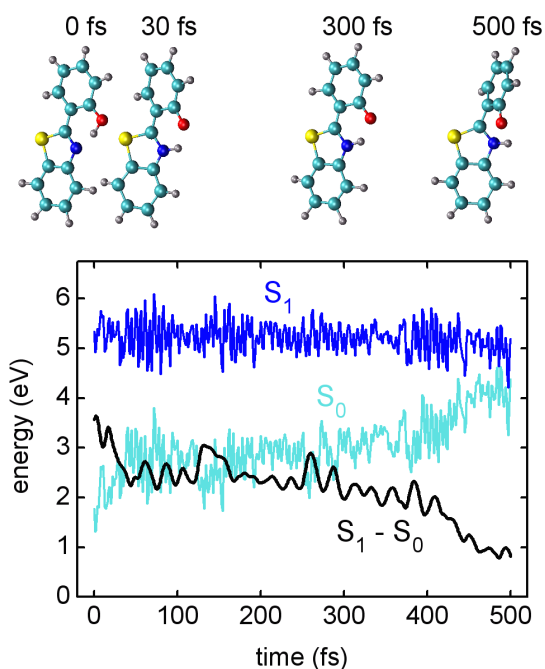


FIG.5:  $S_1$  and  $S_0$  energies of HBT for a selected excited state trajectory. The energy difference between the two states is also plotted. Snapshots are given at 0 fs (Franck-Condon region), 30 fs (proton transfer), 300 fs (beginning of torsional motion), and 500 fs (end of simulation).

This process corresponds to the ESIPT. After that, the energy gap just oscillates around the curve predicted by the torsional potential, moving to regions where the IC is more efficient.

#### IV. E General discussion

In the discussion of the experimental results it was shown that the temporal evolution of the transient absorption for HBT in gas phase is composed of an ultrafast exponential decay and a pronounced damped oscillation with sub-50  $\text{cm}^{-1}$  frequency (0a). There exist only two sub-100  $\text{cm}^{-1}$  normal modes in HBT, the overall butterfly vibration and the overall torsion. Both cannot be excited by optical excitation and are not associated with the ESIPT.<sup>13</sup> Which molecular distortion gives rise to the observed signal is now discussed in the light of the just-described dynamics calculations.

The fact that the dynamics leads toward the conical intersection explains the ultrafast IC. Even though the dynamics calculations do not reach the intersection for technical reasons, they come sufficiently close to it allowing the safe prediction that HBT will indeed reach if not the crossing itself, but at least regions of small energy gaps. The static CASSCF and MR-CI calculations discussed above prove the existence of the intersection. On the other hand, it is difficult to predict actual lifetimes from our trajectories. We want to note already at this point that the torsional motion

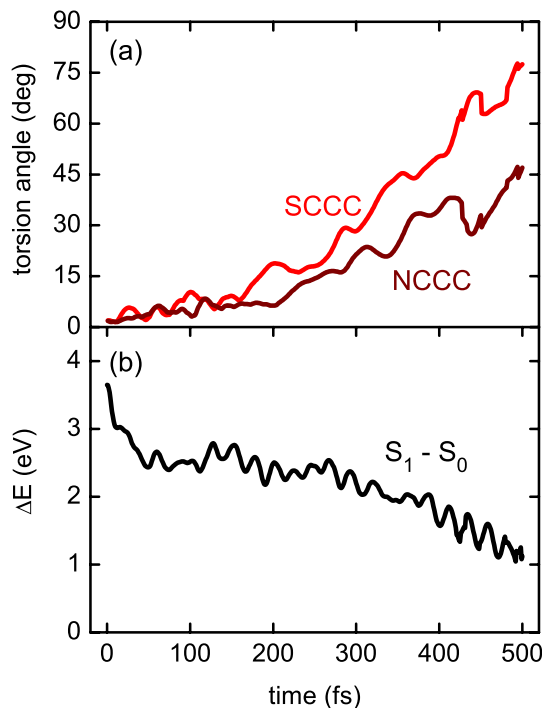


FIG.6: Average over all trajectories of (a) the absolute value of the NCCC (*cis*) and SCCC (*cis*) dihedral angles and (b) of the  $S_1$ - $S_0$  energy gap, both as a function of time.

should not be regarded as a simple one-dimensional process but that, on the contrary, several modes will be coupled. This will be, e.g. the interring stretching mode but also the weak afore-mentioned NH...O hydrogen bond and the NCCC and SCCC torsional angles. Our experience obtained from the analysis of several cases such as substituted ethylenes,<sup>25,63</sup> adenine,<sup>64</sup> and adenine model substances<sup>23,65</sup> is that the molecular motion does not proceed directly to the conical intersection but requires certain vibrational

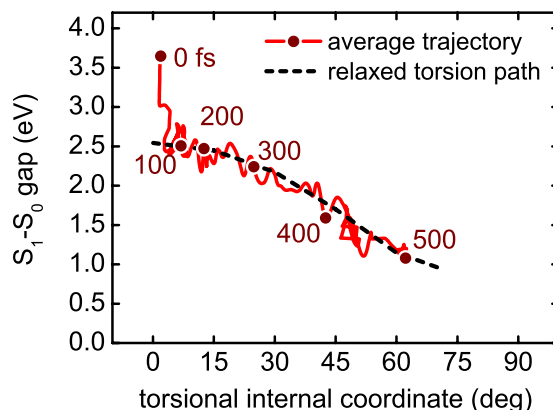


FIG.7:  $S_1$ - $S_0$  energy gap as obtained from the average trajectory and from the relaxed torsional potential energy curves as a function of the torsional internal coordinate. The full circles and the numbers next to them indicate the time in femtoseconds.

adjustments until the switching to the ground state can occur. Thus, it is expected that the actual decay time is significantly longer than the time for the first approach into the region of the conical intersection. Unfortunately, concrete lifetimes cannot be given from the calculations because of the already mentioned breakdown of the TDDFT approach in the neighborhood of the conical intersection.

The second point regards the initial low-frequency damped oscillation observed in the pump-probe experiment in the gas phase (see 0b). A comprehensive theoretical explanation would require the simulation of the pump-probe experiment, which is presently not feasible most of all because of the premature breaking of the TD-DFT trajectories. Therefore, the discussion will be limited to modulations of the intensity of the stimulated emission in the course of the torsional mode as a possible origin for the experimentally observed oscillations. The combination of three effects seems to be responsible for changes in the intensity of the stimulated emission along the torsional mode. The first one is the reduction of the Einstein coefficient  $B$  with the torsional angle displayed in 0c. This factor alone cannot explain the signal modulation because first the reduction in  $B$  is not sufficiently pronounced and second significant reductions in  $B$  are only observed at torsional angles above  $60^\circ$ , which are reached only after about 450 fs whereas the oscillatory mode analyzed in 0 shows the first minimum already at about 430 fs. 0 illustrates this situation by comparison of the experimental  $\Delta T/T_0$  signal divided by the exponential component with the time evolution of the normalized Einstein coefficient  $B$  in the time range that is relevant for the torsional mode.

The second effect contributing to the decrease in the emission intensity consists in an increasing dephasing of the trajectories along the torsional motion, which also leads to a reduction of the transmission signal. The trajectory dephasing (i.e. the

energy spreading) was obtained as explained in the Computational Details. The evolution of the dephasing  $\Phi(t)$  is plotted in 0. Small values of  $\Phi(t)$  imply a wider distribution of  $S_1/S_0$  energy gaps and consequently a reduction of the stimulated emission for a given transition energy. The dephasing shows an early decrease with increasing torsion already in its initial stage and also displays a substructure similar to the one found in the experiment.

The third effect contributing to the signal reduction is the coupling of the torsion with the other vibrational modes and the consequent flow of energy into these modes as it is described, e.g. in Ref.<sup>20</sup> will quickly reduce the amplitude of the torsional oscillations.

Together, the oscillation of the Einstein coefficient, the trajectory dephasing, and the energy dissipation will result in a damped oscillation of the stimulated emission probability.

Finally, it is worth calling attention to the trapping of HBT in the region near the  $S_1$  minimum. This is the main point for the very efficient IC. Were HBT able to reach the conical intersection, but quickly moved into other regions of the potential energy surface, as occurs for example in pyridone,<sup>66</sup> we might not expect any ultrafast behavior. This variability in the dynamical behavior is a key feature that can explain the fact mentioned in the Introduction that IC rates may change almost four orders of magnitude, while the energy gaps change by less than a factor of 1.5.

After the decay to the ground state at the twisted structure, HBT population splits in two branches, keto and trans-keto. While the keto isomer quickly returns to the initial enol isomer by ground state internal proton transfer (GSIPT), the trans-keto isomer takes about 100 ps in order to isomerize into the keto structure and then initiate the GSIPT (see Fig. 1). Note that the back isomerization is possible because in gas phase HBT remains vibrationally hot after the internal conversion.

## V. CONCLUSIONS AND FINAL REMARKS

From the combined theoretical and experimental investigations we gain a thorough understanding of the internal conversion processes following the excited-state intramolecular proton transfer in HBT. For a summary of the entire process cycle as determined by our investigations see Fig. 1. Motivated by preliminary quantum chemical investigations, transient absorption spectra for 2-(2'-hydroxyphenyl)benzothiazole (HBT) were measured in the gas phase for the first time and compared to existing results in cyclohexane. As a very important result it was observed that the internal conversion in gas phase takes place in only 2.6 ps while in solution it takes about 40 times longer. Moreover, the gas phase transient signal showed a damped, low-frequency oscillation superimposed to the exponential decay, a surprising finding which needed explanation as well.

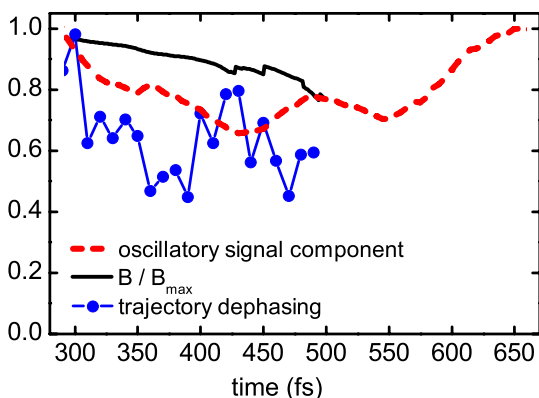


FIG.8: Oscillatory signal component ( $\Delta T/T_0$  divided by exponential component), average Einstein coefficient  $B/B_{\max}$ , and trajectory dephasing  $\Phi(t)$ . All quantities are given as a function of time.

Extended static quantum chemical calculations (MR-CISD, CASSCF, RI-CC2, and TD-DFT) were performed to characterize the stationary points in the ground and in the first excited state, as well as to investigate the relaxed torsional potential. Within the limitations of each method, all of them consistently show a flat but barrierless path starting at the relaxed planar excited state geometry (keto isomer) and leading down into the direction of large torsional angles where a conical intersection between ground and first excited state was expected. MR-CISD and CASSCF calculations allowed explicit verification of the conical intersection occurring at the twisted pyramidalized geometry.

Excited-state dynamics simulations were performed at the TD-DFT level. The results show a general trend of reduction of the  $S_1$ - $S_0$  energy gap due to the torsional motion in the first 500 fs. The torsional motion occurs simultaneously to the pyramidalization. Between 400 fs and 500 fs, the multireference character of the wavefunction starts to become important and it is not possible to continue the simulations due to failures in the TD-DFT method. Nevertheless, the comparison between the  $S_1$ - $S_0$  energy gaps predicted by the dynamics simulations and by the potential energy curves confirms that HBT follows the relaxed torsional path into the direction of large torsional angles where the IC rate is very efficient. However, it should be noted that HBT need not move directly into the conical intersection as it would be expected from a purely one-dimensional model. More possibly, it moves into a region of small energy gaps where the IC rate is relatively high. Therefore, the experimentally observed value of 2.6 ps fits well into the general picture given by the present dynamics simulations even though concrete calculated life times cannot be given. The strong low-frequency ( $40\text{ cm}^{-1}$ ) damped oscillations superimposed to the exponential decay could be tentatively explained by the dependence of the intensity changes of the stimulated emission due to the torsional motion.

After the internal conversion at the twisted structure, HBT splits into two populations, keto and trans-keto. While the first one immediately isomerizes to the enol form closing the proton transfer cycle, the latter requires about 100 ps to do so. This very large difference for completing the proton transfer cycles due a very clear branching event makes HBT especially interesting for control studies.

In summary, we think to have provided a good example for a fruitful cooperation between theory and experiment leading to insights not amenable to separate investigations.

## ACKNOWLEDGEMENTS

This work was supported by the Austrian Science Fund within the framework of the Special Research Program F16 (Advanced Light Sources) and Project P18411-N19. The calculations were partially per-

formed at the Linux PC cluster Schrödinger III of the computer center of the University of Vienna. Financial support by the DFG-Cluster of Excellence: Munich-Centre for Advanced Photonics is gratefully acknowledged.

## REFERENCES

- (1) Barbara, P. F.; Brus, L. E.; Rentzepis, P. M. *J. Am. Chem. Soc.* 1980, 102, 5631.
- (2) Laermer, F.; Elsaesser, T.; Kaiser, W. *Chem. Phys. Lett.* 1988, 148, 119.
- (3) Arthen-Engeland, T.; Bultmann, T.; Ernsting, N. P.; Rodriguez, M. A.; Thiel, W. *Chem. Phys.* 1992, 163, 43.
- (4) Sobolewski, A. L.; Domcke, W. *Chem. Phys. Lett.* 1993, 211, 82.
- (5) Douhal, A. *Acc. Chem. Res.* 2004, 37, 349.
- (6) Aquino, A. J. A.; Lischka, H.; Hättig, C. *Journal of Physical Chemistry A* 2005, 109, 3201.
- (7) Lochbrunner, S.; Schrieffer, C.; Riedle, E. In *Hydrogen-Transfer Reactions*; Hynes, J. T., Klinman, J. P., Limbach, H.-H., Schowen, R. L., Eds.; Wiley-VCH: Weinheim, Germany, 2006; pp 349.
- (8) Sobolewski, A. L.; Domcke, W.; Hättig, C. *J. Phys. Chem. A* 2006, 110, 6301.
- (9) Stock, K.; Bizjak, T.; Lochbrunner, S. *Chem. Phys. Lett.* 2002, 354, 409.
- (10) Lochbrunner, S.; Wurzer, A. J.; Riedle, E. *J. Phys. Chem. A* 2003, 107, 10580.
- (11) Takeuchi, S.; Tahara, T. *J. Phys. Chem. A* 2005, 109, 10199.
- (12) Schrieffer, C.; Barbatti, M.; Stock, K.; Aquino, A. J. A.; Tunega, D.; Lochbrunner, S.; Riedle, E.; de Vivie-Riedle, R.; Lischka, H. *Chem. Phys.* 2008, 347, 446.
- (13) Stock, K.; Schrieffer, C.; Lochbrunner, S.; Riedle, E. *Chem. Phys.* 2008, 349, 197.
- (14) Chudoba, C.; Lutgen, S.; Jentzsch, T.; Riedle, E.; Woerner, M.; Elsaesser, T. *Chem. Phys. Lett.* 1995, 240, 35.
- (15) LeGourriérec, D.; Kharlanov, V. A.; Brown, R. G.; Rettig, W. *Journal of Photochemistry and Photobiology a-Chemistry* 2000, 130, 101.
- (16) Elsaesser, T.; Kaiser, W. *Chem. Phys. Lett.* 1986, 128, 231.
- (17) de Vivie-Riedle, R.; De Waele, V.; Kurtz, L.; Riedle, E. *J. Phys. Chem. A* 2003, 107, 10591.
- (18) Barbatti, M.; Paier, J.; Lischka, H. *J. Chem. Phys.* 2004, 121, 11614.
- (19) Quenneville, J.; Martínez, T. J. *J. Phys. Chem. A* 2003, 107, 829.
- (20) Ishii, K.; Takeuchi, S.; Tahara, T. *Chem. Phys. Lett.* 2004, 398, 400.
- (21) Fujino, T.; Arzhantsev, S. Y.; Tahara, T. *J. Phys. Chem. A* 2001, 105, 8123.
- (22) Michl, J.; Bonačić-Koutecký, V. *Electronic Aspects of Organic Photochemistry*; Wiley-Interscience, 1990.
- (23) Barbatti, M.; Ruckebauer, M.; Szymczak, J. J.; Aquino, A. J. A.; Lischka, H. *PCCP* 2008, 10, 482.
- (24) Migani, A.; Robb, M. A.; Olivucci, M. *J. Am. Chem. Soc.* 2003, 125, 2804.
- (25) Barbatti, M.; Aquino, A. J. A.; Lischka, H. *Mol. Phys.* 2006, 104, 1053.
- (26) Ben-Nun, M.; Martínez, T. J. *Chem. Phys.* 2000, 259, 237.

- (27) Schriever, C.; Lochbrunner, S.; Riedle, E.; Nesbitt, D. J. *Rev. Sci. Instrum.* 2008, 79.
- (28) Swope, W. C.; Andersen, H. C.; Berens, P. H.; Wilson, K. R. *J. Chem. Phys.* 1982, 76, 637.
- (29) Bauernschmitt, R.; Ahlrichs, R. *Chem. Phys. Lett.* 1996, 256, 454.
- (30) Bauernschmitt, R.; Häser, M.; Treutler, O.; Ahlrichs, R. *Chem. Phys. Lett.* 1997, 264, 573.
- (31) Furche, F.; Ahlrichs, R. *J. Chem. Phys.* 2002, 117, 7433.
- (32) Becke, A. D. *J. Chem. Phys.* 1993, 98, 5648.
- (33) Schafer, A.; Horn, H.; Ahlrichs, R. *J. Chem. Phys.* 1992, 97, 2571.
- (34) Christiansen, O.; Koch, H.; Jorgensen, P. *Chem. Phys. Lett.* 1995, 243, 409.
- (35) Hättig, C. *Journal of Chemical Physics* 2003, 118, 7751.
- (36) Köhn, A.; Hättig, C. *J. Chem. Phys.* 2003, 119, 5021.
- (37) Pople, J. A.; Seeger, R.; Krishnan, R. *Int. J. Quantum Chem.* 1977, S 11, 149.
- (38) Bruna, P. J.; Peyerimhoff, S. D.; Buenker, R. J. *Chem. Phys. Lett.* 1980, 72, 278.
- (39) Shepard, R. *The Analytic Gradient Method for Configuration Interaction Wave Functions*. In *Modern Electronic Structure Theory*; Yarkony, D. R., Ed.; World Scientific: Singapore, 1995; Vol. 1; pp 345.
- (40) Binkley, J. S.; Pople, J. A.; Hehre, W. J. *J. Am. Chem. Soc.* 1980, 102, 939.
- (41) Shepard, R.; Lischka, H.; Szalay, P. G.; Kovar, T.; Ernzerhof, M. *J. Chem. Phys.* 1992, 96, 2085.
- (42) Lischka, H.; Dallos, M.; Shepard, R. *Mol. Phys.* 2002, 100, 1647.
- (43) Lischka, H.; Shepard, R.; Brown, F. B.; Shavitt, I. *Int. J. Quantum Chem.* 1981, S.15, 91.
- (44) Lischka, H.; Shepard, R.; Shavitt, I.; Pitzer, R. M.; Dallos, M.; Mueller, T.; Szalay, P. G.; Brown, F. B.; Ahlrichs, R.; Boehm, H. J.; Chang, A.; Comeau, D. C.; Gdanitz, R.; Dachsel, H.; Ehrhardt, C.; Ernzerhof, M.; Hoecht, P.; Irle, S.; Kedziora, G.; Kovar, T.; Parasuk, V.; Pepper, M. J. M.; Scharf, P.; Schiffer, H.; Schindler, M.; Schueler, M.; Seth, M.; Stahlberg, E. A.; Zhao, J.-G.; Yabushita, S.; Zhang, Z.; Barbatti, M.; Matsika, S.; Schuurmann, M.; Yarkony, D. R.; Brozell, S. R.; Beck, E. V.; Blaudeau, J.-P. COLUMBUS, an ab initio electronic structure program, release 5.9.1 2006, [www.univie.ac.at/columbus](http://www.univie.ac.at/columbus).
- (45) Lischka, H.; Shepard, R.; Pitzer, R. M.; Shavitt, I.; Dallos, M.; Müller, T.; Szalay, P. G.; Seth, M.; Kedziora, G. S.; Yabushita, S.; Zhang, Z. Y. *PCCP* 2001, 3, 664.
- (46) Barbatti, M.; Granucci, G.; Lischka, H.; Ruckebauer, M.; Persico, M. NEWTON-X: a package for Newtonian dynamics close to the crossing seam, version 0.13b 2007, [www.univie.ac.at/newtonx](http://www.univie.ac.at/newtonx)
- (47) Barbatti, M.; Granucci, G.; Persico, M.; Ruckebauer, M.; Vazdar, M.; Eckert-Maksic, M.; Lischka, H. *Journal of Photochemistry and Photobiology A: Chemistry* 2007, 190, 228.
- (48) Furche, F.; Ahlrichs, R. *The Journal of Chemical Physics* 2002, 117, 7433.
- (49) Ahlrichs, R.; Bär, M.; Häser, M.; Horn, H.; Kölmel, C. *Chem. Phys. Lett.* 1989, 162, 165.
- (50) Riedle, E.; Beutter, M.; Lochbrunner, S.; Piel, J.; Schenk, S.; Sporlein, S.; Zinth, W. *Applied Physics B-Lasers and Optics* 2000, 71, 457.
- (51) Kozma, I. Z.; Baum, P.; Lochbrunner, S.; Riedle, E. *Optics Express* 2003, 11, 3110.
- (52) Potter, C. A. S.; Brown, R. G.; Vollmer, F.; Rettig, W. *Journal of the Chemical Society-Faraday Transactions* 1994, 90, 59.
- (53) Brewer, W. E.; Martínez, M. L.; Chou, P. T. *J. Phys. Chem.* 1990, 94, 1915.
- (54) Lochbrunner, S.; Schultz, T.; Schmitt, M.; Shaffer, J. P.; Zgierski, M. Z.; Stolow, A. *J. Chem. Phys.* 2001, 114, 2519.
- (55) Vázquez, S. R.; Rodríguez, M. C. R.; Mosquera, M.; Rodríguez-Prieto, F. *J. Phys. Chem. A* 2007, 111, 1814.
- (56) Moriyama, M.; Kosuge, M.; Tobita, S.; Shizuka, H. *Chem. Phys.* 2000, 253, 91.
- (57) Wanko, M.; Hoffmann, M.; Strodet, P.; Koslowski, A.; Thiel, W.; Neese, F.; Frauenheim, T.; Elstner, M. *J. Phys. Chem. B* 2005, 109, 3606.
- (58) Hilborn, R. C. *American Journal of Physics* 1982, 50, 982.
- (59) Müller, T.; Dallos, M.; Lischka, H. *J. Chem. Phys.* 1999, 110, 7176.
- (60) Szalay, P. G.; Karpfen, A.; Lischka, H. *Chem. Phys.* 1989, 130, 219.
- (61) Dallos, M.; Lischka, H. *Theor. Chem. Acc.* 2004, 112, 16.
- (62) Fogarasi, G.; Zhou, X. F.; Taylor, P. W.; Pulay, P. *J. Am. Chem. Soc.* 1992, 114, 8191.
- (63) Zechmann, G.; Barbatti, M.; Lischka, H.; Pittner, J.; Bonačić-Koutecký, V. *Chem. Phys. Lett.* 2006, 418, 377.
- (64) Barbatti, M.; Lischka, H. *J. Am. Chem. Soc.* 2008, 130, 6831.
- (65) Barbatti, M.; Lischka, H. *J. Phys. Chem. A* 2007, 111, 2852.
- (66) Barbatti, M.; Aquino, A. J. A.; Lischka, H. *Chem. Phys.* 2008, 349, 278.
- (67) Lochbrunner, S.; Wurzer, A. J.; Riedle, E. *J. Chem. Phys.* 2000, 112, 10699.



# Danksagung

An dieser Stelle möchte ich mich bei allen herzlich bedanken, die mich rat- und tatkräftig während der Anfertigung dieser Arbeit unterstützt haben. Mein besonderer Dank gilt:

Herrn Prof. Eberhard Riedle für die hervorragende wissenschaftliche Betreuung und seinen großen persönlichen Einsatz. Die, nicht nur im Zusammenhang mit Publikationen, geführten Diskussionen erbrachten stets neue Impulse für meine Aktivitäten im Labor und am Schreibtisch. Insbesondere bedanke ich mich für das Vertrauen und die Förderung auch in den Phasen der Promotion, in denen noch nicht alles wie geplant funktionierte.

Herrn Prof. Wolfgang Zinth, der mir in vielen Gesprächen mit Rat und Tat zur Seite stand und die Ergebnisse meiner Arbeit stets mit Interesse verfolgte.

Herrn Prof. Stefan Lochbrunner für die intensive, gute und produktive Zusammenarbeit während all der Jahre, seine unendliche Geduld bei der Beantwortung aller meiner Fragen, die angenehme Büroatmosphäre und den freundschaftlichen Kontakt, der auch nach seinem Neustart in Rostock andauert.

Bei meinen Kooperationspartnern möchte ich mich herzlich für die erfolgreiche Zusammenarbeit bedanken. Insbesondere gilt mein Dank Frau Prof. Regina de Vivie-Riedle für die vielen Rechnungen, Diskussionen, Erklärungen und die gelungene Vermittlung theoretischer Konzepte in einer dem „Experimentator“ verständlichen Sprache, Herrn Prof. David Nesbitt für exzellente experimentelle Ratschläge und deren tatkräftige Realisierung, Herrn Prof. Hans Lischka und seinen Mitarbeitern für die großartige Unterstützung bei der Interpretation meiner Messdaten, Herrn Dr. Armin Ofial für die erfolgreiche und ausdauernde Zusammenarbeit bei der Deuterierung und NMR Charakterisierung, und Herrn Dr. Hans-Erik Swoboda sowie Herrn Gerald Jung für ihr großes persönliches Engagement bei der Inbetriebnahme, Wiederinbetriebnahme und dem täglichen Betrieb der CPAs und des IMPULSE Systems Nr. 001.

Ich danke allen Mitgliedern, Angestellten und Gästen des Lehrstuhls für die erfolgreiche und anregende Zusammenarbeit und die sehr angenehme Atmosphäre. Mein Dank gilt im Besonderen: Dr. Kai Stock, Dr. Peter Baum, Patrizia Krok, Christian Homann, Michael Opitz, Uli Schmidhammer, Tobias Schrader, Markus Breuer, Dr. Robert Huber, Dr. Peter Gilch, Dr. Ida Kozma, Dr. Tanja Bizjak, Dr. Igor Pugliesi, Stefan Schindlbeck, Andreas Charles Böck, Uwe Megerle, Anton Arsenyev, Rudi Schwarz, Alfons Stork – Harald Hoppe und Christian Hausmann für den Bau einer hervorragenden Probenzelle, und speziell Karl-Heinz Mantel für die freundliche Überlassung eines stillen Kämmerleins zum Schreiben.

Bei meinen Eltern, meinem Bruder und meiner Oma möchte ich mich für ihre beispiellose Unterstützung in allen Lebensbereichen abseits der Physik und für viele guten Ratschläge bedanken.



# Lebenslauf

Name: Schriever  
Vorname: Christian  
Geburtsdatum: 11. April 1977  
Geburtsort: Zwiesel  
Staatsangehörigkeit: deutsch

## Ausbildung:

1983 – 1996      Grundschule und Gymnasium, Zwiesel  
1996              Abitur, Gymnasium Zwiesel  
1996 – 1997      Studium Maschinenbau, Technische Universität München  
1997 – 2003      Studium Physik, Ludwig-Maximilians-Universität München  
2003              Diplom Physik, Ludwig-Maximilians-Universität München  
seit 2003        Wissenschaftlicher Mitarbeiter am Lehrstuhl für Biomolekulare  
Optik, Ludwig-Maximilians-Universität München